VNIVERSITAT DE VALÈNCIA

Searching for Dark Matter and Vector-like top quark production in the ATLAS experiment and AI-driven Anomaly Detection

Tesi Doctoral
Adrián Rubio Jiménez

IFIC Universitat de València - CSIC
Departament de Física Atòmica, Molecular i Nuclear
Programa de Doctorat en Física

Directors:
Dr. José Enrique García Navarro
Dra. María Moreno Llácer

València, 2025

Declaration

This dissertation is the result of my own work, except where explicit reference is made to the work of others, and has not been submitted for another qualification to this or any other university.

Adrián Rubio Jiménez

Just standing on the shoulders of giants

Acknowledgements

First, I would like to express my gratitude to my supervisors, who have made this Thesis possible. Thanks to María for trusting me to begin this journey, and to José for his guidance and support throughout these years. I consider myself very fortunate to have had the opportunity to belong to the ATLAS group at IFIC. In particular, thanks to Salva, Emma, and Carlos for contributing enormously to building a warm and friendly environment. You make working in this group a truly great experience.

I would also like to extend my thanks to the entire ATLAS collaboration. During these years, I have worked on different projects and collaborated with many people from whom I have learned a lot. Let me start by mentioning Stephen Jiggins for his guidance in the Qualification project and his patience during my first year. After that, I joined the Monotop group and had the pleasure of working with Rute, Nuno, and Maura from the LIP institute in Lisbon, not forgetting Annalisa and Ines during these last months. Thanks for your feedback and invaluable contributions in the analysis meetings and for fostering a friendly environment during these years. I also want to thank Trisha, Tim, and Chenliang for your help and commitment when rushing to finish the combination analysis according to the timeline of this Thesis. I truly enjoyed and learned so much working with you. And thanks to Roberto, Sascha, and Polina for sharing their knowledge and experience with me during the Anomaly Detection project. It was a great pleasure to collaborate with you, and I wish you all the best in your new projects.

Moving to a more personal side, I want to mention some people with whom I have shared special experiences during these years. Despite the first years were difficult, I had the unconditional support from Paolo, who was always available to help and to share his knowledge. I will never be able to thank him enough for his patience and advice. Then, I started to work with Josep, my monotoper mentor, who showed me how to face the challenges and problems with serenity and optimism. Thanks a lot for that and for much more. I also feel very fortunate to have had David and Marcos as colleagues during these years. Being together made us stronger, and this union has been essential for me to finish this Thesis.

In addition to them, I had the pleasure to meet different generations of students and postdocs in the group. For sure, the beginning was the most special period, which included to Fabio, Lorenzo, Mariam, and of course, Naseem. With the departure of very special people, some others arrived to fill the gap. Here, I want to highlight the Andalusian signings, Enrique and Marta, and the last Italian representatives, Francesco and Emanuela. Special thanks to the latter for sharing the office with me during these last months and making it a more pleasant place to work. Finally, when it is myself who is about to leave, a third generation arrived, lead by Clara and her lovely spirit. I do not want to forget about Morvan, Sonakshi, Tamar, Judith and the rest of colleagues that I had the pleasure to meet during these last months.

Quiero acabar mencionando a mis amigos y mi familia, pues se cierra otro capítulo y ellos son lo más importante de esta historia. Empiezo agradeciendo a Emilio, Juan y Teresa que hayan hecho tan especial estos últimos años. Gracias por tantas nuevas anécdotas, y gracias por darme un respiro de los problemas. Las semanas se hacen muy largas si no nos vemos el miércoles, y espero seguir tomando malas decisiones con vosotros siempre.

A mi novia, gracias por cuidarme, por quererme y por conocerme mejor que nadie. Gracias por enseñarme tanto sobre mí mismo, y gracias por convencerme de que lo malo acabaría pasando. Estas líneas en las que te menciono son la mejor parte de esta Tesis, del mismo modo que la mejor parte del día es llegar a casa contigo.

A mi hermana, mi ejemplo a seguir desde que tengo memoria. Gracias por seguir siendo mi referente, y por hacerme sentir orgulloso de ser tu hermano en cada paso que das. Gracias a mi cuñado, por convertirse en mi familia y por cuidar tanto a mi hermana. Y finalmente, a mis padres, por enseñarme con vuestro ejemplo qué es el esfuerzo, y por conseguir que nunca me faltara de nada. Gracias por darme la oportunidad de estudiar lo que me apasiona, y por confiar en mí en todo momento. Éste y todos los logros de mi vida son vuestros también.

Contents

Preface **1**

1 Standard Model of Particle Physics **3**
1.1 A brief history of Particle Physics . . . 3
1.2 The interactions of the particles . . . 8
1.3 The mass generation mechanism . . . 13
1.4 Limitations of the theory . . . 15

2 A look into New Physics **19**
2.1 The Dark Matter problem . . . 19
2.2 Vector-like Quarks . . . 33

3 The LHC and the ATLAS experiment **41**
3.1 The Large Hadron Collider . . . 41
3.2 The ATLAS detector . . . 46

4 Event generation and Monte Carlo simulation **53**
4.1 Simulation chain of proton-proton collisions . . . 53
4.2 Monte Carlo generators . . . 60
4.3 Simulated samples of the analyses . . . 61
4.4 Modeling uncertainties . . . 67

5 Event reconstruction **71**
5.1 Object reconstruction . . . 71
5.2 Object definitions in the analyses . . . 80
5.3 Experimental uncertainties . . . 84

6 Monotop search **87**
6.1 Event selection and background estimation . . . 88
6.2 Multivariate analysis . . . 90
6.3 Regions definition . . . 96
6.4 Statistical analysis: likelihood fit . . . 102

6.5 Results . . . 107
6.5.1 Background-only fit . . . 108
6.5.2 Signal-plus-background fit . . . 112
6.5.3 Exclusion limits on the signal models . . . 116

7 Combination of singly-produced vector-like top quark searches 125
7.1 Individual channels . . . 125
7.2 Combination strategy: fit setup and systematics treatment . . . 129
7.3 Results from the statistical combination . . . 131
7.3.1 Background-only fit . . . 132
7.3.2 Signal-plus-background fit . . . 136
7.3.3 Exclusion limits on the signal model . . . 137

8 Anomaly detection 145
8.1 Anomaly detection at the LHC . . . 145
8.2 The Dark Machines benchmark dataset . . . 147
8.3 Turning optimal classifiers into anomaly detectors . . . 150
8.3.1 Machine learning arquitectures . . . 151
8.3.2 Anomaly detection techniques explored . . . 154
8.4 Results . . . 161
8.4.1 Evaluation on the Dark Machines dataset . . . 161
8.4.2 Comparison to the Dark Machines challenge algorithms 164

9 Conclusions 167

A NN-based parameterization of theoretical uncertainties 171
A.1 Calibrated Likelihood Ratio Estimators . . . 172
A.2 Methodology . . . 173
A.3 Results . . . 179
A.4 Conclusions . . . 185

Resumen 189
R.1 Marco teórico: el Modelo Estándar . . . 189
R.2 Dispositivo experimental: LHC y ATLAS . . . 193
R.3 Simulación y reconstrucción de sucesos . . . 196
R.4 Búsqueda de sucesos mono-top . . . 199
R.5 Combinación de búsquedas de quarks vectoriales . . . 210
R.6 Detección de anomalías para buscar nueva física . . . 216
R.7 Conclusiones . . . 223

References 225

Preface

The Standard Model of particle physics is the theoretical framework that provides the best description of the subatomic world. This Thesis begins with a review of the Standard Model of particle physics from both historical and phenomenological perspectives. The discussion revisits the experimental milestones that culminated in the discovery of the Higgs boson and underlines the gauge structure that successfully describes strong, electromagnetic, and weak interactions. After discussing the main properties and predictions of this theory, some of its most relevant limitations are highlighted.

The work presented in this document is mainly related to two open problems in Particle Physics: the Dark Matter and the hierarchy problems. The astronomical and cosmological evidence for non-baryonic matter is synthesized, and the most popular Dark Matter candidates are briefly reviewed. Subsequently, Vector-Like Quarks are presented as an attractive solution to the hierarchy problem that naturally emerges in a variety of theories beyond the Standard Model. In both cases, a special emphasis is placed on the predictive power of a simplified Lagrangian that incorporate the minimal set of free parameters required to capture the essential collider phenomenology.

After the theoretical motivation, the experimental setting is detailed. Key accelerator concepts are explained to introduce the operating conditions of the collisions delivered by the Large Hadron Collider in the period between 2015 and 2018. The data analyzed in the two searches presented in this work correspond to proton-proton collisions at a center-of-mass energy of 13 TeV, with an integrated luminosity of 139 fb^{-1}. The main parts of the ATLAS experiment are described, starting from the different subdetectors and ending with the data acquisition system that triggers and record the proton–proton collision at a very high rate.

The event generation chain is explained in detail, from the initial scattering to the final state of the event, including the full detector response of all particles. The reconstruction of the particle kinematics and its identification from electronic signals are also discussed. These techniques are applied to both the simulations and the real data, for which the efficiencies need to be calibrated to perform data/MC comparisons and apply statistical inference in the posterior

analyses. Both the simulation and the reconstruction procedures introduce systematic uncertainties that are propagated to the final results.

The first search of this Thesis is published in Ref. [1] and is motivated by the Dark Matter problem. Since the Dark Matter is not expected to interact with the detector, the searches for Dark Matter require the production of additional objects to trigger the event. This analysis looks for events with a large missing transverse momentum together with a single top quark, referred to as mono-top events. Two simplified Dark Matter scenarios are considered, in which a different hypothetical mediator is produced in each case to couple the Dark Matter to the Standard Model particles. The results are also interpreted in the context of Vector-Like Quarks, in which a singly-produced top partner decays into a top quark and an invisible Z boson (decaying to neutrinos).

The second analysis presented in this document is published in Ref. [2]. It consists of the first combination of searches for a singly-produced vector-like top quark. This combination is part of the ambitious VLQ program of the ATLAS experiment, which has already explored extensively both the pair and single production modes of VLQs in different decay channels. The three combined channels are interpreted within the same simplified Lagrangian, allowing the combination to improve sensitivity across a broad parameter space. Despite no significant excess being observed in any of the analyses, small excesses in the individual searches could potentially be enhanced from this statistical combination.

The use of advanced Machine Learning techniques have being increasingly used in the last years at the High Energy Physics experiments, allowing to gain sensitivity in the new physics searches. However, the lack of evidences for new phenomena using traditional searches, in which a particular signal is searched for, has led to the development of more generic searches. The Anomaly Detection approach aims to identify deviations from the Standard Model background, without the need of a specific signal hypothesis. The third study of this Thesis, published in Ref. [3], aims to boost the development of Anomaly Detection in collider searches by reporpusing cutting-edge classifiers with minimal tuning. Data from the ATLAS experiment are not used in this study, but the analysis is performed using benchmark simulated datasets produced by the Dark Machines community. These data also correspond to proton-proton collisions at 13 TeV, but with a simplified ATLAS detector simulation.

Finally, an Appendix is included to describe a new technique to parameterize theoretical uncertainties with Neural Networks. This novel technique is tested in this study for hadronization uncertainties. Since the hadronization part of the collisions needs to be generated with approximate phenomenological models, this technique aims to capture in a set of weights the impact from using different hadronization models.

Chapter 1

Standard Model of Particle Physics

This chapter is dedicated to the phenomenological theory of Particle Physics. A historical context is given in the Section 1.1 together with a description of the particles that are considered as "fundamental". Section 1.2 presents the mathematical framework that describes the interactions among the fundamental particles, after which the mechanism that provides mass to the particles is explained in Section 1.3. The chapter ends with Section 1.4, where the main limitations of the theory are briefly described.

1.1 A brief history of Particle Physics

Particle Physics is the field that studies the fundamental particles of the Universe and their interactions. It is important to revisit the path that humanity went through to reach the current understanding about the structure of matter. Since ancient ages this topic only concerned to philosophers, and it was not until the 19th century that the first experiments were able to provide some evidence of an inner structure of the matter. An illustration of the main discoveries of Particle Physics is shown in Figure 1.1.

The discovery of the *electron* by Joseph John Thomson [5] in 1897 initiated the discovery of the fundamental particles, being identified as the component unit of the charged currents observed in the electromagnetism experiments. The electromagnetism theory was developed some decades before and the Maxwell's equations fully described the observed experiments from a macroscopic perspective. However, this theory did not provide information about the structure of matter, and the idea of a continuous material was still assumed to describe the light until the beginning of the 20th century. The first attempt to break with the classic picture came with Albert Einstein and his interpretation

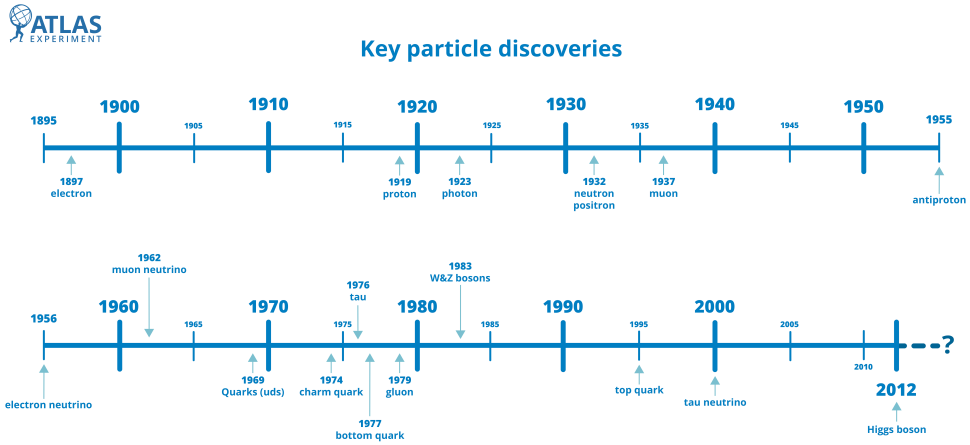

Figure 1.1: Illustration of the discovery of the fundamental particles [4].

of the photoelectric effect in 1905 [6], for which the presence of discrete energy packets (*quanta*) were needed to explain the phenomena. It was in 1923 when Arthur Compton confirmed the existence of the *photon* [7] as the carrier of the electromagnetic forces.

In parallel, the atomic model was being developed based on the gold foil experiment of Hans Geiger and Ernest Marsden [8]. This model already stated that atoms had their mass and electric charge concentrated in a small nucleus. Niels Bohr introduced in this model the idea of quantized energy levels for the electrons, which was able to explain the atomic spectra of the hydrogen atom. This model was so intuitive that even today is the basis to explain the atomic structure. The discoveries of the proton (1919) [9] and the neutron (1932) [10] by Ernest Rutherford and James Chadwick, respectively, allowed to understand the properties of the atoms and the nuclear reactions, as well as classify the observed isotopes.

Despite the success of the Quantum Mechanics describing the particles as probabilistic wave functions, a relativistic quantum theory was needed to derive Lorentz-invariant equations of motion and to handle the annihilation and creation of particles observed in the Nuclear and Particle Physics experiments. Thus, the Quantum Field Theories (QFTs) were developed, and the fundamental particles started to be interpreted as excitations of quantum fields within a Fock space. The Dirac equation [11], introduced by Paul Dirac in 1928, was the first relativistic equation to describe the electron as a quantum field with spin-1/2. This equation also predicted the existence of antimatter, required to account for its negative energy solutions. With identical characteristics than ordinary matter (mass, spin, etc.), antimatter should have opposite-signed quan-

tum numbers. Since such a particle had never been observed, it was considered as a theoretical challenge until the discovery of the *positron* (or *anti-electron*) by Carl Anderson in 1932 in a cosmic rays experiment [12].

At this point, it was supposed that the fundamental particles were the electron, the proton, the neutron and its anti-particles. However, the discovery of the *muon* in 1937 [13] showed that the list was not complete. The muon was a particle with the same charge as the electron but with a mass 200 times larger, and became the first of a series of particles that were discovered in the following years. The existence of the *neutrino* was confirmed in 1956, although the first evidence of its existence was provided by Wolfgang Pauli in 1930 when trying to preserve the conservation of the energy and momentum in the β-decay experiment [14]. This neutrino was associated to the electron, receiving the name *electron neutrino*. The *muon neutrino* was discovered in 1962 and the *tau neutrino* in 2000, which was more challenging since the *tau* particle was not discovered until 1975.

The neutrino was essential to understand the weak interactions, a short-range force whose properties were discovered during the first half of the 20th century, starting with the radioactivity experiments from Rutherford, Becquerel and the Curies in the 1890s. The first theory trying to describe the weak force was developed by Fermi in 1933 [15], in which the β-decay experiment from Pauli was explained with a four-fermion vertex. However, this theory did not explain how these interactions can break the *parity symmetry*, and a proper description should wait until the electroweak theory was developed in the 1960s by Sheldon Lee Glashow, Abdus Salam and Steven Weinberg [16–18]. This theory was able to unify the electromagnetic and the weak forces in a common mathematical framework, being confirmed with the discoveries of the $W^{\pm}$ and Z bosons in 1983 [19] at CERN, which mediate the weak interactions.

Driven by the development of particle accelerators, the second half of the 19th century started with the discovery of a large variety of particles, named *hadrons*, that presented different properties with an unclear relation among them. In this context, Murray Gell-Mann developed in 1961 a symmetry scheme in which the lighter hadrons discovered were classified in terms of valence *quarks* and *anti-quarks*. The first evidence of the existence of such quarks was provided in 1968, when the deep inelastic scattering experiments showed that the proton was a composite of more elementary particles. The final confirmation arrived with the discovery of the quarks *up*, *down* and *strange* in 1969. This scheme was called the *Eightfold Way* and was the first step for the development of the *quark model*. Thus, it was possible to explain the properties of the hadrons, and new quantum numbers and charges were defined, such as the "strangeness" and the "color charge". With the emergence of heavier hadrons, more quarks were postulated and discovered: the *charm* quark in 1974, the *bottom* quark in 1977, and the *top* quark in 1995.

The *Quantum Chromodynamic theory* (QCD) was built on top of the quark model [20, 21] in order to explain these new fundamental particles and its interactions. A different type of interaction was needed to explain the confinement of the quarks in the hadrons, or the protons and neutrons in the atomic nucleus. This force had to be short-ranged and much stronger than the electromagnetic or the weak forces. Such a force was named the *strong force* and was mediated by some postulated bosons called *gluons*[1]. The discovery of the *gluon* in 1976 by PETRA at DESY [22] confirmed the QCD theory.

The term *Standard Model* was coined in 1975 referring to the electroweak theory and when only four quarks had been discovered. The name remained to refer to the theoretical framework that contains the electroweak and the QCD theories, being able to predict the properties of the fundamental particles and their interactions as a function of 19 free parameters. Such free parameters include the masses of the elementary particles, which are explained by the Higgs mechanism. In order to confirm this mechanism and validate some predictions of the Standard Model, the existence of a new particle was necessary, being called *Higgs boson*. This last piece was discovered in 2012 [23, 24] at CERN, closing the list of the fundamental particles of the Standard Model.

The fundamental particles

The fundamental particles of the Standard Model are shown in Figure 1.2 (the anti-particles have opposite quantum numbers). The particles can be classified as fermions or bosons, which a priori only differ in its behavior when belonging to a many-particle system[2]. From statistical physics it is derived that bosons follow the Bose-Einstein statistics while fermions obey the Fermi-Dirac statistics, following the Pauli exclusion principle. This principle states that every occupied quantum state contains at most one fermion, which is the reason why the electrons in the atoms are distributed in different energy levels. This also affects the protons and neutrons in the atomic nucleus, which are also fermions. Thus, the exclusion principle controls the formation of matter, preventing a collapse of the particles into the same quantum state.

According to the Standard Model, quarks and leptons are the fermions constituting the observed matter in the universe. The fermions have spin-

[1] The name "gluons" came from "glue", since it was the responsible for keeping the quarks together.

[2] A physical state of indistinguishable particles is defined in quantum physics by a state vector, in which a permutation of two particles leaves the state of the system unaltered, up to a phase factor. Thus, an exchange of two bosons leaves the state invariant, while an exchange of two fermions introduces a minus sign.

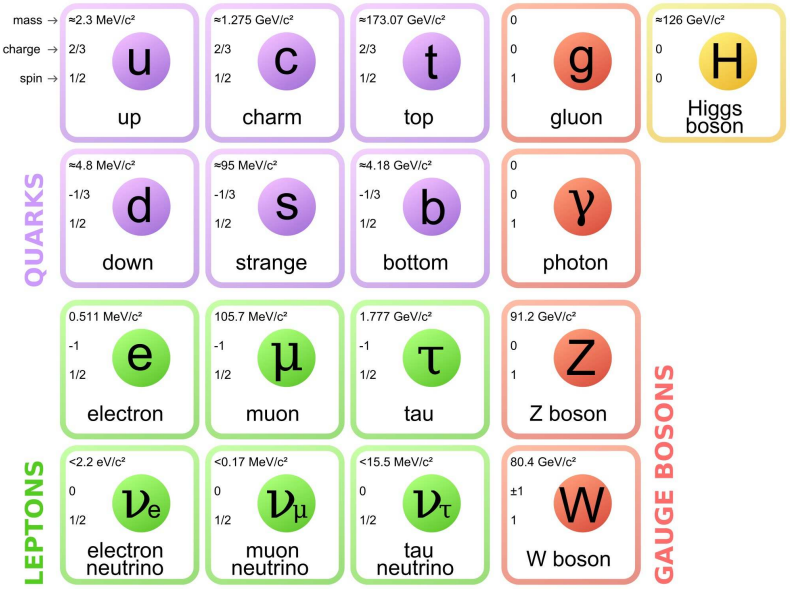

Figure 1.2: The particles of the Standard Model [25].

$1/2$[3], and they are organized in three families or generations, each one with two quarks and two leptons. The three fermionic families have identical properties and only differ in their mass and flavor quantum numbers. The first generation is the lightest one and does not decay further into other particles, being present in the stable matter. The second and third generations are heavier and less stable, being produced only in very energetic processes such as the cosmic rays or collisions in particle accelerators.

The leptons generations are formed by a charged particle (being the electron, the muon or the tau) and its associated neutrino, which is chargeless. The quarks have non-integer electric charges in units of the electron charge. According to the usual terminology, the quarks with electric charge $+2/3$ are called *up-type* quarks (up, charm and top) and the ones with electric charge $-1/3$ are called *down-type* quarks (down, strange and bottom). An important characteristic of quarks is that they have an additional quantum number called *color*, which can take three different values: red, green and blue.

On the other side, the *gauge bosons* are the particles that mediate the interactions between the fermions, which arise from the theory when requiring certain *gauge symmetry* (see next section). The photon is the massless and

[3]It is a common mistake to define the fermions as the particles with half-integer spin, while the bosons are defined as integer-spin particles. Such spin-statistics relation is actually observed in nature, but it appears as a consequence of the special relativity and the fact that the physical laws do not change under Lorentz transformations [26].

electrically neutral boson that mediates the electromagnetic force, which is a long-range force that communicate fermions with the same flavor. The two charged bosons W^+ and W^-, and the neutral boson Z, are the massive mediators of the weak force, which is a short-range interaction responsible for the radioactive decays. The weak interaction is the only one able to change the flavor of the fermions. The gluons are the massless color-charged bosons that mediate the strong force, which is the short-range interaction responsible for the confinement of the quarks in colorless bound states, such as the hadrons introduced previously. In fact, both the quarks and the gluons are never produced in isolation. Finally, the *Higgs boson* is the only scalar particle in the theory and is responsible for the mass generation of the fermions and the gauge bosons through the Brout-Englert-Higgs mechanism [27, 28], which will be explained at the end of this chapter.

1.2 The interactions of the particles

The interactions of the particles are described by the Lagrangian of the Standard Model, which is a function of the fields that contains the dynamical information of a system, from which the equation of motions can be derived. The Lagrangian describes the kinematic of the free particles, and their interactions emerge naturally as additive terms by requiring gauge invariance. An instructive example is the Quantum electrodynamics theory (QED), which is the abelian gauge theory that describes the electromagnetic interactions. The Lagrangian that describes the kinematics of a free electron is the Dirac equation [11]:

$$\mathcal{L}_{QED}^{\text{free}} = \bar{\psi}(i\gamma^\mu \partial_\mu - m)\psi \,, \tag{1.1}$$

where ψ is the electron field, m is the mass of the electron and γ^μ are the Dirac matrices.

There are some physical-motivated symmetries that are assumed for this Lagrangian, and each of them will be associated to a conservation law according to the Noether's theorem [29]:

- Time invariance leads to the conservation of the energy.
- Invariance under translations in space-time leads to the conservation of the momentum.
- Invariance under rotations in space-time leads to the conservation of the angular momentum.

Since the fields are complex but the Lagrangian and the associated probabilities are real quantities, it makes sense to require that the Lagrangian has to

be invariant under any phase transformation, which can be global or dependent of the space-time point.

$$\text{Global:} \qquad \psi \to \psi' = e^{i\alpha}\psi(x)\,, \tag{1.2}$$

$$\text{Local (or gauge):} \qquad \psi \to \psi' = e^{i\alpha(x)}\psi(x)\,. \tag{1.3}$$

The global phase transformation is satisfied and leads to the conservation of the electric charge, while the local phase transformation is not satisfied in the current form of the Eq. 1.1. However, it is possible to introduce a new term in the Lagrangian that compensates the non-invariance of the local phase transformation. This term will contain a new field A_μ that transforms as Eq. 1.5 to make the Lagrangian invariant, as shown in Eq. 1.6.

$$\bar{\psi}\partial_\mu\psi \to \bar{\psi}'\partial_\mu\psi' = \bar{\psi}\partial_\mu\psi - i\bar{\psi}\partial_\mu\alpha\psi\,, \tag{1.4}$$

$$A_\mu \to A'_\mu = A_\mu + \frac{1}{e}\partial_\mu\alpha(x)\,, \tag{1.5}$$

$$i\bar{\psi}(\partial_\mu + ieA_\mu)\psi \to i\bar{\psi}'(\partial_\mu + ieA'_\mu)\psi' = i\bar{\psi}(\partial_\mu + ieA_\mu)\psi\,. \tag{1.6}$$

This new field A_μ is the photon, which is the mediator of the electromagnetic interactions, which is massless by construction since a quadratic term $A_\mu A^\mu$ would break the gauge invariance. The complete Lagrangian of the QED is given by:

$$\mathcal{L}_{QED} = \bar{\psi}(i\gamma^\mu D_\mu - m)\psi - \frac{1}{4}F_{\mu\nu}F^{\mu\nu}\,, \tag{1.7}$$

where $D_\mu = \partial_\mu + ieA_\mu$ is the covariant derivative, and $F_{\mu\nu} = \partial_\mu A_\nu - \partial_\nu A_\mu$ is the electromagnetic field tensor that accounts for the kinematics of the free photon field.

It is said that the Lagrangian of the QED is invariant under the $U(1)_{EM}$ symmetry group, which is the group of the unitary phase transformations. This approach can be extended to the other interactions included in the Standard Model, where the Lagrangian is invariant under different gauge symmetries of a particular *Lie group*[4]. The basis of these groups are the *generators*, which are the elemental transformations of the algebra.

Taking into account these basic ingredients, a description of the different interactions of the Standard Model can be given. To provide a complete picture before describing each interaction the whole Lagrangian of the Standard Model is shown as follows:

[4]Lie groups are mathematical objects that describe continuous symmetries and allow to define an algebra to describe the invariant transformations of the fields.

$$\mathcal{L}_{SM} = \mathcal{L}_{QCD} + \mathcal{L}_{EW} + \mathcal{L}_{Higgs} + \mathcal{L}_{Yukawa}\,, \tag{1.8}$$

where each additive term correspond to a particular fundamental interaction. The first term is the Quantum Chromodynamic Lagrangian, which describes the strong interactions. The second term is the Electroweak Lagrangian, which describes the electromagnetic and the weak interactions. The third term corresponds to the Higgs Lagrangian, which contains the only scalar field of the Standard Model. The last Lagrangian corresponds to the Yukawa interactions that provide mass to the fermions.

The Quantum Chromodynamics

The strong force is described by the Quantum Chromodynamic theory, which is a non-abelian gauge theory. The Lagrangian of the strong force can be interpreted as a generalization of the QED Lagrangian explained before, for which the Lie group is $\mathrm{SU}(3)_C$. The subscript denotes the *color* as the conserved charge of this symmetry, which takes three values: "red", "blue" and "green". The generators of the $\mathrm{SU}(3)_C$ group are the 8 gluons that mediate the strong force. The gluons are massless and have color charge, which means that they can interact with themselves. This is in fact a characteristic of the non-abelian gauge theories, in which the infinitesimal transformations of the fields do not commute. Since leptons are not affected by the strong interaction, they are singlets of the $\mathrm{SU}(3)_C$ group.

The Lagrangian of the Quantum Chromodynamic theory is given by:

$$\mathcal{L}_{QCD} = \sum_f i\bar{q}_f\gamma^\mu D_\mu q_f - \frac{1}{4}G^a_{\mu\nu}G^{a\mu\nu}\,, \tag{1.9}$$

where the summatory runs over the quarks flavor. The covariant derivative is defined as $D_\mu = \partial_\mu + ig_sG^a_\mu T^a$, where g_s is the strong coupling constant, G^a_μ are the gluon fields (gauge bosons mediating the strong force), and T^a are the generators of the $SU(3)_C$ group. The field tensors are defined as $G^a_{\mu\nu} = \partial_\mu G^a_\nu - \partial_\nu G^a_\mu + g_s f^{abc}G^b_\mu G^c_\nu$, where f^{abc} are the structure constants of the SU(3) group.

The strong coupling constant, usually defined as $\alpha_s = g_s^2/4\pi$, is a running constant that decreases as the energy of the interaction increases, a property known as *asymptotic freedom*. At high energy scales (short distances), such as the energies in the LHC collisions, the quarks and gluons are almost free and the strong force can be described using perturbative methods, known as perturbative QCD or *pQCD*. As the energy decreases (and the distances are longer), the strong force becomes stronger and at some point, when it is energetically

favored, the vacuum is excited and new quarks and gluons are produced to form colorless states (hadrons), a process known as *hadronization*.

In fact, the vacuum is a very complex concept in the context of QCD. Apart from be filled of virtual quarks and gluons, as allowed by the Heisenberg uncertainty principle [30], the properties of the ground state and the violation of the CP symmetry is still unclear (and not measured). Without delving into detailed explanations, the presence of such strong CP violation would be parameterized by the vacuum angle θ_{QCD} [31, 32].

The electroweak interactions

The electroweak (EW) theory describes in the same mathematical framework two interactions with very different characteristics: the electromagnetic and the weak forces. The electromagnetic force is a long-range interaction that is responsible for the electric and magnetic phenomena while the weak force is a short-range interaction that is responsible for radioactive decays and neutrino interactions. In contrast to the strong interactions, both quarks and leptons are sensitive to the weak force. The first attempt to describe the weak force was the Fermi theory, which was a four-fermion interaction theory. However, this theory was not able to describe the observed parity violation in the weak interactions[5].

In this context, the *chirality* is an important concept. For massless fermions, the chirality coincides with the *helicity*, which is the projection of the spin of the fermion into the direction of its momentum. The left-handed and right-handed chiral components of the fermions are defined as $\psi_L = \frac{1}{2}(1-\gamma^5)\psi$ and $\psi_R = \frac{1}{2}(1+\gamma^5)\psi$, where $\gamma^5 = i\gamma^0\gamma^1\gamma^2\gamma^3$ is the chirality. The weak force is a chiral theory, which means that the left-handed and right-handed components of the fermions are affected differently by the weak force. In fact, it is said that the weak interaction maximally violates the parity symmetry since only the left-handed components of the fermions are affected by the weak force.

The Vector-Axial theory (V-A theory) was developed to solve the parity problem, which only involves the left-handed projections of the fermions in its Lagrangian. Nevertheless, the V-A theory still violates unitarity, and it is not renormalizable, which is solved in the electroweak theory.

The gauge group of the electroweak theory is $\mathrm{SU}(2)_L \times \mathrm{U}(1)_Y$, where the L subscript indicates that only the left-handed components of the fermions are affected by the weak force, and the Y subscript indicates the *hypercharge*, defined as $Y = Q - T_3$. $\mathrm{U}(1)_Y$ is the symmetry group of the unitary phase transformations of the complex fermion fields (such as the gauge symmetry of the QED). The weak isospin (T_3) is the quantum number associated to the

[5] An interaction violates parity symmetry if its Lagrangian is not invariant under the transformation $\vec{x} \to -\vec{x}$.

$\mathrm{SU}(2)_L$ gauge symmetry of the weak force, in the same way as the intrinsic spin of the particles is the quantum number associated to the SU(2) symmetry of the rotations. The weak isospin is conserved in the weak interactions in the same way the electric and color charges are conserved for the electromagnetic and strong interactions, respectively. The fermion representations associated to the $\mathrm{SU}(2)_L$ symmetry are doublets of their left-handed components in the form:

$$\begin{pmatrix} \nu_l \\ l \end{pmatrix}_L , \quad l = e\,, \mu\,, \tau\,, \tag{1.10}$$

$$\begin{pmatrix} q_u \\ q_d \end{pmatrix}_L , \quad q_u = u\,, c\,, t\,, \quad q_d = d\,, s\,, b\,, \tag{1.11}$$

where the lower component has a weak isospin of $T_3 = -1/2$ and the upper component has $T_3 = +1/2$. On the other hand, the right-handed components of the fermions are singlets of the $\mathrm{SU}(2)_L$ symmetry. The right component of the neutrinos is not considered since they have not been observed. The Lagrangian of the electroweak theory is also the sum of the fermion and the gauge boson terms, which are given by:

$$\mathcal{L}_{EW} = \mathcal{L}^V_{EW} + \mathcal{L}^f_{EW}\,, \tag{1.12}$$

$$\mathcal{L}^V_{EW} = -\frac{1}{4} W^a_{\mu\nu} W^{a\mu\nu} - \frac{1}{4} B_{\mu\nu} B^{\mu\nu}\,, \tag{1.13}$$

$$\mathcal{L}^f_{EW} = \sum_{\psi_L} i\bar{\psi}_L \gamma^\mu D^a_\mu \psi_L + \sum_{\psi_R} i\bar{\psi}_R \gamma^\mu D^b_\mu \psi_R\,. \tag{1.14}$$

The field tensors from Eq. 1.13 are defined as $B_{\mu\nu} = \partial_\mu B_\nu - \partial_\nu B_\mu$ and $W^i_{\mu\nu} = \partial_\mu W^i_\nu - \partial_\nu W^i_\mu + g\epsilon^{ijk} W^j_\mu W^k_\nu$, where ϵ^{ijk} are the Levi-Civita symbols. Similarly to QCD, this last term implies self-interactions among the weak bosons since $\mathrm{SU}(2)_L$ is a non-abelian gauge theory. The first summatory of the fermionic Eq. 1.14 runs over the left-handed fermions and the second summatory over their right-handed components, except for the neutrinos. The covariant derivatives are defined as:

$$D^a_\mu \psi_L = \left[\partial_\mu + ig\frac{\sigma_k}{2} W^k_\mu + ig' B_\mu Y\right] \psi_L\,, \tag{1.15}$$

$$D^b_\mu \psi_R = \left[\partial_\mu + ig' B_\mu Y\right] \psi_R\,, \tag{1.16}$$

where g and g' are the weak coupling constants, Y is the hypercharge operator and σ_k are the Pauli matrices. Again, the 1-spin boson fields are introduced to ensure the gauge symmetry of the Lagrangian. Unitary transformations of these gauge bosons (W^1, W^2, W^3, B) provide the physical eigenstates of the

mediators mentioned in the first section. Since the Y and σ_3 matrices are diagonal, the B and W^3 boson fields do not mix different components of weak isospins and will be related with the photon (A_μ) and the Z boson, while the W^1 and W^2 are related with W^+ and W^-. Such unitary transformations are given by:

$$\begin{pmatrix} Z_\mu \\ A_\mu \end{pmatrix} = \begin{pmatrix} \cos\theta_W & -\sin\theta_W \\ \sin\theta_W & \cos\theta_W \end{pmatrix} \begin{pmatrix} W^3_\mu \\ B_\mu \end{pmatrix} , \tag{1.17}$$

$$W^\pm_\mu = \frac{1}{\sqrt{2}}(W^1_\mu \pm iW^2_\mu) , \tag{1.18}$$

with Weinberg angle θ_W defined as $\tan\theta_W = g'/g$.

The interactions mediated by the $W^\pm$ bosons can mix the flavor of the fermions. The flavor mixing of quarks comes from the fact that their flavor eigenstates (d', s', b') are not the same as their physical eigenstates (d, s, b). This mixing is given by the Cabibbo-Kobayashi-Maskawa (CKM) matrix from Eq. 1.19, a unitary transformation with 4 free parameters that are determined experimentally: 3 mixing angles and 1 CP-violating phase.

$$\begin{pmatrix} d' \\ s' \\ b' \end{pmatrix} = \begin{pmatrix} V_{ud} & V_{us} & V_{ub} \\ V_{cd} & V_{cs} & V_{cb} \\ V_{td} & V_{ts} & V_{tb} \end{pmatrix} \begin{pmatrix} d \\ s \\ b \end{pmatrix} . \tag{1.19}$$

The CKM matrix is almost diagonal, which means that the mixing between quarks of the same family are preferred in the weak interactions. In particular, the element V_{tb} is very close to the unity, meaning that the top quark couples almost exclusively to a bottom quark.

In the lepton sector, a charged lepton only couples to its associated neutrino. Since the Standard Model assumes that the flavor representation of neutrinos coincide with the physical representations, no flavor mixing is considered[6]. Consequently, the total lepton number and the lepton flavor are preserved quantities of any interaction in the Standard Model.

1.3 The mass generation mechanism

The lagrangians of the strong and the electroweak interactions have been described in their massless form. Including masses with quadratic terms of the fields as observed in Eq. 1.7 for the QED Lagrangian would break the gauge invariance, but it is an experimental fact that the particles have mass. It is

[6] This assumption is the direct consequence of assuming that neutrinos do not have masses. However, it has been proven that neutrinos have very small masses and their flavor eigenstates are mixed. This is known as *oscillations*[33]. The analogous to the CKM matrix for the neutrinos is given by the Pontecorvo-Maki-Nakagawa-Sakata (PMNS) matrix.

needed to break the gauge symmetry to introduce the mass terms preserving the unitarity and the renormalizability of the theory.

The method to achieve it is the Brout-Englert-Higgs mechanism [27, 28], which is based on the spontaneous symmetry breaking (SSB) of the electroweak theory. A complex scalar field (Higgs field) with a non-zero vacuum expectation value is introduced, whose interactions with the gauge bosons and the fermions generate the masses of the particles.

The Higgs Lagrangian is given by:

$$\mathcal{L}_{Higgs} = (D_\mu \phi)^\dagger (D^\mu \phi) - V(\phi), \qquad V(\phi) = \mu^2 \phi^\dagger \phi - \lambda (\phi^\dagger \phi)^2 \,, \tag{1.20}$$

where ϕ is the Higgs field and $V(\phi)$ is the Higgs potential. The covariant derivatives of the scalar field is the same as in 1.15. The μ^2 coefficient of the quadratic[7] term of the Higgs field is related to its mass. The λ coupling needs to be positive to have a potential bounded from below, while μ^2 could be positive or negative. The $\mu^2 > 0$ case would provide a trivial solution for which $\langle 0 \,|\phi|\, 0 \rangle = 0$. The $\mu^2 < 0$ case is the one considered in the Standard Model and it provides a potential with a Mexican hat shape, where a local maximum is located at the origin and a degenerate ground state is given by:

$$\min(V(\phi)) = \langle 0 \,|\phi|\, 0 \rangle = \frac{\mu^2}{2\lambda} \equiv \frac{v}{2} \neq 0 \,. \tag{1.21}$$

with v being the vacuum expectation value, a free parameter that is measured experimentally, and it is related to the Fermi constant as $v = (\sqrt{2} G_F)^{-1/2}$. The Higgs field is an isospin doublet of $SU(2)_L$ and the minimum of the potential can be chosen such that its ground state takes the form:

$$\phi_0 = \frac{1}{\sqrt{2}} \begin{pmatrix} 0 \\ v \end{pmatrix} . \tag{1.22}$$

With this choice, the scalar field is electrically neutral and has isospin $-1/2$. Considering an excitation of the scalar doublet around the minimum, the Higgs field can be written as:

$$\phi(x) = \frac{1}{\sqrt{2}} \begin{pmatrix} 0 \\ v + H(x) \end{pmatrix} , \tag{1.23}$$

where $H(x)$ is the Higgs boson with a mass of $m_H = \sqrt{-2\mu^2}$. The term with the covariant derivatives in the Higgs Lagrangian 1.20 generates the mass terms

[7] No cubic terms on the Higgs field can be considered in order to preserve the invariance under phase transformations of the Higgs doublet. Therefore, the SSB breaks the $SU(2)_L \times U(1)_Y$ symmetry of the Lagrangian, but it remains invariant under the $U(1)_{EM}$ gauge group from electromagnetism.

of the gauge bosons as follows:

$$\frac{1}{2}\partial_\mu H \partial^\mu H + (v+H)^2 \frac{g^2}{4}\left\{ W_\mu^+ W^{-\mu} + \frac{1}{2\cos^2\theta_W} Z_\mu Z^\mu \right\} . \tag{1.24}$$

The mass terms contain the physical EW bosons, whose masses are related to the Weinberg angle, the vacuum expectation value and the weak coupling constant as follows:

$$m_A = 0\,, m_Z = \frac{vg}{2\cos\theta_W}\,, m_W = \frac{m_Z}{\cos\theta_W} = \frac{vg}{2}\,. \tag{1.25}$$

The mass terms of the fermions are generated by the Yukawa interactions of the Higgs field. The Yukawa Lagrangian is given by:

$$\mathcal{L}_{Yukawa} = -\sum_f y_f \bar{f}_L \phi f_R + h.c.\,, \tag{1.26}$$

where y_f are the Yukawa couplings, f runs over the fermions and $h.c.$ stands for the hermitian conjugate. Therefore, the masses of the fermions are given by $m_f = \frac{y_f v}{\sqrt{2}}$. It is worth to note that the neutrino masses are not generated by the Higgs mechanism.

The Standard Model is determined by 19 free parameters and all of them have been measured. These are the masses of the quarks (6), the masses of the leptons (3), the CKM matrix elements (4), the couplings constants of the interactions (3), the vacuum expectation value, the mass of the Higgs and the QCD vacuum angle θ_{QCD}.

1.4 Limitations of the theory

The SM is an elegant description of the fundamental particles and their interactions, being able to predict very precisely a wide range of phenomena. Despite its success, there are some theoretical inconsistencies and observations indicating that an extension of this theory is needed.

Theoretical motivations

From a theoretical perspective, the SM is considered to be the low-energy limit of a more general theory. Some main theoretical motivations to extend the SM are briefly explained in the following, being the unification of the forces, the flavor problem and the hierarchy problem, with the latter being further explained in the next chapter.

- **Grand Unified Theories (GUTs):** Theories tend to become more and more general in order to explain a wider range of observations and

to avoid being contradictory with other theories. The history of Physics has already experienced few examples of how two types of phenomena, a priori very different, can be understood under the same theoretical framework. The electromagnetic theory, for instance, described both the electrical and the magnetic experiments despite the two phenomena presented very different characteristics. Something similar happened with the EW interaction, which was able to unify the electromagnetic and the weak interactions as described in section 1.2. Similarly, the motivation of the Grand Unified Theories (GUTs) is to unify the EW and strong interaction into a common force at a certain high energy scale. It is observed that the strength of the interactions depend on the energy, where the strong interaction decreases with the energy, while the electromagnetic and weak interactions increase. According to the SM, the running of the couplings evolve in such a way that at high energies the three couplings take similar values, but not the same. Postulating new particles could make the three couplings to converge at a certain energy scale. This would imply that the gauge group of the SM $\mathrm{U}(1)_Y \times \mathrm{SU}(2)_L \times \mathrm{SU}(3)_C$ is a subgroup of a GUT gauge group G_{GUT}, where the SM particles are embedded into larger multiplets, following particular transformation properties under the GUT group. The breaking of the GUT symmetry would be realized by the Higgs mechanism, in the same way as in the SM, introducing scalar multiplets with VEVs of the order of the new energy scale $m_{\mathrm{GUT}} = 10^{16}$ GeV. The GUTs are considered as an intermediate step through a "Theory Of Everything", where the gravity could also be unified with the other forces at the Planck scale (10^{19} GeV).

- **The flavor problem:** Apart from predicting the experimental results, a complete theory needs to provide a comprehensive interpretation of the phenomena. This lack of comprehension is manifest in the flavor puzzle proposed by the SM, proposing the existence of exactly 3 families of fermions, where the quantum numbers of the particles are repeated in each family. In fact, just one family would be enough to have a consistent model. Another open question is the spectra of the fermion masses. There is a difference of 6 order of magnitude between the top quark and the electron masses, but the mechanism that generates these masses is the same for all the fermions. Similarly, the pattern of the mixing angles of the CKM matrix is not motivated. The absolute values of the CKM matrix elements show an "almost" diagonal matrix, where the diagonal elements are close to 1 and the off-diagonal are significantly smaller. In addition, some mixing between generations are preferred over other, as it is the case of the mixing between the first and the second generations.

- **The hierarchy problem:** The hierarchy problem is not actually a prob-

lem of the SM. If the SM is considered as the ultimate theory, the hierarchy problem does not appear. But since there are several reasons and a few observations to believe that the SM is incomplete, the hierarchy problem is normally associated to the SM itself. In particular, this problem is related to the mass of the Higgs boson. For a given extension of the SM, radiative corrections to the Higgs mass are added according to the new particles of the theory. The magnitude of these corrections are of the order of the energy scale for which the extended model becomes relevant, typically the GUT scale (10^{16} GeV) or the Planck scale (10^{19} GeV). In order to make these corrections compatible with the observed Higgs mass, very precise cancellations of the radiative contributions need to be fine-tuned, which becomes very unnatural. This is why the hierarchy problem is also known as the *naturalness problem*.

Experimental evidences

From an experimental perspective, some main problems are the neutrino masses, the baryon asymmetry in the Universe and the evidence of Dark Matter and Dark Energy, with the *Dark Matter problem* being further explained in the next chapter.

- **Neutrino masses:** The Standard Model assumes that neutrinos are massless, but the discovery of neutrino oscillations [33] implies that neutrinos have non-zero masses. This phenomenon implies that a neutrino can change its flavor while propagating, which is possible since the neutrino mass eigenstates are a mixture of the flavor eigenstates. The lepton mixing matrix is described by the Pontecorvo-Maki-Nakagawa-Sakata (PMNS) matrix, which is analogous to the Cabibbo-Kobayashi-Maskawa (CKM) matrix that describes the mixing between the quark flavor eigenstates. The PMNS matrix is parameterized by three mixing angles and one CP-violating phase (δ_{CP}). The discovery of neutrino oscillations implies that the leptonic mixing matrix can not be eliminated, which is a strong indication that the Standard Model is incomplete. There are several possible solutions to the neutrino masses problem. A simple extension would be to consider the existence of three generations of right-handed neutrinos, which would allow to add a Yukawa term for neutrinos. However, this solution is not popular since it does not explain the small neutrino masses. The most popular solution is the Type-I see-saw mechanism [34], which is based on the existence of a Majorana fermion, which is its own antiparticle. In this case, the smallness of the neutrino masses erases naturally considering large Majorana masses, which is sensible since the Majorana masses are still undiscovered.

- **Baryon asymmetry of the Universe:** The Standard Model is not able to explain the baryon asymmetry in the Universe, which is the fact that there is more matter than antimatter. The Sakharov conditions [35] describe the three necessary ingredients for baryon asymmetry: baryon number violation, C and CP violation, and interactions out of thermal equilibrium. Up to some level, these three phenomena can be found in the Standard Model, but the amount of asymmetry that is able to quantify is not enough to predict the large asymmetry of our Universe.

- **Evidence of Dark Matter and Dark Energy:** Several astronomical observations indicate the existence of a large amount ($\sim 75\%$) of matter in the Universe whose characteristics do not correspond with any of the particles considered in the Standard Model or the *baryonic matter* that can be built from it. The main list of evidences for the existence of Dark Matter are: the rotation curves of galaxies, the gravitational lensing, the cosmic microwave background, the large scale structure of the Universe, and the Bullet Cluster. The Dark Matter problem is further explained in the next section. Also from cosmological observations, the Dark Energy is inferred to be the main energy component of the Universe ($\sim 70\%$), which is responsible for the accelerated expansion of the Universe. While some characteristics about the Dark Matter are understood from the perspective of Particle Physics, a better understanding about the Dark Energy does not seem accessible for the SM.

Chapter 2

A look into New Physics

This chapter extends the previous discussion on some limitations of the Standard Model, such as the Dark Matter and the hierarchy problems. The chapter is divided in two sections. Section 2.1 discusses the Dark Matter problem, explaining the main evidences that motivates its existence and summarizing the possible candidates. The different types of DM searches are also described in this section, focusing on the LHC searches and the simplified models that are relevant for Chapter 6. In Section 2.2 discusses the prediction of Vector-like Quarks as an alternative to solve the hierarchy problem, also focusing on the phenomenology of LHC searches and presenting the simplified Lagrangian that are used in the searches described in Chapters 6 and 7. At the end of each section, a review of the latest results concerning the searches for DM and VLQs is presented.

2.1 The Dark Matter problem

The most clear evidence for the existence of Dark Matter (DM) came from the observations of the rotation curves of galaxies. According to the Newtonian gravity, the velocity of the stars in a galaxy should decrease as the distance to the center of the galaxy increases:

$$v(r) = \sqrt{\frac{GM(r)}{r}}, \qquad M(r) = 4\pi \int_0^r r^2 \rho(r) dr, \tag{2.1}$$

where $v(r)$ is the velocity of the stars at a distance r from the center of the galaxy, G is the gravitational constant, $M(r)$ is the mass enclosed in a sphere of radius r, and $\rho(r)$ is the density profile of the galaxy. Such a trend is analogous to the Solar System, where the velocity of the planets decreases as the distance to the Sun increases. However, observations show that rotation curves do not decrease with the distance [36, 37]. This discrepancy can be explained by the

presence of additional matter content distributed as a halo surrounding the center of the galaxy, known as DM. If the density profile of the DM scales as the quadratic distance to the center of the galaxy, the rotation curve would present a flat trend. An example of the different rotation curves for the nearby galaxy M33 [38] is shown in Figure 2.1.

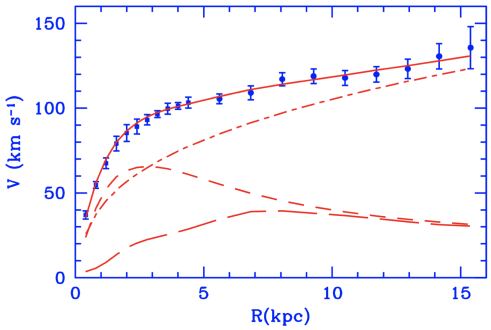

Figure 2.1: M33 rotation curve (points) compared with the best fit model (continuous line). The dashed-dotted line represents the halo contribution, the short dashed line represents the stellar disk and the long dashed line represents the gas contribution [38].

The first evidence of Dark Matter came with the extragalactic studies in the Comma Cluster carried by Fritz Zwicky in 1933 [39]. In this case, the mass of the cluster can be inferred using the virial theorem [40] from the dispersion velocity of the galaxies in the cluster. The obtained mass was approximately 500[1] times greater than the mass corresponding to the luminous matter. After this discovery, many other clusters have shown similar results.

Another evidence for the existence of DM comes from the *gravitational lensing effect* [41]. This effect is one of the main experimental confirmations of the General Relativity theory. The bending of light rays by massive objects is used to measure the mass of the object. Despite a weak distortion is observed in the light of galaxies, more massive structures such as clusters of galaxies show stronger distortions. The mass measured from the lensing effect is much larger than the mass of the luminous matter, serving as an additional evidence for the existence of DM.

The Λ *Cold Dark Matter* (ΛCDM) model includes non-relativistic DM as a component of the Universe [42]. From the success of its predictions, the Dark Matter hypothesis has been widely accepted. Example of this is the large scale structure of the Universe [43], defined as the structure or inhomogeneity of the Universe on scales larger than that of a galaxy, which can not be understood

[1]Such a high estimation was due to the obsolete Hubble constant value that Fritz used. With the correct one, the estimation would have been ~ 8.3

if the Dark Matter do not contribute to the evolution of the Universe. The Cosmic Microwave Background (CMB) [44] is also consistent with the predictions of the ΛCDM model. The CMB accounts for the radiation emitted after the Big Bang, corresponding to a black body of 2.7 K. Such radiation contains information about the early stages of the Universe and the formation of matter. According to recent measurements from the Planck Collaboration [45], it is extracted that the Universe is composed by 4.9% of baryonic matter, 26.6% of DM and 68.5% of Dark Energy.

Despite all the observational evidences learned during decades, some efforts to explain these phenomena without the need of DM have been made. Mostly, these efforts are based on Modified Newtonian Dynamic (MOND) theories [46] or modifications of the General Relativity. However, strong counter-examples have been found for any of these theoretical alternatives. For instance, the Bullet Cluster [47] is the strongest counter example to MOND theories. This consists of two colliding clusters, where the baryonic matter interacts and slows down, while the DM passes through the collision without interacting. As a consequence, the DM tends to distribute far from the region of the collision, which can not be explained with the MOND theories. In addition, the detection of gravitational waves in 2016 [48] moving at the speed of light [49] allowed constraining even more the alternative theories to the General Relativity.

Dark Matter properties and candidates

Since no constraints on the DM mass have been found, the different DM candidates cover a wide range of masses, from pico-eV to the GUT scale (10^{16} GeV) [50]. One of the first proposals were the Massive Compact Halo Objects (MACHOs) [51], including objects such as black holes, neutron stars, brown and white dwarfs, which emit very little light. Primordial black holes [52] also belong to the MACHOs class, but the main downside is that the upper limits on their abundance makes very difficult to explain the large DM content of the Universe [53].

Instead, most efforts in the search for DM are based on "particle-like" candidates, in which the component (or components) of the DM are considered fundamental particles not included in the SM. Despite the nature of such DM candidates is still unknown, some properties are inferred from the observations and existing experiments.

- The composition of DM is not baryonic [53], so the existence of New Physics is required.
- The DM candidates do not interact (emit, reflect or absorb) with light of any frequency [54]. Therefore, either they are electrically neutral or they have at least a very small electromagnetic coupling.

- According to its observed role in the galactic dynamics and the large scale structure of the Universe, the DM is assumed to interact gravitationally with baryonic matter.

- The DM candidates need to be stable, or long-lived with a lifetime much larger than the age of the Universe ($t_0 = 13.08 \pm 0.04$ Gyr) [55].

- The DM is assumed to be cold [56], meaning that it was non-relativistic at the time of the structure formation in the Early Universe (*freeze-out*).

- The DM candidates have been considered to be collision-less if the mass is large enough. Indeed, the upper limit on DM self-interactions is very large ($\sigma_{self}/m < 1$ cm^2/g) [57].

An early candidate came with neutrinos, which were assumed to be massive very soon. However, their relativistic nature makes them a "hot dark matter" candidate, which inhibit the clumping on small scales needed to hold galaxies together. Several other candidates have been proposed, such as the sterile neutrinos [58], the axions [59], the Dark Photons [60], the Kaluza-Klein [61] particles and the Supersymmetric candidates. However, the type of DM candidates that has been most explored are the Weakly Interacting Massive Particles (WIMPs) [62].

The WIMPs are a general set of candidates characterized by being stable, neutral and "cold", interacting weakly with the SM particles via the weak force. The most promising motivation for the WIMPs appearing in many BSM theories is known as the "WIMP miracle", in which the existence of a particle with a mass on the weak scale, approximately between 10 GeV and a few TeV, naturally matches the observed relic density measured in CMB experiments ($\Omega_{DM}h^2 \approx 0.12$ [63]).

The WIMPs are expected to be produced in the Early Universe and its (comoving) number density, n, evolved in thermal equilibrium according to the Boltzmann equation [64]:

$$\frac{dn}{dt} = -3Hn - <\sigma v>(n^2 - n_{eq}^2), \tag{2.2}$$

where H is the Hubble parameter, $<\sigma v>$ is the thermally averaged DM pair-annihilation cross-section, and n_{eq} is the equilibrium number density. At some stage, the Universe was sufficiently large and the density sufficiently low for the annihilation process to be ceased, and the relic abundance remained until this day. This is the so-called *freeze-out* [56], for which $H \sim< \sigma v >$. Figure 2.2 shows how the pair-annihilation rate determines the relic density, which are inversely related, $\Omega_{DM} \propto 1/ <\sigma v>$ [65].

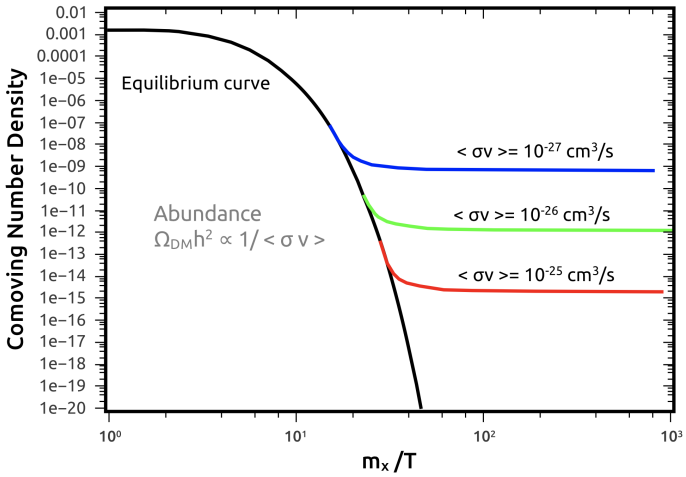

Figure 2.2: Evolution of the relic density of DM in the Universe as a function of the pair-annihilation rate.

Searches for Dark Matter

The DM searches can be classified in three complementary categories: direct detection, indirect detection and collider searches. As illustrated in Figure 2.3, these searches differ in the initial and final states of the interactions that may connect the DM to the SM particles.

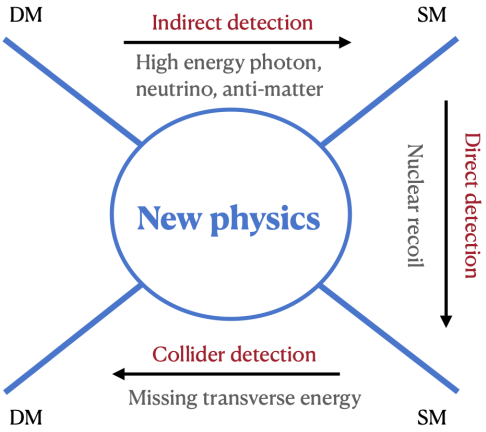

Figure 2.3: Illustration of the different DM searches [66].

The direct detection searches are based on the scattering of DM particles with the nuclei of a detector material, where the DM could be detected looking at the nuclear recoil. Such signal can be measured through either

ionization (charged particles), scintillation (photons), an increase of temperature (phonons) or a bubble nucleation with super-heated fluids. The interpretation on the cross-section of the DM-nucleon scattering is divided into spin-dependent (axial-vector coupling) and spin-independent (scalar or vector coupling) [67]. For the spin-dependent interactions, the amplitude of the cross-section is proportional to the square of the atomic number of the nucleus. For the spin-independent interactions, the spin direction of all the nucleons need to be considered, and many cancellations occur, leading to a lower cross-section.

The experimental setup of direct detection searches can combine different techniques and look for both spin-dependent and spin-independent interactions. Most direct detection techniques are based on the following basic assumptions::

- There is a smooth halo of DM particles in our galaxy described by the Maxwell velocity distribution [68].
- Local DM density is assumed [69].
- The nucleus is considered as a hard sphere characterized by the Helm form factor [70].

Most experiments use noble gases as target material, such as Xenon, Argon and Neon, since they are chemically inert to reduce the noise. The high density of these target materials increase the probability of the interactions, and for the same reason, large volumes are used in these experiments. A summary of important experiments for direct detection is shown in Table 2.1.

The indirect searches aim to detect an excess of SM particles that would be produced in the annihilation or the decay of DM. These experiments are telescopes, since these processes may occur in astrophysical objects. The telescopes for indirect searches can be classified according to the particle that is observed:

- Neutrinos telescopes: since neutrinos interact very weakly, these experiments need a large volume of passive material to increase the probability of the detection. Example of these experiments are the IceCube (under-ice in the Antartic) [80], Super-Kamiokande (a large pool under-ground) and ANTARES [81] or Km3Net [82] (underwater in the Mediterranean Sea).
- Cosmic rays telescopes: looking for particles such as electrons, positrons, anti-protons and deuterons. Targeting rare species allow to reduce the background. PAMELA [83] and AMS [84, 85] experiments are some of the most relevant. Located in the space[2], both telescopes have found

[2]PAMELA was attached in a satellite orbiting the Earth, whereas AMS is installed at the International Space Station.

		Spin int.		Detection technique				
Experiment	Target	SI	SD	I	S	T	B	Ref.
XENON-4T	Xe	✓	neutron	✓	✓			[71]
PandaX	Xe	✓	neutron	✓				[72]
LZ (Lux-Zeplin)	Xe	✓	both	✓	✓			[73]
SuperCDMS	Ge	✓		✓		✓		[74]
DarkSide-50	Ar	✓		✓				[75]
DEAP-3600	Ar	✓			✓			[76]
CRESST-III	$CaWO_4$-O	✓			✓	✓		[77]
NEWS-G	Ne	✓		✓				[78]
Pico60	C3F8 - F	✓	proton				✓	[79]

Table 2.1: Summary of important experiments for direct detection of Dark Matter. The table shows the target material, the detection techniques used and the type of WIMP-nucleon interactions, which can be spin-independent (SI) or spin-dependent (SD). The detection techniques are ionization (I), scintillation (S), temperature (T) and bubble nucleation (B).

excesses compatible with DM signal. However, the excess of positrons is still compatible with positron production by pulsars or supernova remnants [86].

- Photon telescopes: these searches look for frequencies in the radio, X-rays and γ-rays spectra. It is worth to mention the Fermi-LAT (Fermi Large Area Telescope) [87–89], a space observatory that performs γ-ray measurements. This experiment has found some excesses ($\sim 4.5\sigma$) that could be a sign of WIMPs. However, the excesses are not conclusive and could be explained by γ-ray emission from pulsars [90].

And last but not least, collider searches are based on the production of DM particles in the collisions of SM particles. Since the DM particles are assumed to be stable, they escape the detector without interacting and their presence is inferred from an imbalance in the total momentum of the SM particles detected. A particular advantage of the collider searches is that it also provides access to the measurement of the hypothetical bosons mediating the interactions between the DM and the SM particles, commonly named *dark mediators*. Colliders also allow to control the experimental conditions, such as the type and energy of the colliding particles. High energies are required since the constraints on the DM and the dark mediator masses already indicate values in the TeV scale. Accelerators such as the Large Electron Positron collider (LEP) at CERN [91] and Tevatron at Fermilab [92] have performed searches for DM particles, but the most energetic collisions are reached in the LHC at CERN,

where the ATLAS [93] and CMS [94] experiments perform several searches for DM particles.

Phenomenology of Dark Matter searches in the LHC

The LHC is a proton-proton circular collider located at CERN with four collision points, each one with a different detector. The ATLAS [93] and CMS [94] detectors have been designed to explore the SM and to search for New Physics. A detailed description of the LHC and the ATLAS experiment can be found in Chapter 3.

In order to efficiently search for DM at the LHC, common strategies are needed among the experiments. Three benchmark frameworks are commonly used: exploring most plausible BSM scenarios predicting DM, constraining Effective Field Theories (EFTs) coefficients [95] and setting limits in the parameter phase space of simplified models [96, 97].

The results from the first case are the most straightforward to interpret, since the BSM theories provide a clear theoretical input about the possible final states and kinematic distributions that are expected. Therefore, the signal expected in the detector can be well-defined and separated from the SM background processes. The downside of this approach is that the results are only valid for the specific BSM theory considered. Since there are many BSM theories, such as Supersymmetry (SUSY [98]) or extra-dimension theories, predicting DM and none of them have been proved after numerous searches, the other two approaches have become more popular in the last years.

The EFTs introduce minimal assumptions on the new particle spectrum, being the DM the only new state beyond the SM background that is accessible at the LHC. Assuming that the dark mediator is heavier than the energies probed at the LHC, generic *contact interactions* are proposed according to renormalizable operators. Some of such operators in which WIMPs couple to quarks and gluons are shown in Table 2.2 [57, 99]. These terms can be added perturbatively to the SM Lagrangian as long as the power factor $1/M_*$ is small enough, where M_* represents the energy of the process. If the process is due to a mediator of mass M and coupling λ, the operator represents a contact interaction with propagator $\lambda^2/M^2 = 1/M_*$. According to this theoretical framework, just a reduced set of effective couplings or coefficients need to be constrained. The generality of this approach allows the direct detection experiments to set limits on the same effective couplings, as shown in Figure 2.4 [57].

In between the previous two approaches, the simplified models provide a flexible method to explore extensions of the SM that depend on a very reduced set of parameters: the couplings of the mediator to the DM and the SM particles, the mass of the DM particle and the mass of the mediator. The generality of a simplified model depends on how restrictive are its assumptions, which are

Name	Initial state	Int. type	Operator
D1	qq	scalar	$\frac{m_q}{M_*^3}\bar{\chi}\chi\bar{q}q$
D5	qq	vector	$\frac{m_q}{M_*^2}\bar{\chi}\gamma^\mu\chi\bar{q}\gamma_\mu q$
D8	qq	axial-vector	$\frac{m_q}{M_*^2}\bar{\chi}\gamma^\mu\gamma^5\chi\bar{q}\gamma_\mu\gamma^5 q$
D9	qq	tensor	$\frac{m_q}{M_*^2}\bar{\chi}\sigma^{\mu\nu}\chi\bar{q}\sigma_{\mu\nu}q$
D11	gg	scalar	$\frac{1}{4M_*^3}\bar{\chi}\chi\alpha_s(G^a_{\mu\nu})^2$

Table 2.2: Operators in the EFTs for DM-quark and DM-gluon interactions, valid when the energy of the interactions is smaller than M_*. If the process is due to a mediator of mass M and coupling λ, the operator represents a contact interaction with propagator $\lambda^2/M^2 = 1/M_*$. Source: [57].

often minimal. The interpretation of the constraints on the different parameters are extrapolable to any particular BSM theory for which the assumptions remain valid. Different simplified models are proposed according to the nature of the dark mediator. While the DM particles are often assumed to be Dirac fermions, the possible features of the dark mediator, such as its spin and parity, open the floor to different type of interactions. Thus, for spin-0 (spin-1) mediators, searches for scalar and pseudo-scalar (vector and axial-vector) resonances are performed. A Minimal Flavor Violation (MFV) scheme [100] is commonly used, in which the dark sector (consisting of the DM particles and the dark mediators) couples to the ordinary particles following the same flavor structure as the SM, ensuring that flavor constraints are satisfied in these searches. As a consequence, a spin-0 mediator would couple proportionally to the Yukawa coupling. Therefore, as it is the case in many extensions of the SM, the coupling to the top quark is favored by its large mass.

From an experimental point of view, simplified models allow to explore a wide range of final states classified in two types of signatures. The first case corresponds to resonance searches, where the dark mediator is expected to decay into SM particles, from which its properties can be inferred. No DM particles are necessarily produced in this case, in which the only parameters that can be constrained are the coupling mediator-SM and the mass of the mediator. The second one corresponds to the production of DM in association with other SM particles in the final state, which is necessary to trigger the event since the DM particles escapes the detector without interacting. In particular, the mono-X signatures are interesting because processes with a single particle in the final state are very rare in the SM. These processes are characterized by a large missing transverse momentum.

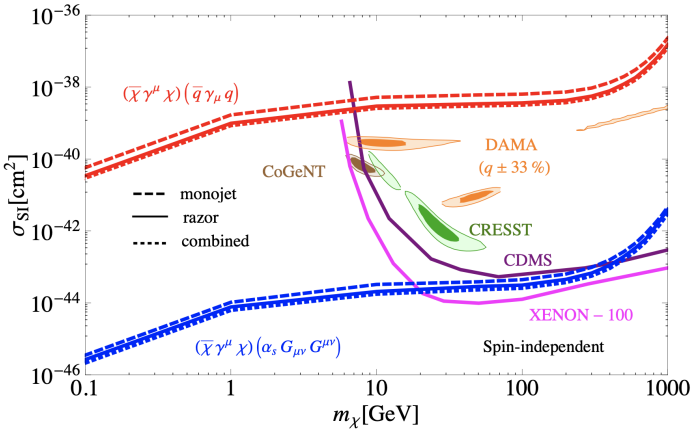

Figure 2.4: Limits on the effective couplings of point-like interactions corresponding SI DM-nucleon interaction by the LHC and direct detection experiments. For DAMA and CoGeNT 90% and 3σ contours and for CRESST 1σ and 2σ contours are also shown. Source: [57].

Simplified models for a mono-top search

This Thesis presents an ATLAS analysis (see Chapter 6) in which DM is searched in events with a large missing energy in association with a top quark, i.e. a *mono-top* signature. In order to remain agnostic to any BSM theory predicting such a signature, this search is based on two simplified models [101–103].

The *scalar DM mediator model* incorporates a colored 2/3-charged scalar boson, ϕ, that is produced as a resonance in the s-channel and decays into a top quark and a spin-1/2 DM particle. This process violates baryon number and is expected in different BSM scenarios, such as MSSM theories or leptoquark models. The Lagrangian is given by:

$$\mathcal{L}_{\text{scalar}} = \lambda_q \phi \bar{d}^c P_R s + y_\chi \phi \bar{t} P_R \chi + \text{h.c.}, \tag{2.3}$$

The *vector DM mediator model* is characterized by an FCNC interaction in which a hypothetical massive vector mediator V connects the up-type quarks of the first and second families to the top quark. The mediator V is produced either in the s-channel or in the t-channel, and decays into a pair of Dark Matter particles. The fact that the SM do not allow FCNC interactions at leading order makes this mechanism particularly interesting in the search for new physics. The Lagrangian is given by:

$$\mathcal{L}_{\text{vector}} = a_r V_\mu \bar{u} \gamma^\mu P_R t + g_\chi V_\mu \bar{\chi} \gamma^\mu P_R \chi + \text{h.c.}, \tag{2.4}$$

Figure 2.5 shows the Feynman diagrams for the two simplified models, where diagram 2.5a corresponds to the scalar mediator and diagrams 2.5b and 2.5c correspond to the vector mediator in the s-channel and t-channel, respectively.

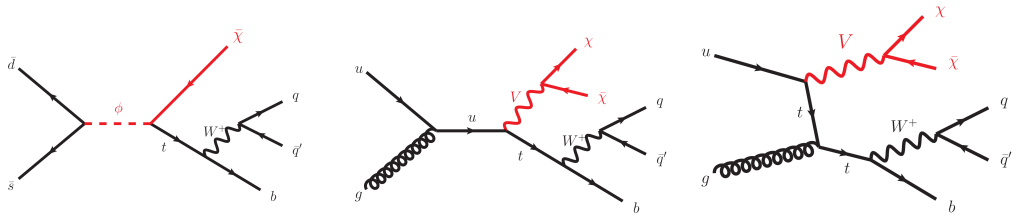

(a) (b) (c)

Figure 2.5: Diagrams for the simplified models considered in the search for Dark Matter: (a) scalar mediator, (b) vector mediator in the s-channel, and (c) vector mediator in the t-channel.

These simplified models depend on a set of free parameters that define the interaction between the DM particle and the SM particles. The former contains the masses of the scalar mediator (m_ϕ) and the DM particle (m_χ), the coupling constant λ_q that measures the strength of the interaction between the scalar mediator and the initial partons, and the mixing parameter y_χ that measures the strength of the interaction between the scalar mediator and the top quark. The latter depends on the masses of the vector mediator (m_V) and the DM particle (m_χ), the coupling a that connects the vector mediator with the top quark through a FCNC interaction, and the coupling g_χ that controls the decay of the vector mediator into a pair of DM particles.

Summary of Dark Matter searches

Since no evidence of DM has been found, the results are interpreted as exclusion limits on the cross-section of the DM-nucleon scattering, based on simplified models [104]. Constraints on the cross-section for spin-independent WIMP-nucleon scattering are compared between LHC and direct detection searches in Figure 2.6a. Analogously, constraints on the spin-dependent WIMP-proton scattering cross-section are shown in Figure 2.6b. In both cases, the comparison is consistent in the context of a simplified model with a leptophobic mediator.

A summary of the latest DM measurements by the ATLAS experiment is shown in Figures 2.7 and 2.8 [104]. In particular, constraints on the production cross-section and the mass of the mediator are shown. Figure 2.7a (2.7b) set limits to the production cross-section of a scalar (pseudo-scalar) mediator ϕ (a) as a function of its mass, which decays into a pair of DM particles. Figure

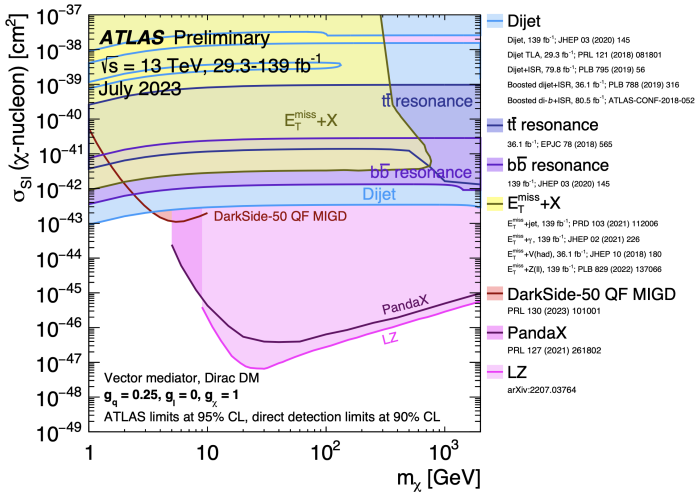

(a)

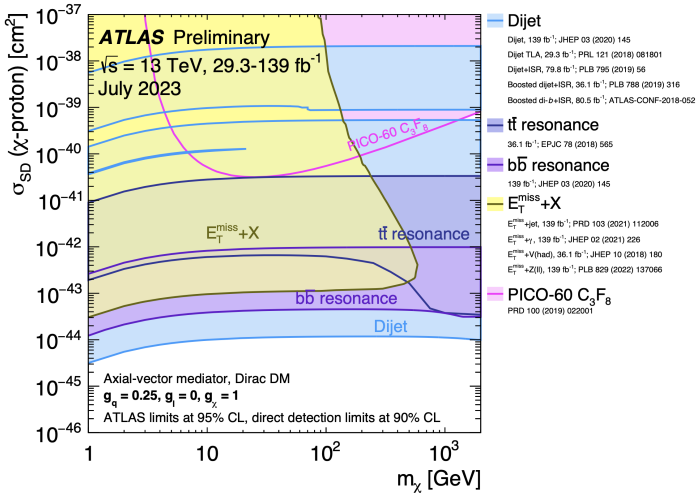

(b)

Figure 2.6: Comparison of the limits on the spin-independent WIMP-nucleon (a) and spin-dependent WIMP-proton (b) scattering cross-sections, in the context of a simplified model with a leptophobic mediator. Constraints from the ATLAS experiment and direct detection experiments are shown, setting limits at 95% and 90% CL, respectively. Source: [104].

2.8a (2.8b) set limits on both DM and mediator masses for the case of a vector (axial-vector) mediator Z'_V (Z'_A). The summary plots for DM searches in CMS can be found in Ref. [105].

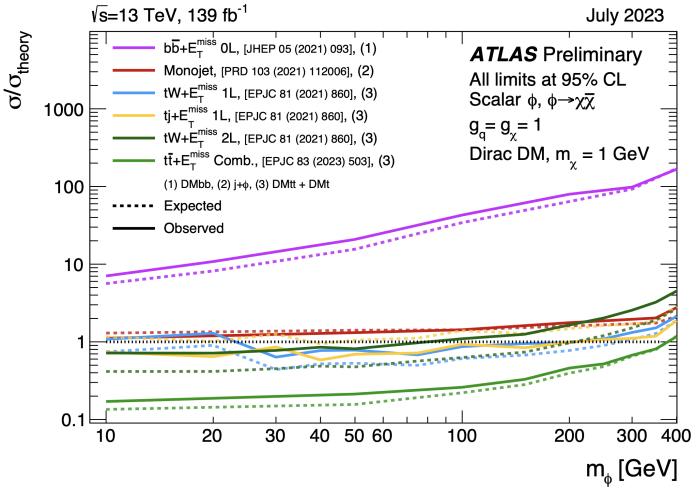

(a)

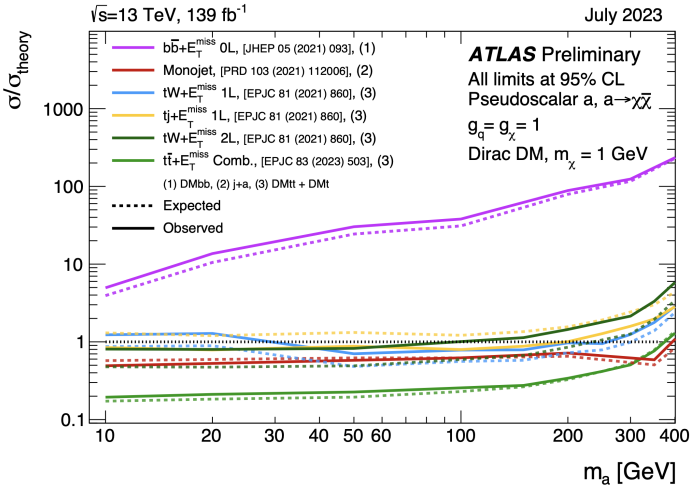

(b)

Figure 2.7: Exclusion limits at 95%CL on the production cross-section and the mass of a scalar ϕ (a) and a pseudo-scalar a (b) mediator by the ATLAS collaboration. The ratio of experimental over theoretical cross-section is shown in the y-axis. The simplified model assumes a color-neutral mediator. Source: [104].

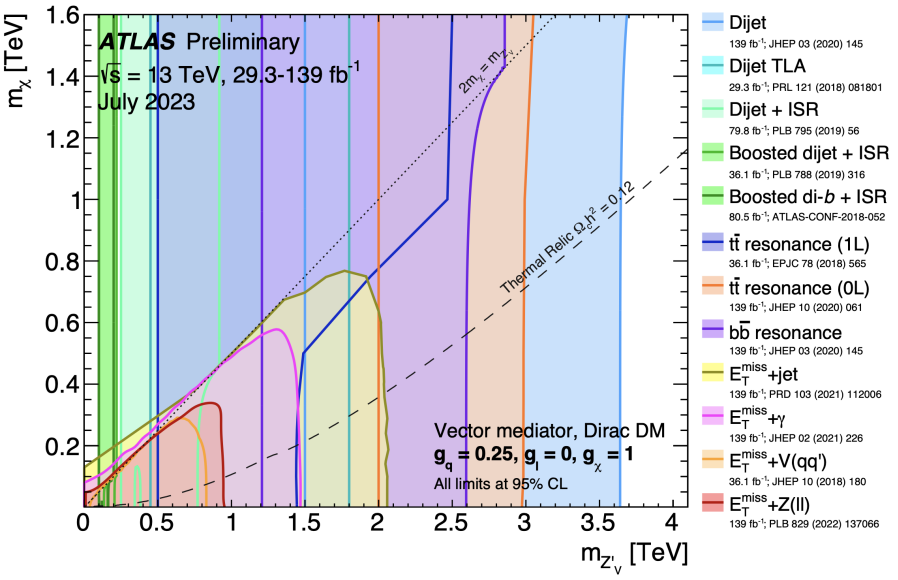

(a)

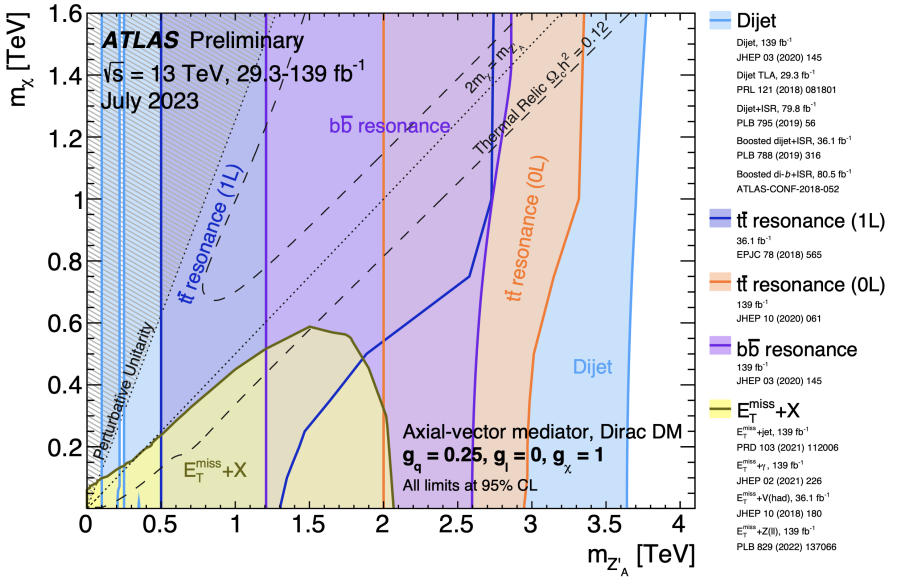

(b)

Figure 2.8: Exclusion limits at 95%CL on the DM mass and the mass of a vector Z'_V (a) or a vector-axial Z'_A (b) mediator by the ATLAS collaboration. The simplified model assumes a leptophobic mediator. Source: [104].

2.2 Vector-like Quarks

After the enormous achievement of the Higgs boson discovery [23, 24], several precision measurements about its mass have being performed. The latest result from the ATLAS experiment, which combines the searches for the diphoton and the four-lepton channels, provides a value of 125.11 ± 0.11 GeV [106]. This effective value is the addition of a bare mass term and radiative corrections from the particles that couple to the Higgs boson, dominated by the 1-loop diagrams of the top quark in the Higgs propagator, as illustrated in Figure 2.9. Such a correction takes the form:

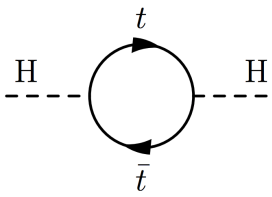

Figure 2.9: Diagram of a 1-loop top quark in the Higgs propagator that dominates the radiative correction to the Higgs mass.

$$m_H^2 = m_{H,0}^2 + \delta m_H^2, \qquad \delta m_H^2 \propto \int_0^{\Lambda_c} \frac{d^4p}{p^2} \propto \Lambda_c^2, \tag{2.5}$$

where $m_{H,0}$ is the bare mass of the Higgs boson, δm_H^2 is the radiative correction, and Λ_c is the cut-off scale up to which the theory predictions are valid. The cut-off scale is expected to be the Planck scale ($\Lambda_c \sim 10^{19}$ GeV), at which the quantum effects of the gravity force start to be relevant. However, these huge corrections to the Higgs mass are not compatible with the low value measured of the Higgs mass, requiring an unnatural fine-tuning to cancel the quadratic divergences.

From a more general perspective and recovering the naturalness principle [107] stated for first time by G. 't Hooft: *at a certain energy scale, a set of parameters is allowed to be very small only if taking zero values increase the symmetry of the system.* In the case of the Higgs mass, there is not a symmetry in the SM that arises when the Higgs mass is zero. It is commonly said that the Higgs mass is not *"protected"* by any symmetry of the SM.

Protecting the naturalness of the Higgs mass

In order to preserve the naturalness, there are two general approaches that physicists have been exploring: a mechanism to lower the cut-off or a new symmetry to protect the Higgs mass. The first approach is often covered by theories

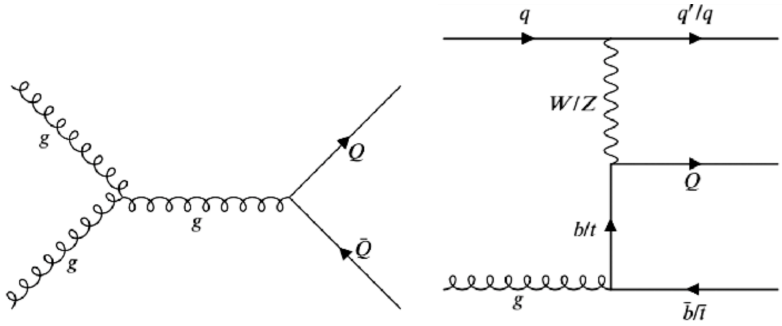

(a) (b)

Figure 2.10: Feynman diagrams for the pair-production (left) and single-production (right) of VLQs at the LHC.

introducing extra dimensions, while the latter is covered by theories such as SUSY [98], introducing a new Bose-Fermi symmetry and predicting new particles that cancel out the quadratic divergences of the Higgs mass. Alternatively, a set of theories introduce a new global symmetry being spontaneously broken, from which the Higgs boson emerge as a pseudo-Nambu-Goldston boson [108]. Examples of this type of theories are the Composite Higgs models [109] and the Little Higgs models [110, 111]. From the new states that arise in these BSM theories, the Vector-like Quarks (VLQs) emerge as a common feature.

VLQs are color-triplet spin-1/2 fermions whose left- and right-handed components have the same transformations under the EW gauge group. Proving the existence of these particles would validate any of the previous theories as a proper extension of the SM where the naturalness of the Higgs mass is preserved. VLQs are the simplest colored fermions still allowed by the experimental results. In fact, extra quarks with quiral fermion couplings, such as a hypothetical 4th generation of quarks, are excluded by Higgs-mediated cross-section measurements in the LHC. Contrary, VLQs mass terms can be added to the SM Lagrangian respecting the gauge invariance, not relying on the Higgs mechanism.

Phenomenology of Vector-like Quarks at the LHC

The search for VLQs at the LHC can be broadly categorized in two production modes: pair and single production. The pair-production is dominant for low masses [112] and, as illustrated in Figure 2.10 (left), it is mediated by the strong force. On the other hand, the cross-section of the single-production mode starts to dominate for values above 1 TeV and is mediated by the EW force, as shown in Figure 2.10 (right).

An advantage of the VLQ searches is that relying on a particular BSM theory is not necessary. For the pair-production mode, since the strong coupling in the vertex ggQ is the same as in the SM, the only unknown parameter that controls the cross-section of the process is the mass of the VLQ. This feature of the pair-production mode allows performing model-agnostic searches by scanning on the VLQ masses. For the single-production, since the VLQ couples to the SM quarks via a $W^{\pm}$, Z or H boson, the cross-section will also depend on the EW interactions of the VLQ.

The spectrum of the VLQ species consists of four particles: $X_{+\frac{5}{3}}$, $T_{+\frac{2}{3}}$, $B_{-\frac{1}{3}}$, and $Y_{-\frac{4}{3}}$, where the sub-index denotes the electric charge of the particle in units of the electron charge. According to their electric charges, the $T_{+\frac{2}{3}}$ ($B_{-\frac{1}{3}}$) quark is conveniently denoted as "top partner" ("bottom partner"). Considering that the scalar sector only contains $\mathrm{SU}(2)_L$ doublets, as is the case of the SM, only seven gauge-covariant multiplets with definite quantum numbers under the SM gauge group $\mathrm{SU}(3)_C \times \mathrm{SU}(2)_L \times \mathrm{U}(1)_Y$ are allowed [113]. The quantum numbers[3] of the VLQ $\mathrm{SU}(2)_L$ multiplets are shown in Table 2.3.

Multiplet	T	B	$\begin{pmatrix} T \\ B \end{pmatrix}$	$\begin{pmatrix} X \\ T \end{pmatrix}$	$\begin{pmatrix} B \\ Y \end{pmatrix}$	$\begin{pmatrix} X \\ T \\ B \end{pmatrix}$	$\begin{pmatrix} T \\ B \\ Y \end{pmatrix}$
Hypercharge	$+2/3$	$-1/3$	$+1/6$	$+7/6$	$-5/6$	$+2/3$	$-1/3$
Weak isospin	0	0	1/2	1/2	1/2	1	1
Color charge	1	1	1	1	1	1	1

Table 2.3: Quantum numbers of the VLQ $\mathrm{SU}(2)_L$ multiplets.

Other theoretical assumptions are often made in most Run 1 and Run 2 searches in the LHC experiments, which are listed below [114]:

- One $\mathrm{SU}(2)_L$ multiplet at a time is assumed.
- No couplings to other BSM particles are explored.
- Since VLQs couple to SM quarks, the couplings of the SM particles to the Z, W and Higgs bosons would be altered. However, this is not assumed in the existing searches.
- Only couplings to third family of quarks are considered, and therefore, the branching ratios obey the following constraint:

$$BR(Q \to Hq) + BR(Q \to Zq) + BR(Q \to Wq') = 1. \qquad (2.6)$$

[3]The hypercharge of a multiplet is computed as the average of the hypercharges of its elements. Since the sum of the third isospin component is zero, $Y_{multiplet}$ corresponds to the average of the electric charges of the particles in the multiplet.

- The Goldstone Equivalence Theorem [115] states that at large masses of the VLQ (> 1 TeV), the decays to Ht and Zt become similar, such that $BR(Q \to Zq) = BR(Q \to Hq)$.
- Narrow Width Approximation (NWA) is required for some interpretations to remain valid. Therefore, only results for which the relative decay width $\Gamma_Q/m_Q < 0.5$ are considered.

Model for singly-produced Vector-like Top quark searches

Different searches for single production of top partners are presented in this Thesis (see Chapters 6 and 7). As it is observed from Figure 2.10b, the single production of a VLQ is mediated by the EW force, and the cross-section of the process depends on the coupling of the VLQ to the SM quarks and the mass of the VLQ. Fortunately, a model-agnostic search can be performed for the single production mode by means of a simplified Lagrangian [114, 116]:

$$\mathcal{L} = \sum_{Q,q,\zeta} \left[\frac{g_w}{\sqrt{2}} \kappa_\zeta^{Qq} \bar{Q} \not{W} P_\zeta q + \frac{g_w}{2c_W} \tilde{\kappa}_\zeta^{Qq} \bar{Q} \not{Z} P_\zeta q + \hat{\kappa}_\zeta^{Qq} H \bar{Q} P_\zeta q \right] + \text{H.c.}, \qquad (2.7)$$

where Q represents a VLQ, ζ is the chirality of the interaction with P_ζ being the corresponding projection operator. The weak-coupling g_w and c_W are introduced for normalization[4]. The SM quarks, both up or down type, are represented by q and couple to Q via the $W^\pm$, Z and H bosons. Such EW couplings are determined by κ_ζ^{Qq}, $\tilde{\kappa}_\zeta^{Qq}$ and $\hat{\kappa}_\zeta^{Qq}$, respectively.

According to Ref. [114], considering the T-quark at the large mass limit, which will be the case of study in Chapters 6 and 7, the Lagrangian in Eq. 2.7 can be re-parameterized in terms of five parameters that control the kinematics of the processes: the T-quark mass m_T, an overall coupling strength κ_T, and the relative couplings to the W, Z and H bosons ξ_W, ξ_Z and ξ_H, respectively, such that $\sum_{V=W,Z,H} \xi_V = 1$. While κ_T represents the overall strength of the T-quark coupling to the SM quarks, the ξ_V parameters correspond to the branching ratios of the T-quark decays $T \to Vq$.

Attending to the Goldstone Equivalence Theorem mentioned above, $\xi_Z = \xi_H$ and the ξ_V parameters and branching ratios can be fully determined by fixing the value of ξ_W: $\xi_Z = \xi_H = (1 - \xi_W)/2$. However, specific values of the relative couplings ξ_V are associated to a given SU(2) representation of the T quark. For instance, the singlet and doublet scenarios correspond to $\{\xi_W, \xi_Z, \xi_H = 0.5, 0.25, 0.25\}$ and $\{\xi_W, \xi_Z, \xi_H = 0, 0.5, 0.5\}$, respectively. This is illustrated in Figure 2.11, where the branching ratios remain constant for

[4]See Section 1.2 where the cosine of the electroweak mixing angle ($c_W = \cos\theta_W$) is introduced when explaining the EW interactions.

large masses. Therefore, the cross-section of the single T-quark production mode depends exclusively on m_T and κ_T : $\sigma(m_T, \kappa_T)$. Such dependence can also be expressed in terms of m_T and the relative decay width Γ_T/m_T, which scales quadratically with m_T and the overall coupling κ_T.

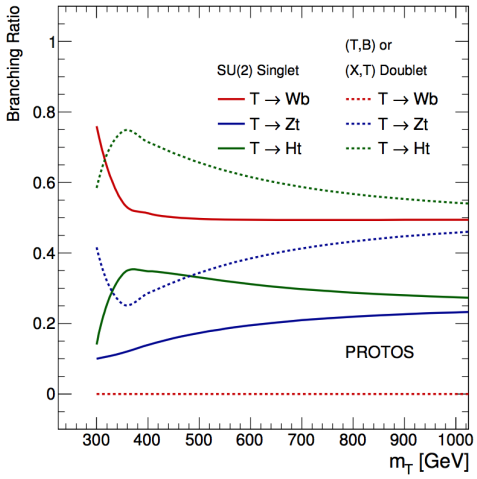

Figure 2.11: Branching ratio of the T-quark as a function of mass for singlet (T) and doublet (X, T) representations [117]. The PROTOS generator [118] was used to simulate the decay of the T-quark.

Summary of Vector-like Quarks searches

Several searches have been performed by the ATLAS and CMS collaborations for both pair and single production of VLQs during the Run-I [112, 119–124] and Run-II [1, 125–135] of the LHC. Focusing on the singlet and doublet representations, a wide range of final states have been explored and very stringent limits on the free parameters have been set. Figure 2.12 shows the excluded range of the VLQ masses for various model assumptions, specifying the largest excluded values. Results for both the pair and single production searches are shown, including the four VLQ species in the SU(2) singlet or doublet representations. In the case of the single production, the results are presented for a VLQ relative decay width (Γ_Q/m_Q) of 20%.

In addition, Figure 2.13 shows the exclusion limits on the VLQ mass and the relative decay width Γ_Q/m_Q for the single production searches of the T and B quarks, interpreted for both the singlet and doublet scenarios [136]. The first paper shown in the legend of Figure 2.13 [1] corresponds to the work presented in Chapter 6 of this Thesis. This is a search for a singly produced vector-like Top together with a large amount of missing energy, a forward jet

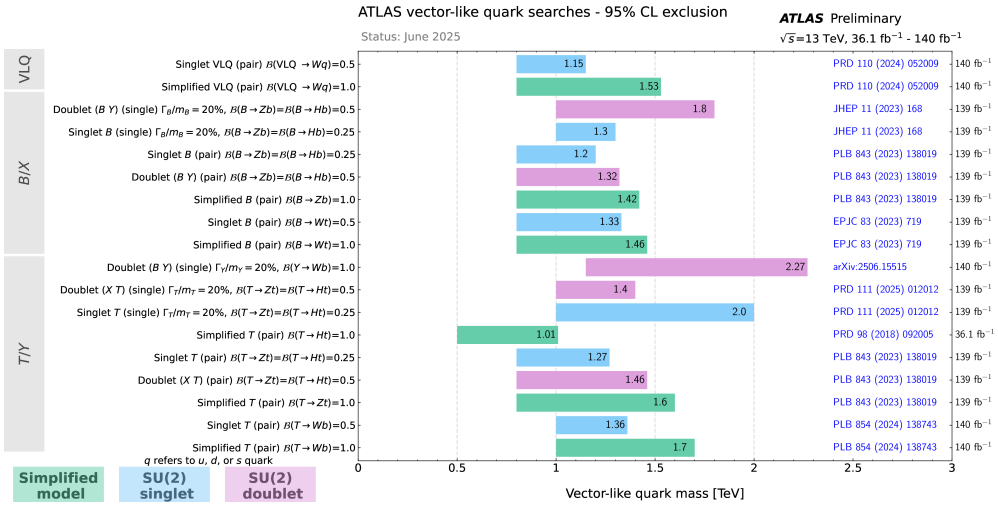

Figure 2.12: Observed exclusion lower limits at 95% confidence level on the mass of vector-like quark (VLQ) for various model assumptions in terms of SU(2) gauge group representations, flavor generation and the branching ratio of the VLQ decay. Some pair-production searches assume a simplified model according to which an exclusive decay into a specific final state is considered with branching ratio equal to 1. In the case of the single-production, the results are presented for a VLQ relative decay width (Γ_Q/m_Q) of 20%. The lower end of the bars shown in this plot refers to the lower edge of the targeted range considered in the respective searches.

and zero leptons. Chapter 7 presents the statistical combination of this search with the second [128] and third [129] referenced papers, targeting final states with different lepton multiplicity.

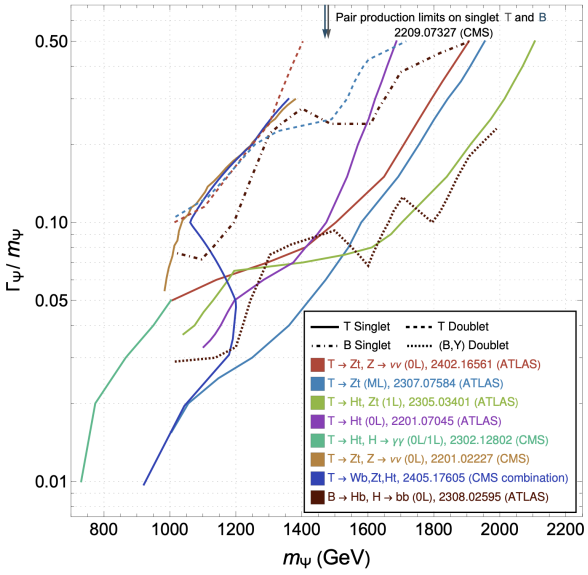

Figure 2.13: Current limits on the VLQ mass from single production searches [136]. The limits are shown as a function of the relative decay width Γ_Q/m_Q.

Chapter 3

The LHC and the ATLAS experiment

This chapter describes the experimental setup to understand the data recorded for the analyses presented in this Thesis. In Section 3.1, the most important magnitudes of colliders are explained, focusing on the characteristics of proton-proton collisions at the Large Hadron Collider. In Section 3.2, the ATLAS detector is described, including its subdetectors and the data acquisition system.

3.1 The Large Hadron Collider

The Large Hadron Collider (LHC) [137, 138] is the world's largest and most powerful particle accelerator, being part of the European Organization for Nuclear Research (CERN) [139]. Located in the border between France and Switzerland, near Geneva, the accelerator was built $\sim$ 100 m underground [1] and has a circumference of 27 km.

The LHC is the last stage of an accelerator chain that starts with the generation of protons in a hydrogen bottle. The hydrogen atoms are first ionized, and the resulting protons are accelerated in the LINAC2 linear accelerator, reaching an energy of 50 MeV. After the Proton Synchrotron Booster (PSB), the beam is accelerated to 1.4 GeV, passing to the Proton Synchrotron (PS), where the beam is accelerated to 25 GeV. At this stage, the beam is splitted in different bunches with 10^{11} protons each, separated temporally by 25 ns. Then, the protons are accelerated in the Super Proton Synchrotron (SPS) to 450 GeV, before being injected into the LHC. Finally, the protons are transferred to the two beam pipes of the LHC. These are not the only accelerators in the CERN complex as seen in Fig. 3.1, as there are other accelerators used for

[1] The underground tunnel was inherited from a previous accelerator called Large Electron-Positron Collider (LEP), which operated from 1989 to 2000.

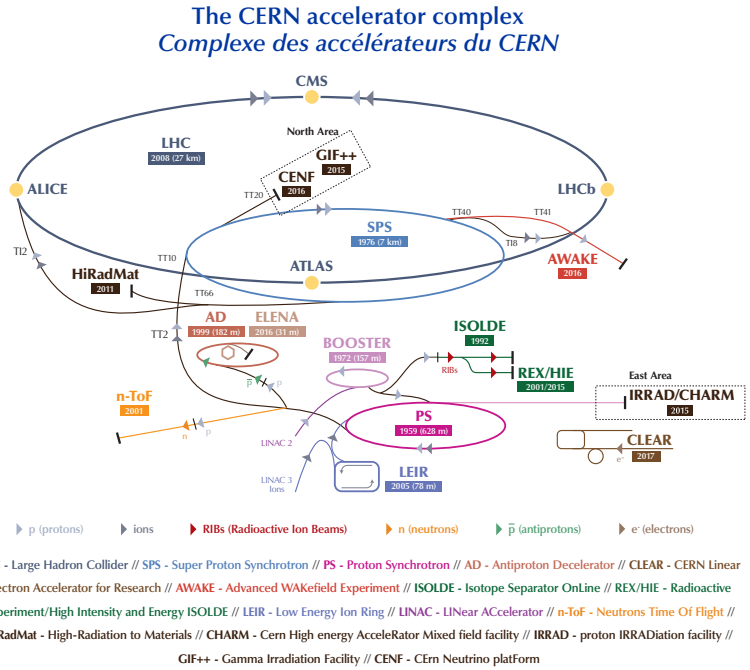

Figure 3.1: Schematic view of the CERN accelerator complex. Source: [140].

different purposes, such as the Antiproton Decelerator (AD) and the Isotope Separator On-Line Device (ISOLDE).

The LHC is designed to accelerate protons or heavy ions (mainly ionized lead, but also xenon) to very high energies along two beam pipes in opposite directions, with four intersection points. Particles are accelerated using electric fields in radio-frequency cavities, reaching $\sim 99.9\%$ of the speed of light. This is only possible by accelerating the particles in an ultra-high vacuum environment (10^{-13}) to avoid collisions with gas molecules. The beams are guided through the LHC ring using superconducting dipole magnets, designed to produce a magnetic field of 8.3 T. To achieve the superconducting state, the magnets are cooled down with a cryogenic system filled with liquid helium, reaching temperatures of 1.9 K.

The detectors located in the intersection points are ATLAS (A Toroidal LHC ApparatuS [93]), CMS (Compact Muon Solenoid [94]), LHCb (Large Hadron Collider beauty [141]) and ALICE (A Large Ion Collider Experiment [142]), which have different purposes. The ATLAS and CMS detectors are general-purpose detectors, whose first goal was to discover the Higgs boson. However, these detectors are designed to study a wide range of physics processes from proton-proton collisions, including precision measurements of the Stan-

dard Model and the search for new particles. Despite their common goals, the two experiments have different designs and strategies, which allows to cross-check the results obtained by each other. The LHCb detector is focused in the study of flavor physics related to the b-quark. This one-sided detector was designed to cover the forward region, since b-hadrons are expected to be mainly produced close to the beam pipe in proton-proton collisions. The ALICE detector is designed to study the properties of the quark-gluon plasma produced in heavy-ion collisions. This state of the matter, in which the strong interactions dominate, allows to reproduce the conditions from the first moments of the Universe after the Big Bang.

Apart from the detectors located in the intersection points, there are other experiments using the LHC beams for specific purposes. The TOTEM experiment [143] is focused on the measurement of the total elastic cross-section of proton-proton collisions, as well as its diffraction properties. The LHCf (LHC forward [144]) experiment perform measurements of particles produced in the forward region to study the properties of energetic cosmic rays. The Monopoles and Exotics Detector at the LHC (MoEDAL [145]) is focused on the search of magnetic monopoles and highly ionizing stable massive particles. Finally, the Forward Search Experiment (FASER [146]) studies neutrinos and looks for light and extremely weakly interacting particles.

LHC performance: energy, luminosity and pile-up

The final goal of the LHC is to supply its main detectors with numerous energetic collisions to increase the probability of rare processes to happen. Therefore, the two main magnitudes that determine the performance of the LHC, and any other collider focused on high energy physics studies, are the center-of-mass energy and the luminosity.

The energy of a collision of two beams in opposite directions is measured at the center-of-mass frame, at which the two beams have the same energy ($E_{cm} = 2E_{beam}$) and the momentum in the transverse plane is zero. The larger is the energy of the beam, the larger is the energy of the collision, and the more probable is the production of interesting processes that contain heavy particles. There are limitations in the energy that the beams can reach in a circular collider. These are mainly related to the curvature of the accelerator and the mass of the particles accelerated, which will contribute to the synchrotron radiation that decelerates the particles. Thus, the larger is the accelerator and the lower is the mass of the particles, the larger is the energy that can be reached.

The luminosity is the quantity that measures the ability of an accelerator to produce the required number of collisions per unit of time and area. Since interesting processes are often very rare (low cross-section), reaching a high

luminosity is crucial to measure a reasonable number of events. Thus, the rate of collisions can be defined as:

$$R = \sigma \times \mathcal{L}, \tag{3.1}$$

where σ is the cross-section and $\mathcal{L}$ is the *instantaneous luminosity*. The unit to measure the cross-section is usually the barn (1 b = 10^{-24} cm^2) and the instantaneous luminosity is measured in inverse barns per second (b^{-1}s^{-1}). Equation 3.1 can be integrated over a period of time to obtain the expected number of events during that period, for which the *integrated luminosity* is needed.

Since this Thesis presents analyses with data from proton-proton collisions, it is interesting to explain the luminosity of this type of interactions. As mentioned before, the beams at the LHC are split in bunches of $\sim 10^{11}$ protons. The collisions occur when the bunches of the two beams cross each other at the interaction points. Since the luminosity will depend on the geometry of the beams, these are squeezed to a very small width that can be modeled with a Gaussian profile. The instantaneous luminosity can be calculated in terms of collider parameters as [147]:

$$\mathcal{L} = \frac{n_1 n_2}{4\pi\sigma_x\sigma_y} f \ , \tag{3.2}$$

where n_1 and n_2 are the number of protons in each bunch, σ_x and σ_y are the widths of the beams in the transverse plane, and f is the bunch crossing frequency.

Another important concept for colliders is the *pile-up* (μ), which is the number of interactions that occur in a single bunch crossing. Since the rate of collisions can be expressed as $R = \mu \times f$, taking into account equation 3.2, the pile-up can be computed as:

$$\mu = \frac{n_1 n_2}{4\pi\sigma_x\sigma_y} \sigma \ . \tag{3.3}$$

Despite a high pile-up allows to increase the probability of rare processes to happen, it is also a problem for the reconstruction of the relevant collisions, since the detector will have to deal with numerous particles coming from different interactions in the same bunch crossing. A minor contribution is possible from the so-called *out-of-time pile-up*, which is the number of interactions that occur in different bunch crossings but are reconstructed in the same event. This is controlled in the LHC by a temporal separation between bunches of 25 ns, being compatible with the *dead time* of the detectors during which an event is being processed, and the readout is not available.

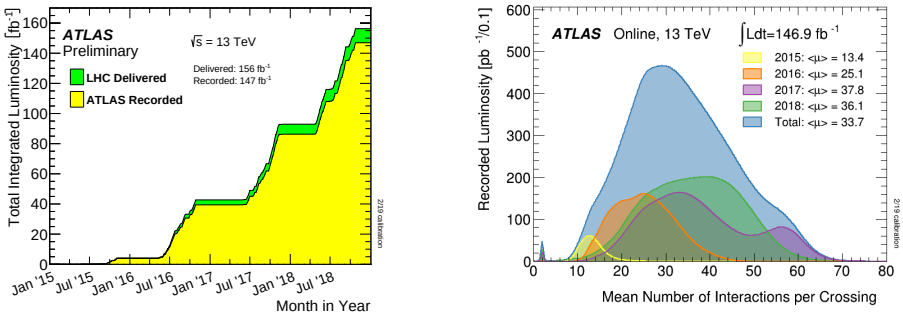

(a) (b)

Figure 3.2: Evolution of the integrated luminosity (a) and the pile-up distribution (b) during Run 2 of the LHC. Source: [149].

LHC operation and future plans

Since the start in 2008, the LHC has been in operation during three data-taking periods or "runs", alternated with two long shutdowns (LS1 and LS2). Run 1 took place from 2009 to 2013, Run 2 from 2015 to 2018, and Run 3 is currently ongoing, with data-taking expected to continue until mid 2026. During Run 1, the proton-proton collisions were recorded at center-of-mass energy of 7 and 8 TeV, delivering an integrated luminosity of 28.26 fb^{-1}. Run 2 increased both the energy of the collisions and the integrated luminosity to 13 TeV and 156 fb^{-1}, respectively. The data recorded by the ATLAS experiment during Run 2 is used in the two analyses presented in this Thesis (see Section 6 and Section 7). Figure 3.2a shows the evolution of the luminosity delivered during Run 2, as well as the luminosity recorded by the ATLAS detector. After the detector and data quality requirements, the total integrated luminosity corresponding to Run 2 used in the presented ATLAS analyses is 139 fb^{-1} [148]. Data for Run 3 is still being recorded, expecting to yield to 300 fb^{-1}at 13.6 TeV. Together with the increase in luminosity, the pile-up has also increased during the LHC operation, starting with an average of collisions around 9 in its first year of operation and reaching averaged values of 50 in Run 3. Figure 3.2b shows the evolution of pile-up during Run 2.

The LHC is expected to be upgraded during a long shutdown period between mid 2026 and 2030 (LS3) to specially increase its luminosity reach, with the High-Luminosity LHC (HL-LHC) [150] project planned to start during 2030. Currently, the HL-LHC operations are foreseen out to end 2041, divided in three data-taking periods and expecting a total integrated luminosity of 3000 fb^{-1}.

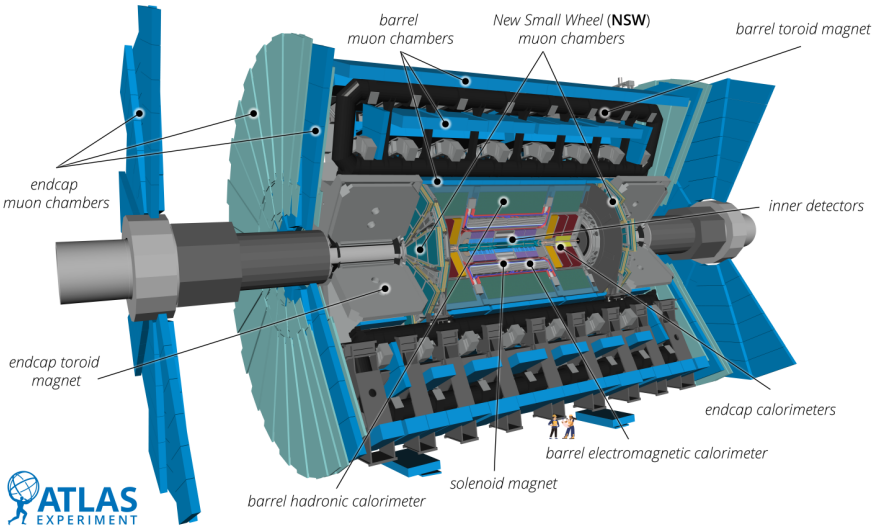

Figure 3.3: Schematic view of the ATLAS detector and its main components. Source: [152]

3.2 The ATLAS detector

The ATLAS detector [151] is a general-purpose detector located in one of the four interaction points of the LHC. It is the largest collider detector ever built, with a toroidal shape whose dimensions are 25 m in diameter and 44 m in length, weighting 7000 tons. A schematic view of the ATLAS detector is shown in Figure 3.3, in which two people are included for scale comparison. It was initially designed to discover the Higgs boson, but it is also used to study a wide range of physics processes from proton-proton collisions, including precision measurements of the Standard Model and the search for new particles.

The ATLAS detector uses a right-handed coordinate system, with the origin at the nominal interaction point, the z-axis pointing along the beam pipe, the x-axis pointing to the center of the LHC ring, and the y-axis pointing upwards. Instead of the usual polar coordinates $(r,\ \phi,\ \theta)$, more convenient coordinates are used: $(r,\ \phi,\ \eta)$, where r is the radial distance in the transverse plane, ϕ is the azimuthal angle, and η is the pseudorapidity, which is defined as $\eta = -\ln[\tan(\theta/2)]$. According to this coordinate system, the angular distance is defined on the $\eta - \phi$ plane as $\Delta R = \sqrt{(\Delta\eta)^2 + (\Delta\phi)^2}$. Also for convenience, the four-momentum of a particle is expressed as $p_\mu = (E, \mathbf{p}) = (E, p_T, \phi, \eta)$, where $p_T = \sqrt{p_x^2 + p_y^2}$ is the transverse momentum.

In order to reconstruct the different type of particles produced in the collisions, the ATLAS detector is composed of several subdetectors with different

characteristics, which are arranged as cylindrical layers around the beam pipe, together with forward and backward end-cap detectors to cover the full solid angle. The innermost detector is the Inner Detector (ID), which is used to measure the trajectories of charged particles from their interaction vertices. The ID is surrounded by the Calorimeters, which are used to measure the energy of particles by stopping them and measuring the energy deposited in the material. These are mainly divided in two types: the Electromagnetic Calorimeter and the Hadronic Calorimeter. The Muon Spectrometer (MS) is the outermost detector, which is used to measure the trajectories of muons, which are able to escape from the detector without loosing all their energy. A trigger system is also used to select the most interesting events for further analysis, reducing the amount of data to be stored and processed.

Inner detector

The Inner Detector is the closest part to the interaction point. With 7 m of length and 2.3 m of diameter, it has a coverage up to $|\eta| < 2.5$. The ID aims to measure the trajectories and impact parameters of charged particles, as well as their primary and secondary vertices. This is possible because the ID is placed within a solenoid magnet, curving the trajectories of charged particles (tracks) by a 2 T magnetic field. In turn, the ID is composed of three subdetectors: the Pixel Detector, the Semiconductor Tracker (SCT) and the Transition Radiation Tracker (TRT). The detection technique of these subdetectors is different, collecting complementary information for the reconstruction of the tracks. Figure 3.4 shows a schematic view of the subdetectors of the ID.

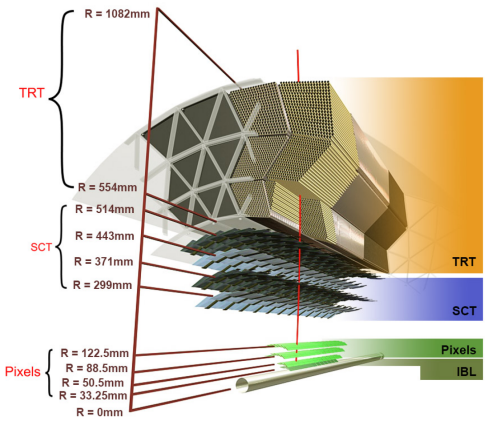

Figure 3.4: Schematic view of the Inner Detector of the ATLAS detector. The Pixel Detector, the SemiConductor Tracker (SCT) and the Transition Radiation Tracker (TRT) are shown. Source: [153]

The Pixel Detector is originally made of 1774 modules arranged in three barrel layers, at radial distances of 5.05, 8.85 and 12.25 cm, as well as two end-caps with three disks each. This allows three measured hits per track along the region $|\eta| < 2.5$, with an intrinsic resolution of 10×60 μm^2. The Insertable B-Layer (IBL) [154] is the innermost layer of the Pixel detectors, located at 3.3 cm from the beam pipe. It was installed during the LS1 in order to improve the impact parameter resolution and the tracking efficiency. It consists of 280 pixel modules arranged along 14 staves, covering the zenithal region $|\eta| < 3$ with an intrinsic resolution of 10×60 μm^2. An overlap of 1.82 between staves ensures a full coverage of the azimuthal direction.

The SCT is placed after the Pixel Detector at a radial distance of 29.9-56.0 cm and consists of 4088 silicon strip modules, arranged in four concentric barrels and two end-caps of nine disks each. Both the SCT and Pixel detectors are cooled to -10°C to reduce the noise from thermal excitations. The coverage of the SCT is also up to $|\eta| < 2.5$. Each module has two layers of silicon microstrips arranged back-to-back with a deviation angle of 40 mrad, providing two-dimensional measurements of the hits. Despite the intrinsic resolution of 17×580 μm^2 is worse than the Pixel Detector, it can provide four hits per track.

The TRT is the outermost part of the ID, covering the region $|\eta| < 2.0$. Unlike the SCT and Pixel detectors, the TRT is not sensitive to the z coordinate, providing one-dimensional measurements on the $r - \phi$ plane with an intrinsic resolution of 130 μm. The TRT is composed of 350848 gas-filled[2] tubes with a diameter of 4 mm, which are placed parallel to the beam pipe in the barrel and perpendicular in the end-caps. Around 30 hits per track are measured through the ionization of the gas, with the tube working as a cathode and containing an anode wire in the center. Both the probability and the amount of ionization depend on the particle type, allowing a better identification.

Calorimeters

The calorimeters are placed after the solenoid magnet that surrounds the ID, being the heaviest part of the ATLAS detector. These are instruments whose response to the passage of particles is the production of a signal proportional to the energy of the particle, for which a total absorption of the particle inside the material is necessary [156]. To achieve this, the layers with detectors (active) are alternated with very dense materials (passive) whose only purpose is to stop the particles. The interaction of the particles with the passive material produces a shower of secondary particles, which are detected by the active ma-

[2]The tubes are filled with a mixture of gases, which was modified for Run 2 to reduce the risk of Xe leakage. The Xe was substituted by Ar and the current composition consists of 70% Ar, 27% CO_2, and 3% O_2 [155].

terial. Similarly to the ID, the response of calorimeters depends on the type of particles, being critical for particle identification since it is also sensitive to neutral particles. The calorimeters are divided in two parts, the Electromagnetic Calorimeter (ECAL) and the Hadronic Calorimeter (HCAL), apart from the Forward Calorimeter (FCal) placed in the end-caps. Figure 3.5 illustrates the different calorimeters of the ATLAS detector.

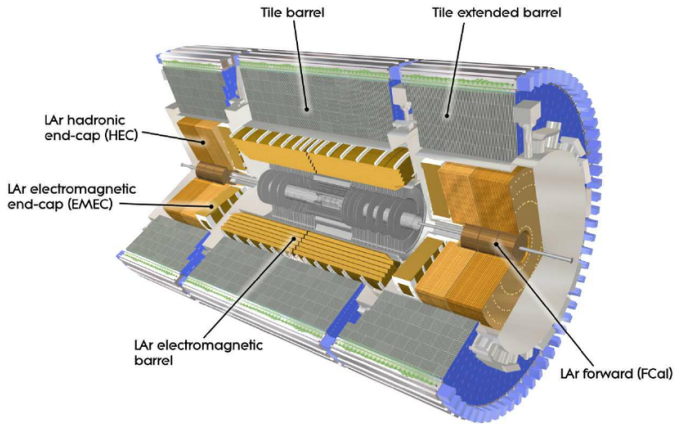

Figure 3.5: Schematic view of the calorimeters of the ATLAS detector. The Electromagnetic Calorimeter (ECAL), the Hadronic Calorimeter (HCAL) and the Forward Calorimeter (FCal) are shown. Source: [157]

The ECAL is the innermost part of the calorimeter. It consists of a barrel covering the region $|\eta| < 1.475$ and two end-caps covering the region $1.375 < |\eta| < 3.2$. The barrel is split in two identical halves separated by a small gap at $z = 0$. Each half contains three layers of passive material made of lead (Pb). When an electron or positron interact with the heavy nuclei of Pb, it emits photons through bremsstrahlung, which are converted into e^+e^- pairs, creating further interactions as a cascade until the energy of these particles is below the threshold to create additional pairs, around 10 MeV. Despite other phenomena also occur during the absorption, such as Compton diffusion and photoelectric effect, the collectable signal only comes from the ionization produced by the charged particles. The active material consists of liquid argon (LAr), which was chosen for its radiation hardness and its linear response with energy. Each end-cap consists of two wheels, each one with three Pb-LAr layers. A cryostat covering the ECAL maintains the LAr at $-184°C$ to keep its liquid state.

The HCAL is placed after the ECAL, covering the region $|\eta| < 1.7$ in the barrel and $1.5 < |\eta| < 3.2$ in the end-caps. Each HCAL end-cap is divided in two wheels, are LAr-based calorimeters and share the cryogenic system with the ECAL end-caps. The barrel is composed by a long central barrel and two

extended barrels at each side, while the end-caps are divided in two wheels each. The passive material of the HCAL is made of steel, which is alternated with plastic scintillators as active material. When the hadrons impact on the nuclei of steel, secondary particles are emitted by the de-excitation or the fision of the nuclei. The emitted photons are detected by the scintillators, which produce a light signal that is amplified and collected by photomultipliers. The main difference with respect to the ECAL is that the response of the HCAL is not linear with the energy. The non-linearities in the response of the HCAL comes from the recoiling of the nuclei and its binding energy, as well as the small fraction of energetic hadrons that escape from the calorimeter. In addition, the electromagnetic cascades previously described are also produced in the HCAL, which introduces asymmetries in the profile of the energy deposits coming from hadronic interactions and affects directly the energy resolution. Different compensation methods exist to mitigate the joint problem of linearity and resolution.

The FCal is placed in the end-caps, covering the region $3.1 < |\eta| < 4.9$. It is composed of three modules, with the first one containing copper (Cu) and the other two containing tungsten (W), alternating again with LAr as active material.

Muon spectrometer

The MS is the outermost and largest part of the ATLAS detector, covering the region $|\eta| < 1.05$ in the barrel and $1.4 < |\eta| < 2.7$ in the end-caps. It is designed to measure the trajectories of muons, which frequently escape from the calorimeters without loosing all their energy. Similarly to the ID, although independent, the muons tracks are bent in the MS due to the magnetic field generated by a toroidal magnet system, which reaches peak strengths of 3.9 T in the barrel and 4.1 T in the end-caps. The components of the MS include different technologies and capabilities. The Monitored Drift Tubes (MDTs) are 30 mm tubes filled with a gas mixture of Ar (93%) and CO_2 (7%), used to measure the drift time of ionization electrons. Positioned in the three barrel layers and two of the end-cap disks, they provide high-precision measurements of muon tracks in the bending direction. In the most forward region, the Cathode Strip Chambers (CSCs) provide a high granularity to handle higher fluxes and background conditions in the $2.0 < |\eta| < 2.7$ region. The Resistive Plate Chambers (RPCs) and Thin Gap Chambers (TGCs) provide measurements of the muon tracks in the orthogonal direction to the bending in the barrel and end-caps, respectively. Unlike the MDTs and CSCs, in which the drift times are relatively long, the RPCs and TGCs provide a fast response and are used in the trigger system. Figure 3.6 shows the different components of the MS. Despite not being shown in this figure, the MS was upgraded during the LS1

with the installation of the New Small Wheels (NSWs) in the end-caps, which are equipped with small-strips TGCs and Micromegas detectors.

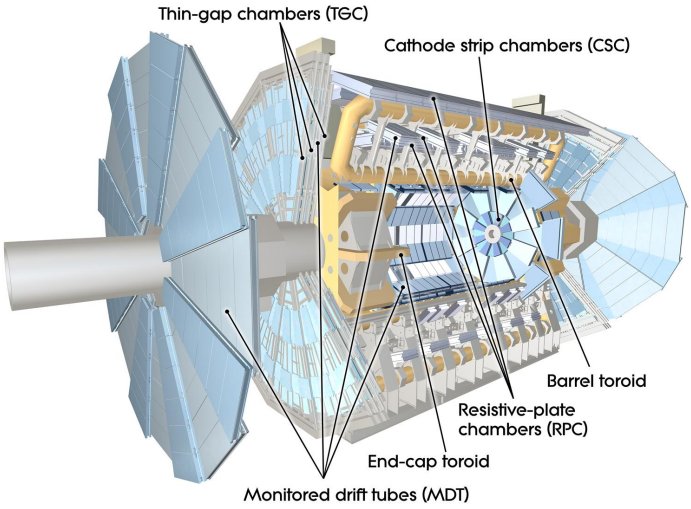

Figure 3.6: Schematic view of the Muon Spectrometer of the ATLAS detector. The Monitored Drift Tubes (MDTs), the Cathode Strip Chambers (CSCs), the Resistive Plate Chambers (RPCs) and the Thin Gap Chambers (TGCs) are shown. The toroidal magnets are also shown. Source: [158]

Trigger system

The vast majority of the collisions produced in the LHC are not interesting for the physics program of ATLAS and the other experiments. Thus, the collisions or events need to be triggered by the experiments according to certain criteria before being stored and processed. The trigger is a fundamental part in the data acquisition (DAQ) system of any type of experiment, but it becomes crucial for the LHC experiments since it is technically impossible to record all the collisions produced. As mentioned in Section 3.1, the bunch crossing rate during the Run-2 of the LHC was 40 MHz, with an average pile-up of 25 interactions per bunch crossing. This would result in a data rate of 60 TB/s recorded by the ATLAS experiment.

The ATLAS collisions during Run-2 were filtered online with a two-level event trigger [159–161]: the Level-1 (L1) trigger and the High-Level Trigger (HLT). The L1 trigger is integrated at hardware level and reduces the total rate by a factor 200, selecting events with a rate of 100 kHz. Low granularity information from the calorimeters and the dedicated muon chambers is used to decide if an event is stored or not in an interval of 2.5 μs. The output of

the L1 trigger consists of Regions of Interests (RoIs) that include the position and transverse momentum of candidate objects. This information is buffered in the Read-Out System (ROS) and sent to the HLT system. The HLT is a software-based trigger that refines the selection using the RoIs from the L1, reconstructing the full event and applying more sophisticated selections. However, this is still a fast process with an acceptance rate of 1.5 kHz and a data storage of 1.5 GB/s. Figure 3.7 shows workflow of the DAQ system of the ATLAS experiment.

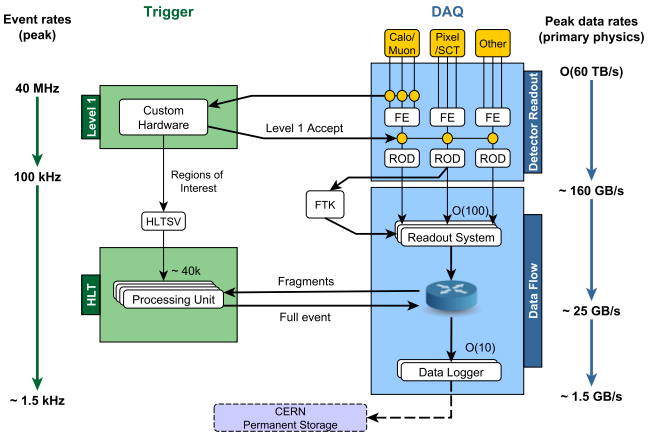

Figure 3.7: Functional diagram of the ATLAS trigger and DAQ workflow used in Run 2, showing expected peak rates and bandwidths through each component. Events passing the L1 hardware trigger are passed to the HLT via the farm supervisor node (HLTSV), now including assembly of ROIs. Simultaneously to this, event data from the detector front-end electronics systems are sent to the ROS via optical links from the RODs in response to a L1 trigger accept signal. These data are then buffered in the ROS and sent to the HLT. Once the HLT accepts an event, this is sent to permanent storage via the Data Logger. Source: [162]

Chapter 4

Event generation and Monte Carlo simulation

This chapter describes the event generation and simulation of proton-proton collisions in the ATLAS experiment. Most of the ATLAS analyses make use of simulated events to estimate the expected yields and kinematic distributions of both the SM and signal processes, which are then compared to the experimental data. The simulated samples are crucial to understand the effect of the selection criteria on the different processes, to validate the analysis techniques and to perform statistical inference from template histograms.

The phenomenology of the collisions is discussed in Section 4.1, detailing the modeling procedure at each stage of the event generation, from the proton structure to the simulation of the detector. Section 4.2 briefly describes the most relevant MC generators involved in the generation of the simulated samples, which are presented in Section 4.3 for both the SM processes and the BSM samples that will be employed in Chapters 6 and 7. Lastly, Section 4.4 outlines the various sources of theoretical uncertainties arising from the imperfect modeling of the simulated events.

4.1 Simulation chain of proton-proton collisions

The interactions with more interest for this Thesis are the proton-proton collisions that take place in the LHC. Protons are a type of hadrons containing three valence quarks (uud) and a sea of quarks and gluons. Since QCD is not perturbative at the energies inside the proton, it is difficult to model these complex systems in order to understand or predict the outcome from proton-proton collisions.

The proton structure: parton distribution functions

The *parton model* is the best approach in this context. First described by R. Feynman in 1969 [163], this model assumes that hadrons consist of point-like constituents, known as partons. The partons, which do not interact among themselves according to this model, carry a fraction x_i of the total momentum P of the hadron: $p_i = x_i P$. It is important to estimate the momentum fraction of the different parton species, since the momentum of the hadron can be controlled in the laboratory but the momentum of the partons, which are the ones that actually interact in a collision, is a priori unknown. Probability density functions (PDFs) are used with this purpose. These functions provide the probability to find a parton type within the proton with a particular momentum fraction at an energy scale Q. Therefore, PDFs are functions of the flavor of the parton and the energy scale: $f(x_i, Q)$. If the proton contained only its valence quarks, the PDFs would correspond to three delta functions centered at $x_i = 1/3$. However, as a consequence of the interactions with the sea of quarks, the PDFs of the valence quarks are smeared out and the PDFs of gluons and other quark flavors become non-trivial.

Since there is not a perturbative method to calculate the PDFs analytically, these need to be estimated from global fits to data in collisions at certain energy scales, being possible to extrapolate to other energies using perturbative QCD. Different estimations come from different data, and the most common set of PDFs are provided by the NNPDF [164], MSTW [165] and CTEQ [166, 167] collaborations. Figure 4.1 shows the PDFs of partons for two different energy scales, 10 GeV^2 and 10^4 GeV^2. It is observed that the valence quarks carry most of the momenta of the proton at low energies, but the larger is the energy the larger is the contribution of the sea, which is dominated by the gluons.

Hard scattering process

The proton-proton collisions can be classified in two types: *elastic* and *inelastic*. The elastic collisions take place at very low energies, in which several non-perturbative effects intervene, but the kinematics of the process can be modeled independently of the structure of the protons. The inelastic collisions, which occur at higher energies, modify the structure of the protons when the partons interact. When an inelastic interaction is sufficiently energetic, the process is known as hard scattering. In a hard-scattering process (see Figure 4.2), a parton from each proton interact independently of the other partons in the proton. In these cases, the parton model and the PDFs provide crucial information of the partons in the initial state.

The cross-section of a hard-scattering process can be calculated through the factorization theorem [168], which postulates that the cross-section can be

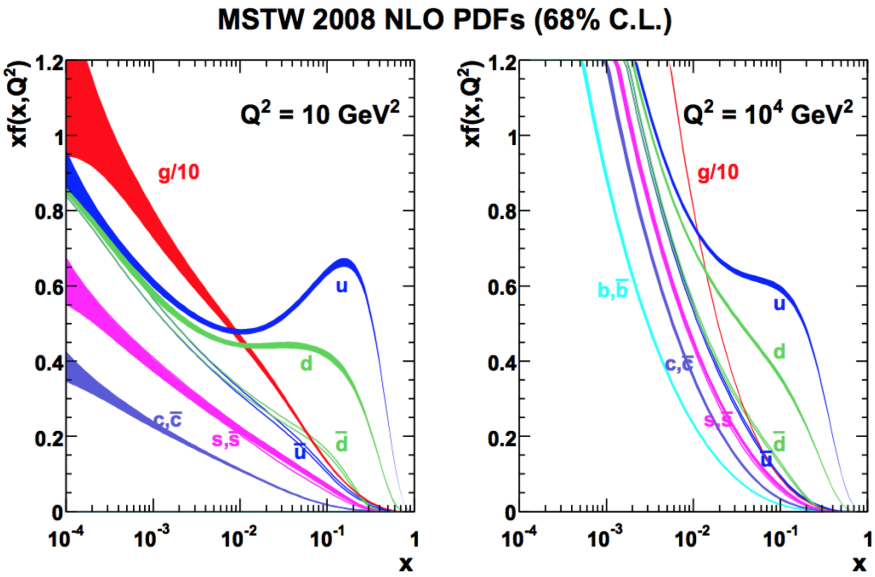

Figure 4.1: MSTW 2008 NLO PDFs of the partons in the proton at two different energy scales: $Q^2 = 10$ GeV^2 (left) and $Q^2 = 10^4$ GeV^2 (right). Source: [164].

factorized into two terms. The first term is universal as it contains the PDFs of the interacting partons, which do not depend on the process. The second term is the partonic cross-section for the particular process. Thus, the cross-section of a hard-scattering process $pp \to X$ is given by:

$$\sigma_{pp\to X} = \sum_{i,j} \int dx_1 dx_2 f_i(x_1, \mu_F^2) f_j(x_2, \mu_F^2) \hat{\sigma}_{pp\to X}(x_i, x_j, \mu_F^2), \tag{4.1}$$

where the sum runs over all the parton flavors i and j, $f_i(x_1, \mu_F)$ and $f_j(x_2, \mu_F)$ are the corresponding PDFs of the partons i and j, and $\hat{\sigma}(ij \to X, \mu_F)$ is the partonic cross-section for the process $ij \to X$ at the factorization scale μ_F. The factorization scale μ_F is the energy scale in which this factorization is considered to be convenient, representing the boundary between low and high energies. The partonic cross-section of the process can be calculated perturbatively. A perturbation series on the QCD running coupling α_s allows computing corrections to the leading order term:

$$\hat{\sigma}_{pp\to X} = \sigma_{LO} + \alpha_s(\mu_R)\sigma_{NLO} + \alpha_s^2(\mu_R)\sigma_{NNLO} + \ldots, \tag{4.2}$$

The running coupling depends on the renormalization scale μ_R, which appear during the regularization process needed to absorb the divergences coming

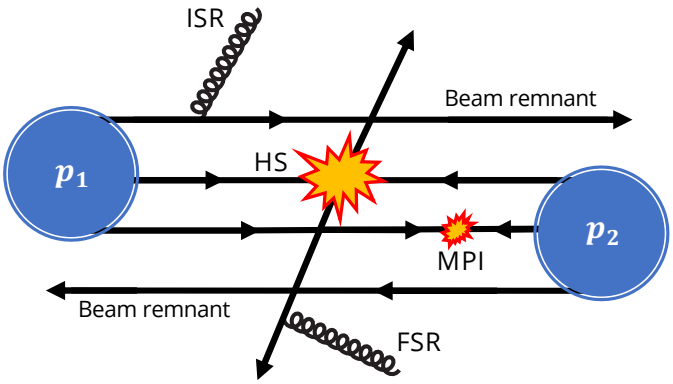

Figure 4.2: Example of a hard-scattering process in a proton-proton collision. The activity corresponding to the underlying event is also shown, which includes the ISR, FSR, beam remnants and an additional MPI.

from the loop corrections. If the series became infinite, the μ_F and μ_R parameters would not be needed, meaning that these are not physical quantities. For the calculations, both parameters are commonly assigned the same value, corresponding to the energy of the process. Since the cross-section will depend on the chosen values, an uncertainty on the result needs to be computed by varying these parameters.

The parton shower

In the vicinity of the hard scattering, the partons are intensely accelerated by the strong force, leading to the emission of gluons and quarks in the form of initial-state radiation[1] (ISR) and final-state radiation (FSR). This is an iterative process that produces a cascade of partons known as *Parton Shower (PS)*. Since the subsequent radiations are less energetic than the hard scattering, the running coupling gets larger and the perturbative approach is insufficient to model the PS. While the matrix-element (ME) calculations can provide a very precise description of the hard scattering process, including higher order corrections in α_s and interference effects, the pQCD calculations can not model the emissions in the *soft-collinear* regime.

MC generators, such as Pythia [169] and Herwig [170], implement the PS algorithms, which emulate the higher order terms in the perturbation expansion of α_s with approximate models. The PS algorithms emulate the higher order terms in the perturbation expansion of α_s with approximate models simulated

[1]The modeling of the ISR brings the additional complication of accounting for these parton emissions and splittings in the PDF.

by MC generators, such as PYTHIA [169] and HERWIG [170]. These models often come with a set of *tune* parameters determined from fits to LHC data, and are sometimes modified depending on the target process. At each order in the perturbation series, the PS models the collinear parton splittings (smaller angle) and the softer gluon emissions (infrared radiation).

In order to combine the hard scattering with the showering process, the ME calculations are interfaced with PS MC generators. Combining both approaches to simulate successive emissions of quarks and gluons can lead to double-counting of the emissions. For instance, a diagram simulated at NLO by ME calculations may overlap with the corresponding LO ME calculation with additional radiation from the PS. Therefore, the phase space of the ME calculations needs to be separated from the phase space of the PS evolution. This is achieved by the so called *ME-PS matching* algorithms, which define a transverse momentum and angular cutoff above which additional radiation is simulated with the ME. Some of the most common algorithms are the CKKW [171] and the MLM [172] matching schemes.

The partons produced from subsequent splittings are less energetic as the PS evolves, starting from the matching scale μ_Q. This is the energy scale above which the ME calculations are used and below which the PS is employed. The development of the PS finishes when the hadronization scale ($\sim$ 1 GeV) is reached.

The hadronization process

The hadronization process is the next step after the PS, leading to the formation of the final-state hadrons. Similarly to the showering process, the hadronization is a non-perturbative effect that can not be modeled by pQCD. The hadronization simulation makes use of phenomenological models that are based on general QCD features to describe the formation of the hadrons. The MC event generators contain parameters that are not determined by first principles, but are adjusted to by comparing to experimental data. The most common models implemented in the MC generators are the *Lund string model* [173] and the *Cluster fragmentation model* [174].

The Lund String model reaches the final hadrons state using a more direct approach based on the linear confinement expected at large distances between partons forming color-singlet objects. As an example, a $q\bar{q}$ system where both partons are moving away from each other feel a potential energy that is proportional to the distance between them. This can be interpreted as a color string that connects both partons, which will continue separating until the string split in two pieces. Such splitting occurs when the increasing potential energy makes energetically possible the creation of another $q'\bar{q}'$ pair, resulting in two colorless systems: $q\bar{q}'$ and $q'\bar{q}$. This phenomenological model is implemented

by Pythia.

The Cluster fragmentation model performs the partons-to-hadrons transition making use of an intermediate stage of cluster objects based on the observed property of pre-confinement. These clusters objects are colorless massive hadron resonances that follow a universal mass distribution of a few GeV (with universal meaning that it does not depend on the scale or nature of the hard process). The evolution of such clusters consists of iterative binary decays whose products are less-excited resonances until the final hadrons remain. The MC generators Herwig and Sherpa [175] implement the Cluster model in their hadronization simulation, but Sherpa also provides an interface based on Pythia to enable the implementation of the Lund String model.

Figure 4.3 illustrates the hadronization process according to both models. Despite both models provide a precise description of the experimental data, using different models can lead to different results. The analyses rely on the comparison of the results obtained with different MC generators to estimate the systematic uncertainties associated to the hadronization process. Appendix A details a novel method based on machine learning to parameterize these theoretical uncertainties, avoiding the need of running the MC generators multiple times with different configurations.

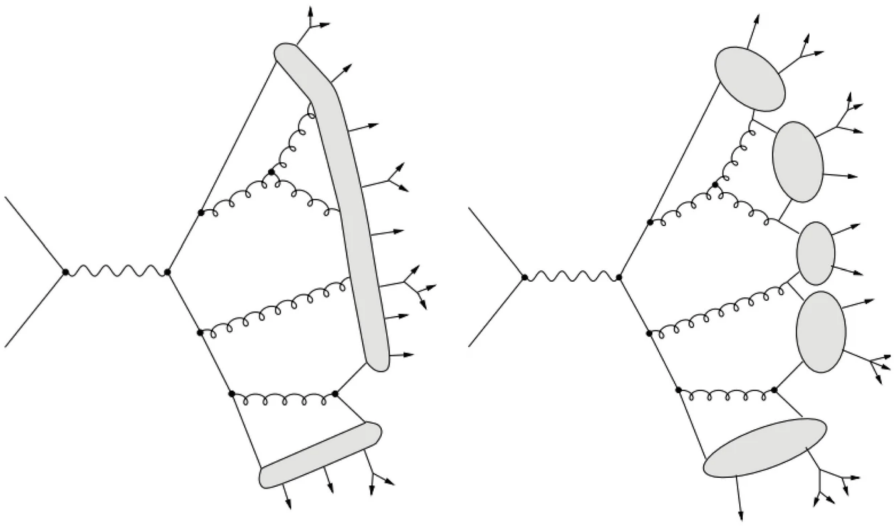

Figure 4.3: Schematic representation of the hadronization process according to the Lund string model (left) and the Cluster fragmentation model (right).

The decay of the heavy hadrons, such as B mesons, is simulated after the PS and the hadronization with the EvtGen program [176]. This program provides a large set of decay channels for the most common hadrons, including

the branching ratios and the angular distributions of the decay products.

Underlying event simulation

Secondary soft effects, different from the ISR and FSR mentioned previously, are produced in a proton-proton interaction, such as beam remnants and multiple parton interactions (MPI) [177]. All the activity accompanying the hard scattering is known as the *underlying event (UE)*. An example of both a hard-scattering process and its UE in a proton-proton collision is illustrated in Figure 4.2. The products of the UE are color-charged partons that also undergo PS and hadronization. These non-perturbative processes are modeled with MPI models depending on a set of *tune* parameters, different for each MC generator and are determined from fits to experimental data [178].

Pile-up simulation

The modeling of pile-up effects was achieved by superimposing on the simulated primary event minimum-bias[2] interactions in the same and adjacent bunch crossings that were generated with Pythia 8.186 [169]. These events used the NNPDF2.3LO parton distribution functions (PDF) [179] and the A3 tune parameters [180]. To accurately reflect the observed average number of interactions per bunch crossing ($\langle\mu\rangle$) in the experimental data, MC events were weighted accordingly. Additionally, a rescaling factor of 1.03 ± 0.04 was applied to the $\langle\mu\rangle$ to enhance the matching between the observed data and the simulations regarding the visible inelastic pp cross-section [181].

Simulation of the ATLAS detector

The output of the MC generators is a list of four-vectors for all stable particles in the final state of the proton-proton collision. This stage of the event generation is known as the *truth-level* or *particle-level*. In order to compare the simulated events with the experimental data, the response of the ATLAS detector to the particles needs to be simulated and an analogous reconstruction of the objects has to be implemented [182]. This final stage of the simulation is known as the *reconstruction-level* (or *reco-level*).

The detector simulation software is based on the GEometry ANd Tracking (Geant4) framework [183], which models the interaction of particles and their decay products with the active and passive materials of the detector. The geometry of all the sub-detectors and their components is precisely implemented, accounting for the acceptance and the resolution of the detector.

[2]The *minimum-bias events* refer to collisions passing minimal trigger requirements to avoid favoring specific event types.

For the simulation, the energy deposits are converted into simulated electronic signals and the readout electronics are emulated to provide realistic responses. This *full simulation* [182] is a highly intensive CPU task that simulates the multiple scatterings, photon conversions, bremsstrahlung radiation and energy loss originated for each particle traversing the detector. In particular, these showers of particles simulated through the calorimeters of the ATLAS detector requires the largest amount of computational resources.

The large amount of resources and time needed for the detector simulation motivates the use of faster and less refined simulation techniques. The so-called *fast simulation* (AFII [184, 185]) is often implemented for alternative samples. The AFII imposes a parameterized description of the particle shower shapes in the calorimeters, reducing the CPU time by one order of magnitude or more, at the expense of a poorer response. However, this effect can be mitigated via dedicated calibration with the experimental data at reconstruction level.

4.2 Monte Carlo generators

The most common MC generators used in the ATLAS experiment are:

MadGraph began as a ME LO event generator, but the most extended version, denoted as MadGraph5_aMC@NLO [186] (or MG5aMC@NLO), automatically calculates the NLO QCD corrections to SM processes. It generates any $2 \to 1$, $2 \to 2$ and $2 \to 3$ processes, including any user-defined Lagrangian that makes this generator very flexible for BSM simulations. The ME predictions feed the PS program, interfaced with Pythia or Herwig, providing NLO+PS calculations based on the automated MC@NLO [187] matching program.

Powheg [188, 189] is a ME event generator of $2 \to 2$ and $2 \to 3$ processes that provides an alternative technique to combine NLO calculations with the PS evolution. It is interfaced with Pythia or Herwig using the Powheg Box framework [190] to provide NLO+PS simulations. The matching is controlled by the h_{damp} parameter, corresponding to the transverse momentum p_{T} of the first additional emission beyond the LO Feynman diagram in the PS.

Sherpa [175] is considered a general purpose MC generator that incorporates the ME generation of $2 \to 2$ processes and its own PS model based on the Catani-Seymour dipole factorization scheme. A complete hadronic final state is simulated according to the Cluster fragmentation model, and the UE is included through a MPI model. It also provides NLO+PS simulations, implementing OpenLoops for the virtual QCD corrections. Sherpa includes

approximately 200 decay tables that contain 2500 decay channels, where the majority of the decaying particles are hadrons.

Pythia [169] is often used to simulate the PS on events coming from a different ME generator. It is regarded as a general purpose MC generator as well, since it also handles ME calculations for $2 \to 1$ and $2 \to 2$ processes at LO. A p_T-ordered PS evolution is considered through a dipole factorization scheme. An MPI model is also included to simulate the UE, while the hadronization is performed using the Lund String model.

Herwig [170] is an alternative to Pythia that implements an angular-ordered PS evolution. Its current version Herwig 7 is also capable of NLO+PS calculations, implementing its own variants of the MC@NLO and Powheg matching for several processes. The Cluster fragmentation model is used for the hadronization process and an eikonal MPI model simulates the UE.

4.3 Simulated samples of the analyses

Simulated samples are used to model the signal and background processes, evaluate the acceptance of the detector, estimate the systematic uncertainties, and to provide a comparison with the experimental data. The generation of all SM and BSM processes involving top quarks assumed a mass of 172.5 GeV, with the top quarks decaying exclusively into a W boson and a b quark. Additionally, the decay of the top quarks, as well as W and Z bosons, is modeled using MadSpin [191, 192] to account for spin correlations.

The description of the simulated background processes given in this section is focused on the Monotop analysis presented in Chapter 6. However, most of the background details can be extended to the other analyses considered for the combination presented in Chapter 7. In addition, the signal samples used both in Chapter 6 and 7 are described in this section.

Background samples

The three analyses presented in Chapter 6 and 7 apply different selection criteria, and therefore, the contribution of the background processes is different at each of them. However, most of the processes passing one of the analysis selections also pass the others but in a different proportion. Since the simulation of the background processes is carried by the collaboration following a centralized procedure, the description of the background samples is common

for all the analyses[3]. The nominal background samples playing a major role in the MONOTOP analysis are the following:

- **Top-quark pair production** ($t\bar{t}$): The production of $t\bar{t}$ pairs is simulated at NLO using POWHEG BOX v2 with the NNPDF3.0NLO PDF set. This is interfaced with PYTHIA 8.230, which uses the NNPDF2.3LO PDF set and the A14 tuning parameters. The h_{damp} parameter is set to 1.5 m_{top}, and the renormalization and factorization scales follow the default functional form $\sqrt{m_{\text{top}}^2 + p_{\text{T}}^2}$, which p_{T} being the average p_{T} of the top and anti-top quarks. The simulated events are normalized to the NNLO QCD cross-section [193–198], which includes resummation of soft gluon emissions at next-to-next-to-leading logarithmic (NNLL) precision, as computed by the TOP++ [194] software.

- **Single top-quark production** (t-channel, s-channel, and Wt-channel): Both the single top tW and *s-channel* productions are simulated at NLO in QCD using the POWHEG BOX v2 generator within the five-flavor scheme[4] with the NNPDF3.0NLO PDF set. The diagram removal (DR) scheme [199] is employed to mitigate interference and overlap between tW and $t\bar{t}$ production. In contrast, single top t-channel production is modeled using the POWHEG BOX v2 generator at NLO in QCD under the four-flavor scheme, using the NNPDF3.0NLONF4 PDF set [200]. The renormalization and factorization scales are set to the top-quark mass for the tW and *s-channel* productions, while for the t-channel production is set to $\sqrt{m_{\text{b}}^2 + p_{\text{T},b}^2}$, where b refers to the spectator b-quark. All single top processes are interfaced with PYTHIA 8.230 [201] employing the A14 tune and the NNPDF2.3LO PDF set. Simulated samples are normalized to the NNLO QCD cross-section [202–204], including resummation of soft-gluon emission corrections, similar to the $t\bar{t}$ process.

- **Top-quark pairs with a W or Z production** ($t\bar{t}V$, tZq): The production of $t\bar{t}$ pairs in association with a W or Z boson is simulated using MG5AMC@NLO 2.3.3 at NLO QCD accuracy with the NNPDF3.0NLO PDF set. This generator is interfaced with PYTHIA 8.230 using the A14 tune and the NNPDF2.3LO PDF set. The renormalization and factorization scales are set to the default scale

[3]The ATLAS collaboration generates the SM processes together with the detector and reconstruction simulation for each data-taking period, adapting the reconstruction part to the particular calibrations applied at the time to ensure the compatibility with the experimental data.

[4]Unlike the four-flavor scheme, the five-flavor scheme considers b quarks as partons in the proton.

$0.5 \times \sum i\sqrt{m_i^2 + p_{\mathrm{T},i}^2}$, where the sum runs over all the particles generated from the ME calculation. Similarly, the production of tZq is modeled using MG5aMC@NLO 2.3.3 with the NNPDF3.0NLO PDF set, maintaining NLO QCD accuracy. Normalization of the samples aligns with NLO QCD and EW cross-sections [187], with the $t\bar{t}Z$ cross-section additionally adjusted for Z-boson off-shell contributions.

- **V+jets processes**: The production of W and Z bosons in association with jets (V+jets) is simulated using the Sherpa 2.2.1 generator, where the ME calculations are NLO accurate for up to two emitted partons and LO accurate for up to four additional partons. These calculations employ the Comix [205] and OpenLoops [206] libraries. The ME+PS matching is employed across various jet multiplicities [207]. These are then integrated into an inclusive sample using an enhanced CKKW merging procedure [171, 208], which is refined to NLO accuracy under the MEPS@NLO framework [209]. The NNPDF3.0NLO PDF set is used [200], and both processes are normalized to the NNLO cross-section [210].

- **Diboson production** (WW, WZ and ZZ): Diboson events are simulated using the Sherpa 2.2.1 generator, with the ME calculations containing all diagrams with four EW vertices. The ME is computed for one parton at NLO and up to three partons at LO using the same procedure as for the V+jets processes. The NNPDF3.0NLO PDF set is used, and the samples are normalized to the NLO cross-section provided by Sherpa.

The other two analysis considered in Chapter 7 (HtZt and Osml) include additional minor backgrounds. The HtZt analysis is sensitive to the $t\bar{t}H$ process, considered part of the $t\bar{t}V$ category and simulated using Powheg Box v2 in the five-flavor scheme at NLO QCD accuracy with the NNPDF3.0NLO PDF set. The Pythia 8.230 generator is used for the PS and hadronization and the h_{damp} parameter is set to $3/4 \times (\mathrm{m}_t + \mathrm{m}_{\bar{t}} + \mathrm{m}_H) = 352.5$ GeV. The Osml analysis includes the $t\bar{t}WW$ and $t\bar{t}t\bar{t}$ processes in the $t\bar{t}V$ category. These processes have been simulated using MadGraph 5 and Pythia 8 using the NNPDF2.3LO PDF set and the A14 tune. This analysis also considers the tWZ process in the single top category, simulated using MG5aMC@NLO 2.3.3 with the NNPDF3.0NLO PDF set and interfaced with Pythia 8 using the A14 tune.

A summary of the configuration of the simulated backgrounds is presented in Table 4.1. The EvtGen 1.6.0 [176] program is used for the properties of b- and c-hadron decays for all samples showered using Pythia or Herwig, except for the $t\bar{t}$ $+W/Z$ processes where EvtGen 1.2.0 is used. Alternative simulation samples were used to analyze the modeling uncertainties related to top

Process	ME event generator	ME PDF	PS and hadronization	UE tune	Cross-section calculation
$t\bar{t}$	POWHEG BOX v2	NNPDF3.0NLO	PYTHIA 8.230	A14	NNLO+NNLL [193–198]
Single top	POWHEG BOX v2	NNPDF3.0NLO	PYTHIA 8.230	A14	NNLO+NNLL [202–204]
$t\bar{t}V$ ($V = W/Z$); tZq	MG5AMC@NLO2.3.3	NNPDF3.0NLO	PYTHIA 8.230	A14	NLO [187]
V+jets ($V = W/Z$)	SHERPA2.2.1	NNPDF3.0NLO	SHERPA	Default	NNLO [213]
Diboson	SHERPA2.2.1	NNPDF3.0NLO	SHERPA	Default	NLO
$t\bar{t}H$	POWHEG BOX v2	NNPDF3.0NLO	PYTHIA 8.230	A14	NLO [187]
tWZ	MG5AMC@NLO2.3.3	NNPDF3.0NLO	PYTHIA 8	A14	NLO [187]
$t\bar{t}WW$, $t\bar{t}t\bar{t}$	MADGRAPH 5	NNPDF2.3LO	PYTHIA 8	A14	LO [187]

Table 4.1: Overview of the nominal simulated background samples used in the MONOTOP analysis, described in Chapter 6. Single-top production includes the t-channel, the tW-channel and the s-channel. The lower part correspond to additional background samples that are exclusively considered in the HTZT or OSML analyses, presented in Chapter 7.

quarks[5]. For these samples, the MG5AMC@NLO generator was employed for ME calculations, using the NNPDF3.0NLONF4 PDF set and the PS was simulated with HERWIG7, applying the H7UE tune [211] and the MMHT2014LO PDF set [212]. For the tW associated production, the diagram subtraction scheme [199] was applied to manage the interference with $t\bar{t}$ production and to assess related uncertainties. Further description of the modeling uncertainties can be found in Section 4.4.

Dark Matter samples

Simulated samples corresponding to the scalar and vector DM mediator models presented in Chapter 2 were generated with MADGRAPH5_AMC@NLO 2.8.1 [186]. The ME was calculated at LO using the NNPDF3.0NNLO PDF set. The PS was handled by PYTHIA 8.244 with the A14 tune [214] and the NNPDF2.3LO PDF set [179]. A total of 256 signal points were generated for both models by varying the values of their parameters in order to cover the parameter space with a high granularity. Since the simulation of the detector response is computationally expensive, most of these signal samples were generated only at *truth-level*. Figure 4.4 shows the grid of simulated signal samples. The black points correspond to the signal samples that were generated at the *truth-level*, while the red and green points correspond to the signal samples that were simulated at the reconstruction level (*reco-level*).

A reweighting technique has been developed to estimate the *reco-level* distributions of the signal points for which only the *truth-level* simulation is available. To do this, the red signal points in Figure 4.4, for which both *truth-level*

[5]This includes $t\bar{t}$ and single top-quark production, excluding other minor top quark-related backgrounds.

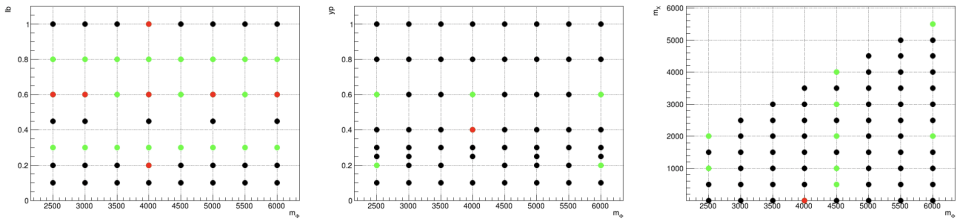

(a)

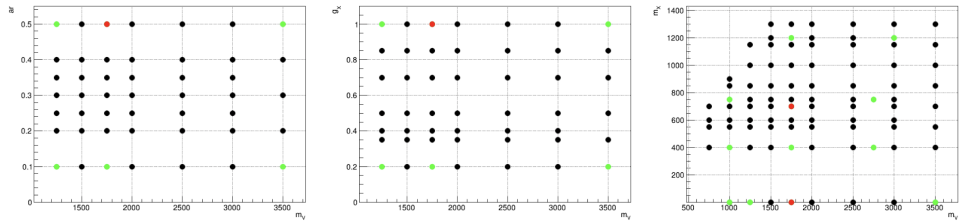

(b)

Figure 4.4: Summary maps of the produced simulation in the (a) scalar and (b) vector DM mediator model parameter space. The green points indicate that the sample includes the simulation of the detector response and the object reconstruction steps, while black points are instead generated at truth-level. The red points are the ones used as reference for the reweighting, which also include the simulation of the detector response and the object reconstruction.

and *reco-level* samples are available, were used as a reference to extract the reweighting factors. The *reco-level* samples of additional signal points were generated later to validate the reweighting procedure in different regions of the parameter space, corresponding to the green points in the figure.

The reweighting factors are computed with *truth-level* information as follows:

$$w_{\text{target}} = w_{\text{reference}} \times \overbrace{\frac{\epsilon_{\text{target}}}{\epsilon_{\text{reference}}}}^{\text{Acceptance}} \times \overbrace{\frac{\sigma_{\text{target}}}{\sigma_{\text{reference}}}}^{\text{Cross-section}} \times \overbrace{\frac{y^i_{\text{target}}}{y^i_{\text{reference}}}}^{\text{Shapes}} \tag{4.3}$$

where *target* refers to the signal point for which only *truth-level* samples are available, and *reference* refers to the signal point for which both *truth-level* and *reco-level* samples are available. The computation of the reweighting factors takes into account three different aspects:

- The normalization of the signal will be affected by the acceptance of different signal points for the selection criteria of the analysis. Such

effect is estimated from the ratio of acceptances between the target and reference signal points, both computed at *truth-level*.

- The different cross-sections between the reference and the target signal points also affects the normalization.

- Similarly, a different parameter choice can imply a variation in the kinematics of the signal events between the reference and the target signal point. To correct for this shape effect, the E_T^{miss} distribution of the target point at *truth-level* is reweighted bin-by-bin to match the E_T^{miss} distribution of the reference point at *truth-level*.

Vector-Like Quark samples

The single production of a vector-like T quark is simulated at LO according to the phenomenological model described in Ref. [114] and briefly presented in Chapter 2. The ME computed with MG5aMC@NLO 2.3.3 includes all relevant tree-level processes, including non-resonant production, and employs NNPDF3.0LO PDFs with the four-flavor scheme. The PS and hadronization are simulated with Pythia 8.212.

Separate samples are generated for the production modes $Wb \to T \to Zt$, $Zt \to T \to Zt$, $Wb \to T \to Ht$ and $Zt \to T \to Ht$. The cross-section computed at LO is corrected by a factor that accounts for finite-width effects [215], as well as a factor that accounts for the non-resonant [216] T-quark production. In addition, LO-to-NLO k-factors are computed in the Narrow Width Approximation [217]. The branching ratio is computed for fixed values of the relative couplings (ξ_W, ξ_Z, ξ_H) corresponding to the singlet scenario: $BR(T \to Wb) = 2 \times BR(T \to Zt) = 2 \times BR(T \to Ht) = 0.5$.

The signal samples were generated for a default value of the overall coupling κ_T and different values of the T-quark mass m_T between 1.1 and 2.7 TeV, in steps of 0.2 TeV. In order to increase the granularity of the parameter space, internal weights are calculated during the generation allowing to interpolate the intermediate mass points and to cover a range of κ_T down to 0.1. Despite no important variations in the kinematics are expected for different κ_T values, the width of the T-quark spreads as κ_T takes lower values. The $Wb \to T \to Zt$ and $Wb \to T \to Ht$ production modes, dominant in the singlet scenario, are not very sensitive to this effect and were generated for a κ_T value equal to 1. Instead, the $Zt \to T \to Zt$ and $Zt \to T \to Ht$ production modes, dominant in the doublet scenario, were generated for values of $\kappa_T = 1.0, 0.7, 0.4$ and 0.2, such that a smoother extrapolation is achieved.

In addition, a change in the dynamic scale in MG5aMC@NLO at the threshold $\Gamma_T/m_T = 0.1$ leads to a discontinuity in the cross-section [216],

which is mitigated averaging the cross-section between the two scales around the threshold with the following formula:

$$\sigma(\Gamma_T/m_T) = \begin{cases} \sigma_{\text{low}}(\Gamma_T/m_T) + \frac{1}{2}[\sigma_{\text{high}}(0.1) - \sigma_{\text{low}}(0.1)], & \text{if } \Gamma_T/m_T < 0.1, \\ \sigma_{\text{high}}(\Gamma_T/m_T) - \frac{1}{2}[\sigma_{\text{high}}(0.1) - \sigma_{\text{low}}(0.1)], & \text{if } \Gamma_T/m_T \geq 0.1. \end{cases} \tag{4.4}$$

This effect will not introduce an additional systematic in the statistical analysis, but it will be added in some limit plots in the form of band uncertainties around the theoretical cross-sections, illustrating the small impact on the final results.

4.4 Modeling uncertainties

The modeling uncertainties account for the fact that the generation of the processes is not perfect and that the exact values of the internal parameters of the generator are unknown. The main sources of modeling systematic uncertainties are described in the following, for both the SM and BSM processes presented in the previous section.

Since each of the analyses explored in this Thesis target different final states and the background composition is different, some modeling uncertainties are specific to each analysis. In addition, the analyses perform different treatments to their backgrounds in order to improve Data/MC discrepancies that may arise from an MC mismodeling. These background treatments (e.g. normalization or shape reweighting of a particular background process) result in additional analysis-specific sources of uncertainties. However, the main sources of modeling uncertainties are common to all analyses:

PDF uncertainties: The impact of PDF uncertainties is evaluated for top-quark pairs, single-top, $V+$jets and diboson backgrounds following the PDF4LHC recommendations [218] with a comparison of a hundred variations of the NNPDF3.0 PDF set against the nominal sample. The resulting envelope is then used to estimate the impact on the expected yields of each bin included in the fit.

ME, PS and hadronization uncertainties: The uncertainties arising from the choice of the ME generator are assessed for the top-quark pairs background by comparing the baseline setup of Powheg Box+Pythia8 with the alternative setup of MG5aMC@NLO+Pythia8. A *two-point systematic*[6] variation is also considered evaluating the PS and the hadronization

[6]Two-point systematics refer to those uncertainties that are evaluated by comparing two generators that model differently a specific part of the event generation.

uncertainties for top-quark pairs. The baseline generation makes uses the Lund String model, which is compared with the alternative sample POWHEG BOX+HERWIG7 that implements the Cluster fragmentation model. The Wt-channel includes an additional two-point systematic uncertainty related to the overlap between $t\bar{t}$ and tWb final states. In this case, the baseline diagram removal (DR) procedure is evaluated against the diagram subtraction (DS) scheme.

The uncertainties due to missing higher-order QCD corrections are addressed by varying the renormalization and factorization scales by factors of 0.5 and 2 in the baseline simulation for both top-quark pairs and single-top backgrounds, as well as for the DM signal samples. Uncertainties due to ISR are assessed by varying the corresponding the A14 PS tune `Var3c` [219] in PYTHIA and the renormalization scale for QCD emissions, respectively.

For weak boson production associated with jets (which includes both $V+$jets and VV +jets production), uncertainties from the resummation and PS matching uncertainties are evaluated following the procedure described in Ref. [220]. Here, a parameterization at truth-level is developed to derive a set of weights for different values of the renormalization and factorization scales. A minimal set of weights are then applied to the nominal events to estimate the associated systematic effect.

Heavy-Flavor jet production uncertainties: Since the MONOTOP analysis presented in Chapter 6 apply selections on the b-jets multiplicity in the final state, a specific uncertainty related to heavy-flavor jet production is addressed for the weak boson production associated with jets. A normalization uncertainty of 30% [221] is associated with rates of events featuring $V+b$-jets and $V+c$-jets. $V+b$-jets are identified by events with at least one jet in the final state that is truth-matched with at least one B-hadron. The matching is performed through an improved CKKW procedure [171, 208]. When no B-hadrons are found, the event is labeled as $V+c$-jets if at least one D-hadron is truth-matched with a jet.

Normalization uncertainties: Theoretical uncertainties affect the cross-section calculations of all background processes, influencing their normalization. A detailed summary of the normalization uncertainties for each background is provided in Table 4.2. It is noted that no cross-section uncertainties for $t\bar{t}$ and $V+$jets are included, as their normalization within the analysis phase space is determined through normalization factors that are free-floated parameters in the fit. Similarly, the normalization uncertainties on the signal cross-section are not accounted for, since the signal strength is also a free parameter in the fit.

Background	Uncertainty		Ref.
t-channel	+4.0%	−3.4%	[204]
$\bar{t}$-channel	+5.0%	−4.5%	[204]
tW-channel	+5.3%	−5.3%	[202]
s-channel	+3.6%	−3.1%	[203]
Diboson	+6%	−6%	[222]
$t\bar{t}V$	15%	−15%	[223]

Table 4.2: Summary of the normalization uncertainties on the different background processes. Note that no cross-section uncertainties for $t\bar{t}$ and $V+$jets are included, since normalization factors are fitted in the analysis phase space.

DM signal reweighting uncertainties: Additional discrepancies need to be considered for the DM signal models due to the reweighting procedure applied to cover the parameter phase space (see Eq. 4.3). The reweighting uncertainties are classified into two categories:

- Shape discrepancies: the kinematics of the target samples were reweighted from the normalized $E_{\mathrm{T}}^{\mathrm{miss}}$ distributions, and therefore, some shape discrepancies are expected when looking to another variable, which needs to be accounted. Since the variable to be fitted is the BDT score, the *truth-level* and *reweighted-level* shapes are compared for the normalized score distribution of all the target points along every "direction" in the parameter space. Such comparisons provide bin-by-bin uncertainties corresponding to the largest discrepancy observed in a particular "direction", resulting in a 22% (6%) uncertainty for the scalar (vector) DM mediator model.

- Reco acceptance: The detector response introduces a bias in the reconstructed quantities, due to detector resolution and inefficiencies or the use of non-optimal reconstruction algorithms. Such a bias can modify the acceptance of the signal when applying the selection criteria on the kinematic variables. Since these effects can not be computed systematically, samples at *reco-level* were simulated for some target points (the green points in Figure 4.4) to estimate these uncertainties. The maximum discrepancy of 10% was taken conservatively as an overall uncertainty for any DM signal, which has been tested to impact the final upper limits around 1%.

Chapter 5

Event reconstruction

The reconstruction of the objects produced in the collisions is explained in this chapter. Section 5.1 describes the reconstruction procedure of the objects used in Chapters 6 and 7, whose specific definitions and working points are given in Section 5.2. Finally, Section 5.3 outlines the experimental uncertainties arising from intrinsic detector limitations and imperfections in the reconstruction and identification techniques, which are propagated to the final results of the analyses presented in this Thesis.

5.1 Object reconstruction

As it was mentioned in Chapter 3, the different subdetectors of the ATLAS experiment are designed to measure particular properties of the particles. The reconstruction of the objects usually requires the combination of the information collected by more than one subdetector. Figure 5.1 shows how the subdetectors are specialized in the detection and reconstruction of different objects.

Since there is not a unique criterion to identify a reconstructed object with a certain particle, each definition relies on different algorithms or working points. Similarly, it is important to take into account that any reconstruction method or algorithm used will introduce systematic uncertainties that might have an impact in the posterior analyses. Only the reconstructed objects that appear in the analyses of this Thesis are described, as well as their working points and main sources of systematic uncertainties.

Tracks and vertices

The tracks are the reconstructed trajectories of the charged particles, which are mainly determined in the ID. The track reconstruction [225, 226] is performed

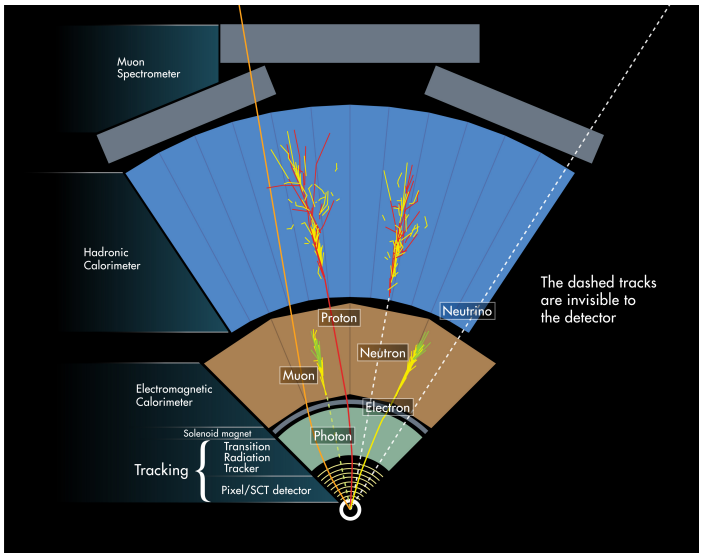

Figure 5.1: Schematic view of the ATLAS detector showing the different sub-detectors and the particle types they are specialized in the detection and reconstruction. Source: [224]

with two sequential algorithms, named *inside-out* and *outside-in*. The inside-out algorithm starts from the center of the ID and works outwards, taking into account the positional information of the hits in the Pixel and SCT detectors and extrapolating the tracks to the TRT. The different hits are combined into track candidates, assigning a track score to prioritize the most reliable ones. The inside-out procedure accounts for most of the tracks reconstructed in ATLAS, but it is complemented by the outside-in algorithm, which starts from the TRT hits and continues inwards. To reduce the processing time, only tracks with a transverse momentum above 400 MeV are evaluated by the outside-in algorithm. The performance of the track-fitting is enhanced by the Kalman filter reconstruction method [227], which takes into account the non-linearity coming from the energy loss of the particles in the material.

The vertices, which are the points where the tracks are originated, are also reconstructed. The primary vertex (PV), defined as the vertex with the highest sum of the transverse momentum of its tracks, is identified as the interaction point of the hard-scattering process[1]. The compatibility of the tracks with the PV is evaluated by the impact parameters d_0 and z_0, which are the transverse and longitudinal distances between the track and the PV, respectively. In particular, the d_0 is the closest transverse distance between the track and the

[1]Secondary vertices are also reconstructed by analyzing the tracks of charged particles left by decaying particles.

beam line, while the z_0 is its distance along the z-axis to the PV. The impact parameters are crucial in the definition of the reconstructed objects, since they need to be compatible with the PV in order to reconstruct the full event coming from the hard-scattering process.

Electrons

The proper identification of an electron combines the information from the ID and the ECAL [228, 229]. The ECAL is divided in the $\eta \times \phi$ space as a grid with 200×256 elements, corresponding to an angular resolution of $\Delta\eta \times \Delta\phi = 0.025 \times 0.025$ radians. In the radial direction, cells are stacked in towers and are activated when a particle deposits energy in them. The electromagnetic cascade produced by a particle will activate a cluster of topologically connected cells (topo-cluster), whose total energy is an approximation to the energy of the original particle. The bremsstrahlung radiation emitted by the electrons may also produce satellite clusters around a barycenter topo-cluster. Thus, dynamic clusters named *superclusters* are built with clustering algorithms in order to reconstruct the total energy of the original electron [230]. To be identified with an electron, the seeded barycenter cluster is required a minimum transverse energy of 1 GeV, and to be matched with a track in the ID with at least 4 hits, which improves the resolution at low energies. If no track is associated to the cluster, the energy deposit is labeled as a photon candidate.

Electrons produced in the hard collision are called *prompt electrons*, but additional electrons can be produced in the decay of secondary particles with a relatively long lifetime, such as the b-hadrons. Moreover, other objects can be misidentified as electrons, being called *fake electrons*. The identification of prompt electrons is optimized by a likelihood-based method (LH) that combines information from the cluster shape with the cluster energy to track momentum ratio and other discriminating variables. The LH method provides three levels of identification: *loose*, *medium* and *tight*, where the set of tight electrons candidates is a subgroup of the medium candidates, which in turn is a subgroup of the loose candidates.

Isolation criteria are also applied to the electron candidates to reduce the contamination from nearby particles. To require isolated electrons, thresholds on maximum activity are set, which are quantified by the sum of transverse energy (calorimeter-based) and momentum (track-based) in certain ΔR cones around the electron candidate. Usually, $\Delta R = 0.2$ for calorimeter isolation and $\Delta R = 0.2$ or 0.3 for track isolation. Four working points are defined for the isolation criteria, which combine different thresholds on the calorimeter and track-based variables: Gradient, HighPtCaloOnly, Loose and Tight [229][2].

[2]The working points for the isolation of electrons have evolved in the last years, but the ones given in the text correspond to the definitions used for the analyses in this Thesis.

The identification and isolation efficiencies need to be corrected between data and MC simulation, which is done through the *tag-and-probe* method [231] in $Z \to e^+e^-$ and $J/\Psi \to e^+e^-$ events. This method takes events with two opposite-signed electrons whose invariant mass is compatible with the Z or J/Ψ resonances and very strict selection criteria are applied to one of the electrons (*tag* electron). Then, the selection efficiency is measured on the other electron (*probe* electron) at different working points. Thus, some scale factors are calculated as the ratio of the efficiencies in data and MC simulation, which are applied to the MC simulation to match the data efficiencies and are propagated to the analyses. These scale factors and their uncertainties are propagated to the analyses.

Muons

Muons identification mostly use information from the ID and the MS, which could also be combined with calorimeter information. Four different muon definitions in ATLAS, depending on which subdetectors are used [232, 233]:

- Combined muons (CB) are reconstructed using a combined track fit to match the ID and the MS tracks, taking into account the lost energy in the calorimeters. This definition is valid in the $|\eta| < 2.5$ region.
- The inside-out muons (IO) and the Segment-tagged muons (ST) are reconstructed using the ID track and extrapolating to the MS. The IO reconstruction requires at least three aligned hits in the MS and performs a combined track fit. The ST definition is used when the muon only crosses one MS layer, probably due to a low transverse momentum, and its track parameters are taken directly from the ID fit.
- Calorimeter-tagged muons (CT) are reconstructed from a track in the ID that matches with energy deposits in the calorimeters consistent with a minimum-ionizing particle[3]. These muons are restricted to the $|\eta| < 0.1$ track parameters will be taken from the ID track fit.
- Extrapolated muons (ME) are reconstructed using the MS and the calorimeters, which are required to have a track in the MS and a matching energy deposit in the calorimeters.

Analogously to electrons, the identification working points are also in loose, medium and tight (except for the ST and CT which only consider loose definition). An additional high-p_T ($p_T > 100$ GeV) working point is optimized for

[3] A minimum-ionizing particle is a theoretical charged particle whose mean energy loss through matter is minimum. The closest example in the Standard Model to such a particle is the muon, reason for which it can escape from the calorimeters

muon identification. The conditions on the impact parameters for the prompt muon candidates are $|d_0/\sigma(d_0)| < 3$ and $|z_0 \sin\theta| < 0.5$ mm, which are less strict than the ones for the electrons. The isolation criteria also apply track and calorimeter-based variables, which are combined in different ways to define seven isolation operation points [233]. Scale factors are extracted to correct the identification and isolation efficiencies, for which the *tag-and-probe* method is also used in $Z \to \mu^+\mu^-$ and $J/\Psi \to \mu^+\mu^-$ events.

Jets

As discussed in Chapter 1 when introducing the quark model and QCD theory, quarks exist in confined systems called hadrons. When a quark (or gluon) is produced in a collision (*parton level*), it excites the surrounding quark sea, transferring energy to create new quarks and gluons that form colorless hadrons (*truth level*). This process, known as *hadronization*, results in a shower of particles distributed in a cone, referred to as a *jet*, centered around the direction of the initial quark, with the total momentum of the particles matching that of the original quark. The properties of the original quark or gluon needs to be inferred from the properties of the jet, which is reconstructed from information at detector level (*reco level*).

The most popular algorithm for jet reconstruction is the anti-k$_t$ algorithm [234]. The energy deposited by the shower of particles is not homogeneous. The cells activated around the cone axis register more energy, while the deposits become softer and spreader as the distance to the axis increase. Similarly to the branches of a tree, where the stronger branches are closer to the trunk. The anti-k$_t$ algorithm takes advantage of this structure to merge iteratively those branches of activated cells that are closer to the hardest branch. With this goal, two distances are defined:

$$d_{ij} = \min(k_{t,i}^{-2}, k_{t,j}^{-2}) \frac{\Delta_{ij}^2}{R^2}, \quad d_{iB} = k_{t,i}^{-2}, \tag{5.1}$$

where k_t, i is the transverse momentum of an object i, Δ_{ij} is the angular distance between the objects i and j, and R is the chosen radius of the cone that defines the jet. While d_{iB} is a measure of the distance of an object i to the beam, d_{ij} measures the distance of two objects i and j. A small value of d_{ij} imply that the i and j objects are close and at least one of them have a large transverse momentum.

An iterative algorithm compares the smallest distance d_{ij} with d_{iB} every time. If $d_{ij} < d_{iB}$, the two objects are merged and considered part of the same jet, and if $d_{ij} > d_{iB}$ the object i is considered a different jet by itself and is removed from the process. This procedure combines the soft particles to the

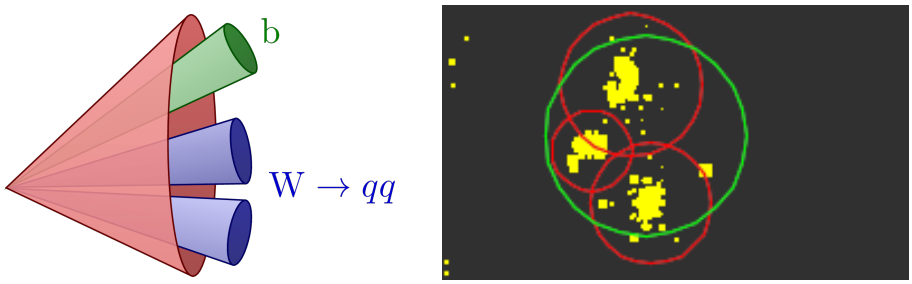

Figure 5.2: Schematic view of the jet topologies produced by the hadronic decay of a boosted top quark. The decay products are collimated in the direction of the parent particle, which is reconstructed with a large-R jet. Source: [235]

energetic ones to form *infrared* and *collinear* (IRC) safe jets[4].

Most ATLAS analyses define *small-R* jets with a radius of $R = 0.4$. However, heavy boosted particles (such as W bosons or *top* quarks) can decay hadronically and produce a different jet topology, as shown in Figure 5.2 for a boosted top quark. For these cases, the *large-R* jet reconstruction with a radius of $R = 1.0$ are very useful.

The reconstruction of jets makes use of energy deposits in both the ECAL and the HCAL, the charged-particle tracks or an algorithmic combination of both. The topo-clusters built from the activated cells are used as input for the anti-k$_t$ algorithm. When the energy is defined from the topo-clusters at EM scale, the reconstructed jets are called *EM jets*. The particle-flow (PF) algorithm allows to combine the reconstructed tracks in the ID with the calorimeter measurements (EM jets) to exploit the better momentum resolution of the tracks, specially at the low regime. Thus, the energy deposits in the calorimeter associated to charged tracks are replaced by their momenta. The jets reconstructed using this algorithm are called *PFlow jets* [236].

The jets are calibrated to correct their energy scale and resolution [237]. The jet energy scale (JES) is affected by the non-linear response of the calorimeters, the energy losses in the material and the pile-up contamination. In first place, the pile-up contribution is subtracted based on the momentum density along the jet area. Secondly, the jet energy and direction is corrected using truth-level[5] information of simulated jets. Then, the *global sequential calibration* technique improves the jet momentum resolution and the associated uncertainties. Finally, an *in-situ* calibration is applied to data to correct remaining discrepancies with simulation. The jet energy resolution (JER) measurements

[4]The IRC safety is imposed to jets in order to ensure that the possible soft and collinear emission of gluons in the outer part of the jet are contained in the reconstruction.

[5]The particle-level or truth-level refer to the final state of the event after the hadronization, before the interaction with the detector.

are limited by intrinsic detector limitations. To estimate these limitations, events where the momentum of jets can be precisely obtained are used, such as back-to-back dijet events. In order to match the resolution of simulations with that in data, a smearing is applied to simulated events when the momentum resolution in data is larger than in simulation.

In order to identify if a jet comes from the hard-scattering process or from pile-up interactions, the jet vertex tagger (JVT) algorithm is used [238]. This algorithm evaluates the compatibility of the tracks constituting the jet with the primary vertex, and assigns a score to the jet. While the JVT algorithm is applied to central and soft jets, for which $|\eta| < 2.4$ and $20 < p_T < 60$ GeV, the *forward JVT* or *fJVT* algorithm [239] is used for jets in the forward region, with $20 < p_T < 50$ GeV and $2.5 < |\eta| < 4.5$.

Large-R jets allow the reconstruction of heavy boosted particles whose decay products are collimated in the direction of the parent particle. Apart from the large-radius cone produced, these objects present a different substructure with respect to the small-R jets. The large-R jets are also reconstructed with the anti-k$_t$ algorithm, but the input objects can be either topo-clusters, particle-flow objects, Track-Caloclusters or Unified Flow Objects (UFOs). For the MONOTOP analysis presented in this Thesis, the large-R jets are reconstructed using the topo-clusters as input objects. The energy scale of the topo-clusters is defined at EM scale through the local cell weighting (LCW), which accounts for different effects such as the out-of-cluster energy and the energy deposited in dead material.

Similarly to the small-R jets, the energy scale of the large-R jets (LJES) is calibrated [240]. Firstly, a trimming technique [241] is often used to remove contamination from pile-up, soft emissions and the underlying event. In second place, the energy and direction is corrected using truth-level information of simulated jets. In this case, the jet mass resolution (JMR) is also improved by combining the masses obtained from the calorimeter and the ID tracks. Subsequently, two *in-situ* calibrations are applied to data to correct remaining discrepancies concerning the jet energy and jet mass scales [242].

Flavor tagging

After the jet reconstruction, additional techniques are used to discern if a jet comes from a gluon or a quark, and in the latter, to identify its flavor. Despite the lighter flavor quarks produce similar jets to the gluons, the heavier flavors produce jets with different properties. This is specially true for b-quarks, which have a relatively long lifetime and travel some distance before decaying and producing a *b-jet*. On the other side, top quarks decay before hadronizing since their lifetime is shorter than the hadronization timescale. Therefore, as it was explained previously, the decay products of a boosted top quark can be

reconstructed as a large-R jet.

The b-tagging techniques consist of two steps that make use of low-level and high-level algorithms [243]. First, low-level algorithms are used to reconstruct the most relevant features of the b-jets, such as their long lifetime, their high mass, their high decay multiplicity or their fragmentation properties. The high-level algorithms allow to improve the b-tagging efficiency by using multivariate analysis techniques that combine the information from the low-level algorithms. The DL1r [244] algorithm is used for the analyses presented in this Thesis, and make use of a Deep Neural Network (DNN) that provides three scores corresponding to the probability of the jet for coming from a light-flavor quark (or a gluon), a c-quark or a b-quark. These three probabilities (p_l, p_c and p_b, respectively) are then combined to define the following discriminant variable:

$$D_{\mathrm{DL1r}} = \ln\left(\frac{p_b}{f_c \cdot p_c + (1 - f_c) \cdot p_l}\right), \tag{5.2}$$

where f_c is the effective c-jet fraction in the training sample. Different working points can be defined according to the desired b-tagging efficiency.

Five pseudo-continuous bins for 60%, 70%, 77%, 85% and 100% efficiencies are defined. Efficiency evaluated in both data and simulation are used to extract scale factors that correct the b-tagging efficiencies in the simulation [243]. Such scale factors are then smoothed, extrapolated to the high-p_T regime and corrected for dependencies on the event generator. The uncertainties of the scale factors are also taken into account, which accounts for both b-tagging identification uncertainties and misidentification uncertainties for c-jets and light-flavor jets [245, 246].

Concerning the tagging of large-R jets as top-quark jets [247], the main misidentification comes from the W and Z bosons, which also decay hadronically and produce large-R jets. MVA techniques exploit discriminant features of large-R jets originated from a top quark, such as the reconstructed mass or the clustering structure of the decay products [248, 249]. The top-tagger algorithm used for the analysis presented in the MONOTOP search consists of a DNN-based tagger trained on $t\bar{t}$ events that consider the lepton+jet final state. Two definitions of a top-tagged jet are defined: the *contained* tagger considers a jet as top-tagged if all the energy from the hadronic decay products are contained in the reconstructed large-R jet, while the *inclusive* tagger extend the definition to large-R jets that partially contain the hadronic top-quark decay. Additionally, efficiency working points of 50% and 80% are set for this algorithm. The scale factors for the top-tagger are extracted comparing the data and simulation efficiencies as well, with a similar calibration and extrapolation to the high-p_T regime as for the b-tagging. Uncertainties concerning the top-tagger identification and misidentification efficiencies are also considered.

Overlap removal

The reconstructed objects in the event can overlap in the detector, which can lead to double counting of the same physical particle. To avoid this, a hierarchical-ordered overlap removal procedure is applied to the objects in the event. Firstly, an electron is removed if it shares a track with another electron with higher p_T. CM muons are removed if it shares a track with an electron, but the electron is removed for a different muon type. Any non-b-tagged jet found within a ΔR of 0.2 of an electron is removed, and any electron subsequently found within a $\Delta R < \min(0.4, 0.04 + 10\text{GeV}/p_T^e)$ of a jet is removed. Similarly, if any non-b-tagged jet with less than 3 tracks is within $\Delta R < 0.2$ of a muon, or if any of the tracks correspond to a muon, the jet is removed. As well as any muon subsequently found within $\Delta R < \min(0.4, 0.04 + 10\text{GeV}/p_T^\mu)$ of a jet is removed. These criteria are summarized in Table 5.1.

Reject	Against	Criteria
Electron	Electron	shared track and $p_T^{e1} < p_T^{e2}$
Muon	Electron	is calo-muon and shared ID track
Electron	Muon	shared ID track
Jet	Electron	not a b-jet and $\Delta R < 0.2$
Electron	Jet	$\Delta R < \min(0.4, 0.04 + 10\text{GeV}/p_T^e)$
Jet	Muon	not a b-jet and less than 3 tracks and ($\Delta R < 0.2$ or ghost-associated [250])
Muon	Jet	$\Delta R < \min(0.4, 0.04 + 10\text{GeV}/p_T^\mu)$

Table 5.1: Overlap removal criteria applied to the reconstructed objects of an event in descending order.

Missing transverse momentum

By the conservation of momentum, the sum of the momenta in the transverse plane to the beam axis of all the collision products should be zero. However, detector inefficiencies and particles that escape from the detector without interacting (such as the neutrinos or the dark matter candidates) can lead to an imbalance in the final transverse momenta [251]. The missing transverse momentum, whose absolute magnitude is denoted as E_T^{miss} or MET, is defined as the negative vector sum of the transverse momentum of all the reconstructed objects in the event:

$$\mathbf{p}_T^{\text{miss}} = -\sum_e \mathbf{p}_T^e - \sum_\mu \mathbf{p}_T^\mu - \sum_\tau \mathbf{p}_T^\tau - \sum_\gamma \mathbf{p}_T^\gamma - \sum_{\text{j}} \mathbf{p}_T^{\text{j}} - \sum_{\text{soft}} \mathbf{p}_T^{\text{soft}}, \qquad (5.3)$$

where the soft contribution comes from the reconstructed tracks associated to the PV but not matching any reconstructed object. Since both the reconstructed objects and the soft-term tracks are associated to the PV, the E_T^{miss} is relatively insensitive to the pile-up contamination.

The quality of the E_T^{miss} is evaluated by analyzing data and simulated collisions with different event topologies. The detector resolution is estimated by measuring the E_T^{miss} in $Z \to l^+l^-$ events, where the signature is very clean, and the missing transverse momentum is expected to be very low. The E_T^{miss} scale is studied with $W \to l\nu$ events, which produce high-p_T neutrinos. Finally, $t\bar{t}$ events are used to test the robustness of the E_T^{miss} in a multijet environment.

The systematic uncertainties concerning the E_T^{miss} are estimated by propagating the resolution and scale uncertainties from the reconstructed objects and the soft-term. Based on comparisons between data and simulations, the latter includes modeling uncertainties coming from the underlying event and its impact on the p_T scale and resolution of unclustered energy. The analyses presented in this work include 1σ scale variations and a smearing according to the resolution uncertainty.

5.2 Object definitions in the analyses

The object definitions are set independently for each analysis mentioned in this Thesis to enhance their sensitivity. However, similar object definitions allows to facilitate the combination in Chapter 7. The objects defined are electrons, muons, small-R jets, large-R jets and $E_{\text{T}}^{\text{miss}}$, where both the small-$R$ and large-R jets are subject to tagging requirements.

Electrons: To ensure a robust association with the PV, each electron is required to satisfy the track-to-vertex criteria of $|d_0|/\sigma < 5$ and $|\Delta z_0 \sin\theta| < 0.5\,\text{mm}$. In addition, electrons must lie within the pseudorapidity regions $|\eta| < 1.37$ or $1.52 < |\eta| < 2.47$ and not originate from problematic clusters. For the 2016 data, clusters from regions with bad high voltage in the electromagnetic end-cap are also removed. The selection further diverges in transverse momentum and isolation requirements: vetoed electrons in the MONOTOP analysis must have $p_{\text{T}} > 25\,\text{GeV}$, the HTZT analysis requires $p_{\text{T}} > 30$ GeV and *loose* isolation, and $p_{\text{T}} > 28\,\text{GeV}$ in the OSML analysis. Across all analyses, the `TightLH` identification working point is uniformly applied to ensure high-quality electron reconstruction. This information is summarized in Table 5.2.

Muons: Table 5.3 outlines the muon selection criteria for the three analyses. For a robust association with the PV, muons must satisfy $|d_0|/\sigma < 3$ and $|\Delta z_0 \sin\theta| < 0.5\,\text{mm}$. All muons are required to lie within $|\eta| < 2.5$ and

Feature	Criterion
Pseudorapidity range	$(\lvert\eta\rvert < 1.37) \,\lvert\rvert\, (1.52 < \lvert\eta\rvert < 2.47)$
Energy calibration	`es2018_R21_v0` (ESModel)
Track-to-vertex association	$\lvert d_0\rvert/\sigma < 5$ and $\lvert\Delta z_0 \sin\theta\rvert < 0.5\,\text{mm}$
Object quality	Not from a bad calorimeter cluster
	Remove clusters from regions with EMEC bad HV (2016 data only)
Transverse momentum	$p_\text{T} > 25\,\text{GeV}$ (Monotop)
	$p_\text{T} > 30\,\text{GeV}$ (HtZt)
	$p_\text{T} > 28\,\text{GeV}$ (Osml)
Identification	`TightLH`
Isolation	`FCLoose` (HtZt)

Table 5.2: Electron selection criteria in the Monotop, HtZt and Osml analyses.

are calibrated using a sagitta correction to ensure precise momentum measurements. The transverse momentum thresholds differ slightly between analyses: $p_\text{T} > 25\,\text{GeV}$ for Monotop, $p_\text{T} > 30\,\text{GeV}$ for HtZt, and $p_\text{T} > 28\,\text{GeV}$ for Osml. While the muon identification is set to `Medium` across all analyses, an isolation requirement is applied only in the HtZt and Osml analyses.

Feature	Criterion
Pseudorapidity range	< 2.5
Momentum calibration	Sagitta correction used
Track-to-vertex association	$\lvert d_0\rvert/\sigma < 3$ and $\lvert\Delta z_0 \sin\theta\rvert < 0.5\,\text{mm}$
Transverse momentum	$p_\text{T} > 25\text{GeV}$ (Monotop)
	$p_\text{T} > 30\text{GeV}$ (HtZt)
	$p_\text{T} > 28\text{GeV}$ (Osml)
Identification	`Medium`
Isolation	`FCTightTrackOnly` (HtZt and Osml)

Table 5.3: Muon selection criteria in the Monotop, HtZt and Osml analyses.

Small-R jets: PFlow jets are reconstructed with the anti-k_t clustering algorithm with a fixed radius parameter of $R = 0.4$. All jets are required to pass cleaning criteria and to have transverse momentum $p_\text{T} > 25\,\text{GeV}$. While central jets lie within $|\eta| < 2.5$, jets in the forward region are defined by $2.5 < |\eta| < 4.5$. Pile-up effects are mitigated for central jets: in the Monotop analysis, jets with $20 < p_\text{T} < 60\,\text{GeV}$ and $|\eta| < 2.4$ must satisfy JVT > 0.5; the HtZt analysis applies a threshold of JVT > 0.59 (0.11) to central jets with $p_T < 120\,\text{GeV}$ and $|\eta| < 2.4$ ($2.4 < |\eta| < 2.5$); and the Osml analysis requires

JVT > 0.59 for jets with $p_T < 60\,\text{GeV}$ and $|\eta| < 2.4$. Furthermore, forward pile-up suppression is implemented exclusively in the HtZt analysis, where jets in the region $2.5 < |\eta| < 4.5$ with $p_T < 120\,\text{GeV}$ must satisfy fJVT > 0.5. Details of these reconstruction and selection criteria are provided in Table 5.4.

Jets originated from b-quarks (b-jets) are identified using the `DL1r` algorithm for b-tagging, with a fixed operating point corresponding to an efficiency of 77%. A second type of jets, denoted as *track-jets*, are used exclusively by the HtZt analysis for b-tagging. These jets are reconstructed from charged particle tracks and clustered using the anti-k_t algorithm with a variable radius allowed to vary between $R = 0.02$ and $R = 0.4$. Track-jets are selected if they have $p_\text{T} > 20\,\text{GeV}$ and lie within $|\eta| < 2.5$.

Feature	**Criterion**
Reconstruction setup	
Algorithm	`Anti-`k_t
Parameters	$R = 0.4$
Input constituents	EMPFlow
Selection requirements	
Jet cleaning	`LooseBad`
p_T	$> 25\,\text{GeV}$
$\|\eta\|$	< 4.5
Pile-up suppression	
Central jets	JVT > 0.5, $p_T < 60\,\text{GeV}$, $\|\eta\| < 2.4$ (Monotop) JVT > 0.59 (0.11), $p_T < 120\,\text{GeV}$, $\|\eta\| < 2.4$ ($2.4 < \|\eta\| < 2.5$) (HtZt) JVT > 0.59, $p_T < 60\,\text{GeV}$, $\|\eta\| < 2.4$ (Osml)
Forward jets	fJVT > 0.5, $p_T < 120\,\text{GeV}$, $2.5 < \|\eta\| < 4.5$ (HtZt)
b**-tagging**	
Jet collection	`AntiKt4EMPFlowJets` (Monotop and Osml) `AntiKtVR30Rmax4Rmin02` (HtZt)
Algorithm	DL1r
Operating point	Fixed, Eff = 77 %

Table 5.4: Jet reconstruction and pile-up suppression information for small-R jets in the Monotop, HtZt and Osml analyses. The b-tagging criteria is also included.

Large-R jets: Boosted top quarks and weak bosons decaying hadronically are reconstructed from their collimated decay products in single large-R jets. These type of jets are obtained in the Monotop analysis by applying the anti-k_t algorithm on calorimeter topo-clusters with a radius parameter $R = 1.0$. To subtract the pile-up contamination, the jet constituents are groomed by

applying anti-k_t with $R = 0.2$ such that the constituents with p_{T} less than a 5% of the reclustered jet p_{T} are removed. Large-R jets are considered if they fulfill the kinematic requirements of $p_{\mathrm{T}} > 250\,\mathrm{GeV}$ and $|\eta| < 2.0$. In the HtZt and Osml analyses, large-R jets are reconstructed from calibrated small-R jets with the anti-k_t algorithm and a variable radius parameter. The large-R jets are selected if they have $p_{\mathrm{T}} > 200\,\mathrm{GeV}$ and $|\eta| < 2.0$, and a mass greater than 50 GeV. In the HtZt and Osml analyses, the large-R jets are re-clustered from calibrated small-R jets using the anti-k_t algorithm with a variable radius parameter up to $R = 1.5$ and density parameter $\rho = 550$ GeV [252]. These variable-R re-clustered jets, referred to as *vRC jets*, are selected if they have $p_{\mathrm{T}} > 200\,\mathrm{GeV}$ and $|\eta| < 2.0$, and a mass greater than 50 GeV. Both reconstruction techniques and selection criteria are summarized in Table 5.5.

Feature	**Criterion**
Reconstruction setup	
Algorithm	Anti-k_t (Monotop)
	variable-R anti-k_t (HtZt and Osml)
Parameters	$R = 1.0$ (Monotop)
	$\rho = 550\,\mathrm{GeV}$, $R < 1.5$ (HtZt and Osml)
Input constituent	LCTopo (Monotop)
	calibrated small-R jets (HtZt and Osml)
Grooming algorithm	Trimming $f_{cut} = 0.05$ (and $R_{trim} = 0.2$ for Monotop)
Selection requirements	
p_{T}	$> 250\,\mathrm{GeV}$ (Monotop)
	$> 200\,\mathrm{GeV}$ (HtZt and Osml)
$\lvert\eta\rvert$	< 2.0 (Monotop)
	< 2.0 (HtZt and Osml)
Mass	$> 50\,\mathrm{GeV}$ (HtZt and Osml)

Table 5.5: Large-R jet definition and selection criteria in the Monotop, HtZt and Osml analyses.

The Monotop analysis need to identify which of the large-R jets are originated from a hadronically decaying top quark. For this purpose, the DNN top-tagger technique is applied at the contained-50% efficiency working point. The details of this top-tagger are described in Table 5.6. Instead, both the HtZt and Osml analyses employ a cut-based approach for the tagging of the top quark jets, but also for the tagging of the W/Z and Higgs bosons. The selection criteria on the p_{T}, mass and η of the vRC jets are summarized in Table 5.7.

Feature	Criterion
Jet collection	AntiKt10LCTopoTrimmed
Jet selection	$p_{\mathrm{T}} > 350$ GeV
	$\lvert\eta\rvert < 2.0$
Algorithm	TopQuarkContained
WP	Eff = 50 %
Calib	MC16_20201216_50Eff

Table 5.6: DNN top-tagger information in the MONOTOP analysis.

Feature	t-tag	h-tag	V-tag
$p_{\mathrm{T}} >$ (GeV)	400 HtZt / 200 OSML	350	350
Mass (GeV)	> 140	[105,140]	[70,105]
N_c	$\geq$2 if $p_{\mathrm{T}} < 700$ GeV	=2 if $p_{\mathrm{T}} < 600$ GeV	=2 if $p_{\mathrm{T}} < 450$ GeV
	$\geq$1 if $p_{\mathrm{T}} > 700$ GeV	$\leq$2 if $p_{\mathrm{T}} > 600$ GeV	$\leq$2 if $p_{\mathrm{T}} > 450$ GeV

Table 5.7: vRC boosted object tagging criteria in the HTZT and OSML analyses. N_c refers to the number of jet constituents in the large-R jets.

5.3 Experimental uncertainties

The experimental uncertainties account for the intrinsic detector limitations and the inefficiencies of the reconstruction and identification techniques. Most experimental uncertainties are common to all analyses, but the use of alternative reconstructions and calibrations can lead to different sets of Nuisance Parameters (NPs). The main sources of experimental uncertainties considered in the MONOTOP, HTZT and OSML analyses are explained.

Luminosity: The combined luminosity uncertainty for the entire Run 2 is 1.7% [253], as determined using the LUCID-2 detector [254] for primary luminosity measurements. This uncertainty impacts all background and signal estimations since it is essential for accurately normalizing the MC event yields to the observed data.

Pile-up: To accurately represent the effect of pile-up, the MC events are reweighted to align with the observed pile-up profile in the data. The analyses consider the associated uncertainty from these adjustments.

Leptons: Data-to-MC scale factors are applied to correct the efficiencies of the trigger, reconstruction and identification. These scale factors and their associated uncertainties are derived using tag-and-probe techniques on data and

simulated samples of $Z \to \ell^+\ell^-$ events. Uncertainties are also considered on the scale and resolution of the electron energy and muon p_{T}. These uncertainties are not considered for the MONOTOP analysis since it applies a veto on charged leptons.

Small-R jets: The JES uncertainties are determined through a series of calibration steps using both data and MC events [255]. The effect of these uncertainties is broken down into 27 uncorrelated NPs, each with up/down variations: 15 NPs from in-situ calibrations against well-calibrated reference objects (e.g., Z bosons), 4 related to the calibration of forward region jets versus central jets, three linked to jet flavor, 3 pertaining to pile-up effects, 1 for punch-through effects[6], and 1 associated with high-p_{T} jet modeling.

The JER uncertainty is quantified by the quadrature difference between the JER in data and MC, as detailed in Ref. [256]. The residual differences are addressed by the *FullJER* scheme in the MONOTOP analysis, considering 13 effective NPs. The HTZT and OSML analyses use the *SimpleJER* scheme, which involves 7 NPs.

The resolution and scale of the small-R jet mass are included in the HTZT analysis based on preliminary studies on *in situ* measurements. The JMS is estimated by comparing each nominal sample to two corresponding alternative event samples with varied mass scales ($\pm 10\%$). The JMR uncertainty is determined by comparing the nominal samples to an alternative sample in which the jet mass is smeared by a Gaussian function whose width is shifted by 20%.

Small-R jets are required to come from the primary vertex using a JVT score threshold [257], but the JVT efficiency is not perfectly replicated in the MC simulations. Consequently, a NP accounts for this efficiency uncertainty [238]. In the case of fJVT for the HTZT analysis, an additional NP is considered by using different generators for the simulation of the $Z+$jets events.

Small-R jet b-tagging: The b-tagging uncertainties of PFlow jets involve 9 NPs related to the efficiency of b-jet identification: 4+4 NPs that address the mistagging uncertainty for both c-jets and light-jets, and 2 NPs describing extrapolations to extend the calibration regimes. The first extrapolation NP is added for high-p_{T} jets that are outside the kinematic reach of the calibration data sample. The second extrapolation NP is assigned to the calibration of τ-flavor jets[7], since these jets are assigned the same scale factors as c-jets. An

[6] Punch-through effects involve particles that pass through a detector without being fully absorbed, potentially compromising jet measurements.

[7] The hadronic decay of τ-leptons produces a jet, unlike electrons and muons that leave a track in the detector.

equivalent set of NPs is considered for the b-tagging of track-jets in the HtZt analysis, except for a less amount of NPs (5) accounting for the b-tagging efficiency.

Large-R jets: The LJES uncertainties involve 24 NPs that cover a range of sources including detector effects, selection criteria, modeling, statistical factors, and calibration in the forward region. The large-R Jet Mass Scale (LJMS) uncertainties, as described in [242, 258], include 18 NPs addressing issues such as forward folding and R_{trk} techniques, interpolation across different mass bins, and discrepancies in jet mass response between jets from top quarks and from other quarks and gluons. Large-R JER (LJER) uncertainties comprise 12 NPs, reflecting additional considerations beyond detector influences, selection criteria, statistical variations, and modeling due to discrepancies between data and MC. Lastly, the large-R JMR (LJMR) uncertainties [242, 258] include 10 NPs, which account for the forward folding method, a flat 20% uncertainty outside the technique's validity range, and interpolation between different mass bins.

Large-R jet top-tagging: The uncertainties related to the use of the DNN-based top-tagging algorithm involve 23 NPs. These parameters address various factors including efficiency aspects for both signal and background, tagger inefficiencies, and a component that accounts for extrapolation at high-p_{T} values.

Missing transverse momentum: Systematic uncertainties affecting all components used in the $E_{\mathrm{T}}^{\mathrm{miss}}$ reconstruction are propagated to the $E_{\mathrm{T}}^{\mathrm{miss}}$ calculation. Additionally, uncertainties from deposits associated with soft terms are accounted for. These uncertainties give rise to 3 NPs: one related to the $E_{\mathrm{T}}^{\mathrm{miss}}$ p_{T}-scale, and the other two impacting the $E_{\mathrm{T}}^{\mathrm{miss}}$ resolution in planes perpendicular and parallel to the beam axis. The HtZt analysis also applies an additional 2% normalization uncertainty to cover for discrepancies between data and MC on the $E_{\mathrm{T}}^{\mathrm{miss}}$ trigger efficiency.

Chapter 6

Monotop search

This chapter presents an analysis published in Ref. [1] that explores the data recorded by the ATLAS detector during the LHC Run 2 period (2015-2018), with a total integrated luminosity of 139 fb^{-1}. A previous round of the analysis was performed with 36 $\text{fb}^{-1}$of data, and the results were published in Ref. [259]. The search is motivated by the Dark Matter problem, which is one of the most compelling open questions in modern physics. Since the Dark Matter is not expected to interact with the detector, the searches for Dark Matter require the production of additional objects to trigger the event. This search looks for events with a large missing transverse momentum together with a single top quark, referred to as *mono-top* events.

The production channels in which new particles couple to a top quark is of great interest since it is the heaviest particle in the SM, and such couplings are expected to be favored by some BSM theories. The *mono-top* signature is also clearer than targeting light-jets in the final state (*mono-jet* searches) because fixing the flavor of the final state quark allows to reduce the possible configurations of initial partons. As a signature-based search, it is possible to gain interpretability for different models that might produce the same final state. Thus, the results are also interpreted in terms of VLQs, which are predicted by some extensions of the SM to solve the hierarchy problem. The single production of a vector-like top quark, decaying into a top quark and a Z boson, which in turn decays invisibly to neutrinos, also produce a final state with a single top quark and a large missing transverse momentum. The signal models considered in this search were introduced in Chapter 2.

The identification of *mono-top* signal events is a challenging task due to the low production cross-section of the signal processes and the large background contributions from the SM that mimic the signal signature. This chapter presents the refined analysis strategy that has been designed to enhance the sensitivity of the search. First, a phase space that is sensitive to signal

events is defined in Section 6.1 by selecting events with a large missing transverse momentum and a top-tagged large-R jet. The signal and background discrimination is enhanced by training a Multivariate Analysis (MVA) technique, based on the principles of decision tree ensembles using the XGBoost library, as described in Section 6.2. Subsequently, signal-enriched regions are defined by selecting events with a high MVA score and additional kinematic requirements, which are explained in Section 6.3. Dedicated control regions are also defined to estimate the normalization of the main background processes, $t\bar{t}$ and $V+$jets. The MC simulations for all background and signal processes used in this analysis were presented in Chapter 4. Distributions from the data and MC simulations are used to perform the statistical inference analysis described in Section 6.4, for which the systematic uncertainties presented in Sections 4 and 5 are taken into account as nuisance parameters. Finally, the results are interpreted in Section 6.5, providing exclusion limits when no significant excess over the expected SM background is observed in the data.

6.1 Event selection and background estimation

The selection criteria are designed to enhance the signal-to-background ratio. Adopting general requirements allows the analysis to remain sensitive to both the DM simplified models and the VLQ model presented in Section 2, which also lead to a *mono-top* signature but with an additional forward jet. The *pre-selection* criteria are summarized as follows:

- A veto on leptons is applied.
- The $E_{\mathrm{T}}^{\mathrm{miss}}$ is required to be above 250 GeV, reducing the multi-jet background drastically.
- At least one top-tagged large-R jet is required, for which the large-R jet kinematics need to lie in the calibration range of the DNN tagger: $p_T \in [350, 2500]$ GeV, $|\eta| < 2.0$ and $m_T \in [40, 600]$ GeV, where m_T is the reconstructed transverse mass of the large-R jet.
- A minimum angular distance in the transverse plane between the $E_{\mathrm{T}}^{\mathrm{miss}}$ and any small-R jet, $\Delta\phi(E_{\mathrm{T}}^{\mathrm{miss}}, \mathrm{j})$, larger than 0.2 is required to suppress the contamination from the beam-induced background (BIB) [1].
- The event must fulfil the jet-cleaning criteria, containing exactly zero

[1] The BIB background comes from the beam losses, mainly produced from interactions with the gas in the beam pipe.

loose bad jets[2].

Before exploring the presence of any New Physics process in the data that passes the pre-selection criteria, it is necessary to understand the background composition predicted by the Standard Model. The yields and the kinematic distributions of the background processes are determined from the MC simulations detailed in Table 4.1, which are normalized to their theoretical cross-sections. As illustrated in Figure 6.1, the dominant backgrounds are $t\bar{t}$ ($\sim 80\%$) and $V+$jets (~ 15), followed by single-top and diboson processes. The breakdown of yields for the background and signal processes is shown in Table 6.2. The benchmark signal point is shown in the table for the Scalar (Vector) mediator model with parameters $m_\phi = 4$ TeV, $m_\chi = 1$ GeV, $\lambda_q = 0.6$, $y_\chi = 0.4$ ($m_V = 1.75$ TeV, $m_\chi = 1$ GeV, $a = 0.5$, $g_\chi = 1$). As well as for the VLQ model, whose benchmark parameters are $m_T = 1.7$ TeV, $\kappa_T = 0.5$.

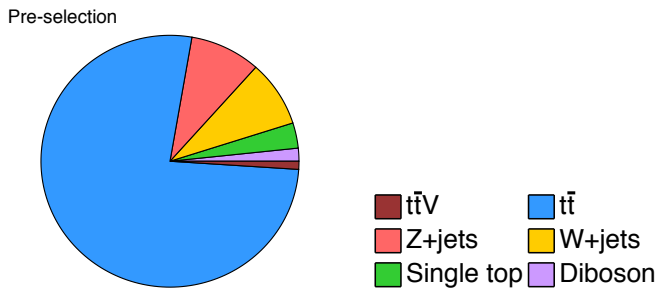

Figure 6.1: Expected contribution of the different backgrounds in the pre-selection region, which are normalized to their theoretical cross-section.

Some relevant variables are shown in Figure 6.2 to show the proper modeling of the MC simulation kinematics. An overestimation of the main background simulations is observed, which will be properly estimated during the likelihood fit as it will be explained in Section 6.5. This overestimation is mainly related to the top-tagging selection applied in the highly boosted regime of this analysis, which is different from the phase space where the top-tagger algorithm was calibrated. Figure 6.2a shows the $E_{\mathrm{T}}^{\mathrm{miss}}$ distribution, which is the kinematic variable that provides a better separation between the background and the different signal processes. Figure 6.2b shows the transverse

[2]Jets with $p_{\mathrm{T}} > 20$ GeV and $|\eta| < 2.4$ are identified as loose if they satisfy the kinematic requirement $f_{\mathrm{ch}}/f_{\mathrm{max}} < 0.1$. Here, f_{max} is the maximum energy fraction in any single calorimeter layer, and f_{ch} is the jet charged fraction, defined as the scalar sum of the p_{T} of tracks originating from the primary vertex associated with the jet divided by the p_{T} of the jet. Loose jets are likely *fake* jets, which affect severely the reconstruction of the $E_{\mathrm{T}}^{\mathrm{miss}}$.

Process	Events
$t\bar{t}$	12600 ± 2300
Z+jets	1450 ± 270
W+jets	1390 ± 270
tZq	1.6 ± 0.3
Wt-channel	510 ± 140
t-channel (t)	11.2 ± 1.6
t-channel ($\bar{t}$)	4.4 ± 0.8
s-channel	2.8 ± 0.7
Diboson	290 ± 60
Total background	16400 ± 2500
Scalar med. DM	47 ± 7
Vector med. DM	400 ± 50
VLQ	60 ± 8
Data	14019

Table 6.1: Event yields in the preselection region for real data and simulations of the backgrounds and signal processes, which are normalized to their theoretical cross-section. The signal points shown correspond to the scalar DM mediator model ($m_\phi = 4.0$ TeV, $m_\chi = 1.0$ GeV, $\lambda_q = 0.6$, $y_\chi = 0.4$), the vector DM mediator model ($m_V = 1.75$ TeV, $m_\chi = 1.0$ GeV, $a = 0.5$, $g_\chi = 1.0$) and the VLQ model ($m_T = 1.7$ TeV, $\kappa_T = 0.5$) models. The signal and backgrounds are normalized to their theoretical predictions.

mass of the top-tagged large-R jet and the reconstructed $E_{\mathrm{T}}^{\mathrm{miss}}$[3]. Figures 6.2c and 6.2d show the $\Delta\phi(E_{\mathrm{T}}^{\mathrm{miss}}, \mathrm{j})$ and the number of b-tagged jets ($N_{b-\mathrm{jets}}$), which are used to define the background-enriched regions (control regions) and the signal-enriched regions (signal regions), as it will be explained in the following subsection. A MVA technique is used as well to enhance the signal-to-background ratio in the signal regions.

6.2 Multivariate analysis

Multivariate analyses (MVA) are performed to enhance the sensitivity to the signal processes. The MVA technique chosen is based on the principles of decision tree ensembles using the XGBoost (eXtreme Gradient Boosting) library [261, 262]. Boosted Decision Trees (BDTs) are one of the most common MVA techniques used in the ATLAS experiment for event classification, due

[3]This was the fitted distribution in the first iteration of this analysis [260].

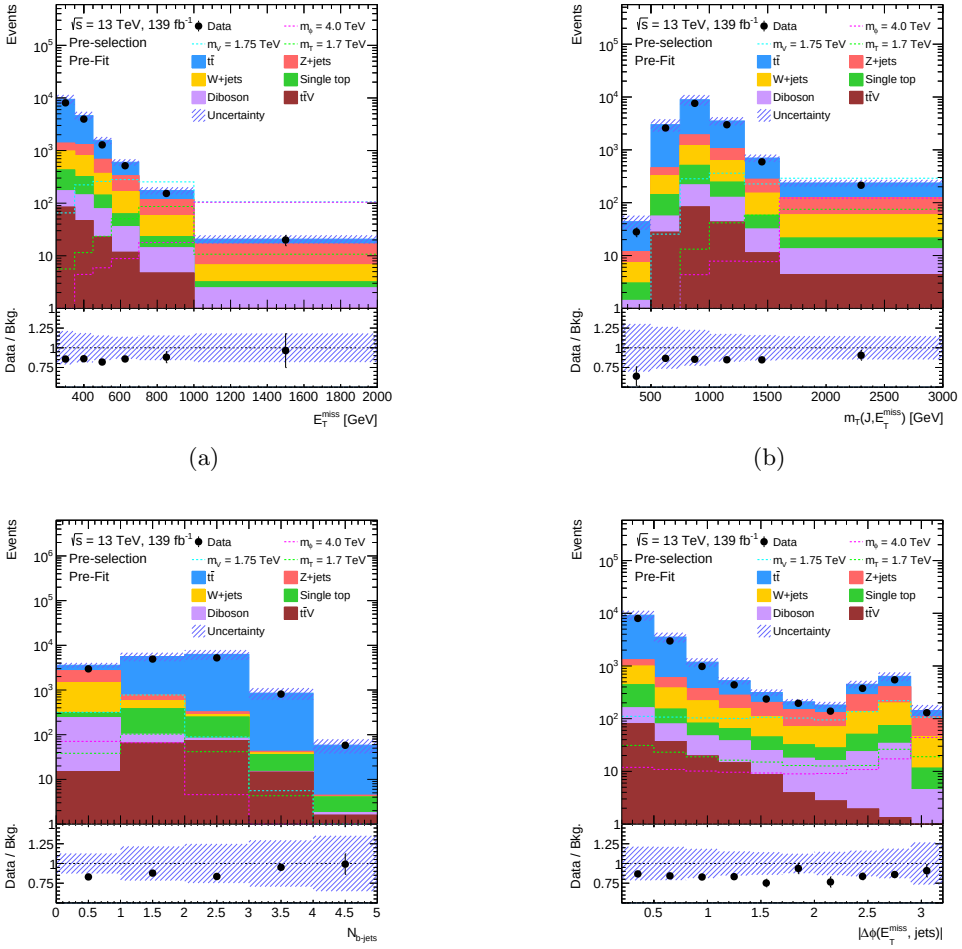

(a) (b)

(c) (d)

Figure 6.2: Comparison of data and SM predictions for (a) the $E_{\mathrm{T}}^{\mathrm{miss}}$, (b) the $m_{\mathrm{T}}(E_{\mathrm{T}}^{\mathrm{miss}}, J)$, (c) the $N_{b-\mathrm{jets}}$ and (c) the $\Delta\phi(E_T^{\mathrm{miss}}, \mathrm{j})$ distributions at pre-selection level. The expected distributions for the scalar DM mediator model ($m_\phi = 4.0$ TeV, $m_\chi = 1.0$ GeV, $\lambda_q = 0.6$, $y_\chi = 0.4$), the vector DM mediator model ($m_V = 1.75$ TeV, $m_\chi = 1.0$ GeV, $a = 0.5$, $g_\chi = 1.0$) and the VLQ model ($m_T = 1.7$ TeV, $\kappa_T = 0.5$) are scaled by a factor of 3 for visibility purposes. The last bin of the distributions includes the overflow. The uncertainty bands include all systematic uncertainties. The lower panel shows the ratio of data to SM prediction.

to its high performance and the simplicity to interpret the results in terms of the input features. The tree structure consists of a set of nodes splitting the feature space to maximize the separation between the signal and background processes. Such binary decisions are taken recursively until no further improvement is achieved, which defines the leaves of the tree. Since very deep trees can lead to overfitting[4], the boosting technique is used to create an ensemble that combines sequentially the predictions of multiple *weak classifiers*, which are typically shallow trees trying to correct the errors of the previous ones[5]. In particular, in the gradient boosting algorithm implemented in XGBoost, the trees are added to the ensemble to minimize a loss function through a gradient descent algorithm.

All simulated events passing the pre-selection criteria are used either for training or testing. Three BDTs are trained corresponding to each signal model, for which the benchmark signal points are used. In order to enhance the performance of the training, higher statistics were generated for the scalar mediator and vector mediator DM models, with approximately 210 000 and 57 000, respectively. The statistics were more limited for the VLQ model, for which three different signal points were grouped in the signal class for the training, corresponding to m_T values of 1.5, 1.7 and 1.9 TeV with $\kappa_T = 0.5$. It has been ensured that the performance is not significantly degraded when evaluating the trained BDT to other signal points of the parameter space, which may differ in the kinematics of the events.

Input variables

The BDT is fed with kinematical and high-level features that are sensitive to the signal processes. The variables $N_{b-\text{jets}}$ and $\Delta\phi(\text{j}, E_{\text{T}}^{\text{miss}})$ are not included in the training, since they are used separately to define the signal and background-enriched regions. The variables entering any of the three trainings are:

- $E_{\text{T}}^{\text{miss}}$: The magnitude of the missing transverse momentum of the event. Mono-top events are expected to have a larger $E_{\text{T}}^{\text{miss}}$ compared to background events.

- $\Delta p_{\text{T}}(J, \text{jets})$: Difference of the p_{T} of the leading large-R jet with respect to the sum of p_{T} of all the small-R jets in the event. In signal events, all high-p_{T} jets are expected to originate from the top quark, so this variable peaks around 0.

[4]The overfitting problem arises when the algorithm learns aspects of the training data that do not generalize to the test data, leading to a worse performance in the latter.

[5]Traditionally, such as in the AdaBoost algorithm [263], subsequent trees are trained to correct the errors of the previous ones by giving more weight to the misclassified events. Similarly, each of the trees can be weighted according to their misclassification rate, which is used to compute the final output of the ensemble.

- Ω: Ratio of the difference between $E_{\mathrm{T}}^{\mathrm{miss}}$ and the p_{T} of the leading large-R jet to their sum ($\Omega = \frac{E_{\mathrm{T}}^{\mathrm{miss}} - p_{\mathrm{T}}(J)}{E_{\mathrm{T}}^{\mathrm{miss}} + p_{\mathrm{T}}(J)}$). Signal events, particularly in the scalar DM mediator model, are expected to have a symmetric distribution centered at zero due to the back-to-back alignment of large-R jet p_{T} and $E_{\mathrm{T}}^{\mathrm{miss}}$.

- N_{jets}: small-R jet multiplicity. Mono-top events are expected to have fewer jets in the final state compared to $t\bar{t}$ events.

- ΔR_{max}: Maximum ΔR between small-R jets in the event. Mono-top events, characterized by a boosted decay of the top quark, are expected to have jets closer together compared to $t\bar{t}$.

- $m_{\mathrm{T,min}}(E_{\mathrm{T}}^{\mathrm{miss}}, b\text{-jets})$: Reconstructed transverse mass of the $E_{\mathrm{T}}^{\mathrm{miss}}$ with the closest b-jet. In semileptonic $t\bar{t}$ events (in which one top decays as $t\bar{t} \to bq\bar{q}\,\bar{b}l\nu$) with a missing lepton, this distribution peaks around the top mass, while the mono-top signal does not show this feature.

- m_{top}: Mass of the large-R jet that is top-tagged. This peaks around the top-quark mass for mono-top events but shows a less pronounced peak for $t\bar{t}$ (due to the dominance of semileptonic events) and $V+$jets events.

- H_{T}: Sum of the $E_{\mathrm{T}}^{\mathrm{miss}}$ and the p_{T} of all the small-R jets in the event. Signal and background events are expected to exhibit different hadronic activity.

- $H_{\mathrm{T}}/E_{\mathrm{T}}^{\mathrm{miss}}$: Ratio of H_{T} to $E_{\mathrm{T}}^{\mathrm{miss}}$. Mono-top events expect a balance between these quantities, while $t\bar{t}$ events are expected to exhibit asymmetry.

- $\Delta E(E_{\mathrm{T}}^{\mathrm{miss}}, J)$: Difference in transverse energy between the $E_{\mathrm{T}}^{\mathrm{miss}}$ and the leading large-R jet. Signal events are expected to have values close to zero, whereas $t\bar{t}$ background events are highly unbalanced.

- $\Delta\phi(E_{\mathrm{T}}^{\mathrm{miss}}, J)$: Angular distance in the transverse plane between the $E_{\mathrm{T}}^{\mathrm{miss}}$ and the leading large-R jet. Mono-top events are expected to show a back-to-back alignment of the large-R jet and $E_{\mathrm{T}}^{\mathrm{miss}}$.

- $m_{\mathrm{T}}(E_{\mathrm{T}}^{\mathrm{miss}}, J)$: Reconstructed transverse mass of $E_{\mathrm{T}}^{\mathrm{miss}}$ with the large-R jet. Signal events are expected to have significantly larger values compared to backgrounds.

- $\Delta\phi(b\text{-jet}, J)$: Angular distance in the transverse plane between the leading b-jet and the leading large-R jet. In mono-top events, these objects are expected to be angularly closer.

- $m(J)$: Mass of the leading large-R jet. Signal events are expected to distribute around the top-quark mass, including those signal events for which the top-tagging algorithm fails.

The training optimization drops those variables that do not provide any discrimination power, and the final set of variables used in the training is shown in Table 6.2. The variable providing the highest separation power for the three signal models is the $E_{\mathrm{T}}^{\mathrm{miss}}$, specially for the scalar DM mediator model.

Variable	Scalar DM med.	Vector DM med.	VLQ
$E_{\mathrm{T}}^{\mathrm{miss}}$	✓	✓	✓
Δp_{T} (J,jets)	✓	✓	
Ω	✓	✓	✓
$\mathrm{N}_{\mathrm{jets}}$	✓	✓	✓
ΔR_{max}	✓	✓	✓
$m_{\mathrm{T,min}}(E_{\mathrm{T}}^{\mathrm{miss}}, b\text{-jet})$	✓	✓	✓
m_{top}	✓		
H_{T}		✓	✓
$H_{\mathrm{T}}/E_{\mathrm{T}}^{\mathrm{miss}}$		✓	✓
$\Delta E(E_{\mathrm{T}}^{\mathrm{miss}}$,J)		✓	✓
$\Delta\phi(E_{\mathrm{T}}^{\mathrm{miss}}, J)$		✓	✓
p_{T} (J)			✓
$m_{\mathrm{T}}(E_{\mathrm{T}}^{\mathrm{miss}}$,J)			✓
$\Delta\phi(b\text{-jet}, J)$			✓
m(J)			✓

Table 6.2: List of variables used in the training of the XGBoost classifier for the scalar DM mediator, vector DM mediator and VLQ models. The symbol ✓ indicates that the corresponding variable is included in the training.

Training setup

This MVA task is a binary classification in which a signal process (labeled as 1) is discriminated from the background processes, which are grouped into a single class (label as 0). The XGBoost algorithm provides a score between 0 and 1 to each event, interpreted as the probability of the event to correspond with the signal process. The selected loss function to minimize is known as the binary cross-entropy, which is defined as the negative log-likelihood of the true labels given the predicted probabilities[6]. An optimal minimization of the loss

[6]The expression of the binary cross-entropy is given by $\mathcal{L}_{\mathrm{entropy}} = -\sum_{i=1}^{N} y_i \log(p_i) + (1 - y_i)\log(1 - p_i)$, where y_i is the true label of the event i and p_i is the predicted probability of the event i being signal.

function during the training process depends on the hyperparameters choice, which may differ for each classification task (see Table 6.3):

- *n_estimators*: the number of trees in the ensemble.
- *max_depth*: the maximum depth of each tree.
- *learning_rate*: the step size at each epoch when moving towards the minimum of the loss function.
- *min_child_weight*: the minimum sum of instance weights required in a leaf node.
- *scale_pos_weight*: the ratio of the sum of the weights of the positive (signal) class to the negative (background) class, needed specially when the classes are imbalanced.

Parameter	Scalar med. DM	Vector med. DM	VLQ
n_estimators	2000	4000	2000
max_depth	3	3	3
learning_rate	0.12	0.01	0.1
min_child_weights	2	10	1
scale_pos_weight	8	78	5

Table 6.3: Optimized parameters in the training of the XGBoost classifier for the scalar DM mediator, vector DM mediator and VLQ models.

The k-folding method is used to exploit the whole statistics available for training and testing, at the same time that avoiding the overfitting. This method splits randomly the whole dataset in K subsets of identical size, $K-1$ of which are used for training and the remaining one for testing. Thus, K trainings are performed, each time using a different subset for testing. In this case, the training is performed with $K = 5$ folds, which means that the training is performed 5 times, each time using 80% of the data for training and 20% for testing, as illustrated in Figure 6.3. Thus, the BDT score of any simulated event is obtained from the BDT that did not consider such event during the training. Similarly, the real data are randomly split in 5 subsets, each of which is evaluated with one of the 5 classifiers. Since the data have not been used either for training or testing during the optimization, a good agreement between the data and the MC samples in the BDT score distribution serves as a further validation of the procedure. Such comparison is shown in Figure 6.4.

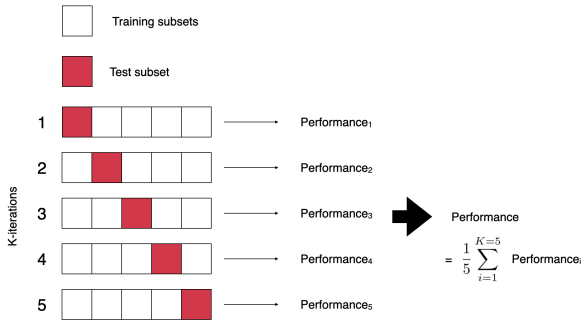

Figure 6.3: Illustration of the k-folding method used in the training of the BDT. The whole simulated dataset is randomly split into 5 subsets, each of which is used for testing once.

Classification performance

The performance of a binary classifier is typically evaluated with the area under the ROC [7] curve (AUC), which is a measure of the separation power. AUC=1 indicates a perfect separation, while AUC=0.5 indicates that the classifier is not able to distinguish between the two classes and provides random predictions. Thus, the global performance is computed as the average of the AUCs provided by the five trained BDTs. The AUCs for the scalar and vector mediator models are respectively 0.986 and 0.918, while a value of 0.882 is obtained for the VLQ model.

6.3 Regions definition

In the search for a new physics signal, the pre-selection phase space is divided in different regions, some of which are defined to have a higher signal sensitivity (*signal regions*) and others in which the signal is not expected, being mainly populated by background processes. Some of these regions can be used for background estimation (*control regions*) and some others are used to validate the estimation of the background processes (*validation regions*), ensuring that their modeling is correct in the vicinities of the signal-enriched regions. Thus, any possible deviation between the data and the background prediction in the SRs would not be attributed to a mismodeling of the background processes.

Table 6.4 summarizes the selection criteria for the signal, control and validation regions, while Figure 6.5 illustrates these regions in the $N_{b\text{-jets}}$-$\Delta\phi(\mathrm{j}, E_{\mathrm{T}}^{\mathrm{miss}})$ plane.

[7] The ROC (Receiver Operating Characteristic) curve is a graphical representation of the true positive rate (TPR) against the false positive rate (FPR) for different thresholds.

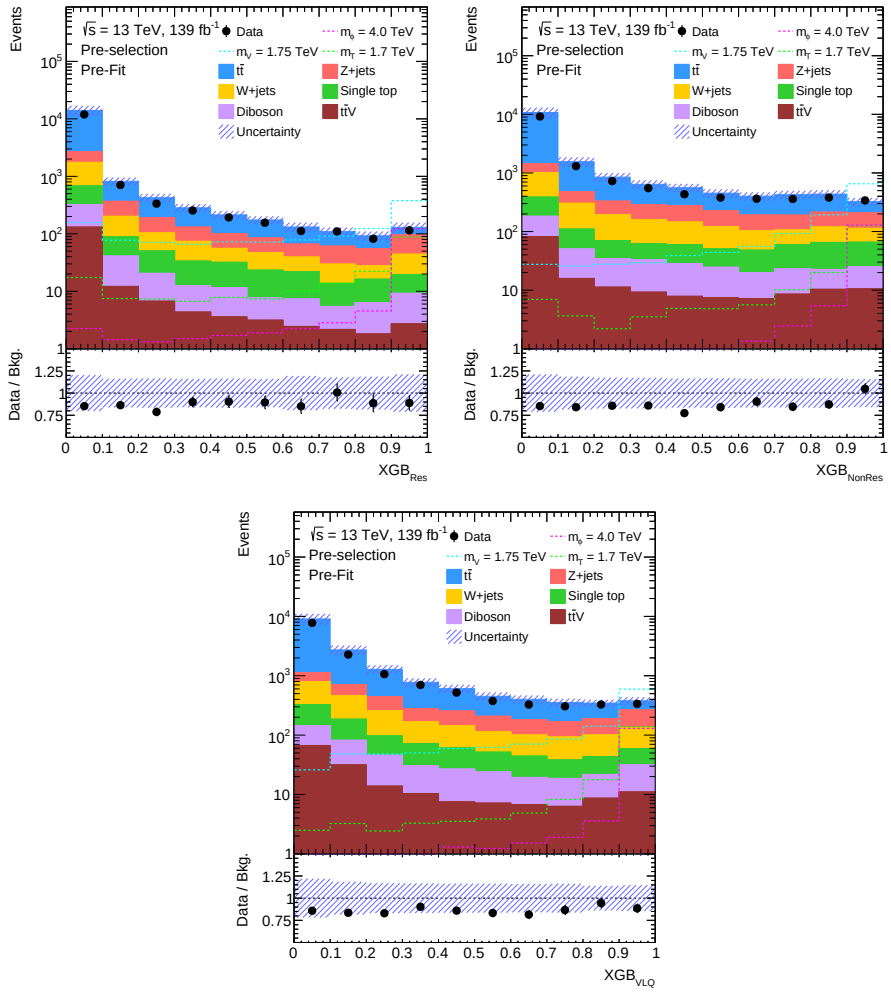

Figure 6.4: XGBoost score distribution in the training region for (a) the scalar med. DM, (b) the vector med. DM and (c) the VLQ models. The expected distributions for the scalar DM mediator ($m_\phi = 4.0$ TeV, $m_\chi = 1.0$ GeV, $\lambda_q = 0.6$, $y_\chi = 0.4$), vector DM mediator ($m_V = 1.75$ TeV, $m_\chi = 1.0$ GeV, $a = 0.5$, $g_\chi = 1.0$) and VLQ ($m_T = 1.7$ TeV, $\kappa_T = 0.5$) models are scaled by a factor of 3 for visibility purposes. The uncertainty bands include all systematic uncertainties. The lower panel shows the ratio of data to SM background.

	$N_{b\text{-jets}}$	$\Delta\phi_{\min}(j, E_{\mathrm{T}}^{\mathrm{miss}})$	XGBoost score	$N_{\text{f-jets}}$
TCR	≥ 2	$\in [0.2, 1]$	-	-
TVR1bLPhi	1	$\in [0.2, 1]$	-	-
TVR1bHPhi (1f)	1	≥ 1	< 0.5	- (≥ 1)
TVR2bHPhi	≥ 2	≥ 1	-	-
VCR	0	$\in [0.2, 1]$	-	-
VVR (1f)	0	≥ 1	< 0.5	- (≥ 1)
SR0b (1f)	0	≥ 1	≥ 0.5	- (≥ 1)
SR1b (1f)	1	≥ 1	≥ 0.5	- (≥ 1)

Table 6.4: Summary of the event selections used to define the signal, control and validation regions. The signal regions are denoted by SR0b and SR1b, the $t\bar{t}$ (V+jets) dominated control regions are denoted by TCR (VCR) and the validation regions enhanced in $t\bar{t}$ (V+jets) are labeled as TVR1bLPhi, TVR1bHPhi and TVR2bHPhi (VVR). The "(1f)" notation in the signal and validation region rows indicates the additional requirement of at least one forward jet in the event that is applied for the search of a single vector-like T quark. $N_{b\text{-jets}}$ ($N_{\text{f-jets}}$) indicates the number of b-tagged (forward) jets required. The symbol - indicates that no requirement on the variable is applied.

Signal regions

Since this analysis explores three different signal models, the signal region definitions are optimized for each of them. The signal regions are defined applying cuts on the XGBoost score, the number of b-tagged jets ($N_{b\text{-jets}}$) and the minimum azimuthal angle between the $E_{\mathrm{T}}^{\mathrm{miss}}$ and any small-R jet ($\Delta\phi_{\min}(j, E_{\mathrm{T}}^{\mathrm{miss}})$). While a different XGBoost classifier is trained for each signal model, the selections applied on the $N_{b\text{-jets}}$ and $\Delta\phi(\mathrm{j}, E_{\mathrm{T}}^{\mathrm{miss}})$ variables are common for the signal regions of the three signal models. The distributions of the $N_{b\text{-jets}}$ and $\Delta\phi(\mathrm{j}, E_{\mathrm{T}}^{\mathrm{miss}})$ variables at preselection level are shown in Figures 6.2c and 6.2d, respectively.

The $\Delta\phi(\mathrm{j}, E_{\mathrm{T}}^{\mathrm{miss}})$ variable is required to be above 1.0 in accordance to the back-to-back topology between the missing transverse momentum and the boosted top quark. This cut is also useful to suppress $t\bar{t}$ events decaying semileptonically in which the lepton is misidentified as a jet. In such events, the missing transverse momentum coming from the *invisible* neutrino is aligned with the lepton[8].

[8]Instead, if the lepton from the top quark decay is not reconstructed, the $t\bar{t}$ event can produce a mono-top signature. Such contamination of $t\bar{t}$ processes will also populate the control region dedicated to estimate the $t\bar{t}$ production.

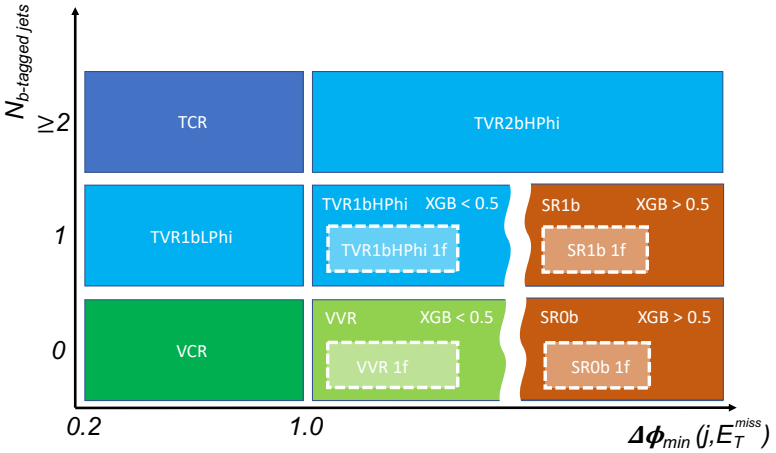

Figure 6.5: Schematic representation of the control, validation and signal regions. Regions are defined in terms of b-tagged jet multiplicity $N_{b\text{-tagged jets}}$ and the minimum distance in the azimuthal angle between a jet and $E_{\mathrm{T}}^{\mathrm{miss}}$ $\Delta\phi_{\mathrm{min}}(j, E_{\mathrm{T}}^{\mathrm{miss}})$. The notation "XGB< 0.5" and "XGB> 0.5" indicates the requirement on the XGBoost score of the validation and signal regions, respectively. These regions are schematically separated by the curly vertical line. The "1f" label stands for requiring at least one forward jet in the event. The selections used to define the regions are described in the text and in Table 6.4.

Since a mono-top signal is expected to have at most one b-tagged jet, coming from the top quark decay, the signal regions are defined by requiring $N_{b\text{-jets}} \leq 1$. It was observed that the background composition was different if 0 or 1 b-tagged jets were required. As it can be seen in Figure 6.2c, the background composition is dominated by $V+$jets events when 0 b-tagged jets are required, while $t\bar{t}$ events dominate the background when 1 b-tagged jet is required. In order to better control the background estimation in the regions with a higher signal sensitivity, two signal regions are defined for each signal model with exactly 0 and 1 b-tagged jets, which are respectively referred as SR0b and SR1b. Since the VLQ signal is expected to produce an additional jet in the forward direction, at least 1 forward jet is required for this model. The notation of these signal regions turns into SR0b1f and SR1b1f.

The scores of the XGBoost classifiers are used to enhance the sensitivity on the three signal models independently. These optimal variables, whose distributions are shown in Figure 6.4, accumulate the background processes at low values of the scores. Therefore, the events entering the signal regions are

required to have a score above 0.5.

Thus, a total of 6 signal regions are defined, 2 for each signal model. The breakdown of the yields for each of the background and the signal processes, as well as for the experimental data passing the signal regions selection, is shown in Table 6.5. Piecharts in Figure 6.6 illustrate that the three SR1b regions are dominated by $t\bar{t}$ events, while the SR0b regions are dominated by $V+$jets events since 0 or 2 b-tagged jets are expected in such processes. Thus, the major background contributions along the SR0b regions are $V+$jets ($\sim 85\%$), diboson ($\sim 10\%$) and $t\bar{t}$ ($< 8\%$) production. The SR1b regions are dominated by $t\bar{t}$ events ($\sim 65\%$), followed by $V+$jets ($\sim 20\%$) and single-top ($\sim 10\%$) production. For background estimation, such a disentanglement in the background composition will be useful to normalize the background yields to data with high accuracy, avoiding large correlations between the normalization factors (see Section 6.4).

Process	SR0b (Scalar DM med.)	SR1b (Scalar DM med.)	SR0b (Vector DM med.)	SR1b (Vector DM med.)	SR0b1f (VLQ)	SR1b1f (VLQ)
$t\bar{t}$	6 ± 5	170 ± 50	32 ± 7	470 ± 110	5 ± 4	44 ± 15
Z+jets	100 ± 40	38 ± 14	290 ± 100	79 ± 23	42 ± 11	6 ± 6
W+jets	49 ± 12	21 ± 7	154 ± 35	44 ± 13	22 ± 5	4.7 ± 2.2
tZq	-	0.03 ± 0.04	0.02 ± 0.05	0.08 ± 0.04	-	0.027 ± 0.023
Wt-channel	2.9 ± 2.6	35 ± 17	8 ± 4	82 ± 31	2.1 ± 2.0	10 ± 5
t-channel (t)	-	-	-	0.07 ± 0.19	-	-
t-channel ($\bar{t}$)	-	0.03 ± 0.07	0.04 ± 0.16	0.08 ± 0.20	-	-
s-channel	0.03 ± 0.04	-	0.03 ± 0.05	0.02 ± 0.05	-	0.00 ± 0.06
Diboson	14.2 ± 3.2	5.3 ± 2.4	45 ± 9	13 ± 5	7.5 ± 2.1	2.0 ± 1.2
$t\bar{t}V$	0.33 ± 0.20	4.1 ± 1.0	1.3 ± 0.4	12.4 ± 2.7	0.53 ± 0.19	2.2 ± 0.5
Res.	18 ± 6	17 ± 3	19 ± 6	17 ± 3	1.7 ± 0.6	1.5 ± 0.3
Non-Res.	44 ± 8	150 ± 20	66 ± 10	200 ± 30	12 ± 2	30 ± 4
VLQ	7.3 ± 1.3	21 ± 3	8.7 ± 1.7	23 ± 3	5.5 ± 1.0	13 ± 2
Total background	180 ± 40	270 ± 60	530 ± 110	700 ± 130	80 ± 13	69 ± 18
Data	165	238	448	642	60	79

Table 6.5: Predicted (pre-fit) event yields for the different models SRs. The signal points shown correspond to the scalar DM med. ($m_\phi = 4.0$ TeV, $m_\chi = 1.0$ GeV, $\lambda_q = 0.6$, $y_\chi = 0.4$), vector DM med. ($m_V = 1.75$ TeV, $m_\chi = 1.0$ GeV, $a = 0.5$, $g_\chi = 1.0$) and VLQ ($m_T = 1.7$ TeV, $\kappa_T = 0.5$) models. The signal and backgrounds are normalized to their theoretical predictions. The uncertainties include both statistical and systematic contributions, as described in Section 6.4.

Control regions

Dedicated control regions are defined to estimate the main backgrounds, $t\bar{t}$ and $V+$jets production. The control regions are fully cut-based and common for the three signal models, independent of the MVA implementation. The selection cuts are chosen to achieve populated regions that are enriched in the main backgrounds, maintaining always the signal contamination below 5%. The control regions require $\Delta\phi(\mathrm{j}, E_{\mathrm{T}}^{\mathrm{miss}}) < 1.0$ (in opposition to the signal regions requirement), being constrained from below by the pre-selection cut

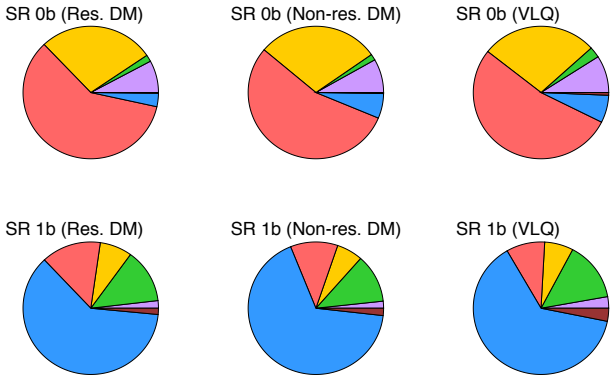

(a)

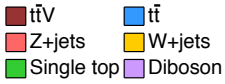

(b)

Figure 6.6: Expected contribution of the different backgrounds in the different SRs. These results are previous to the normalization fit described in Section 6.4.

$\Delta\phi(\mathrm{j}, E_{\mathrm{T}}^{\mathrm{miss}}) > 0.2$. The one enriched in $t\bar{t}$ events (96%), referred to as TCR, is required to have at least 2 b-tagged jets, which are expected from the decay of the top quarks. The events entering the control region dedicated to the $V+$jets production (58%), named as VCR, are required to have exactly 0 b-tagged jets. The $t\bar{t}$ population in the VCR is 34%, coming from events where the b-jets are not being reconstructed or the b-tagging algorithm fails to tag them. The breakdown of the yields for each of the background and the signal processes, as well as for the experimental data passing the control regions selection, is shown in Table 6.6.

Validation regions

Validation regions are defined to ensure that the background processes are correctly modeled, before and after performing the likelihood fit, in the vicinities of the signal regions, maintaining low signal contamination ($< 10\%$) in all cases. The $t\bar{t}$ process is validated in three regions, two of which are denoted as TVR1bLPhi and TVR2bHPhi and are common for the three signal models. These are defined in the $N_{b\text{-jets}}$-$\Delta\phi(\mathrm{j}, E_{\mathrm{T}}^{\mathrm{miss}})$ plane by requiring the cuts $N_{b\text{-jets}} = 1$ and $\Delta\phi(\mathrm{j}, E_{\mathrm{T}}^{\mathrm{miss}}) < 1.0$, and $N_{b\text{-jets}} \geq 2$ and $\Delta\phi(\mathrm{j}, E_{\mathrm{T}}^{\mathrm{miss}}) > 1.0$,

Process	TCR	VCR
$t\bar{t}$	6600 ± 1700	730 ± 220
Z+jets	26 ± 27	520 ± 80
W+jets	27 ± 8	710 ± 160
tZq	0.49 ± 0.18	0.15 ± 0.08
Wt-channel	139 ± 31	43 ± 12
t-channel (t)	4.5 ± 0.9	1.0 ± 0.5
t-channel ($\bar{t}$)	1.5 ± 0.5	0.5 ± 0.4
s-channel	1.4 ± 0.5	0.21 ± 0.15
Diboson	5.8 ± 2.4	111 ± 24
$t\bar{t}\,V$	72 ± 15	10.7 ± 2.5
Total background	6900 ± 1700	2130 ± 320
Data	5843	1810

Table 6.6: Predicted (pre-fit) event yields for the $t\bar{t}$ and V+jets control regions (TCR and VCR, respectively). The simulated background yields are normalized to theoretical predictions. Uncertainties include both statistics and systematic contributions.

respectively. The third validation region for $t\bar{t}$ production (TVR1bHPhi) and the unique validation region for V+jets production (VVR) require the same selection as the corresponding SR1b and SR0b regions, but the score of the XGBoost classifier is required to be below 0.5. For the VLQ case, in which the signal regions are required to have at least 1 forward jet, the notation of these validation regions turn into TVR1bHPhi1f and VVR1f.

6.4 Statistical analysis: likelihood fit

After defining the regions in which the signal and background processes are expected to be found, a statistical analysis is needed to estimate the background yields and to search for a possible signal. This search follows a template histogram approach in which binned histograms are used to represent the distributions of certain observables in the signal and control regions. The statistical analysis is based on a profile likelihood fit of the Monte Carlo (MC) simulations to the experimental data, in which a set of parameters are estimated. The likelihood function is defined as the product of Poisson probabilities for each bin of the distributions entering the fit. Such a function will depend on free-floating parameters and constrained systematic uncertainties. The free-floating parameters are the normalization factors (NFs) of the background processes and the *signal strength*, which is the ratio of the observed yields over the expected yields of the signal process. Each source of systematic uncertainties is included as a

nuisance parameter (NP) that is modeled according to a Gaussian distribution.

The expected number of events accounts for the statistical and systematic uncertainties. Such expected yields at the i-th bin of a distribution can be written as:

$$\nu_i(\mu, \boldsymbol{\theta}) = \mu s_i(\boldsymbol{\theta}) + b_i(\boldsymbol{\theta}), \tag{6.1}$$

where s_i and b_i are the expected signal and background yields, respectively, $\boldsymbol{\theta} = NF_{t\bar{t}}, NF_{V+\text{jets}}, \theta$ is the set of NFs and NPs, and μ is the signal strength. Thus, the probability of observing n_i events in the i-th bin is given by the Poisson distribution:

$$\text{Pois}(n_i|\nu_i) = \frac{\nu_i^{n_i}}{n_i!} e^{-\nu_i}. \tag{6.2}$$

The need to estimate the parameters μ and $\boldsymbol{\theta}$ leads to the construction of some *estimator*, denoted as $\hat{\mu}$ and $\hat{\boldsymbol{\theta}}$. According to the Maximum Likelihood Principle, the maximization of the likelihood function (or the minimization of the negative log-likelihood function) provides the best estimate of the parameters, named as maximum likelihood estimators (MLE). The likelihood function $\mathcal{L}$ is defined as:

$$\mathcal{L}(\mu, \boldsymbol{\theta}) = \prod_{j=1}^{N} \text{Pois}(n_j|\nu_j) \prod_{k=1}^{M} \text{Gauss}(a_k, \sigma_k|\theta_k), \tag{6.3}$$

where the first product corresponds to the Poisson probabilities of N bins, and the second product accounts for M auxiliary calibration measurements that allow to constrain the NPs. The likelihood function built for this analysis considers $N = 10$, corresponding to two SRs with four bins each and two CRs with one bin each. A total of $M = 175$ NPs are considered to account for the effect of all the theoretical and experimental sources of uncertainties.

The Gaussian distributions of the NPs are determined by the center values a_k and the uncertainties σ_k, obtained from the calibration measurements, but they are usually introduced in the fit as normalized distributions $\mathcal{N}(0, 1)$. If the mean of a NP is shifted from 0 at *post-fit* level it is said that the NP is *pulled*, and if the width is below 1, the NP is *constrained*. A lower uncertainty of the post-fit NP value can indicate that the fit to data has provided additional information about the systematic uncertainty with respect to the prior knowledge from the calibration measurements. On the contrary, a post-fit width above 1 (*unconstrained* NP) is symptomatic of a poor modeling of the systematic uncertainty or a minimization problem during the fit.

Once the (unconditional) likelihood has been maximized with the MLEs, $\hat{\mu}$ and $\hat{\boldsymbol{\theta}}$, it is necessary to estimate the compatibility of the observed data with a certain hypothesis, such as the background-only hypothesis ($\mu = 0$) or the signal-plus-background hypothesis ($\mu = 1$). Assuming a hypothetical or test

value of μ, the set of parameters $\hat{\hat{\boldsymbol{\theta}}}$ will maximize the *conditional* likelihood $\mathcal{L}(\mu, \hat{\hat{\boldsymbol{\theta}}})$. Thus, the profile likelihood ratio is defined as:

$$\lambda(\mu) = \frac{\mathcal{L}(\mu, \hat{\hat{\boldsymbol{\theta}}})}{\mathcal{L}(\hat{\mu}, \hat{\boldsymbol{\theta}})}. \tag{6.4}$$

This ratio will take values between 0 and 1 as the denominator is the maximized value of the likelihood function. The closer is this ratio to 1, the more compatible are μ and $\hat{\hat{\boldsymbol{\theta}}}$ with the MLEs $\hat{\mu}$ and $\hat{\boldsymbol{\theta}}$, and the more compatible is the hypothesis with the data.

It is important to note that the distribution of the estimator $\hat{\mu}$ may take negative values, which would not be valid in the context of the signal strength. However, this could be physically interpreted as long as the mean value of the distribution of $\hat{\mu}$ is not negative and the expected yields from Eq. 6.1 are always positive.

When looking for a positive excess of data over the background-only hypothesis, the *discovery test statistic* is often defined:

$$q_0 = \begin{cases} -2\ln\lambda(0) & \hat{\mu} \geq 0 \\ \\ 0 & \hat{\mu} < 0 \end{cases} \tag{6.5}$$

While $0 \leq \lambda(\mu) \leq 1$, the test statistic q_0 can take values between 0 and infinity, with higher values indicating a larger incompatibility between the data and the hypothesis. Disagreement with the background-only hypothesis is considered only if the best estimate of the signal strength is positive ($\hat{\mu} > 0$), since a very negative value would indicate a poor modeling of the background processes or a misinterpretation of the systematic uncertainties. A two-sided version of this test statistic would be appropriate in the case that both upward and downward fluctuations could be expected[9]. However, in the context of this document, the search is focused on the presence of a signal, so the one-sided test statistic is more appropriate.

The compatibility of the data with the hypothesis $\mu = 0$ can be quantified by the p-value, which is the probability of observing a value of the test statistic equal or larger than the observed one, which can be expressed as:

$$p = \int_{q_{0,\text{obs}}}^{\infty} f(q_0|\mu = 0)dq_0. \tag{6.6}$$

According to the Wilks' theorem, under certain conditions that are reasonable in most contexts in high energy physics, the distribution of $-2\ln\lambda(\mu)$

[9] A good example of this could be a search for neutrino oscillations, in which the no-oscillation hypothesis could be rejected if the data shows an excess or a deficit of events.

is asymptotically a χ^2 distribution with one degree of freedom, which in turn follows a Gaussian distribution when the number of observations is large (Wald approximation), which is always the case in the LHC. However, the one-sided definition of the test statistic in Eq. 6.5 leads to a distribution of q_0, denoted as $f(q_0|\mu = 0)$, that is not symmetric around the mean value.

Therefore, the p-value can be computed as[10]:

$$p = 1 - \Phi\left(\sqrt{q_{0,\text{obs}}}\right), \tag{6.7}$$

where Φ is the cumulative distribution function of the standard normal distribution.

Equivalently, the disagreement between the data and the background-only hypothesis can be quantified by the number of standard deviations in which the observed value of the test statistic is away from the mean value of its distribution, which is known as the *significance*:

$$Z = \Phi^{-1}(1 - p) = \sqrt{q_{0,\text{obs}}}, \tag{6.8}$$

where the second equality makes use of the definition of the p-value in Eq. 6.6.

Once the compatibility of the data with the background-only hypothesis has been quantified by computing the p-value and significance Z of the discovery test statistic, the next step is to set *upper limits* on the signal strength. The upper limits provide the largest signal strength that is compatible with the data at a certain confidence level (CL), so if such signal were present in the data, its strength should be lower than this value. A test statistic that can be used for this purpose is:

$$q_\mu = \begin{cases} -2\ln\lambda(\mu) & \hat{\mu} \leq \mu \\ \\ 0 & \hat{\mu} > \mu \end{cases} \tag{6.9}$$

where this test statistic is not a generalization of the previous one defined in Eq. 6.5. While q_0 was zero when $\hat{\mu} < \mu$, the conditional form of q_μ considers $\hat{\mu} < \mu$ as the relevant range, as this is the case in which the signal strength is larger than the best estimate from the fit.

The p-value and significance can be computed for any given hypothesis μ using the test statistic in Eq. 6.9. If the p-value is below a certain threshold α, set to 0.05 by convention, the hypothesis is rejected at the $(1 - \alpha)$% CL. The threshold value of μ that corresponds to a p-value equal to α, denoted as μ_{up}, is the *upper limit* on the signal strength at the 95% CL, and can be computed from the normal distribution as:

$$\mu_{\text{up}} = \hat{\mu} + \hat{\sigma} \times \Phi^{-1}(1 - \alpha), \tag{6.10}$$

[10]For the double-sided version of the test statistic, in which the gaussian distribution presents two tails, the p-value would be computed as $2 \times (1 - \Phi\left(\sqrt{q_{\mu,\text{obs}}}\right))$.

where $\hat{\sigma}$ is the standard deviation of the distribution of $\hat{\mu}$ and depends in general on the hypothesized value of μ. Thus, the upper limit can be extracted numerically as the value of μ that satisfies $p_\mu = \alpha$.

The upper limit on the signal strength can be translated into an upper limit on the cross-section of the signal process, which is a more relevant quantity from the physics perspective:

$$\sigma_{\text{up}}^{95\%CL} = \mu_{\text{up}} \times \sigma_{\text{theory}}, \tag{6.11}$$

Similarly, $\sigma_{\text{up}}^{95\%CL}$ is the maximum cross-section that is compatible with the data at the 95% CL, and if the signal were present in the data, its cross-section would be expected to be below this value.

Systematics treatment

The `RooFit` [264] and `RooStats` [265] packages contained in the `ROOT` framework are used to perform the profile likelihood fit and to compute the test statistics. These statistical tools are implemented within `TRexFitter` [266], which provides a versatile framework to build histogram templates and adjust the configuration and parameters of the fit.

As explained previously, the NPs representing the systematic uncertainties are included explicitly as Gaussian priors in the likelihood function in the constraint term of Eq. 6.3. However, the effect of these NPs on the expected yields will be asymmetric in general. This asymmetry in the expected yields is modeled at each bin with a certain interpolation function. The selected interpolation functions are piecewise functions that interpolate linearly the nominal yields with the 'up' and 'down' variations of the NPs.

In order to build the simplest template histograms that are possible, the effect of the NPs on the expected yields at each bin is symmetrized, such that the 'up' and 'down' variations of the NPs have the same impact on the expected yields of the bins to be fitted. This is performed conservatively by taking the maximum variation of the 'up' and 'down' variations of the NPs:

$$\text{up} = \text{nominal} + \max\left(|\text{up} - \text{nominal}|, |\text{down} - \text{nominal}|\right), \tag{6.12}$$

$$\text{down} = \text{nominal} - (\text{up} - \text{nominal}). \tag{6.13}$$

This symmetrization strategy is applied to all the NPs, including those special cases in which both the 'up' and 'down' variations of the NP change the expected yields in the same direction, known as *one-sided* systematic uncertainties. Examples of *one-sided* systematics in this analysis correspond to the perpendicular and parallel $E_{\text{T}}^{\text{miss}}$ resolution, the ME generator and the PS model uncertainties. The *two-point* systematics, for which only one variation exists (corresponding to the expected yields of the alternative sample), are also

symmetrized taking the opposite variation on the yields of the alternative sample. The only exception to this symmetrization strategy are the cross-section uncertainties of the s-channel and t-channel single-top processes, but whose contributions to the total yields are minor.

The overall effect of a systematic uncertainty on the distributions to be fitted can be divided into "shape" and "normalization" components. The normalization component is the effect of the NP variation on the integrated yields of the distribution to be fitted. Instead, the shape component is the bin-by-bin effect of the NP variation on such normalized distributions. The shape effect strongly depends on the statistical precision of each bin, which can lead to large fluctuations that do not represent the bin-by-bin impact of the NP. To prevent the fit to be dominated by such non-physical behavior, a *smoothing* procedure is applied to the shapes of the varied distributions.

Subsequently, a *pruning* is applied to improve the stability of the fit. The NPs for which the normalization and shape impact are below 1% are removed from the fit, where the shape impact is determined from the bin with the largest variation.

Due to the limited statistics of the simulations, the template histograms are not ideal descriptions of the underlying distributions, being necessary to achieve a good balance between the statistical precision of each bin and the descriptive power of the distributions. Multiplicative Poisson terms are added to the likelihood function from Eq. 6.3 to account for the MC statistical uncertainties, in which one *gamma* parameter[11] per bin scales the expected yields penalizing the likelihood as auxiliary measurements. The main difference with respect to the NPs is that the uncertainties of the gamma parameters can not be constrained. The reason is that the real data is not affected by the MC statistics precision, and hence, nothing can be learned about it by fitting to data.

6.5 Results

This section presents the results of the profile likelihood fit to the data. The background-only hypothesis is presented in Section 6.5.1, while the signal-plus-background hypothesis is discussed in Section 6.5.2. Since no significant excess over the background is observed, exclusion limits on the production cross-section of the signals are obtained, which is also interpreted as limits on the parameter space of each signal model. The limits are presented in Section 6.5.3.

[11] Assuming a flat prior of this scaling parameter, the posterior distribution corresponds to a Gamma function, receiving its name.

6.5.1 Background-only fit

The background-only hypothesis considers the absence of any signal ($\mu = 0$) and the fit to data aims to estimate the expected yields of the background processes in the phase space of the analysis. When the background yields are fitted to data in the two control regions, with TCR and VCR being single-binned histograms, an exact fitting to data is obtained by free-floating the two normalization factors (NFs) of the $t\bar{t}$ and $V+$jets backgrounds. The likelihood function is maximized for $\mathrm{NF}_{t\bar{t}} = 0.85 \pm 0.23$ and $\mathrm{NF}_{V+\mathrm{jets}} = 0.83 \pm 0.21$, being compatible with unity within the uncertainties. Values of the NFs below 1 compensate the overestimation introduced from a different data/MC efficiency of the top-tagger, as it was already illustrated at preselection level in Table 6.6 and Figures 6.2 and 6.4.

In order to assess the compatibility of the data with the background-only hypothesis in the regions where the signal is expected to be produced, a simultaneous fit to data in both control and signal regions is performed, in which the distributions of the BDT score in the SRs are included. Three fits are required since different SRs were defined: $\mathrm{SR0b}_{\mathrm{Scalar}}$ and $\mathrm{SR1b}_{\mathrm{Scalar}}$ for the scalar DM mediator model; $\mathrm{SR0b}_{\mathrm{Vector}}$ and $\mathrm{SR1b}_{\mathrm{Vector}}$ for the vector DM mediator model; and $\mathrm{SR0b1f}_{\mathrm{VLQ}}$ and $\mathrm{SR1b1f}_{\mathrm{VLQ}}$ for the VLQ model. Figure 6.7 shows the post-fit distributions of the BDT score in the SRs of the three models, with the dashed line indicating the pre-fit total background prediction at pre-fit level.

The fitted distributions in the SRs are these BDT score distributions, which are divided in 4 bins in the range [0.5, 1.0] with edges at 0.7, 0.85, 0.95 and 1.0. This binning choice is optimal since the signal is expected to be concentrated in the high BDT score region. Selecting an appropriate binning is crucial for enhancing the sensitivity of the analysis, as it strikes a balance between capturing the shape profile and maintaining statistical power. Since the fit is performed along ten bins (two from the CRs and eight from the SRs), the two NFs do not allow matching exactly the data bin contents as in the previous fit to the CRs. However, the overestimation of the background is again corrected by the fit with the NFs values shown in Figure 6.8, which are compatible with the unity within 1σ, except $\mathrm{NF}_{V+\mathrm{jets}}$ for the vector DM mediator model and for the VLQ model, which are compatible with the unity within 2σ. The discrepancy observed in $\mathrm{NF}_{V+\mathrm{jets}}$ between the fits targeting DM and vector-like T signals is explained by the different phase spaces of the corresponding signal regions, in particular due to the requirement of at least one forward jet in the VLQ signal regions.

In addition, the NPs are pulled and constrained through the minimization procedure to provide the best agreement between the data and the background-only hypothesis. Figure 6.9 shows the post-fit values of the NPs for the

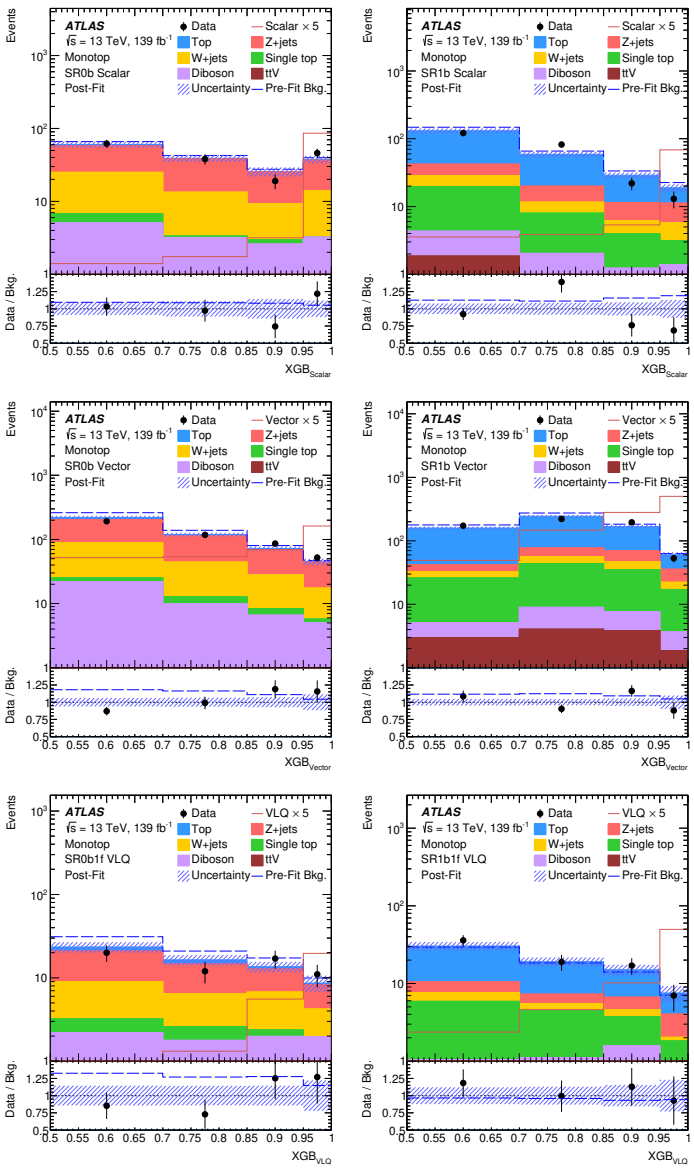

Figure 6.7: Comparison of data and simulated events for the BDT score distribution in the different SRs: (first row) the scalar DM mediator production, (second row) the vector DM mediator production and (third row) the single vector-like T quark production. The background predictions result from the background-only fit to data in control and signal regions. The dashed line indicates the pre-fit total background prediction. The overlaid signal distributions are scaled by a factor 5.

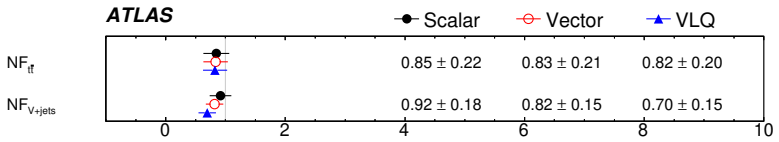

Figure 6.8: Comparison of the fitted normalization factors of the $t\bar{t}$ and V+jets background processes in the fits to data in control and signal regions under the background-only hypothesis. An independent fit is performed for each signal model, using the respective signal regions.

background-only fit in the CRs and SRs for the three signal models. The green (yellow) bands represent the $\pm 1(2)\sigma$ variation of the NPs at pre-fit level. Each NP is shown relative to its nominal value and in units of its pre-fit uncertainty. Overall, it is observed that the NPs stay consistent with their pre-fit estimation, pointing out that data is well described by the background simulation. Residual pulls and constraints are obtained for $t\bar{t}$ and single-top modeling uncertainties along the three different fits. The reason is that their variations have a significant effect on the shape of the BDT score distribution. In particular for the vector DM mediator model, the "top-tagging γ-jet modeling NP" presents a $\sim 1\sigma$ pull, as the variation follow the shape of the fitted data distribution.

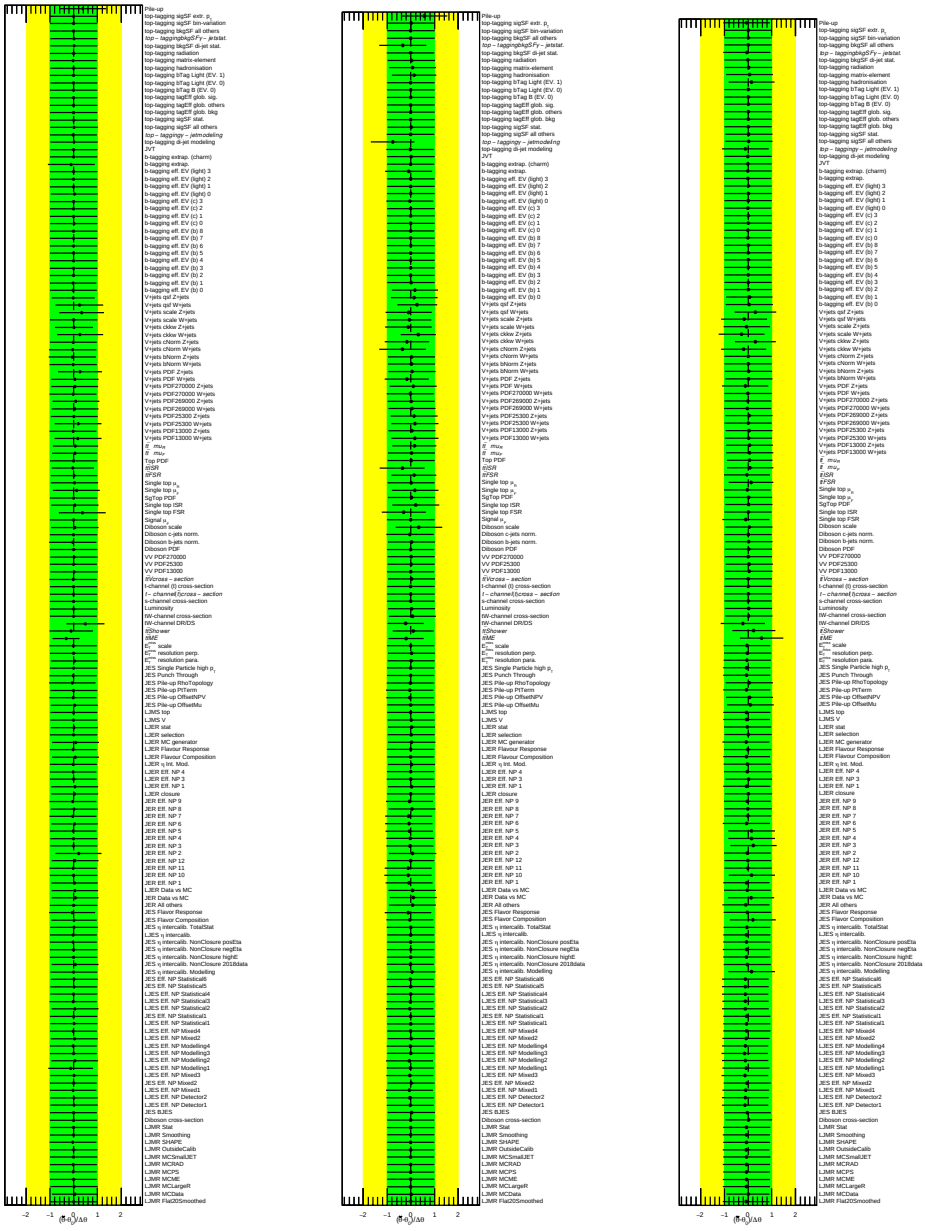

(a) (b) (c)

Figure 6.9: Post-fit systematic uncertainties obtained from the fit under the background-only hypothesis in the control and signal regions for (a) the scalar DM mediator, (b) the vector DM mediator and (c) the VLQ model. The green (yellow) area represent the $\pm 1(2)\sigma$ band on the pre-fit systematic uncertainty. The black points show the best-fit values of the nuisance parameters, with the error bars representing the post-fit uncertainties. Each nuisance parameter is shown relative to its nominal value, θ_0, and in units of its pre-fit uncertainty.

6.5.2 Signal-plus-background fit

In the absence of any significant excess, a fit under the signal-plus-background hypothesis should provide a signal strength compatible with zero. However, this does not necessarily mean that no signal is present in the data. It could be possible that the data is not sensitive enough to observe it since its cross-section is below the sensitivity of the analysis. Introducing the signal in the fit will provide additional information concerning the correlations and the impact of each parameter of the fit on the signal strength.

Figures 6.10, 6.11 and 6.12 show the correlation matrices of the fit parameters for the scalar DM mediator, vector DM mediator and VLQ models, respectively. Only those NPs that have any correlation larger than a 20% are included in the correlation matrices. The largest correlations are related to NFs, observed for NPs with a large impact on the backgrounds yields in the CRs, which is independent from the signal model considered. Thus, $\mathrm{NF}_{t\bar{t}}$ shows important correlations with $t\bar{t}$ PS and FSR modeling, as well as with the top-tagging hadronization systematics. The $t\bar{t}$ ME and PS modeling uncertainties also show important correlations with $\mathrm{NF}_{V+\mathrm{jets}}$, which in turn is highly correlated to the $V+$jets modeling uncertainties.

In the scalar DM mediator case, the signal strength shows a $\sim 65\%$ correlation with the b-tagging extrapolation uncertainty, which is related to the b-jets calibration in the high-p_{T} regime in which this signal is expected to be important. In the vector DM mediator case, a $\sim 58\%$ correlation of the signal strength is observed with the uncertainty associated with the tW-channel DR/DS scheme selection. This uncertainty shows a large effect on the last two bins of the BDT score distribution, which contains most of the vector DM mediator signal events and where the observed data distribution follows a similar flat shape. Instead, no large correlations are observed for the signal strength in the VLQ case.

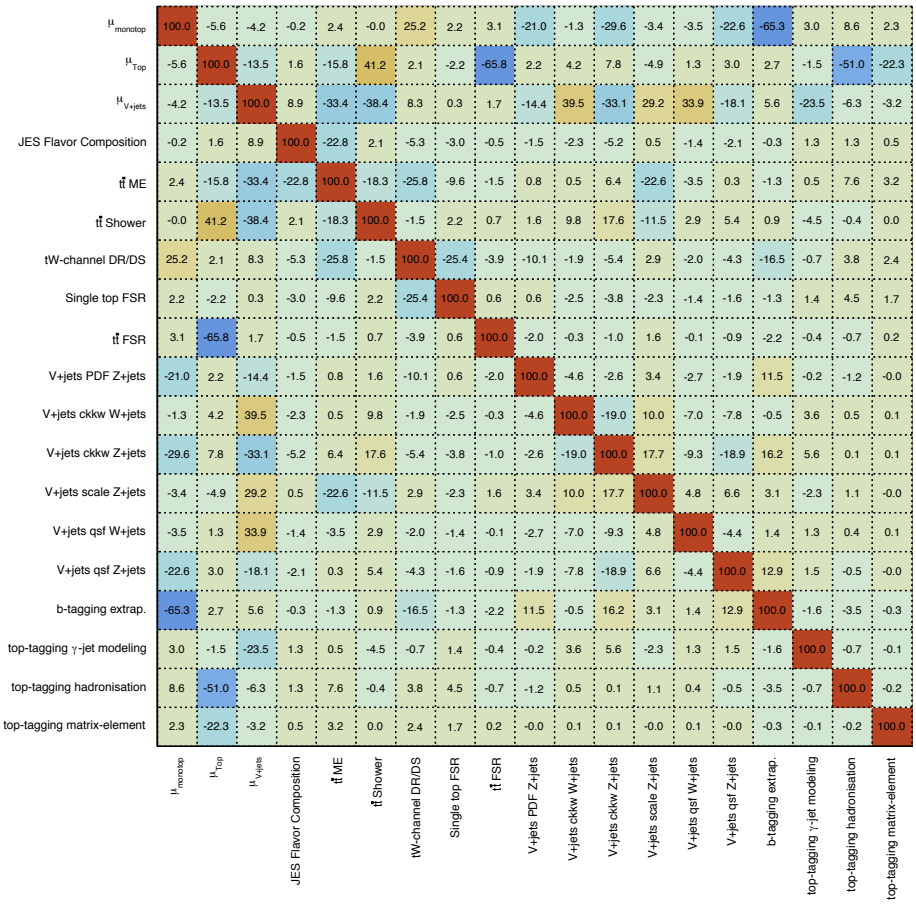

Figure 6.10: Correlation matrix of the free parameters and the NPs included in the data fit in the control regions and the scalar DM mediator model SRs under the signal-plus-background hypothesis. Only NPs with a correlation above 20% are displayed. The fit is performed using $\lambda = 0.6$, $y_\chi = 0.4$, $m_\chi = 1$ GeV and $m_\phi = 4$ TeV as parameters of the model.

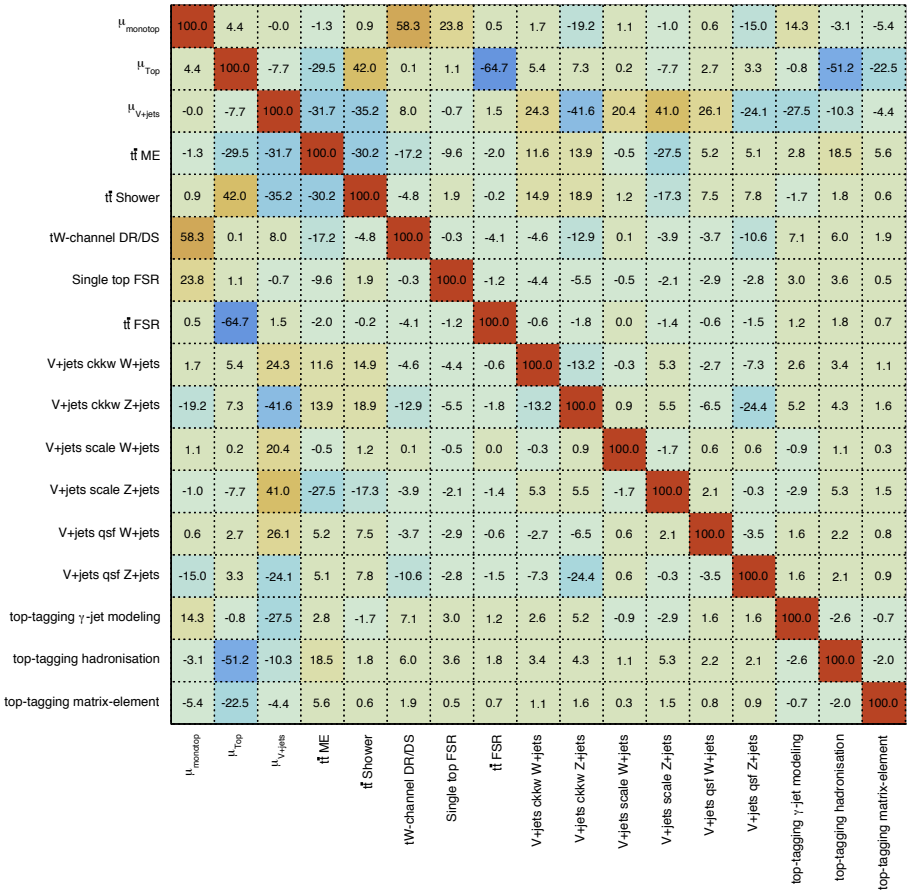

Figure 6.11: Correlation matrix of the free parameters and the NPs included in the data fit in the control regions and the vector DM mediator model SRs under the signal-plus-background hypothesis. Only NPs with a correlation above 20% are displayed. The fit is performed using $a = 0.5$, $g_\chi = 1$, $m_\chi = 1$ GeV and $m_V = 1.75$ TeV as parameters of the model.

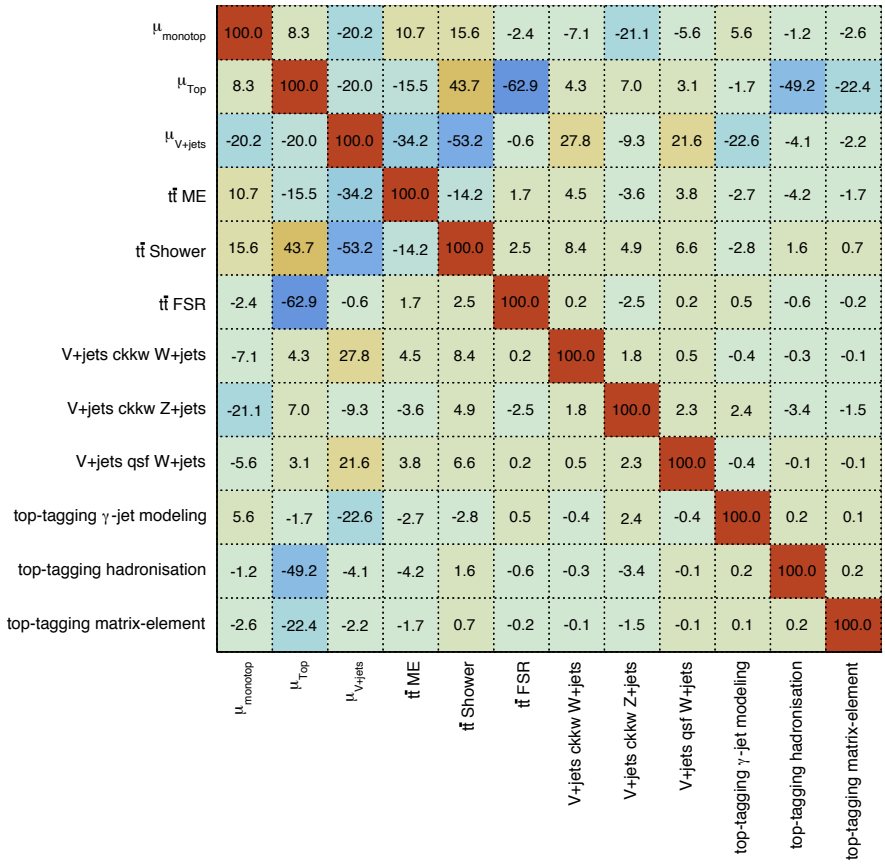

Figure 6.12: Correlation matrix of the free parameters and the NPs included in the data fit in the control regions and the VLQ SRs under the signal-plus-background hypothesis. Only NPs with a correlation above 20% are displayed. The fit is performed using $\kappa_T = 0.5$ and $m_T = 1.7$ TeV as parameters of the model.

Impact of the fit parameters on the signal strength

In order to further evaluate the impact of any fit parameter θ on the signal strength μ, pre-fit (post-fit) 1σ variations $\Delta\theta$ ($\Delta\hat{\theta}$) on the estimated parameter $\hat{\theta}$ are introduced in the fit. This allows to quantify the impact $\Delta\mu$ from the four possible variations of θ ($\hat{\theta}\pm\Delta\theta$ and $\hat{\theta}\pm\Delta\hat{\theta}$) independently for each NP and NF. The 20 highest-ranked parameters in terms of impact on the signal strength are shown in Figures 6.13a, 6.13b and 6.13c for the scalar DM mediator, vector DM mediator and VLQ models, respectively. The nominal best-fit estimation of the fit parameters also appear in the figures.

As expected, the parameters that have the highest impact generally correspond with those NPs and NFs that showed the largest correlations with the signal strength in Figures 6.10, 6.11 and 6.12. For the scalar DM mediator model, the b-tagging extrapolation uncertainty is the most important parameter, followed by the systematic uncertainties on $Z+$jets modeling. For the vector DM mediator model, the uncertainty on the choice of tW-channel DR/DS scheme is the most impactful parameter, followed again by the systematic uncertainties on the $Z+$jets modeling and by the $t\bar{t}$ FSR uncertainty. For the VLQ model, the modeling uncertainties on the $Z+$jets and $t\bar{t}$ processes are the leading parameters, including $\mathrm{NF}_{V+\mathrm{jets}}$. Systematics related to the large-R jet reconstruction are also important in the latter case.

6.5.3 Exclusion limits on the signal models

The SM background has shown to be in good agreement with data and the signal-plus-background hypothesis led to a measured signal strength compatible with zero within 1σ for the three models. As discussed in Section 6.4, from all the values of the signal strength that would be compatible with the background-only hypothesis at 95% CL, the maximum value has a special interest since it evaluates the sensitivity[12] of the analysis. This magnitude is the expected upper limit on the signal strength, $\mu_{\mathrm{up}}^{\mathrm{exp}}$, which is related to the expected upper limit on the cross-section according to the expression 6.11. Analogously, the maximum value of the signal strength that would be compatible with the experimental data at 95% CL is the observed upper limit on the signal strength, μ_{up}.

In the same way as the signal-plus-background fits described previously assumed the nominal parameters of the signal models, the fits are repeated for the whole parameter space of each signal model. The signal grid is then divided in two regions: the excluded region, with the signal points for which

[12]The results of a statistical analysis does not only depend on the signal-plus-background ratio in the fitted regions and the number of NPs included in the fit. The analysis strategy also include the treatment of the systematics, the choice of the variables to fit or the binning of the fitted histograms, having a relevant impact on the sensitivity of the analysis.

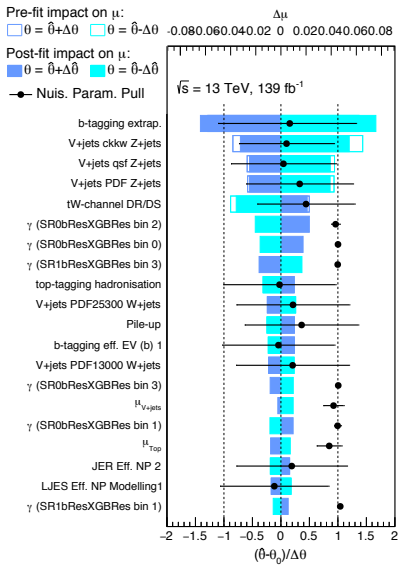

(a)

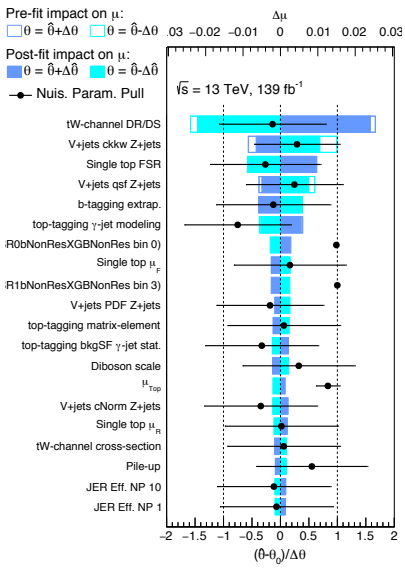

(b)

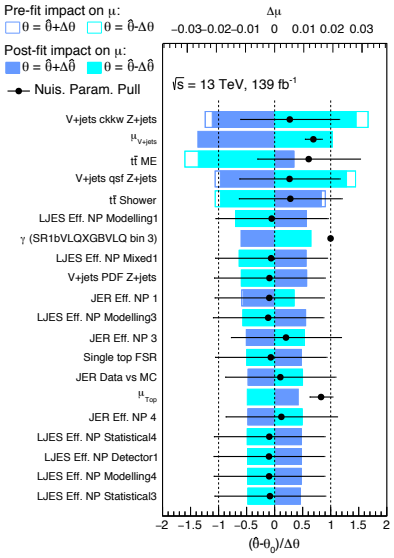

(c)

Figure 6.13: The nuisance parameters ranked according to their post-fit impacts on the best-fit value of μ. Only the 20 nuisance parameters with the largest impacts are shown. The empty (solid) blue rectangles illustrate the pre-fit (post-fit) impacts on the parameter of interest μ, corresponding to the top axis. The black points show the best-fit values of the nuisance parameters, with the error bars representing the post-fit uncertainties. Each nuisance parameter is shown relative to its nominal value, θ_0, and in units of its pre-fit uncertainty.

$\sigma_{\text{up}}^{95\%\text{CL}} < \sigma_{\text{theory}}$, and the allowed region, with the signal points for which $\sigma_{\text{up}}^{95\%\text{CL}} > \sigma_{\text{theory}}$ and that can not be excluded by the analysis. From this division, exclusion limits on the parameters of the models are obtained.

Mass scan of cross-section limits

Figure 6.14 shows the observed upper limit (solid black lines) and the theoretical cross-section (red lines) for different values of a mass parameter: the scalar mediator mass m_ϕ for the scalar DM mediator model, the vector mediator mass m_V for the vector DM mediator model and the top partner mass m_T for the VLQ model. The dashed black line represents the expected upper limit on the cross-section, and the yellow (green) band represents the $\pm 1\sigma$ ($\pm 2\sigma$) uncertainty of the expected upper limit on the cross-section. Thus, the y-axis represents cross-section values in units of femtobarns (fb), while the x-axis shows the values of the mentioned mass parameter in TeV units. The smooth profile is obtained from a linear interpolation between the available mass points.

The cross-section of the scalar DM mediator model, fixing the model parameters to $m_\chi = 1$ GeV, $\lambda = 0.6$ and $y_\chi = 0.4$, is excluded for values above ~ 2 fb, which allow excluding masses of the scalar mediator below 4.3 TeV, as this is the value in which the theoretical cross-section is equal to the upper limit on the cross-section. This results in an improvement of around 800 GeV with respect to the previous mono-top search. A degradation of the cross-section limit as the m_ϕ value increases is observed, justified by a general decrease in the event selection efficiency at the high boosted regimes. For the vector DM mediator model, taking $a = 0.5$, $g_\chi = 1$ and $m_\chi = 1$ GeV, the cross-section is excluded for values above ~ 20 fb, which allow excluding masses of the vector mediator below 2.3 TeV. This corresponds to an improvement of around 300 GeV with respect to the previous iteration of the mono-top search [260]. Finally, for the VLQ model, fixing $\kappa_T = 0.5$ in the singlet scenario ($\mathcal{B}(T \to Zt) = 25\%$), the cross-section is excluded for values above ~ 15 fb, which allow excluding masses of the top partner below 1.8 TeV. The degradation of the excluded cross-section for low values of m_T is a consequence of the lower mass splitting between the top partner and the SM top quark, which results in a lower $E_{\text{T}}^{\text{miss}}$ and a lower selection efficiency of the analysis. No exclusion limits on m_T was provided by the previous search for the benchmark coupling $\kappa_T = 0.5$. As it will be discussed in the next chapter, the sensitivity of this search is competitive with similar searches of singly-produced top partners looking for different final states.

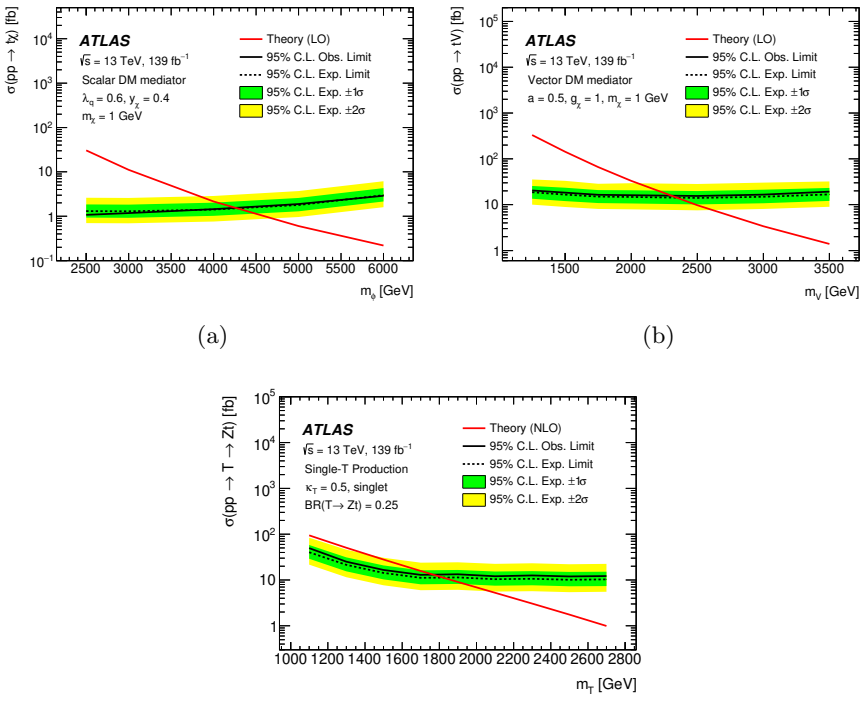

Figure 6.14: 95% CL upper limits on the cross-section of the considered signal models as a function of: (a) the DM scalar mediator ϕ mass (for fixed model parameters of $\lambda_q = 0.6$, $y_\chi = 0.4$ and $m_\chi = 1$ GeV), (b) the DM vector mediator V mass (for $a = 0.5$, $g_\chi = 1$ and $m_\chi = 1$ GeV) and (c) the vector-like T quark mass (for $\kappa_T = 0.5$).

Two-dimensional limit maps

The parameter space has been explored, and two-dimensional maps were built varying two parameters of the signal model, with the z-axis representing the upper limit on the signal strength: $\mu_{up}^{95\%\mathrm{CL}} = \sigma_{\mathrm{up}}^{95\%\mathrm{CL}}/\sigma_{SM}$. In such a representation, the contour that indicates the excluded region corresponds with $\mu_{up}^{95\%\mathrm{CL}} = 1$. Figure 6.15 (6.16) shows three maps for the scalar (vector) DM mediator model, with the mediator mass in the x-axis in all cases. The solid (dashed) black lines represent the observed (expected) exclusion contours at 95% CL, while red (blue) lines represent the $\pm1\sigma$ ($\pm2\sigma$) uncertainty of the expected exclusion contour. The color scale in the z-axis illustrates the observed upper limit on the signal strength.

From the (λ_q,m_ϕ) and (y_χ,m_ϕ) planes, corresponding to Figures 6.15a and

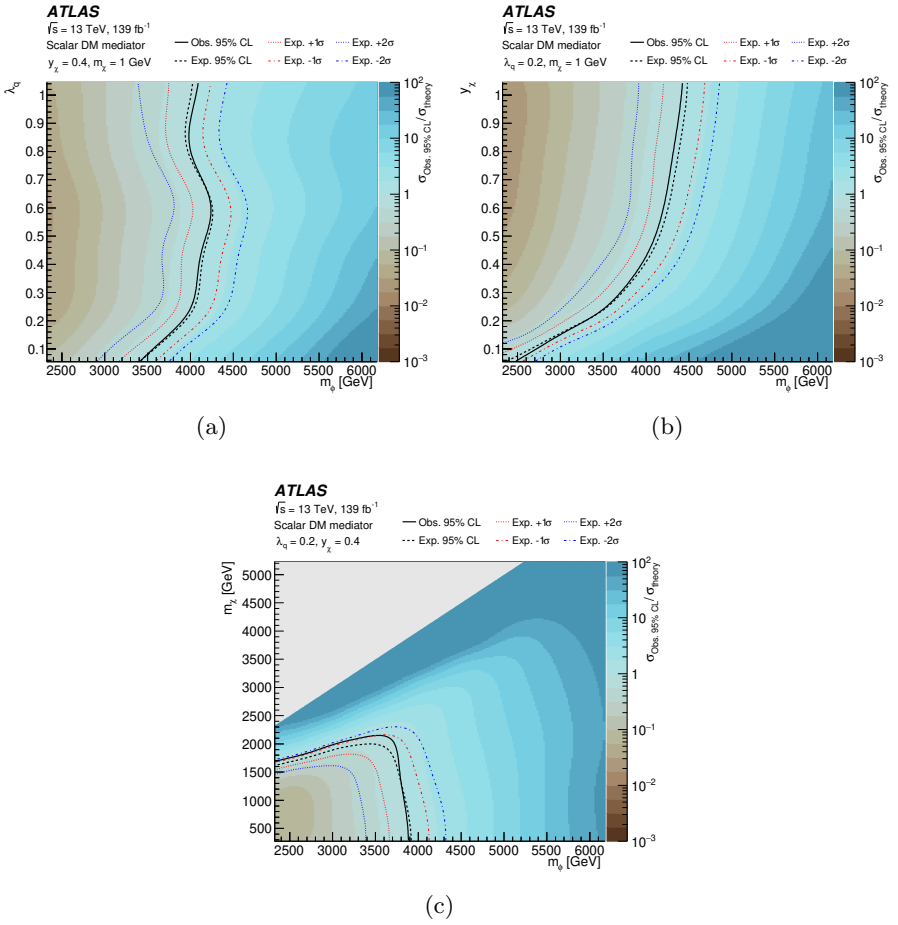

Figure 6.15: Observed 95% CL upper limits on the scalar-mediated DM signal strength in three planes of the model parameters space: (a) (m_ϕ, λ_q), (b) (m_ϕ, y_χ) and (c) (m_ϕ, m_χ). The observed (expected) 95% CL exclusion limits on the parameters are drawn as solid (dashed) lines. The ± 1 and ± 2 standard deviations around the expected limit are also shown.

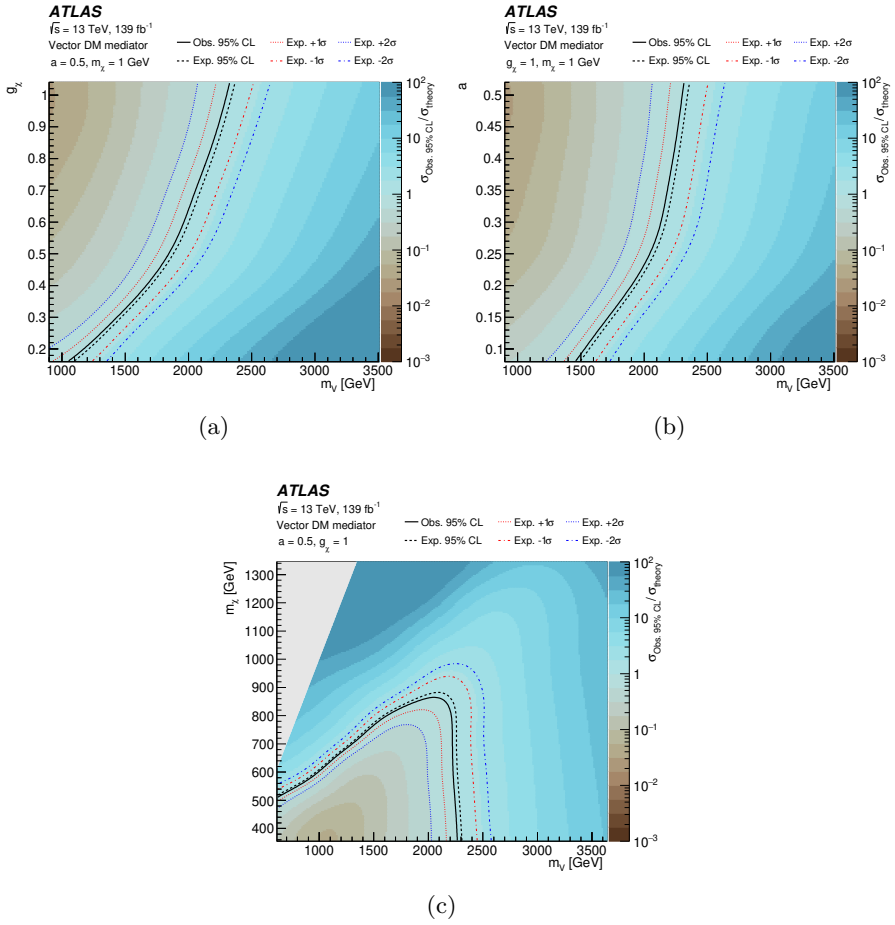

Figure 6.16: Observed 95% CL upper limits on the vector-mediated DM signal strength in three planes of the model parameters space: (a) (m_V, g_χ), (b) (m_V, a) and (c) (m_V, m_χ). The observed (expected) 95% CL exclusion limits on the parameters are drawn as solid (dashed) lines. The ± 1 and ± 2 standard deviations around the expected limit are also shown.

6.15b respectively, it is observed that the limits on m_ϕ are almost constant for different values of λ_q and y_χ, except for low values of y_χ, for which the sensitivity decreases significantly. This is understood from the Feynman diagram in Figure 2.5a. Lower values of the λ_q and y_χ couplings reduce the theoretical production cross-section of the scalar mediator and its branching ratio, but they will not affect the kinematics of the final state. Therefore, the sensitivity of the analysis remains similar as long as the signal cross-section is not very reduced. Thus, m_ϕ values below $\sim$ 4 TeV are excluded for all values of λ_q (y_χ) above 0.2 (0.4) with $m_\chi = 1$ GeV, but m_ϕ limits up to 3.4 (2.5) TeV are excluded for λ_q (y_χ) equal to 0.1 . The (m_χ,m_ϕ) plane, from Figure 6.15c, shows that the limit on m_ϕ is also constant for low values of m_χ, excluding a maximum value of m_χ equal to 2.2 TeV. However, the kinematics of the final state objects are highly affected for larger values. In fact, the analysis is not sensitive in the region for which $(m_\phi - m_\chi) < 500$ GeV, corresponding to the gray area, as such a small difference would not allow to produce a boosted top-quark in the final state.

Similarly, the (a,m_V) and (g_χ,m_V) planes for the vector DM mediator model, in Figures 6.16a and 6.16b respectively, show a soft dependence of the mediator mass limit on the couplings. In this case, the limits on m_V slightly decrease as a and g_χ take lower values, but the strongest sensitivity dependence is again on the mediator mass. Figure 6.16c shows the (m_χ,m_V) plane with constant limits on m_V for low values of m_χ, but the sensitivity decreases for larger values of m_χ. In addition, the region $m_V > 2m_\chi$ is energetically forbidden (see Figures 2.5b and 2.5c) and corresponds to the gray area. All the explored values of a and g_χ are excluded for m_V below 1.1 TeV and 1.5 TeV, respectively, and a maximum m_V limit of 2.3 TeV is achieved in the three planes. The limit on the DM mass m_χ reaches 850 GeV for the fixed parameters $a = 0.5$ and $g_\chi = 1$.

The (κ_T,m_T) plane for the VLQ model in Figure 6.17a shows a saturation of the excluded signal strength for low values of m_T and κ_T. This occurs because the production cross-section is reduced for low κ_T at the same time that the excluded cross-section is degraded in the low m_T range, which was already noticed in Figure 6.14c as a consequence of an acceptance reduction. Thus, the excluded signal strength remains constant for $m_T < 1.6$ TeV, excluding all values of κ_T above 0.4. The top partner mass is excluded up to 1.9 TeV for values of κ_T around 0.6. The results are only interpreted for the region in which the relative decay width of the top partner Γ_T/m_T is below 0.5, where the theoretical assumptions remain valid. Since $\Gamma_T/m_T \propto \kappa_T^2 m_T^2$, isolines of the relative decay width can be plotted in the (κ_T,m_T) plane, as illustrated in Figure 6.17b. A particular assumption on the relative decay width corresponds with a particular exclusion limit on the κ_T and m_T parameters. Such a correspondence can be mapped from the intersection of the isolines (dashed

gray lines) with the exclusion contour (solid black line). It can be observed that the analysis is sensitive to Γ_T/m_T above 5%.

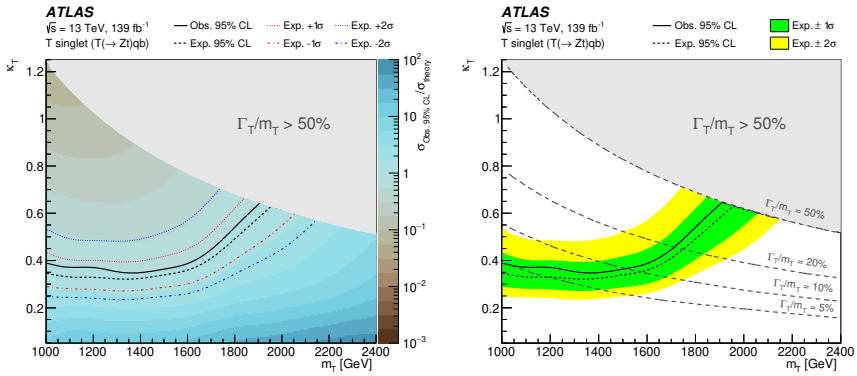

(a) (b)

Figure 6.17: Exclusion limits in terms of the universal coupling constant κ_T and the T quark mass in the singlet SU(2) scenario, in the regime where $\Gamma_T/m_T \leq 50\%$, for which the theory calculations are known to be valid. (a) Observed 95% CL upper limits on the T quark signal strength as a function of κ_T and the T quark mass. The observed (expected) 95% CL exclusion limits on the parameters are drawn as solid (dashed) lines, with all values of κ_T above the black contour line being excluded at each mass point. The ± 1 and ± 2 standard deviations around the expected limit are also shown. (b) Expected (dashed line) and observed (solid line) 95% CL exclusion limits on κ_T and the T quark mass. Different Γ_T/m_T hypotheses are shown as dashed lines. The shaded bands correspond to ± 1 and ± 2 standard deviations around the expected limit.

As it was mentioned previously, this analysis explores the scenario in which the top partner is a singlet of SU(2), which implies that the relative coupling to the W boson ξ_W is 50%. Since the relative couplings to the SM bosons coincide with the corresponding branching ratios in the large mass limit, these follow the same relation: $\xi_Z = \xi_H = (1 - \xi_W)/2 = 0.25$. The exclusion limits on the VLQ model can be generalized for any value of ξ_W different to 50%, maintaining the relation $\xi_Z = \xi_H$. The $(\Gamma_T/m_T, \xi_W)$ plane shown in Figure 6.18 shows the exclusion limits for ξ_W values from 0.5 to 0.9. The z-axis represents the observed mass limit of the top partner, with the solid (dashed) contours corresponding to isolines of the same observed (expected) mass limit. The most stringent exclusion limits are obtained for $\xi_W = 0.5$, as it corresponds to the singlet scenario explored in the analysis, providing mass limits of ~ 1.8 TeV. As expected, the mass limit is degraded for large values of ξ_W since the branching ratio into the Z boson decreases. The case $\xi_W = 1$ is

not considered since the acceptance is totally suppressed. Values of ξ_W below 0.5 are not considered either since the $T(\rightarrow Zt)qb$ production mode becomes subdominant with respect to $T(\rightarrow Zt)qt$, which do not provide a mono-top signature.

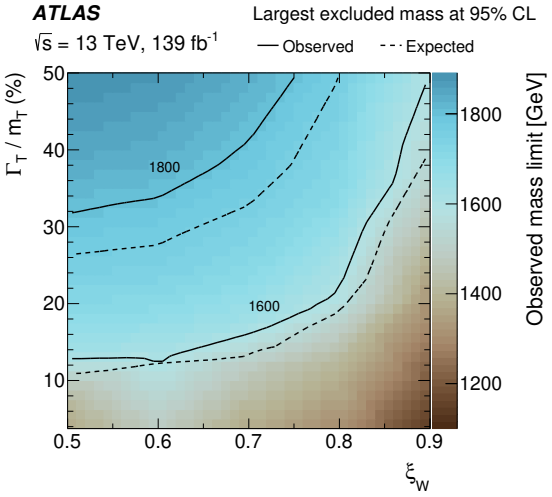

Figure 6.18: Observed 95% CL exclusion limits on the T quark mass in the singlet SU(2) scenario as a function of the relative resonance width Γ_T/m_T and the relative coupling parameter ξ_W. The solid (dashed) contour lines denote observed (expected) exclusion limits of equal mass in units of GeV.

Chapter 7

Combination of singly-produced vector-like top quark searches

This chapter presents the first combination of searches for a singly-produced vector-like top quark [2], which make use of the full Run 2 dataset collected by the ATLAS experiment at the LHC, at a collision energy of $\sqrt{s} = 13$ TeV and corresponding to an integrated luminosity of 139 fb^{-1}. This combination is part of the ambitious VLQ program of the ATLAS experiment, which has already explored extensively both the pair and single production modes of VLQs in different decay channels. The individual searches entering the combination look for singly-produced vector-like top quarks, since the cross-section is larger than its pair production for masses above 1 TeV. Despite no significant excess being observed in any of the analyses, small excesses in the individual searches could potentially be enhanced from this statistical combination.

Section 7.1 describes the three individual analyses entering the combination, emphasizing the production modes and decay channels targeted by each of them. The combination procedure is then described in Section 7.2, with special emphasis on the correlations of the systematic uncertainties along the different channels. Finally, the results of the combination are presented in Section 7.3, including the observed and expected limits on the cross-section, as well as the interpretation in terms of the model parameters.

7.1 Individual channels

The analyses entering the combination explore the decay modes of the top partner into Ht and Zt. An illustration of the leading order Feynman diagram of single vector-like T-quark production in association with a t (W-mediated)

or b (Z-mediated) quark and subsequent decay to either Ht or Zt is shown in Figure 7.1. The different analyses are orthogonal by construction according to the lepton multiplicities in their final states: the MONOTOP analysis targets the Zt decay mode in the 0-lepton channel, the HTZT analysis targets the Ht and Zt decay modes in the 1-lepton channel, and the OSML analysis targets the Zt decay mode in the 2-lepton and 3-lepton channels. The target signals and decay channels of each analysis are summarized in Table 7.1.

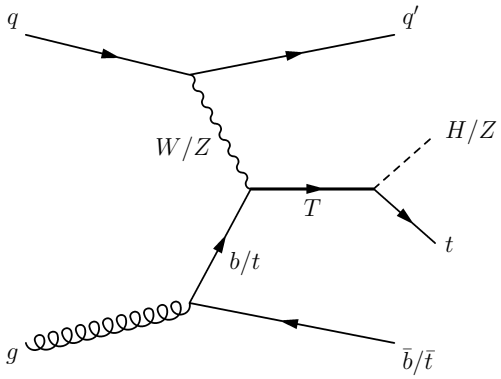

Figure 7.1: Leading order Feynman diagram of single vector-like T production in association with a t or b quark and subsequent decay to either Ht or Zt.

Analysis	Target signal	Decay channels	Discriminants
MONOTOP	$Wb/Zt \to T \to Zt$	$Zt \to \nu\nu bqq$ (0ℓ)	BDT score
HTZT	$Wb/Zt \to T \to Ht/Zt$	$Ht/Zt \to bbb\ell\nu/qqb\ell\nu$ (1ℓ)	m_{eff}
OSML	$Wb/Zt \to T \to Zt$	$Zt \to \ell\ell b\ell\nu$ (3ℓ), $Zt \to \ell\ell bqq$ (2ℓ)	Z boson p_{T}

Table 7.1: Summary of the target signal and decay channels for the three analyses included in the combination and the discriminating variables used.

The Monotop analysis

This analysis [1], described in the previous chapter, is designed to search for events with a single top quark produced in association with DM particles, where the top quark decays hadronically and the DM particles escape detection. Therefore, a large missing transverse momentum is expected in the final state. Such a signature also allows searching for the production of a single vector-like T-quark decaying into a top quark and a Z boson, where the Z boson decays to neutrinos. The most sensitive channel for this search is a W-mediated process

in which a forward jet is also expected in the final state.

The selected data events are required to pass at least one of the $E_{\mathrm{T}}^{\mathrm{miss}}$ triggers, imposing lower thresholds which varied from 70 to 120 GeV depending on the data-taking period. The trigger targeting high-p_T jets aimed to recover possible inefficiencies of $E_{\mathrm{T}}^{\mathrm{miss}}$ triggers in specific phase spaces, but no events passed both this trigger and the further analysis selection. However, event passing this trigger were useful to study the multijet production.

The dominant backgrounds are $t\bar{t}$ and W/Z+jets events, as the requirement of a high $E_{\mathrm{T}}^{\mathrm{miss}}$ (greater than 250 GeV) suppresses contributions from multi-jet processes. Events are also required to pass a preselection in which a top-tagged large-R jet is the leading jet, with a p_T within $[350, 2500]$ GeV and a reconstructed mass within $[40, 600]$ GeV. Beam-induced backgrounds are reduced by requiring a minimum azimuthal angle between the $E_{\mathrm{T}}^{\mathrm{miss}}$ and any small-R jet larger than 0.2. Additionally, in order to ensure hadronic decays, a veto on leptons is implemented. To accurately model the main backgrounds, two CRs have been defined: one enriched with $t\bar{t}$ events and other enriched with W/Z+jets events. The control regions are defined based on the b-tagged jet multiplicity, with both control regions being restricted to $\Delta\phi_{\mathrm{min}}(j, E_{\mathrm{T}}^{\mathrm{miss}}) < 1$ to suppress signal contamination. No b-tagged jets are required for the W/Z+jets control region, while 2 or more b-tagged jets are required for the $t\bar{t}$ control region. On the other side, a BDT is used to maximize the sensitivity in the SRs, which also require $\Delta\phi_{\mathrm{min}}(j, E_{\mathrm{T}}^{\mathrm{miss}}) > 1$ and a forward jet with $p_T > 40$ GeV. The signal discrimination fit is performed on the distribution of the BDT output score in the signal regions, while single bins are used in the CRs to simultaneously constrain the normalization and modeling of the main backgrounds.

No significant deviation from the SM predictions is observed in this analysis, such that exclusion limits on the cross-section are obtained for a variety of signal processes with different masses and parameters. This analysis plays a major role in the singlet interpretation of the vector-like top quark model, while the sensitivity to the doublet model is almost negligible.

The HtZt analysis

This analysis, published in Ref. [129], explores the single production of a vector-like T-quark in the four production modes mentioned previously and illustrated in Figure 7.1, in which the subsequent decays $H \to b\bar{b}$ or $Z \to q\bar{q}$ are targeted. Events passing at least one of the single-electron or single-muon triggers are selected. The lowest unprescaled $E_{\mathrm{T}}^{\mathrm{miss}}$ trigger is chosen for each run period. Events which only pass a $E_{\mathrm{T}}^{\mathrm{miss}}$ trigger are required to have offline $E_{\mathrm{T}}^{\mathrm{miss}} > 200\,\mathrm{GeV}$ to ensure that they are on the trigger efficiency plateau.

Data are analyzed in the lepton+jets final state, characterized by an isolated lepton and multiple jets and b-jets. Events are preselected by requiring

the presence of exactly one lepton with $p_{\mathrm{T}} > 30$GeV, at least five small-R jets, and at least one b-tagged VR-track jet.

To test for the presence of signal, a likelihood fit is performed on the distribution of the effective mass (m_{eff}) variable [1] across a set of 24 "fit regions" constructed from events in the preselection sample. These fit regions are categorized based on the multiplicities of small-R jets in the central and forward regions, b-tagged track jets, and tagged boosted objects in the event.

The fit regions are designed to be pure in one or more of the four targeted signal modes ($Wb/Zt \to T \to Ht/Zt$), or in specific background processes. The combined use of these regions in the fit allows the search to retain sensitivity to all the processes that can occur simultaneously in a benchmark model, and the signal-depleted regions serve to improve the description of the expected background. The main source of background in the fit regions are $t\bar{t}$+jets production. In particular, regions with three or more b-jets are dominated by $t\bar{t}$+$\geq$1c and $t\bar{t}$+$\geq$1b backgrounds, while $t\bar{t}$+light-jets processes dominate in regions with one and two b-jets. Subdominant backgrounds come from single-top production and W+jets events. Simulated samples are used to model all background processes, and a data-driven kinematic reweighting is applied to $t\bar{t}$+jets, Wt and W/Z+jets events to correct for known mismodelings in these processes. These pre-corrected samples are used to build the background hypothesis in the likelihood fit.

OSML analysis

This analysis searches for single production of vector-like top partners decaying via $T \to Zt$, with a subsequent $Z \to \ell\ell$ decay. The search is conducted in events with at least two same-flavored electrons or muons of opposite-signed charge (OSSF) consistent with originating from a Z boson decay. The analysis is published in Ref. [128].

Events are required to pass at least one of the single-lepton triggers. Triggers with a p_{T} threshold of 20 GeV (26 GeV) in 2015 (2016–2018) for isolated muons are combined in logical OR with triggers with a 50 GeV p_{T} threshold for muons with no isolation requirement. A complementary barrel region only trigger with a 60 GeV p_{T} threshold is added for the 2017–2018 data-taking period. Similarly, electron triggers with isolation and identification requirements and p_{T} thresholds of 24–26 GeV are combined with triggers with higher p_{T} thresholds between 120 GeV and 140 GeV that require no isolation and less restrictive identification criteria.

The analysis is divided into two orthogonal channels which are statistically combined to obtain the final result: a channel with exactly two leptons (dilep-

[1] The effective mass is defined as the scalar sum of central small-R jets, leptons, and the $E_{\mathrm{T}}^{\mathrm{miss}}$ in the event.

ton) and an orthogonal channel with at least three leptons (trilepton). The trilepton channel has higher signal purity. Both channels require a preselection that includes a pair of OSSF leptons with an invariant mass within a 10 GeV window of the Z-boson mass. The dilepton preselection additionally requires at least one vRC jet, the Z-boson candidate to have $p_{\mathrm{T}} > 200\,\mathrm{GeV}$ and the scalar sum of the p_{T} of jets in the event, H_{T} being larger than 300 GeV. $Z+$jets events are the dominant background for this channel, with minor contributions from $t\bar{t}$ and diboson processes. Three CRs, two VRs, and one SR are defined according to the number of forward, b-tagged, and top-tagged/vetoed jets in the events. On the other hand, the trilepton preselection requires the presence of at least two central jets in the event. The presence of a third lepton that do not comprise the Z-boson candidate lead to a higher contamination from diboson and $t\bar{t}+Z$ events, with smaller contributions from $t\bar{t}+W$ and $t\bar{t}t\bar{t}$. Three CRs, one VR, and one SR are defined based on cuts on the number of forward and b-tagged jets, $\Delta\phi$ between the Z-boson candidate and the third lepton, and $\Delta\phi$ between the Z-boson candidate and the leading b-tagged jet.

An estimate for the contribution of the SM background is taken from MC simulation and controlled by signal-depleted categories that participate in a simultaneous likelihood fit to the data. The leading background in the dilepton channel comes from Z boson production in association with jets, while diboson processes and $t\bar{t}$ in association with a vector boson dominate the background composition in the trilepton channel. Each channel derives event-by-event reweighting factors at the preselection regions to correct for data/MC mismatch. The inputs to the statistical fit are binned distributions of the transverse momentum of the leptonic Z candidate.

7.2 Combination strategy: fit setup and systematics treatment

A combined likelihood function is constructed as a product of Poisson probability terms over all bins considered in each analysis. Similarly to the individual fits, the parameter of interest in the combined fit is the signal strength, μ. But in the combined fit, μ scales the total cross-section of the four production modes considered: WTZt, ZTZt, WTHt and ZTHt. Systematic uncertainties are implemented as NPs with constraints described by Gaussian distributions. Despite some experimental systematic uncertainties being common among the three searches, different sources of systematic uncertainties are considered, corresponding to alternative reconstruction algorithms, different background contributions and the type of objects considered in the final state.

Although the three searches explore different phase spaces, the dominant backgrounds are $t\bar{t}$ (and $t\bar{t}V$), $Z/W+$jets and VV production. Each analysis

applies a different background treatment. While the HtZt analysis apply a reweighting on their main MC background samples prior to the fit, the Monotop and Osml analyses estimate some NFs during the fit minimization. Thus, the NFs and modeling uncertainties are considered to be uncorrelated for the combination, even when these refer to the same background process. Correlating these parameters would propagate constraints between phase spaces without controling the effect on the more signal-enriched regions.

Reconstruction uncertainties are applied to both signal and background samples. These include systematics pertaining to the lepton measurement and identification, missing transverse momentum measurement, and jet-related quantities. The correlations among analyses are considered when the object reconstruction and selection criteria are compatible. The $E_{\mathrm{T}}^{\mathrm{miss}}$ reconstruction is a common source of systematic uncertainties in the three analyses. This is dominated by the soft-term systematics, related to the p_{T}-scale and its energy resolution. While no lepton-related systematics are considered in the Monotop analysis, since a veto on leptons is applied, these are correlated for the HtZt and Osml analyses. The jet reconstruction described in Section 5.2 is very similar among the three analyses but some of the associated systematic uncertainties are taken as uncorrelated:

- Different uncertainty configurations are used for the JER uncertainties. The Monotop analysis uses a more detailed scheme (FullJER), in which the JER smears both (pseudo-)data and MC as appropriate. The corresponding NPs are uncorrelated from those used in the other analyses, which only smear the MC (SimpleJER). It was decided to decorrelate these different sets of NPs as a conservative approach, but no impact has been observed on the combination result coming from this choice.

- The JMR uncertainties are uncorrelated between the Monotop and HtZt analyses, as the former uses the NPs recommended for Run 2 related to large-R jets, while the latter applies a 20% flat uncertainty to the mass resolution of small-R jets[2]. The Osml analysis does not use JMR uncertainties.

- The JES uncertainties are partially correlated for small-radius jets and large-radius jets. This is implemented via a set of NPs, a subset of which are common to both types of jets, while other NPs in the set apply only to one of the two types of jets. Most of these NPs are correlated among the three analyses, except some related to large-radius jets that are only considered in the Monotop channel.

[2]Such systematic is a conservative flat uncertainty applied by the HtZt analysis when no recommendations on JMR systematics were available.

Furthermore, the HtZt analysis uses track-based jets for the b-tagging implementation. This leads to uncorrelated systematic uncertainties between this channel and the other two, which took identical implementations for b-tagging. However, the Osml channel considers additional NPs related to c- and light-flavor jets. A summary of the correlation scheme for the systematic uncertainties is shown in Table 7.2.

Category	**Monotop**	**HtZt**	**Osml**	**Correlating**
E_T^{miss} uncertainties				
$E_{\mathrm{T}}^{\mathrm{miss}}$	✓	✓	✓	All
Lepton uncertainties				
Electron		✓	✓	All
Muon		✓	✓	All
Jet uncertainties				
JES	✓	✓	✓	All
JER	✓	✓	✓	HtZt and Osml
JMS		✓		None
JMR	✓	✓		None
Tagging uncertainties				
Flavor-tagging	✓	✓	✓	Monotop and Osml
Top-tagging	✓			None
Theory uncertainties (constrained)				
Background modeling	✓	✓	✓	None
Background normalization factors (unconstrained)				
$t\bar{t}$	✓			None
V+jets	✓			None
Z+light-jets			✓	None
Z+heavy-flavor			✓	None
$t\bar{t}V$			✓	None
VV			✓	None

Table 7.2: Summary of the correlation scheme of the systematic uncertainties and normalization factors included in the combined likelihood fit. A ✓indicates the uncertainty is included in a specific channel, with the last column specifying the correlations. The normalizations of the largest backgrounds in the HtZt analysis are constrained with nuisance parameters subject to Gaussian constraints.

7.3 Results from the statistical combination

The different analyses provided the binned histograms to be fitted as files in RooWorkspace format, which were built using the `TRexFitter` [266] framework. These files contain all the information needed to build the combined

likelihood, which is constructed as a product of the likelihood functions of the individual analyses with the correlated NPs accounted for as required. The combination is performed using the `workspaceCombiner` [267] tool, and all the fits are performed using the `quickFit` tool, which is based on the `RooFit` [264] and `RooStats` [265] frameworks.

This section presents the results following the same order as in Chapter 6. First, the background-only hypothesis is tested, for which the likelihood is maximized with respect to all NPs and NFs, but setting the signal strength to zero. This allows to study the behavior of the fit parameters and to estimate the background modeling in the whole phase space, at the same time that the compatibility of the data with the background-only hypothesis is measured. Subsequently, the signal-plus-background hypothesis is considered introducing the signal strength as a free-floated parameter. The signal sample includes the four production modes (WTZt, ZTZt, WTHt and ZTHt) along the three combined channels, with each mode normalized to its relative contribution[3]. Finally, in the absence of a significant excess, the observed and expected upper limits on the cross-section at 95% CL is computed for each m_T and κ_T values, assuming either the singlet or doublet scenario. Results are interpreted just for those m_T and κ_T values for which the relative decay width Γ_T/m_T is below 0.5. In addition, it is possible to generalize the results to any branching ratio (or relative coupling) value of the top quark decaying to Wb, which take a fixed value of 0.5 (0.0) in the singlet (doublet) scenario.

7.3.1 Background-only fit

Table 7.3 shows the best fit values of the different NFs free-floated in the background-only fit for the individual channels, as well as the comparison with the combined fit. Two of them correspond to the Monotop channel, in which the $t\bar{t}$ and $V+$jets normalizations are determined by the fit, and the rest correspond to the Osml analysis. The Osml channel with 2 leptons in the final state considers two NFs for the $Z+$jets production with ligth- or heavy-flavor jets, while the 3 lepton channel includes two NFs to account for the $t\bar{t}V$ and VV processes. Instead, the HtZt analysis applied a data-driven technique and a reweighting procedure to estimate the main backgrounds, not including any NFs in the fit. The values of these NFs are compatible between the individual and combined fits, showing an excellent agreement with the results obtained in the different analyses.

The values of the NPs at post-fit level are shown in Figure 7.2 for the electron, muon and jet reconstruction uncertainties, including the flavor tagging

[3]The signal sample has been normalized such that the four production modes sum up a total cross-section of 0.1 pb. The arbitrary normalization of the signal at pre-fit level does not affect the cross-section exclusion limits.

Norm. factor	Combined	Monotop	HtZt	Osml
$NF_{t\bar{t}}$	$0.84^{+0.21}_{-0.21}$	$0.83^{+0.18}_{-0.18}$	—	—
$NF_{V+\text{jets}}$	$0.70^{+0.14}_{-0.14}$	$0.70^{+0.15}_{-0.15}$	—	—
NF_{2lZhf}	$1.09^{+0.13}_{-0.13}$	—	—	$1.09^{+0.13}_{-0.13}$
NF_{2lZlf}	$0.94^{+0.10}_{-0.10}$	—	—	$0.94^{+0.10}_{-0.10}$
NF_{3lVV}	$0.99^{+0.19}_{-0.19}$	—	—	$0.99^{+0.19}_{-0.19}$
$NF_{3lt\bar{t}V}$	$1.19^{+0.36}_{-0.36}$	—	—	$1.19^{+0.36}_{-0.36}$

Table 7.3: Best fit values of the normalization factors from the background-only fit in the individual channels and in the combined fit.

and other associated experimental uncertainties. Figure 7.3 shows the pulls on the NPs associated with the background modeling for the HtZt, Monotop and Osml analyses. The pulls and constraints of the NPs after the combined fit are dominated by the strongest constraints observed in the fits from the individual channels. If a pulled or constrained NP is correlated among different analyses, as it is the case for some of the experimental uncertainties (see Table 7.2), the pull or constraint will be propagated to the other regions of the phase space, potentially altering other correlated parameteres and producing additional pulls and constraints that are not present in the individual fits. However, such effects are not observed and the behavior observed in the NPs is consistent with the results obtained in the individual fits. In addition, pulls of the same NP in opposite directions for different channels tend to compensate each other, leading to a reduced pull in the combined fit. A good example of this is the "JET_EtaIntercalibration_Modeling" uncertainty, as shown in Figure 7.2a.

The pulls of all the NPs are contained within $\pm 1\sigma$ of the pre-fit uncertainties. The only exception of this is one modeling uncertainty in the HtZt channel ("SPT_HTZT_TTBARLIGHT_PS_HJ_g2boost" in Figure 7.3a). This pull was studied in detail and found to be consistent with a statistical fluctuation in low-statistics bins. The constraints of the NPs are also compatible with the individual analysis, including the JMR uncertainty of small-R jets corresponding to the HtZt channel ("JET_JMR" in Figure 7.2a). This systematic uncertainty is strongly constrained for both the individual and combined fits, which is explained by two reasons. First, as explained in the previous section, the HtZt analysis applied a conservative prior 20% flat uncertainty to the mass resolution of small-R jets. Second, the HtZt analysis defines several

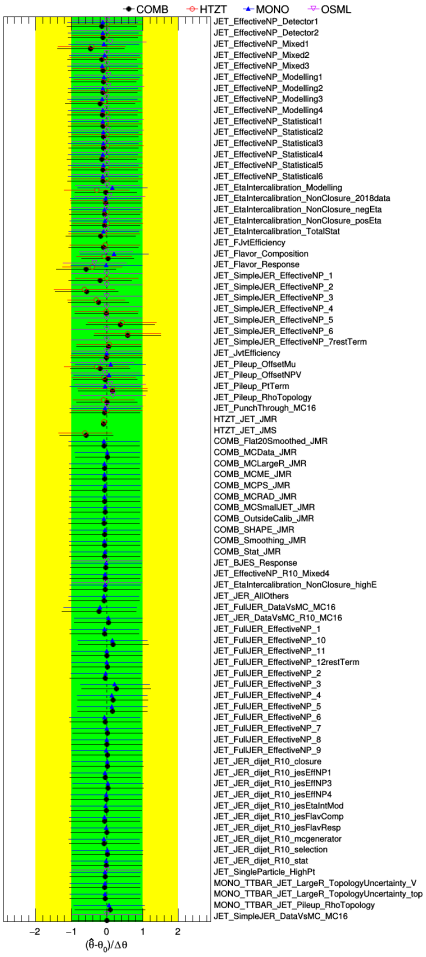

(a) Jets

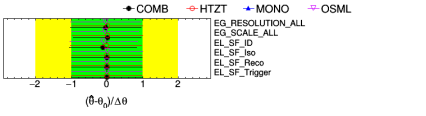

(b) Electrons

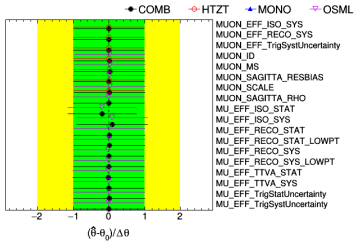

(c) Muons

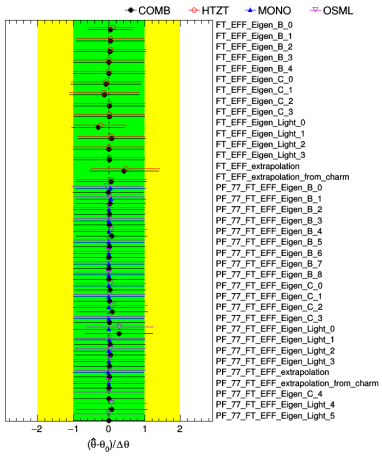

(d) Flavor tagging

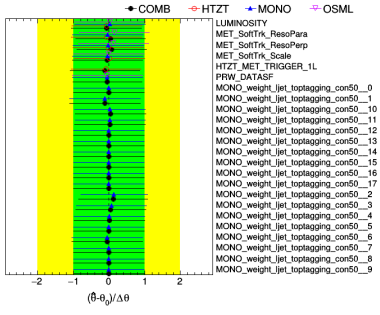

(e) Others

Figure 7.2: Pulls and constraints of the NPs associated with experimental uncertainties. The HtZt, Monotop, and Osml channels are shown in red, blue and pink, respectively, while the combined fit is shown in black.

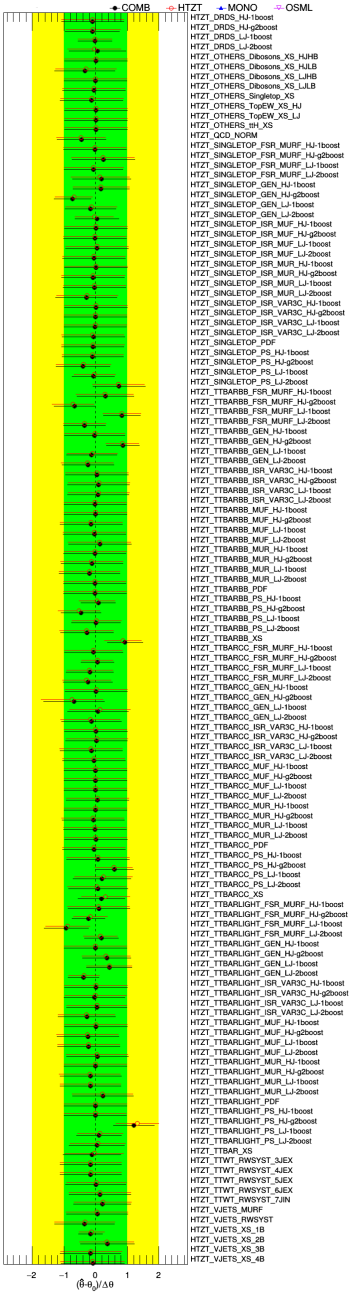

(a) HtZt

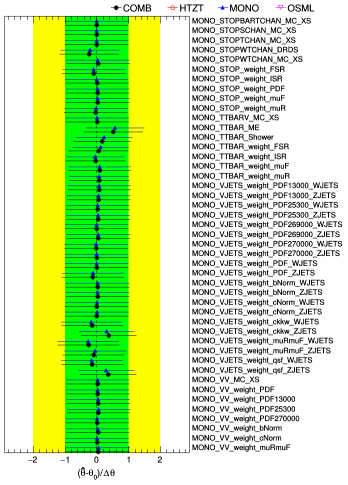

(b) Monotop

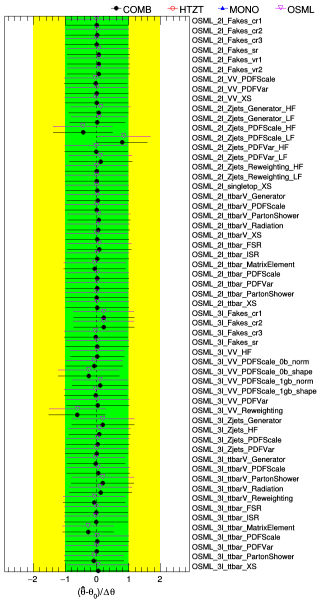

(c) Osml

Figure 7.3: Pulls and constraints of the NPs associated with background modeling for each analysis.

signal regions according to the multiplicity of boosted hadronic objects. Since the boosted object tagging is primarily based on the mass of the reclustered jets, the overestimated pre-fit JMR systematic is heavily constrained in the fit.

7.3.2 Signal-plus-background fit

Since no significant excess is being observed along the whole phase space, a signal-plus-background fit should provide a signal strength that is compatible with zero. The signal samples contain the four production modes considered in these searches: WTZt, ZTZt, WTHt and ZTHt, each of them normalized to their relative contributions.

The NFs and NPs are also fitted in the signal-plus-background fit, allowing new correlations to appear between the signal strength and the rest of the fit parameters. The behavior of the NFs and NPs is consistent with the background-only fit presented previously. The more relevant correlations in the combined fit are those observed from the individual fits, meaning that no important correlations among systematics uncertainties from different channels appear.

Figure 7.4 shows the ranking of the 10 most-impactful parameters on the signal strength. These rankings correspond to the combined fits assuming benchmark signal points for both the singlet and doublet scenarios, with $m_T = 1600$ GeV and $\kappa_T = 0.5$. The ranking of NPs is coherent with respect to the individual analyses. The most important uncertainties in the channel that has the best sensitivity to a given SU(2) multiplet interpretation tend to be ranked highest in the combination fit for that signal scenario. Thus, the $Z+$jets modeling uncertainties from the Monotop and Osml analyses and the $t\bar{t}$ ME uncertainty from the Monotop analysis are ranked highest for the singlet scenario. The branching ratio of the $T \to Ht$ decay mode, only considered by the HtZt analysis, is twice as large for the doublet representation of the T-quark than for the singlet. Consequently, the relative importance of the uncertainties related to multi-b final states in the HtZt channel is also higher. The highest ranked uncertainties for this scenario are the modeling uncertainties on the $t\bar{t}+ \geq 1b$ backgrounds from the HtZt analysis.

The fact that the best fitted value of the signal strength $\hat{\mu}$ is compatible with zero does not necessarily mean that no signal is present in the data. It could be possible that the data are not sensitive enough to observe it since its cross-section is below the sensitivity of the analysis. As explained in Section 6.4, the p_0-value can quantify the compatibility of the best-fitted signal strength $\hat{\mu}$ with the background-only hypothesis for a given data. Scanning across the m_T and κ_T parameters, the most significant p_0-value of 0.14 (0.10) for the SU(2) singlet (doublet) interpretation is found for the signal point $m_T = 2.1$ TeV and $\kappa_T = 0.1$.

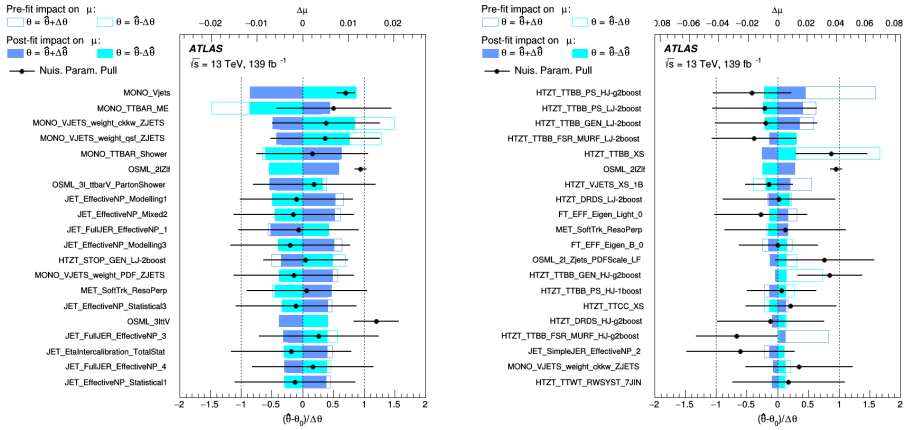

(a) (b)

Figure 7.4: Ranking of NPs based on their impact on the parameter of interest for the (a) singlet and (b) doublet interpretations. The fit is being performed on real data. The benchmark signal point is being considered, with $M_T = 1600$ GeV and $\kappa_T = 0.5$.

7.3.3 Exclusion limits on the signal model

Once the data and the background prediction have been compared and the signal-plus-background hypothesis has been studied, upper limits on the total cross-section[4] are obtained to evaluate the sensitivity of the analysis. The expected (observed) upper limits on the cross-section provide the maximum cross-section of the signal that is compatible with the background-only prediction (data), which will be computed for each m_T and κ_T point, assuming both the SU(2) singlet and doublet scenarios.

Mass scan of cross-section limits

The exclusion limits on the cross-section can be translated into exclusion limits on the parameters of the signal model. Figure 7.5 shows the observed (solid black line) and expected (dashed black line) 95% CL upper limits on the total cross-section $\sigma(pp \to T \to Ht/Zt)$ as a function of m_T in the SU(2) singlet representation assuming 7.5a $\kappa_T = 0.3$ and 7.5b $\kappa_T = 0.5$. The upper limits have been computed every 100 GeV, and the excluded range of T-quark masses correspond to the m_T values for which the upper limit on the cross-section is lower than the theoretical prediction (red line). The expected upper limits of

[4] According to Eq. 6.11, the upper limits on the signal strength are multiplied by 0.1 pb, which is the scaled value of the cross-section of the signal samples used in the fitted histograms.

the individual analyses are also shown. The HtZt analysis (blue dotted line) is only included in the limit calculation up to $m_T < 2.1$ TeV, since no signal samples were available for higher masses in this channel. Therefore, the combined limit for $m_T > 2.1$ TeV is driven by the Monotop and Osml analyses. Figure 7.6 shows the upper limits for the SU(2) doublet representation. The line corresponding to the Monotop analysis is not shown due to its very low sensitivity in this scenario, but the Monotop channel is included in the combined upper limit calculations for completeness.

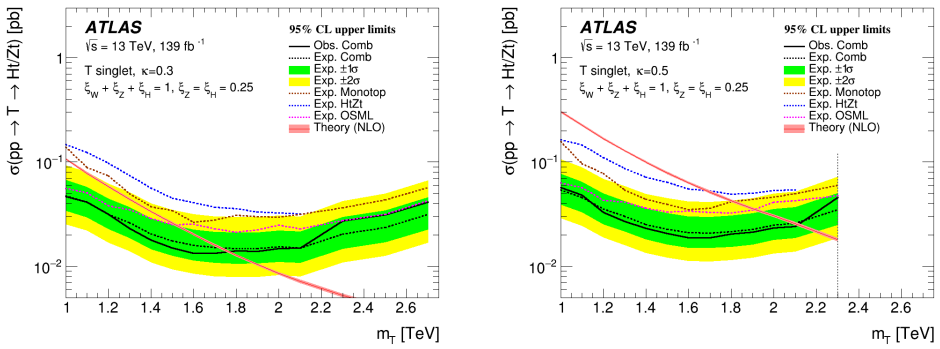

(a) (b)

Figure 7.5: Observed (solid line) and expected (dashed line) 95% CL upper limits on the total cross-section $\sigma(pp \to T \to Ht/Zt)$ as a function of T-quark mass in the SU(2) singlet representation assuming (a) $\kappa_T = 0.3$ and (b) $\kappa_T = 0.5$.The green and yellow bands correspond respectively to 1 and 2 standard deviations around the expected limit. A vertical dashed line is drawn to indicate the lower edge of the region with $\Gamma_T/m_T > 50\%$ for which the theoretical calculations are no longer valid. The expected limits for the individual analyses are shown. The HtZt analysis is only included in the limit calculation for $m_T < 2.1$ TeV. The red line shows the NLO theoretical cross-section prediction, with the surrounding shaded band representing the corresponding uncertainty.

The small shaded area around the red line corresponds to the uncertainty of the theoretical prediction, which comes from a change in the dynamic scale of the signal generation with MadGraph5_aMC@NLO. Such uncertainty is not included in the calculation of the upper limits. Since the theoretical calculations are valid for values of the relative decay width Γ_T/m_T lower than 50%, there are some higher m_T values for which the results are not shown. The $\Gamma_T/m_T = 50\%$ boundary, indicated with the vertical dashed line, is extended to lower masses for higher κ_T values because the relative decay width scales as $\Gamma_T/m_T \propto m_T^2 \kappa_T^2$.

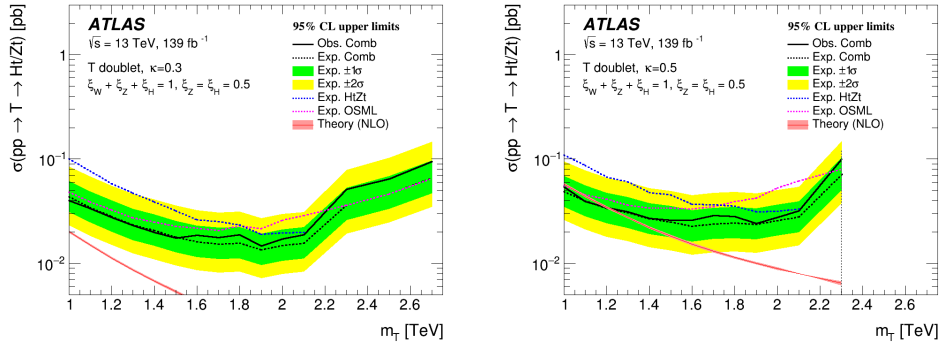

(a) (b)

Figure 7.6: Observed (solid line) and expected (dashed line) 95% CL upper limits on the total cross-section $\sigma(pp \to T \to Ht/Zt)$ as a function of T-quark mass in the SU(2) doublet representation assuming (a) $\kappa_T = 0.3$ and (b) $\kappa_T = 0.5$. The green and yellow bands correspond respectively to 1 and 2 standard deviations around the expected limit. A vertical dashed line is drawn to indicate the lower edge of the region with $\Gamma_T/m_T > 50\%$ for which the theoretical calculations are no longer valid. The expected limits for HtZt and Osml analyses are shown; the Monotop analysis is not shown due to substantially less sensitivity in this scenario. However, the Monotop analysis is included in the combined limit calculation. The HtZt analysis is only included in the limit calculation for $m_T < 2.1$ TeV. The red line shows the NLO theoretical cross-section prediction, with the surrounding shaded band representing the corresponding uncertainty.

The complementarity of the different analysis channels is also evident in Figures 7.5 and 7.6. For example, the Osml analysis is most sensitive at low masses, while the sensitivity of the HtZt analysis can be seen to improve at higher masses. This is especially true in the SU(2) doublet representation, as the HtZt analysis includes signal regions that are specifically designed to target Z-mediated production processes. In the Osml analysis, the degradation of the cross-section limit above 2.1 TeV is due to the choice of binning of the discriminant (the reconstructed Z boson p_{T}), which was optimized to search for T-quarks with masses less than 2.0 TeV.

The results show that the most stringent limits are obtained for the SU(2) singlet representation, excluding masses of the T-quark up to 1.8 (2.1) TeV for $\kappa_T = 0.3(0.5)$ at 95% CL. For the SU(2) doublet representation, masses up to 1.2 TeV for $\kappa_T = 0.5$ are excluded at 95% CL, but no masses are excluded in the explored range for $\kappa_T = 0.3$. In both scenarios, the combination of the three analyses improves the sensitivity to the signal model, providing more stringent

limits than the individual analyses. The upper limit on the cross-section is improved by approximately a factor 2 in the singlet scenario, extending the excluded mass range by 200 GeV. The excluded mass range is also extended by 100 GeV in the doublet scenario.

Two-dimensional limit maps

Exclusion limits can be set simultaneously to the m_T and κ_T parameters by computing the upper limit on the cross-section for every point in the (m_T,κ_T) plane[5]. Figures 7.7 and 7.8 show in the z-axis the observed and expected upper limits on the cross-section for the SU(2) singlet and doublet representations, respectively. The observed (expected) exclusion contours are shown as white solid (dashed) lines, corresponding to the m_T and κ_T values for which the observed (expected) upper limit on the cross-section is equal to the theoretical prediction. The area above the dashed black line correspond to the region where $\Gamma_T/m_T > 0.5$, in which the theoretical calculations are no longer valid.

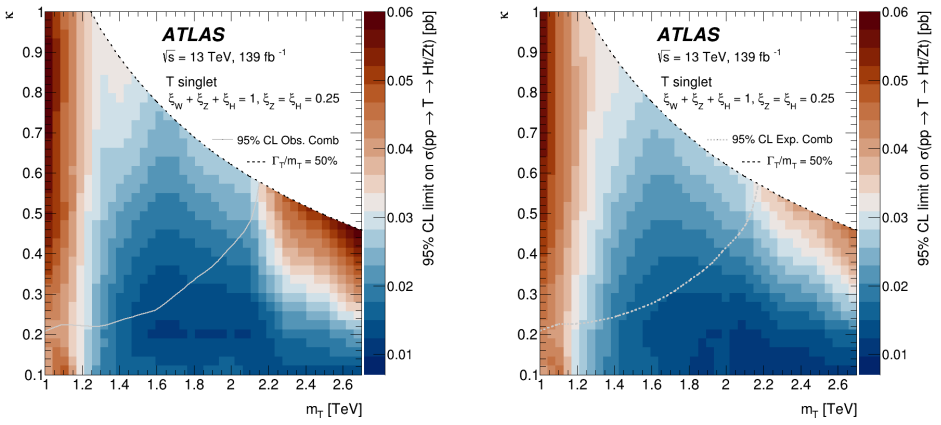

(a) (b)

Figure 7.7: (a) Observed and (b) expected 95% CL exclusion limits on the total cross-section $\sigma(pp \to T \to Ht/Zt)$ as a function of the universal coupling constant κ_T and the T-quark mass in the SU(2) singlet representation. All values of κ_T above the white contour line are excluded at each mass point. Limits are only presented in the regime $\Gamma_T/m_T < 50\%$, where the theory calculations are known to be valid.

[5]However, the number of points in the grid is finite, and the limits are interpolated using a piecewise function [268] to obtain a continuous shape for the exclusion contours in the (m_T,κ_T) plane.

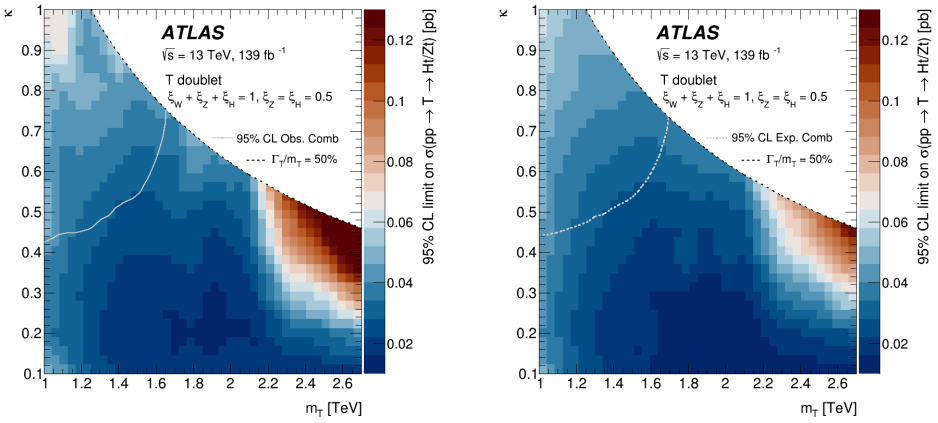

(a) (b)

Figure 7.8: (a) Observed and (b) expected 95% CL exclusion limits on the total cross-section $\sigma(pp \to T \to Ht/Zt)$ as a function of the universal coupling constant κ_T and the T-quark mass in the SU(2) doublet representation. All values of κ_T above the white contour line are excluded at each mass point. Limits are only presented in the regime $\Gamma_T/m_T < 50\%$, where the theory calculations are known to be valid.

In the SU(2) singlet representation, the coupling parameter κ_T is excluded above 0.2 for a T-quark mass of 1.0 TeV, increasing to 0.5 for a mass of 2.1 TeV. The cross-section is constrained to be below 18 fb for masses in the range of 1.4–2.1 TeV and $\kappa_T = 0.3$ for the SU(2) singlet representation. Similarly, in the SU(2) doublet representation, the coupling parameter κ_T is constrained up to 0.4 for a mass of 1.0 TeV, increasing to 0.7 for a mass of 1.7 TeV. The cross-section is constrained to be below 20 fb for masses in the range of 1.4–2.1 TeV and $\kappa_T = 0.5$ in the SU(2) doublet representation. In both the SU(2) singlet and doublet representations, the observed cross-section limits are slightly higher than the expected cross-section limits for $\kappa_T = 0.3$ and 0.5 for $m_T > 2.2$ TeV.

Figure 7.9 overlays the observed and expected exclusion contours for the combination of the three analyses, for both the SU(2) singlet (a) and doublet (b) representations. The expected exclusion contours for the individual channels are also shown for comparison. The combination of the three searches significantly improves the exclusion limits from the individual channels, with an increase of around 200 GeV on the m_T exclusion with respect to the best-performing channel for both the singlet and doublet representations. The lowest excluded κ_T is reduced with the combination by 1.5 units for large masses

around 2 TeV in the singlet scenario and around 1.5 TeV in the doublet scenario. The improvement is less significant for lower masses, where the OSML analysis is considerably more sensitive.

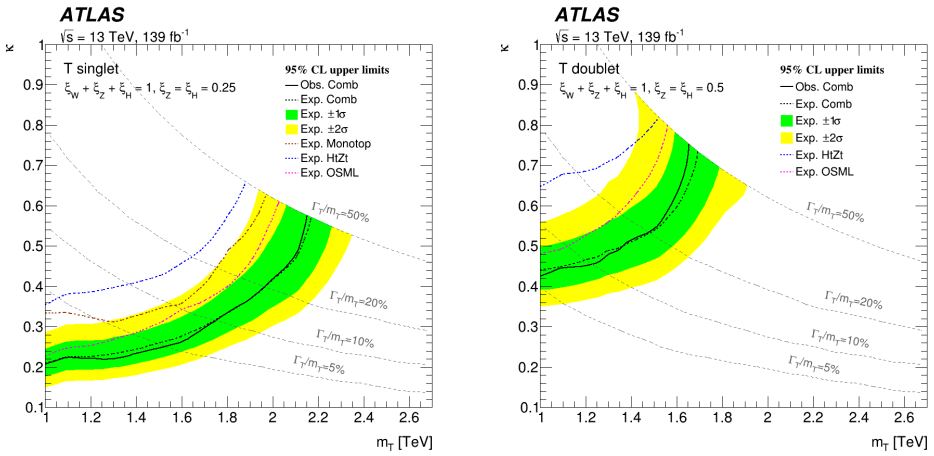

(a) (b)

Figure 7.9: Observed (solid line) and expected (dashed line) 95% CL exclusion limits on the universal coupling constant κ_T as a function of the T-quark mass in the (a) SU(2) singlet and (b) SU(2) doublet representations for the combination. All values of κ_T above the black contour lines are excluded at each mass point. The colored bands correspond to 1 and 2 standard deviations around the expected limit. Also shown are the expected limits for the individual analyses. The gray dashed lines represent configurations of (m_T, κ_T) resulting in equal values of the relative resonance width Γ_T/m_T. Limits are only presented in the regime $\Gamma_T/m_T < 50\%$, where the theory calculations are known to be valid.

Isolines of the relative decay width of the T-quark $\Gamma_T/m_T \propto m_T^2\kappa_T^2$ are shown in Figure 7.9, which are represented by the grey dashed lines. This plane could be inverted to obtain the exclusion limits in the (m_T,Γ_T/m_T) plane, such as the one shown in Figure 2.13. Such a correspondence is calculated from the intersection of the exclusion contours with the isolines. Table 7.4 summarizes the observed and expected mass limits for the SU(2) singlet ($\xi_W = 0.5$) and doublet ($\xi_W = 0.0$) representations for benchmark values of the relative decay width Γ_T/m_T.

The exclusion limits can be generalized for arbitrary values of the relative coupling ξ_W, which correspond to the relative branching ratio of the T-quark decaying into the W boson in the limit of large masses (> 1 TeV). Figure 7.10 shows the observed and expected exclusion limits at 95% CL on the T-quark

Representation	Γ_T/m_T [%]	Obs./Exp. mass limit [TeV]
SU(2) singlet ($\xi_W = 0.5$)	20	2.0 / 2.0
SU(2) singlet ($\xi_W = 0.5$)	50	2.1 / 2.1
SU(2) doublet ($\xi_W = 0.0$)	20	1.4 / 1.4
SU(2) doublet ($\xi_W = 0.0$)	50	1.6 / 1.7

Table 7.4: Summary of mass limits for SU(2) singlet and doublet representations with varying Γ_T/m_T ratios. Both observed (Obs.) and expected (Exp.) limits are presented.

mass as a function of the relative resonance width Γ_T/m_T and the relative coupling parameter ξ_W. As it was explained in Chapter 2, the theoretical assumptions $\xi_Z = \xi_W$ (Goldstone equivalence) and $\xi_Z = \xi_H = 1 - \xi_W$ are considered. For $\xi_W = 0.5$ (SU(2) singlet), the most stringent limits are obtained since this scenario allows the Z- and W-mediated production modes at the same time that the decays of the T-quark into Zt and Ht correspond to a 50% of the total branching ratio. For $\xi_W = 0.0$ (SU(2) doublet), only the Z-mediated production mode is allowed, and for ξ_W approaching to 1, the decays of the T-quark into Zt and Ht are suppressed, which results in a complete loss of acceptance in these channels.

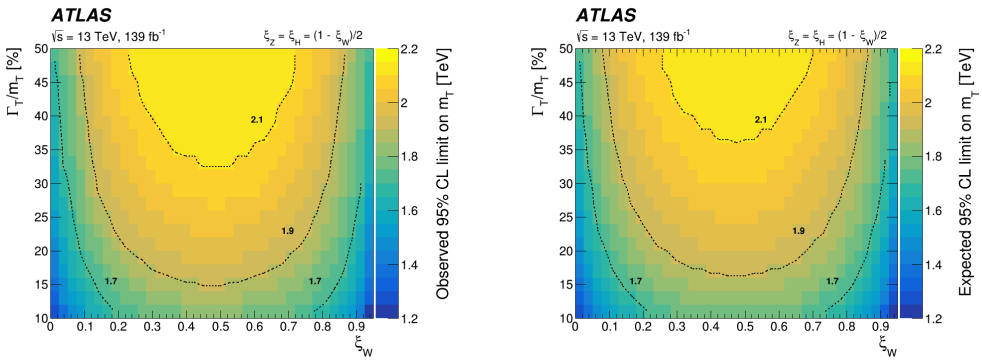

(a) (b)

Figure 7.10: (a) Observed and (b) expected upper limits at 95% CL on the T-quark mass as a function of the relative resonance width (Γ_T/m_T) and the relative coupling parameter ξ_W, for the assumption $\xi_Z = \xi_W$. The values $\xi_W = 0.5$ and $\xi_W = 0.0$ correspond to the SU(2) singlet and SU(2) doublet representations, respectively. The dashed contour lines denote exclusion limits of equal mass in units of TeV.

Chapter 8

Anomaly detection

Motivated by the limitations of the SM described in the first two chapters of this thesis, a huge effort has been dedicated to the search for new physics by the HEP experiments. Many of these searches have been integrating ML techniques into the analysis chain, increasing their sensitivity to specific new physics processes and defining optimal signal-enriched regions. Thus, a classifier learns to discriminate signal against background simulated events following a "supervised" training. Some of the most common classifiers used in the LHC experiments are based on Deep Neural Networks (DNNs) and BDTs. Despite the development of sophisticated classifiers and the large amount of data analyzed along thousands of searches, no significant evidence of new physics has been observed so far. This model-specific search strategy assisted by supervised ML techniques seems no longer to be the most efficient approach to search for new physics, forcing the HEP community to explore different strategies.

This chapter presents a study that is published in Ref. [3], which explores different methods to transform cutting-edge classifiers into anomaly detectors with minimal tuning. The chapter is structured as follows: Section 8.1 introduces the concept of anomaly detection (AD) and its relevance in the context of the LHC. Section 8.2 describes the benchmark dataset provided by the Dark Machines Anomaly Score Challenge, which is used in this study. Section 8.3.1 presents the architectures used in this work and Section 8.3.2 describes the AD techniques employed to transform the classifiers into anomaly detectors. Finally, Section 8.4 presents the results of the study, including a comparison of the performance of different architectures and techniques.

8.1 Anomaly detection at the LHC

In this context, AD is emerging as a model-agnostic approach to search for new physics in the LHC experiments. AD does not target a specific signal model,

but rather looks for deviations or anomalies in the data. In fact, AD can be performed without ML techniques, but it is boosted with ML techniques in the same way it occurred in the model-dependent searches.

In the absence of a specific target signal model, a supervised training on a labeled dataset to discriminate signal (label 1) from background (label 0) is not possible. The new training techniques for AD mostly rely on the background simulation or the experimental data directly. Thus, "less-than-supervised" strategies emerge in this context, differing in the degree of supervision they require during training:

- Weakly supervised [269]: it makes use of noisy labels, meaning that the train data are not perfectly labeled. In these cases, prior domain knowledge allows to construct one set containing a low proportion of signal events and another set containing a high proportion of signal events. Then, a supervised training is performed to discriminate between the two sets. An example of this is the *Classification Without Labels (CWoLa) method* [270], which has been employed in the ATLAS experiment for *bump hunting* [271].

- Semi-supervised: the training learns from unlabeled events, but a certain amount of labeled data are exploited to guide the training and enhance the signal sensitivity.

- Unsupervised: the training is performed without any labeled data. The model learns the underlying structure of the train data and identifies anomalies based on deviations from this learned structure.

However, minimizing a loss function based on unlabeled experimental data, which may potentially contain new physics, brings some concerns. First, there is no guarantee that the model will identify the SM events present in the data as *normal* and the BSM events as *anomalies*. And second, it is difficult to assess whether a trained model performs better than other ones, as a priori there is no labeled data to compare with. Therefore, optimizing unsupervised AD techniques by training them on simulated background events is an extended option. Then, once the model is optimized, it can be evaluated on experimental data. This approach allows to learn the underlying structure of SM events, relying on the assumption that the experimental data are well described by the simulation. Instead, using simulated label events to train seems to fit better the "semi-supervised" category than the "unsupervised" one. Both namings can be found in the literature to refer to this approach, and the choice of one or

another depends on the authors rigor with the terminology[1]. Similarly, relying on simulated background events results in a SM-dependent search. But the important difference with respect to the traditional supervised strategies is to remain "signal-agnostic".

The LHC community has already been exploring the use of AD techniques to search for new physics. Both ATLAS and CMS have already completed several AD searches covering a large variety of BSM scenarios [271–275]. Additional search programs were also carried out to boost the development of new AD techniques in the context of the LHC experiments, such as the LHC Olympics [276] and the Dark Machines Anomaly Score Challenge [277].

8.2 The Dark Machines benchmark dataset

Dark Machines [278] is an international and open research collaboration of physicists, statisticians and data scientists. The Dark Machines initiative integrates the development of new ML techniques into different fields of HEP physics, such as astroparticle and collider physics. Focusing on the search for DM, this interdisciplinary program aims to provide benchmark datasets and techniques to orientate the efforts of the community towards well-defined goals. This study makes use of the dataset [279] provided for the Dark Machines Anomaly Score Challenge [277]. Unlike other benchmarks, such as the one provided for the LHC Olympics [276], this dataset contains the final state information of the events, after the reconstruction stage. This is the relevant information for AD in the context of new physics searches, such that it is not necessary to perform any additional reconstruction. In addition to SM processes, the dataset also includes several simulated BSM signals. This allows to assess the sensitivity of the trained models for discriminating phenomena for which dedicated supervised searches already exist. However, the performance of an unsupervised training can not be measured according to its sensitivity on a particular signal.

Event generation and simulation

Proton-proton collisions were simulated at a center-of-mass energy of 13 TeV. The hard scattering events were generated using MadGraph5_aMC@NLO version 2.7 [280]. The convolution of the parton-level ME with non-perturbative PDFs was performed using `LHAPDF6` where the NNPDF3.1LO [281] was set with $\alpha_S(M_Z^2) = 0.118$, using the 5 flavor scheme. For the PS, MadGraph was

[1] Since this work did not have access to experimental data, the training was necesarily performed on simulated background events and the "unsupervised" category is used to refer to the techniques that followed this approach. "Semi-supervised" will be refer when simulated signal events are used to guide the training (see Section 8.3.2).

interfaced to Pythia version 8.239 [282]. The matching of the matrix elements with different parton multiplicities to the PS algorithm was performed using the the MLM merging scheme [283] and a merging scale of $Q_0 = 30$ GeV. The effect of MPI and pile-up was not included in the event generation.

A fast detector simulation was performed using `Delphes` version 3.4.2 [284] with a modified ATLAS detector card [285], and jet clustering is performed with FastJet [286] using the anti-k_t algorithm with a jet radius of 0.4. Jets are b-tagged following a similar procedure to Ref. [287]. More details on the generation of the dataset can be found in Ref. [277].

Dataset description

The data samples contain the event-level information of the simulated collisions, where only the four-momentum of the reconstructed objects and the object-tagging are saved at each event. Seven different object types are considered: jet, b-jet, electron, positron, muon, anti-muon and photon. The minimum selection criteria applied on the final state objects are:

- Jet or b-jet: $p_T > 20$ GeV and $|\eta| < 2.8$.
- Lepton: $p_T > 15$ GeV and $|\eta| < 2.7$.
- Photon: $p_T > 20$ GeV and $|\eta| < 2.37$.

All events in the dataset fulfill at least one of the following requirements:

- At least one jet or b-jet with $p_T > 60$ GeV and $|\eta| < 2.8$.
- At least one electron with $p_T > 25$ GeV and $|\eta| < 2.47$, except for the crack region $1.37 < |\eta| < 1.52$.
- At least one muon with $p_T > 25$ GeV and $|\eta| < 2.7$.
- At least one photon with $p_T > 25$ GeV and $|\eta| < 2.37$.

These selection criteria are not realistic in terms of what LHC experiments can afford to record after the online data selection (trigger) system, but the goal of this dataset is to create a flexible sample with a general enough selection criteria. However, the η range of the objects is consistent with the restrictions applied by the ATLAS experiment. In addition to the previous requirements, the SM processes with the largest cross-section, $W/Z/\gamma$+jets and multi-jet production, are also required $H_T > 100$ GeV and $H_T > 600$ GeV, respectively[2].

In order to explore the sensitivity of the AD techniques along different event topologies, the Dark Machines dataset is divided into four channels, for

[2]Here, H_T is defined as the scalar sum of the transverse momenta of all jets.

which the additional requirements summarized in Table 8.1 are applied. The background processes passing the selection criteria of a particular channel are grouped into a single file. The event weight[3] is equal to 1 for all events, such that the number of events per process is proportional to its cross-section. Thus, the total number of SM events per channel is given by the considered luminosity: 7.8 fb^{-1}(214K), 309.6 fb^{-1}(20K), 7.8 fb^{-1}(340K) and 8.0 fb^{-1}(8.5M) for Channel 1, 2a, 2b and 3, respectively.

Selection Criteria	**Channel 1**	**Channel 2a**	**Channel 2b**	**Channel 3**
H_T [GeV]	≥ 600	-	≥ 50	≥ 600
E_T^{miss} [GeV]	≥ 200	≥ 50	≥ 50	≥ 100
E_T^{miss}/H_T	≥ 0.2	-	-	-
b-jets with $p_T > 50$ GeV	≥ 4	-	-	-
b-jet with $p_T > 200$ GeV	1	-	-	-
N^{lep} (with $p_T^{lep} > 15$ GeV)	-	≥ 3	≥ 2	-

Table 8.1: Selection criteria for the four Dark Machines channels.

Several BSM processes characterized by the production of DM candidates that escape the detector have been generated. These signal models are divided into two categories: exotic processes with a hypothetical Z' boson and SUSY processes with and without R-parity conservation. The signal processes are described as follows:

Z'+monojet [288–290]: a Z' boson with 2 TeV of mass is produced, decaying invisibly into a pair of Dirac DM particles with a 50 GeV mass, together with a jet coming from QCD radiation in the initial state.

$Z' + W/Z$ [288–290]: a Z' boson with 2 TeV of mass is produced, decaying invisibly into a pair of Dirac DM particles with a 50 GeV mass, together with an ISR W or Z boson.

Z'+single top [288–290]: a Z' boson with a 200 GeV mass is produced together with a top quark.

Z' lepton-violating $U(1)_{L_\mu - L_\tau}$ [291, 292]: a 50 GeV Z' boson decaying to leptons and neutrinos. Two samples are generated corresponding to 3 and 4 leptons in the final state.

SUSY R-parity violating stop-stop [293, 294]: pair production of 1 TeV supersymmetric stops decaying to leptons and b-quarks.

[3]The event weights of a particular process would be computed as $w = \sigma/N \times L$.

SUSY R-parity violating squark-squark [293, 294]: pair production of 1.4 TeV squarks decaying to neutralinos and quarks. Each 0.8 TeV neutralino decays into a pair of leptons and one neutrino.

SUSY gluino-gluino [295–297]: pair production of 1 TeV gluinos decaying to a pair of quarks and one stable neutralino that escapes the detector. Two samples are generated for different mass choices, one with 1.4 TeV gluinos and 1.1TeV neutralinos and another with 1.6 TeV gluinos and 0.8 TeV neutralinos.

SUSY stop-stop [295–297]: pair production of 1 TeV stops decaying to a top quark and a 0.3 TeV neutralino scaping the detector.

SUSY squark-squark [295–297]: pair production of 1.8 TeV squarks decaying to a quark and a 0.8 TeV stable neutralino.

SUSY chargino-neutralino [295–297]: charged-current production of a chargino and a neutralino. The chargino decays into a W boson and a stable neutralino. Two mass choices are generated: one with a 200 GeV chargino and a 50 GeV neutralino, and another with a 250 GeV chargino and a 150 GeV neutralino.

SUSY chargino-chargino [295–297]: neutral-current pair-production of charginos, each decaying into a W boson and a stable neutralino. Three mass choices are generated: a 300 GeV chargino and a 140 GeV neutralino, a 400 GeV chargino and a 60 GeV neutralino, and a 600 GeV chargino and a 200 GeV neutralino.

Table 8.2 lists the BSM processes considered in each channel. Channel 1 (38K BSM events) focuses on hadronic activity with significant missing energy, making it particularly sensitive to mono-jet dark matter signatures as well as colored SUSY signals. Both Channel 2a (11K BSM events) and Channel 2b (90K BSM events) reduce background by requiring the presence of leptons, thereby enhancing their sensitivity to electroweak signals, such as those from charginos and neutralinos. Finally, Channel 3 (1M BSM events) is designed to be more inclusive and captures most signals (except for the softer electroweak ones).

8.3 Turning optimal classifiers into anomaly detectors

This study [3] presents a method for transforming state-of-the-art supervised classifiers into effective anomaly detectors with only minimal modifications. As

BSM process	Channel 1	Channel 2a	Channel 2b	Channel 3
$Z' +$ monojet	×	×		×
$Z' + W/Z$				×
$Z' +$ single top	×			×
Z' in lepton-violating $U(1)_{L_\mu - L_\tau}$		×	×	
$\not{R}$-SUSY stop-stop	×		×	×
$\not{R}$-SUSY squark-squark	×			×
SUSY gluino-gluino	×	×	×	×
SUSY stop-stop	×			×
SUSY squark-squark	×			×
SUSY chargino-neutralino		×	×	
SUSY chargino-chargino			×	

Table 8.2: BSM processes considered in each analysis channel.

classifier architectures continue to evolve into more sophisticated models, such as graph networks and transformers, these advances can be leveraged for AD. The current lack of benchmark architectures for AD motivates reporpusing the best-performing supervised classifiers, potentially extending the applicability of AD across the analyses performed at the LHC with minimal additional cost.

Three AD techniques are studied with this purpose: DeepSVDD [298], Deep Robust One-Class Classification (DROCC) [299] and Discriminatory Detection of Distortions (DDD). Each technique transforms a supervised classifier into an anomaly detector without altering its core architecture or optimizing the hyperparameters. Three different architectures are used in combination with the previous three AD techniques. Two of these architectures are based on the Particle Transformer model (ParT) [300], and the third one is a basic multi-layer perceptron (MLP) that serves as baseline.

A detailed description of the architectures is provided in Subsection 8.3.1, followed by an overview of the AD techniques in Subsection 8.3.2. Finally, the results of the study are presented in Section 8.4.

8.3.1 Machine learning arquitectures

The classifiers based on the ParT model used for this study are cutting-edge classifiers taken from Ref. [301]. The MLP classifier is a simple yet effective architecture that serves as a benchmark for the performance of the more complex architectures. This comparison will be useful to evaluate if the greatest classifiers can be also the best anomaly detectors without further tuning.

Multi-Layer Perceptron

This MLP consists of two fully-connected hidden layers, with 16 and 8 neurons, respectively, and a final output layer with a single neuron. The non-linearity

is applied to the hidden layers, using the Rectified Linear Unit (ReLU) activation function, which sets negative values to zero and keeps positive values unchanged. In addition, each hidden layer is followed by a batch normalization layer to ensure that the data fed into the next layer is normalized. This helps to stabilise the learning process and improve convergence speed. Figure 8.1 illustrates an MLP with two hidden layers.

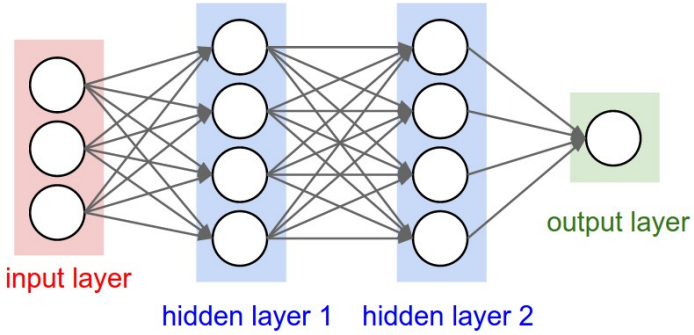

Figure 8.1: The architecture of the MLP model with two hidden layers.

Particle Transformer

The Particle Transformer (ParT) [300] is a transformer-based architecture designed for jet tagging, inspired by techniques from natural language processing [302]. Figure 8.2 shows the complex structure of the ParT algorithm [300], which was designed to learn the underlying structure of the data and to capture the correlations between the particle constituents inside jets. Analogously to the jet tagging application, the constituents of the jets can be replaced by the reconstructed objects in the event, such as leptons and jets, to train for event classification.

Two input sets are fed into the network: the four-momentum of the particles (or objects) in the event and the pairwise interaction variables. The logarithms of ΔR_{ij} and m_{ij}^2, were selected based on the work in Ref. [301]. Here, ΔR_{ij} measures the angular distance between two particles in the detector, and m_{ij}^2 is the invariant mass squared of two particles. The logarithm of these features is taken for better numerical handling and improved learning efficiency. Additionally, the missing transverse momentum and its azimuthal angle are provided later to the network through a dedicated fully-connected sub-network that is integrated into the original MLP at the last stage of the ParT architecture. In this way, the network can also learn event-level features as auxiliary information.

The ParT network is structured in three main stages: the embedding stage,

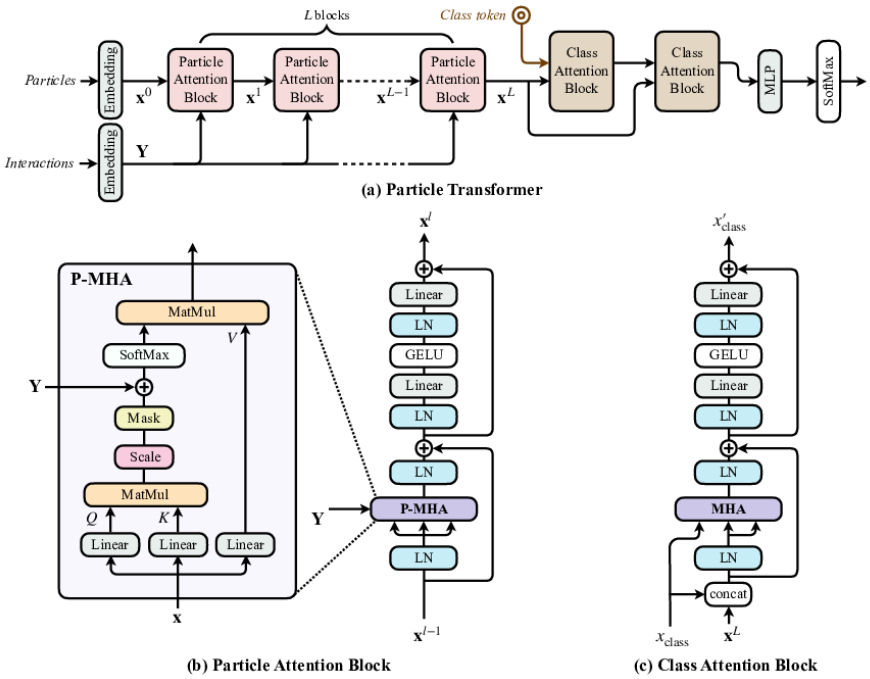

Figure 8.2: The architecture of (a) Particle Transformer, (b) Particle Attention Block and (c) Class Attention Block.

the particle attention blocks and the class attention blocks.

Embedding Stage: This is crucial for converting low-level kinematic and interaction details into a more abstract feature space, facilitating the learning of intricate dependencies in subsequent attention mechanisms. This is achieved through two distinct 3-layer MLPs, in which each layer applies the GELU[4] [303] activation function followed by batch normalization to ensure robust feature scaling.

Particle Attention Blocks: These are crucial for refining object-level representations by capturing complex inter-object correlations. Arranged sequentially in $L = 8$ layers, each block processes its input x^ℓ and is characterized by using a multi-head attention mechanism, expressed as:

$$\text{P-MHA}(Q, K, V) = \text{SoftMax}\left(\frac{QK^T}{\sqrt{d}} + \mathbf{U}\right)V, \tag{8.1}$$

[4]The Gaussian Error Linear Unit (GELU) is a stochastic activation function that weights the input by its cumulative distribution function.

where Q, K, and V are trainable d-dimensional linear transformations of the input $\mathbf{x}^{\ell}$. $\mathbf{U}$ is an interaction matrix that is added to emphasize significant pairwise interactions. The attention mechanism correlates every object with all others, allowing the model to handle varying numbers of objects and maintain permutation equivariance.

Class Attention Blocks: Similarly to the Particle Attention Blocks, two class attention blocks are used to enhance the attention on the object type or class. A total of $C = 7$ classes are considered: jets, b-jets, e^-, e^+, μ^-, μ^+ and γ. Here, the multi-head attention implemented is the standard one from Eq. 8.1 without an interaction matrix $\mathbf{U}$, and the input concatenates the class token x_{class} with the output of the Particle Attention Blocks x^L. The class attention blocks are designed to learn the correlations between different classes, allowing the model to focus on specific object types. The output of the Class Attention Blocks is then concatenated with the output of the Particle Attention Blocks and fed into a final MLP to produce the final classification label.

In summary, the attention mechanism serves to correlate each object with all others and is applicable to a variable numbers of particles. Although the self-attention mechanism itself is *equivariant* to permutations of the objects, its implementation within the Particle Transformer ensures *permutation-invariance* by treating the input as an unordered set and processing particle interactions based on their features, ensuring the output is unaffected by input order.

Particle Transformer with Standard Model couplings

As it was mentioned before, the ParT architecture can be extended to include additional pairwise features that encode physical information about the particles interactions. Thus, in addition to the logarithms of ΔR_{ij}, m_{ij}^2, a third pairwise feature makes use of the SM running couplings. This is added as an interaction matrix in which the entries indicate the strength of the interaction between particles, calculated using the running couplings of the strong, weak and electromagnetic forces. Such implementation of the ParT is named as ParT+SM [301]. This additional feature is expected to improve the performance in the AD task, as new physics signals may manifest as deviations from the SM interactions.

8.3.2 Anomaly detection techniques explored

The previously described architectures were originally developed for supervised classification tasks. This section presents three methods for adapting these architectures for AD. These are the DeepSVDD [298], DROCC [299] and DDD techniques. The first two methods are well-established techniques for AD, while

the DDD method is an original approach developed specifically for this work. The main goal of these methods is to transform a classifier into an anomaly detector without further hyperparameter optimization. The modifications rely on either changes in the datasets or adjustments to the loss function, except minor changes in the network structure when necessary. Table 8.3 summarizes the type of changes introduced by each of the three methods.

Method	Network	Loss Function	Dataset
DeepSVDD	✓	✓	
DROCC		✓	
DDD			✓

Table 8.3: Summary of the type of changes introduced by each AD method.

DeepSVDD: Deep Support Vector Data Description

DeepSVDD is recognized as a well-established method for AD [298, 304–306]. The DeepSVDD method was identified as one of the best performing methods in the Dark Machines challenge[277]. However, the use of complex architectures in combination with this technique remained unexplored.

DeepSVDD is a one-class classifier that maps the input features of an event into an output hyperspace and measures the euclidean distance to a particular point (or center) of this hyperspace. The training process corresponds to the minimization of the distance of the events from this center (loss function). Since the training is performed only on background events, the model learns to map these *normal* events into a hypersphere in the output space. Thus, events that deviate significantly from the center are classified as anomalies. Figure 8.3 illustrates how the DeepSVDD technique operates, showing the mapping of the input data into a hypersphere in the feature space.

There are infinite possibilities for the choice of a center in the output space, but the option taken in this study is proposed in Ref. [298]. The center is computed as the mean of the network representations that results from an initial forward pass on the training data. Removing all bias terms from the network is also needed to avoid the "sphere collapse" phenomena, in which the model predicts the output independently of the input. In addition to these considerations, not making use of dropout[5] has been shown to be a convenient approach, enhancing significantly the stability of the training.

In order to further improve the robustness of the predictions, separate models are trained with 2, 4, 8, and 16 output dimensions, respectively. The per-

[5]Dropout is a regularization technique that randomly sets a fraction of the neurons of a layer to zero during training, which helps to prevent overfitting.

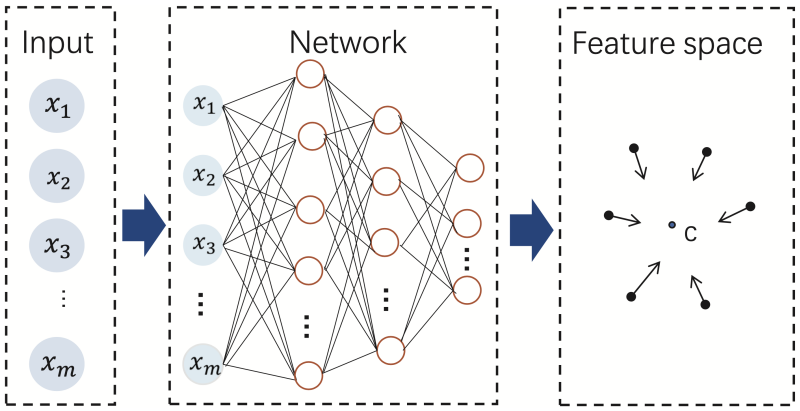

Figure 8.3: DeepSVDD architecture. The input data are processed by a neural network, which maps the data into a hypersphere in the feature space. The distance from the center of this hypersphere is used to determine if the input sample is an anomaly. Source [307].

event scores from these models are then combined to form an ensemble, as proposed in Ref. [304]. Taking the mean of the scores from the different models helps to reduce the variance and improve the overall performance of the technique. Any classifier can be transformed into an anomaly detector taking into account the considerations described above. The procedure is summarized in Algorithm 1.

Algorithm 1: Procedure of the DeepSVDD method.

Step 1: Network Modification
for $d \in \{2, 4, 8, 16\}$ **do**
  Add an output layer with d nodes to obtain model M_d;
  Remove all bias terms from the base classifier;
  Remove any dropout layers;
end
Step 2: Center Computation
for *each model* M_d **do**
  Initial forward pass to obtain outputs $\{f_d(x) : x \in D_{\text{bkg}}\}$;
  Compute the center $c_d = \frac{1}{|D_{\text{bkg}}|} \sum_{x \in D_{\text{bkg}}} f_d(x)$
end
Step 3: Training
for *each model* M_d **do**
  for *each batch* $B \subset D_{bkg}$ **do**
    Compute network outputs $f_d(x)$;
    Compute loss:

$$\mathcal{L} = \frac{1}{|B|} \sum_{x \in B} \|f_d(x) - c_d\|^2$$

    Update the parameters of M_d to minimize $\mathcal{L}$;
  end
end
Step 4: Ensemble anomaly scores
for *each test event* x **do**
  Compute the anomaly score for each model;
end
Average the scores across the models;

DROCC: Deep Robust One-Class Classification

The DROCC [299] method, which has not been extensively explored in the context of LHC physics, is a one-class classification approach that relies on the hypothesis that normal (target) data resides on a well-sampled, locally linear, and low-dimensional manifold. The loss function is modified to include a component that actively searches for adversarial examples near the 'normal' data points. These adversarial examples are synthetic data points that are slightly perturbed versions of the normal data and are hypothesized to lie close to the decision boundary between normal and anomalous classes. The objective is to ensure that the model can correctly classify these challenging examples as anomalies, thereby enhancing its robustness to real anomalous

data it may encounter to avoid the phenomenon of 'sphere collapse'.

As shown in Table 8.3, no changes in the datasets are specified for the DROCC method. The reason is that the synthetic outlier events are generated automatically during the training process, so no prior effort is needed to modify the datasets as occurs for the DDD method. The training is conducted entirely with background (target class) events to compute the cross-entropy loss and the adversarial loss.

Signals are introduced exclusively during the validation phase to monitor the stability of the training. These signals, obtained from Ref. [308], are different from those used in the final test phase that were presented in Section 8.2. This semi-supervised strategy was motivated by the inherent instability observed during the minimization of the adversarial loss functions. Monitoring the AUC after each epoch helps optimize the training configuration to ensure a more robust model convergence. Consequently, the DROCC method remains a one-class classification technique during training while still benefiting from signals in the validation phase. A step-by-step outline of the DROCC method is provided in Algorithm 2.

Algorithm 2: Procedure of the DROCC method. See Ref. [299] for more details.

Step 1: Training:
for *batch in* X_{bkg} **do**
  Generate adversarial examples X_{adv} for X_{bkg}:
    Apply small random perturbations to X_{bkg};
    Project perturbed samples onto a Hypersphere constraint;
  Compute loss:
    $L_{\text{original}} = \text{CrossEntropy}(f_{\text{model}}(X_{\text{bkg}}), +1)$;
    $L_{\text{adv}} = \text{CrossEntropy}(f_{\text{model}}(X_{\text{adv}}), -1)$;
    $\text{TotalLoss} = L_{\text{original}} + L_{\text{adv}}$;
  Update model parameters θ to minimize the TotalLoss;
  Validation Phase:
  Evaluate f_{model} on validation set $(X_{\text{val\_bkg}}, X_{\text{val\_sig}})$;
  Compute the AUC to monitor overfitting and guide early stopping;
end
Step 2: Testing
Evaluate f_{model} on test set $(X_{\text{test\_bkg}}, X_{\text{test\_sig}})$;
Compute final metrics.

DDD: Discriminatory detection of distortions

This work introduces a novel AD method named DDD, referring to Discriminatory Detection of Distortions. This approach aims to enhance AD by training a discriminator model on both original and artificially modified (background) datasets. Most importantly, as it was specified in Table 8.3, the DDD method requires no modification to the classifier or to the loss function of a binary classifier, which is the most common approach in LHC searches. The transformation of a classifier into an anomaly detector is achieved simply by substituting the signal samples employed for the training by a distorted version of the background data. Such distorsion integrates simultaneously[6] the following modification:

1. **Data Shifting**: Kinematic variables are adjusted using a normal distribution centered at 1 with a certain standard deviation (σ). The shifting is applied to energy E, pseudorapidity η, and azimuthal angle ϕ. The transverse momentum p_T is recalculated based on the modified energy E and pseudorapidity η to preserve the mass of the particle.

2. **Object Addition**: Random addition of new objects from other background events, including object type and 4-vector with a certain probability p.

3. **Object Removal**: Random removal of existing objects with the same specified probability p.

If the background is distorted excessively, the distinction becomes too trivial; if the distortion is minimal, however, the task is too challenging. Therefore, the level of distortion is fine-tuned by monitoring the AUC until the background data are optimally distorted. In this study, an AUC value of 0.85 is targeted, as it was found to be consistent with previous supervised searches [301]. This is an important difference to other methods that distort the data to find anomalies[309, 310]. As with the deepSVDDs, an ensemble of the four best models that come closest to the target AUC value of 0.85 was used to stabilize the method. The final metrics are calculated based on the average predictions of these four models. The DDD method is summarized in Algorithm 3.

One of the strengths of the DDD method lies in the general approach followed to modify the data. However, there is still room for improvement to analyse distortions of the background data on a case-by-case basis. Furthermore, it is important to emphasize once again that the application of the

[6] The simultaneous combination of these modifications was determined to be more effective compared to their exclusive implementations, such as the "shifting+adding objects" or "shifting+removing objects" approaches.

Algorithm 3: Procedure of the DDD method.

Step 1: Data Modification
Split $D_{\text{background}}$ into $D_{\text{original}}$and $D_{\text{mod\_source}}$;
for *each event in* D_{mod_source} **do**
  Apply the data shifting on the kinematic variables following $N(1, \sigma)$, with σ ranging from 0.00 to 0.10 ;
  for *each object in the event* **do**
    Add a new object with a probability p;
    remove an existing object with the same probability p;
  end
end
Once the modified set D_{modified} is created, merge it with D_{original} to form a new dataset D_{combined};
Label D_{original} as '0' and D_{modified} as '1';
Step 2: Training
Train the model $M_{\text{discriminator}}$ to discriminate original from modified background events.;
Step 3: Evaluation
Calculate the AUC score using predictions on D_{original} and D_{modified};
Step 4: Adjust data distorsions
if *the AUC score deviates significantly from 0.85* **then**
  Adjust σ and p accordingly;
  Repeat the process from Step 1 until the desired AUC score is achieved;
end
Step 5: Ensemble anomaly scores
Select the four best models based on the AUC score;
Average the scores across the four models;

method does not require a change in the network structure used for supervised binary classifications, which already exist in many HEP analyses[7].

[7]The method also uses ratios of probability densities and is invariant to variable transformations, which may be advantageous for some applications [311].

8.4 Results

The performance of an unsupervised method can not be determined by evaluating the model in a particular signal, as it is the case for supervised methods. If an unsupervised model performs well in a particular signal, it does not mean that is in general a good model to detect anomalies. Subsection 8.4.1 evaluates the trained models on the Dark Machines dataset described in Section 8.2, corresponding to the four Dark Machines challenge channels [277]. Subsection 8.4.2 combines the performance along the BSM signals and channels explored to present the overall performance of the explored techniques, comparing them to the best-performing ones in the Dark Machines challenge.

8.4.1 Evaluation on the Dark Machines dataset

Figure 8.4 shows the performance of the eight models trained in this study: DeepSVDD MLP, DeepSVDD ParT, DeepSVDD ParT+SM, DROCC MLP, DROCC ParT, DROCC ParT+SM, DDD ParT and DDD ParT+SM. The models are evaluated on the four channels of the Dark Machines dataset, which target different final states and are sensitive to different BSM signals. The AUC and the signal efficiency (ϵ_S) for a background efficiency (ϵ_B) of 1% are shown for each signal and channel.

In addition, a *significance improvement* (SI) equal to 1 is indicated by a vertical line in the plots. The SI measures the improvement of the significance[8], $\sigma = S/\sqrt{B}$, after applying a cut on the AD score:

$$\text{SI} = \frac{\sigma'}{\sigma} = \frac{S'}{\sqrt{B'}} \times \frac{\sqrt{B}}{S} = \frac{\epsilon_S\, S}{\sqrt{\epsilon_B\, B}} \times \frac{\sqrt{B}}{S} = \frac{\epsilon_S}{\sqrt{\epsilon_B}}\,, \tag{8.2}$$

such that SI>1 indicates that the AD selection improves the significance of the signal over the background.

Since the four channels are characterized by different statistics and signal-to-background ratios, as well as different event selections, the performance of the models varies across the channels:

- **Channel 1** exhibits high AUC values across most models, indicating strong AD capabilities. The ParT with pairwise interactions, including SM couplings, demonstrates superior performance in this channel. This highlights the ability of the ParT architecture to handle complex correlations effectively. While the MLP shows competitive results, it generally

[8]The significance is defined as the ratio of the signal yield S to the square root of the background yield B, where the number of background yields is large enough to approximate the Poisson distribution with a Gaussian one. In such case, $\sqrt{B}$ is the standard deviation and the significance indicates the number of standard deviations above the background expectation.

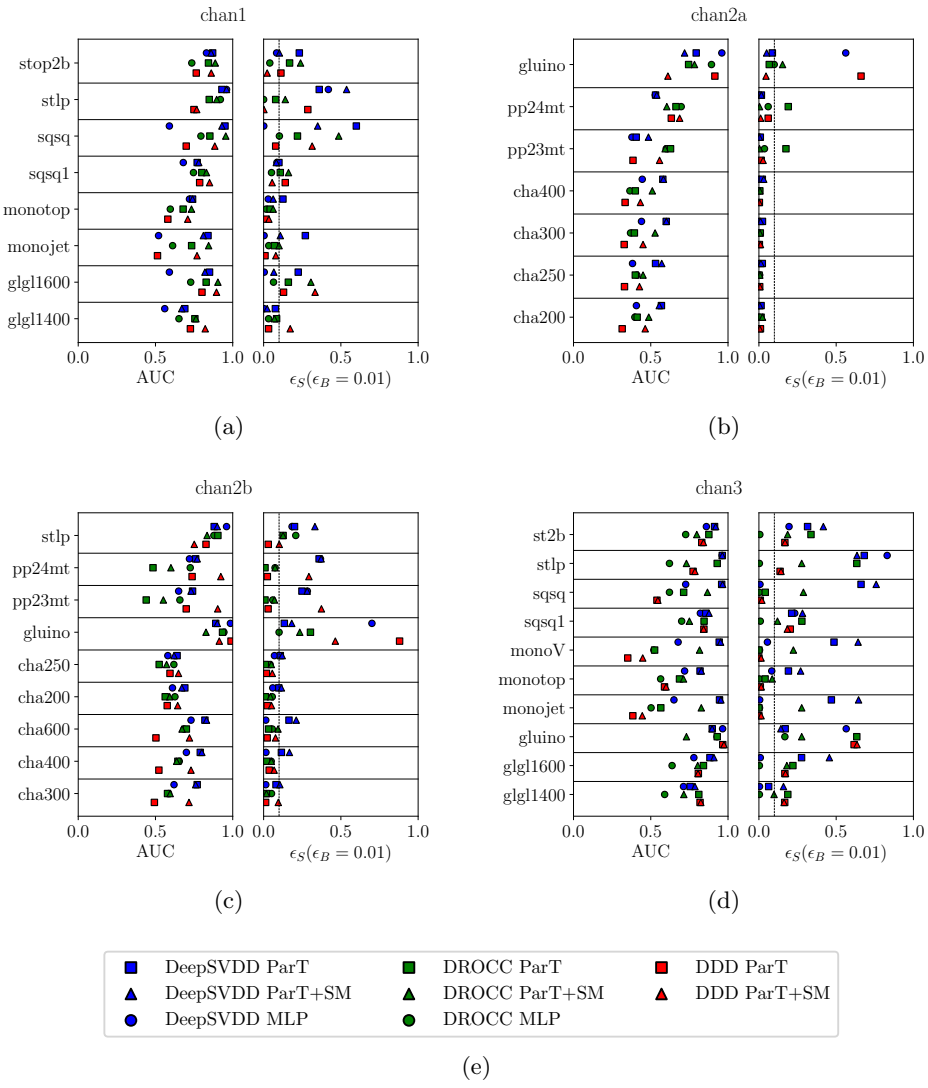

Figure 8.4: This figure shows the performance of the eight models on the four channels of the Dark Machines dataset: Channel 1 (first row, left), Channel 2a (first row, right), Channel 2b (second row, left) and Channel 3 (second row, right). For each channel, different signals are evaluated. The performance metrics shown are the AUC and the signal efficiency (ϵ_S) assuming a background efficiency (ϵ_B) of 1%. A vertical line is added to indicate a significance improvement equal to 1. A color code is used to distinguish among the three training techniques: DeepSVDD (blue), DROCC (green) and DDD (red). Different shapes are used for each architecture: a circle for the MLP, a square for the ParT with no interactions, and a triangle for the ParT with SM couplings.

lagged behind the more sophisticated ParT architectures, suggesting that simpler architectures might not capture the intricate patterns as the advanced ones. Most of the signals from Channel 1 are characterized by large E_T^{miss} and p_T of the jets compared with the background. This suggests that the presence of these energetic objects contributes to the strong performance observed across all models.

- **Channel 2a** is characterized by lower statistics, which makes more difficult to learn the inherent complexity of the dataset. This could be even harder for large and complex architectures, since these need to tune a large number of parameters during the training. However, the ParT models continued to outperform the MLP in general, indicating that the ParT could serve as an anomaly detector when the data are limited. In this leptonic channel, E_T^{miss} is less relevant than in Channel 1 and the p_T of leptons plays an important role in discriminating signal against background.

- **Channel 2b** shows more robust results than Channel 2a, since it contains larger statistics. The kinematic variables given as input also indicate that leptonic features are key discriminators.

- **Channel 3** contains the largest dataset and provided the best overall performance metrics. The extensive dataset in this channel allows the models to generalize better and detect anomalies with higher precision, demonstrating the importance of a large amount of training data for improving model performance. Similar to Channel 1, hadronic final states are dominant in this channel, with E_T^{miss} and the p_T of jets being the most discriminative quantities.

From the architecture perspective, the MLP shows the lowest performance along the four channels. The few cases where it outperforms the ParT models correspond to simple tasks in which all the models are accurate. Such cases are characterized by an input variable that already discriminates very well the signal from the background. In contrast, the ParT+SM architecture is the best performing one in most cases, especially when combined with the DROCC and DDD techniques. This is consistent with the fact that the learning task proposed in the DeepSVDD method is simpler than the one proposed by the DROCC and DDD methods, which could explain why the information added by the SM couplings is less relevant in this case.

From the perspective of the AD techniques, the best method corresponds to DeepSVDD, being the most robust and stable across all channels. This method was already shown to provide great performances in the Dark Machines challenge [277]. However, the DROCC and DDD methods have proven to also

be effective, showing similar performances to the DeepSVDD method and even outperforming it in some cases. The main advantage of these methods is that they do not require any modification to the classifier, so that no prior knowledge of the network architecture is needed. In addition, since the DDD method is a new approach developed in this work, there could still be room for improvement by exploring different data distortions and hyperparameter tuning.

8.4.2 Comparison to the Dark Machines challenge algorithms

Based on the SI, the total improvement (TI) is used to quantify the maximum SI across the various physics signals for each of the AD techniques and to combine the signals in multiple channels. The minimum, median and maximum values of the TI along the physics signals is defined to obtain overall performance metrics that measure the robustness of the trained models.

Figure 8.5 provides a comparative analysis of the TI values for different models, including the results of different models in the Dark Machines challenge and the mixture of theories from Ref. [308]. The TI is calculated over different background efficiency cuts ($\epsilon_B = 10^{-2}, 10^{-3}$, and 10^{-4}), and the maximum is taken, which typically leads to $TI > 1$.

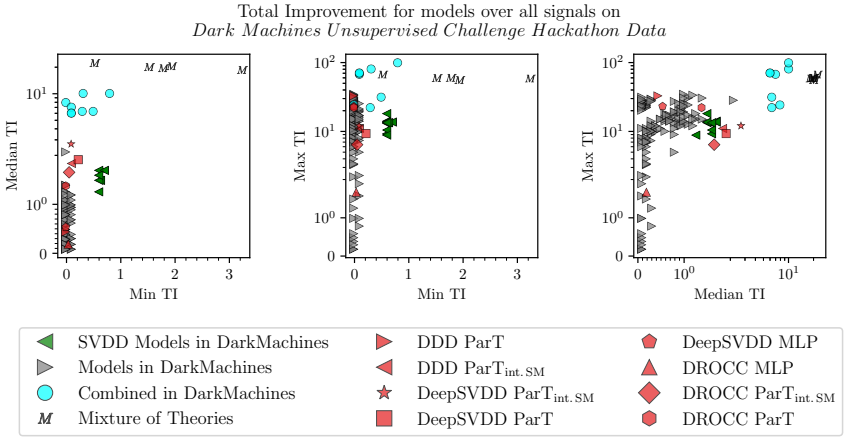

Figure 8.5: The minimum, median and maximum best total improvements for each technique. The metrics are computed with the description and channels of the Dark Machines challenge datasets.

The predictions show remarkably high median TI values, especially for the DeepSVDD models based on ParT architectures, both with and without the pairwise interaction matrix. The DDD method applied to the ParT with pairwise features also shows significant performance. Despite the models from the

Dark Machines challenge also show high median TI values, a direct comparison shows that the methods presented in this work are competitive, with comparable results or slightly higher values in some cases.

In terms of maximum TI, the models trained for this study, particularly the DeepSVDD and DDD with ParT architectures, reach a maximum TI of about 10. This is consistent with the best-performing models from the Dark Machines challenge. However, one notable difference is the minimum TI score, where these models exhibit a lower minimum TI compared to the Dark Machines models.

It should be noted that the winning models in this challenge were combinations of SVDDs with normalizing flow-based models [312] (called "combined in DarkMachines" in Figure 8.5). A combination with flow models would probably also further improve the performance of the trained models on this ranking. The M models shown in the figure were created using a supervised classifier trained on a mixture of BSM signals, a method described in Ref. [308]. This method could be superior to unsupervised methods if the signal has similar properties to the 'BSM mixture'.

An additional point to take into account is that no hyperparameter optimization was performed for the models trained in this work. The goal was to explore the feasibility of turning a classifier into an anomaly detector with no further effort, rather than presenting the best possible model for detecting anomalies. Thus, the ParT architectures were trained with the same hyperparameters as those used in the supervised task presented in Ref. [301]. The comparative analysis based on the median TI scores shows that these models perform quite well, specially in combination with the DeepSVDD and DDD techniques.

These results emphasize the potential of turning state-of-the-art classifiers into anomaly detectors with minimal changes and using their capabilities to improve AD in HEP experiments. In fact, this contribution expects to motivate the LHC community to consider the reinterpretation of their supervised searches as AD tasks, in addition to the traditional regions selection and fitting, by converting their classifiers into anomaly detectors following the guidelines presented in this work.

Chapter 9

Conclusions

This Thesis presents different efforts that contribute to the search for New Physics with the ATLAS detector. First, the SM has been presented in Chapter 1 as an elegant description of the fundamental particles and their interactions, showing its success in predicting very precisely a wide range of phenomena. After describing some of its most important observational and theoretical inconsistencies, the DM and the hierarchy problems have been introduced in Chapter 2. The DM problem is one of the most important evidences that motivates the existence of new physics. Several astronomical observations, such as the rotation curves of galaxies, the gravitational lensing effect and the CMB radiation indicates that around a 75% of the matter in the Universe correspond to DM. On the other side, the hierarchy problem arises when introducing new massive particles at very large energy scales, introducing enormous radiative corrections to the Higgs boson mass. Thus, unnatural tunings become necessary to recover the effective mass of the Higgs boson that is measured in the experiments. VLQs appear in different BSM models to solve this problem since their masses can be introduced respecting the gauge invariance without relying on the Higgs mechanism.

Before presenting the analyses of this work, the experimental setup was described in Chapter 3, where important magnitudes of collider physics are introduced with a special focus on the pp collisions at the LHC, whose operation periods and future plans are described. The ATLAS analyses presented in this work are based on $\sqrt{s} = 13$ TeV collisions recorded by the ATLAS detector during the Run 2 of the LHC, corresponding to an integrated luminosity of 139 fb^{-1}. This chapter also presents the different subsystems of the ATLAS detector to understand how the kinematical features of the particles are measured. This includes the DAQ system that processes the collisions into electric signals to build physical observables, being possible to trigger on-line the relevant processes according to their kinematics. Subsequently, Chapter 4 presents

the simulation chain followed by the ATLAS collaboration. Both the collisions and the interaction of the final state particles with the detector are simulated with a high precision, which allows for data/MC comparisons. Modeling uncertainties are derived from these MC simulations, which come from the lack of knowledge or precision in some calculations and from technical limitations of the MC generators. Similarly, the object reconstruction procedure explained in Chapter 5 also carries certain experimental uncertainties that are associated to detector inefficiencies or the reconstruction algorithms.

In particular, Chapter 6 presents a search for events with a single top quark and missing transverse momentum. This analysis is known as MONOTOP [1]. The results are interpreted in terms of two simplified models that predict the production of DM particles, one of them mediated via a scalar resonance and the other mediated by a vector mediator. The stable DM particles escapes from the detector leaving a large amount of missing transverse momentum in the final state. Since an additional object is needed to trigger the events, the DM particles are produced together with a top quark, which decays hadronically in a highly boosted regime and the decay products are reconstructed in a large radius jet. These two models depend on a few free parameters, such as the masses of the DM particles and the mediators, and the couplings of the mediators with the SM particles and the DM: m_χ, m_ϕ, λ_q and y_χ for the scalar mediator model; and m_χ, m_V, a and g_χ for the vector mediator model. The results are also interpreted in terms of a simplified VLQ lagrangian, exploring the channel in which a singly-produced T-quark decays into a top quark and a Z boson that decays invisibly into neutrinos. The only free parameters of this model are the T-quark mass m_T and an overall coupling κ_T to the SM bosons. The results are only interpreted for the region in which the relative decay width of the top partner ($\Gamma_T/m_T \propto \kappa_T^2 m_T^2$) is below 0.5, where the theoretical assumptions remain valid. In addition, this model also depends on three relative couplings, which take fixed values for the SU(2) multiplet representation of the T-quark.

No significant excess over the SM predictions has been observed but competitive upper limits on the cross-section at 95% CL have been set for each model. The upper limits have been computed by scanning across different values of the model parameters, covering a wide parameter space. The excluded regions on this parameter space allow to set exclusion limits on the model parameters. The upper limits obtained for both DM models show a low dependence on the coupling parameters, except at low values corresponding to small cross sections. For the scalar mediator model, the mediator mass m_ϕ values below 3.4(2.5) TeV are excluded for all values of λ_q (y_χ) above 0.2 (0.4) with $m_\chi = 1$ GeV. The exclusion limits on m_ϕ are also constant for m_χ values below 1.5 TeV, excluding values of m_ϕ (m_χ) up to 4.3 (2.2) TeV, taking the benchmark values of the couplings $\lambda_q = 0.2$ and $y_\chi = 0.4$. This corre-

sponds to an improvement of around 500 GeV for the mediator mass limits with respect to the previous iteration of the mono-top search [260]. Equivalently, for the vector mediator model, all the explored values of a and g_χ are excluded for m_V values below 1.1 TeV and 1.5 TeV, respectively. A maximum of 2.3 (1.5) TeV is excluded for m_V (m_χ), taking the benchmark values of the couplings $a = 0.5$ and $g_\chi = 1$. This corresponds to an improvement of around 300 GeV for the mediator mass limits with respect to the previous iteration. On the other hand, the VLQ model shows a strong dependence between the exclusion limits of the m_T and κ_T parameters. While all values of κ_T above 0.4 are excluded for m_T values below 1.6 TeV, a maximum value of m_T =1.9 TeV is excluded for κ_T values around 0.6 . Despite the SU(2) singlet scenario $\xi_Z = \xi_H = (1 - \xi_W)/2 = 0.25$ is considered in this search, a generalization of the limits is obtained for different values of ξ_W between 0.5 and 0.9, showing a significant degradation of the limits as ξ_W takes larger values.

Chapter 7 presents a combination of three searches for singly-produced T-quarks in the ATLAS collaboration, published in Ref. [2]. These searches make use of the same simplified Lagrangian, depending on the same free parameters: m_T, κ_T and the relative coupligns. The Monotop analysis presented in the previous chapter is combined with the analyses HtZt and Osml to enhance the sensitivity of the individual searches. However, both the HtZt and Osml analyses are also sensitive to the SU(2) doublet representation of the T-quark, for which the relative couplings are fixed to $\xi_Z = \xi_H = (1 - \xi_W)/2 = 0.5$. This combination set limits on the inclusive cross-section of the four production modes considered in the analyses: $T(\to Zt)qb$, $T(\to Ht)qb$, $T(\to Zt)qt$ and $T(\to Ht)qt$. Analogously, the upper limits on the cross-section at 95% CL obtained by scanning across different values of m_T and κ_T allows to find an excluded region in the parameter space. The results show that the most stringent limits are obtained for the SU(2) singlet representation, for which the cross-section is constrained to be below 15 fb for masses in the 1.5–1.7 TeV range and $\kappa_T = 0.3$. All values of κ_T above 0.2 are excluded for m_T approaching to 1.0 TeV and a maximum m_T value of 2.1 TeV is excluded for κ_T around 0.7 . For the SU(2) doublet representation, the cross-section is constrained to be below 30 fb for masses in the 1.2–1.6 TeV range and κ_T values between 0.5 and 0.6 . All values of κ_T above 0.45 are excluded for m_T =1.0 TeV and a maximum m_T value of 1.7 TeV is excluded for κ_T around 0.7 . The combination of the three searches significantly improves the exclusion limits from the individual channels in both representations, with an increase of around 200 GeV on the m_T exclusion limit with respect to the best-performing channel. For large masses, corresponding to 2 TeV in the singlet and 1.5 TeV in the doublet scenario, the lowest excluded κ_T is reduced in the combination by 1.5 units. The improvement is less significant for lower masses, where the Osml analysis is already very sensitive.

The last analysis presented in Chapter 8 is an effort that aims to boost the development of AD techniques in ATLAS searches. AD emerges as an alternative to the model-specific searches traditionally performed in HEP experiments, such as the ones presented in this Thesis, which have not shown significant excesses over the SM predictions. This study [3] makes use of simulated data from the Dark Machines Anomaly Score Challenge, which serves as a benchmark for the LHC community in which pp collisions are simulated with a simplified ATLAS detector. This dataset contains simulated events from SM processes and different BSM models that are used to test the capabilities of the AD techniques to identify these signals as anomalies. Since this BSM models are characterized by different final states, four different channels are provided in this dataset to explore different topologies. Two transformer-based classifiers, denoted as ParT and ParT+SM (including the SM running couplings as pairwise features), have been compared to a MLP. These architectures are used for AD in combination with three different techniques, named DeepSVDD, DROCC and DDD. No hyperparameter optimization or additional tuning has been performed when applying these techniques, but the major modifications are applied to the loss function or the train data. The evaluations on the signal processes are interpreted in terms of the AUC and the signal efficiency ϵ_S for a background efficiency ϵ_B of 1%. On one side, the ParT+SM architecture showed to be the best-performing anomaly detector overall, which indicates that the best classifiers have the potential to become the best anomaly detectors. On the other side, the three techniques show similar performances, with the deepSVDD providing the best results along the four channels. Finally, more general metrics are defined to evaluate the performance across all the BSM models and the different channels. These results show that the trained models from this study are competitive with respect to the best-performing models of the challenge, which indicates that these AD techniques do not require a dedicated tuning of the networks for this task, enabling the adaptation of the existing classifiers without much more effort.

Appendix A

NN-based parameterization of theoretical uncertainties

The studies performed in large experiments like the ones carried out in the LHC usually require the use of large amount of events produced using MC simulations. By doing so, it is possible to compare the real data obtained from the experiment with MC samples corresponding to some physical model. When producing a particular process using an event generator, not an unique set of configurable parameters is possible since there are theoretical uncertainties coming from the incomplete understanding of the theory or from simulation limitations. Some of these uncertainties are controlled by certain parameters and different values can be assigned directly at the production stageand stored *on-the-fly* as event weights. However, some other uncertainty variations require an alternative production, including the event generation, the detector simulation and the reconstruction step. Generating alternative samples anytime that is required in every ATLAS analyses carries important problems, such as huge CPU costs and disk space availability, which will be even more critical in the next HL-LHC era.

The goal of this work is to test a new technique [313] based on Machine Learning that aims to parameterize theoretical uncertainties that are not taken into account as event weights during the MC production. Encapsulating the theoretical variations at truth level in a set of weights allows to avoid the detector and reconstruction simulation of an alternative sample, which are the most expensive steps. This technique based on Calibrated Likelihood Ratio Estimators and named *CARL* technique is presented in Section A.1. Section A.2 describes the methodology followed to parameterize hadronization uncertainties with the CARL technique, focusing on dijet events. The performance of this parameterization is evaluated in Section A.3 for dijet events, but also for $t\bar{t}$ and Vqq processes. Section A.4 summarizes the conclusions of this work and

the future steps to be followed.

A.1 Calibrated Likelihood Ratio Estimators

If two MC samples are generated for the same process according to two different set of configurable parameters θ_n (nominal) and θ_a (alternative), the corresponding probability density functions can be denoted $p(x|\theta_n)$ and $q(x|\theta_a)$, in which x is any point in a very high dimensional phase space. The variations between these probability density functions should be parameterized according to the ratio:

$$r(x) = \frac{p(x|\theta_n)}{q(x|\theta_a)} \ , \tag{A.1}$$

However, the explicit expression of the probability density functions are not accessible and a small error in $q(x|\theta_a)$ (δq) would have a large effect in the estimation of the ratio. Instead, a direct estimation of the ratio $\bar{r}(x)$ can be achieved using a calibrated Neural Network (NN) that is trained to classify events from the nominal sample against events from the alternative sample. If the output node of the NN makes use of the softmax activation function, the output value y will have a probabilistic nature, taking values between 0 (meaning an alternative event) to 1 (nominal event). Thus, given a set of input features $\vec{x}$ for an event, the output of the calibrated NN will be the probability of such event to belong to the nominal sample, denoted as $\mathcal{P}(y = 1|\vec{x})$. Considering also that $p(\vec{x}|\theta_n) = \mathcal{P}(\vec{x}|y = 1)$ and $q(\vec{x}|\theta_a) = \mathcal{P}(\vec{x}|y = 0)$, the estimated ratio is obtained as:

$$\bar{r}(\vec{x}) = \frac{\mathcal{P}(\vec{x}|y=1)}{\mathcal{P}(\vec{x}|y=0)} = \frac{\mathcal{P}(y=1|\vec{x})}{\mathcal{P}(y=0|\vec{x})} = \frac{\mathcal{P}(y=1|\vec{x})}{1-\mathcal{P}(y=1|\vec{x})} \ , \tag{A.2}$$

where the Bayes Theorem has been applied in the second equality: $\mathcal{P}(\vec{x}|y) = \mathcal{P}(y|\vec{x})\mathcal{P}(\vec{x})/\mathcal{P}(y)$. How precise is the approximation $r(x) \sim \bar{r}(\vec{x})$ will roughly depend on two factors: the selection of an appropriate set of input features showing noticeable variations between the two models and an optimal training of the NN.

Hadronization on dijet events

The hadronization part of the event generation is a good example in which this technique could be used. As explained in Chapter 4, the hadronization represents the transition from the partonic state, formed by quarks and gluons, to the final state with the observable hadrons. As a non-perturbative phenomenon, this part of the events are simulated using models that, although

inspired by QCD, contain parameters that are not determined by first principles but are adjusted by comparing with experimental data [314]. The most successful hadronization models implemented in event generators are the *Cluster* and the *Lund String* models.

The main study of the hadronization uncertainties is carried out on dijet events, generated with SHERPA 2.2.5. SHERPA implements the Cluster model but also provides an interface from PYTHIA to enable the implementation of the Lund String model. Dijet processes have been chosen for their simplicity and for the clear information about the hadronization simulation, not being influenced so far by other interactions different from QCD. Table A.1 shows the most relevant information of these dijet samples, such as the different selection on the leading jet p_T (p_T-ordered) and the effective cross section for each Data Set IDentifier (DSID).

DSID *Cluster / Lund String*	**slicing**	p_T **range (GeV)**	**XS*FiltEff [pb]**
364677 / 364686	JZ1W	20-60	3.086e+07
364678 / 364687	JZ2W	60-160	4.575e+05
364679 / 364688	JZ3W	160-400	5.244e+03
364680 / 364689	JZ4W	400-800	8.251e+01
364681 / 364690	JZ5	800-1300	3.949e+01
364682 / 364691	JZ6	1300-1800	1.389e+00
364683 / 364692	JZ7	1800-2500	9.845e-02
364684 / 364693	JZ8	2500-3200	3.286e-03
364685 / 364694	JZ9	3200-3900	1.179e-04

Table A.1: Information related to dijet SHERPA 2.2.5 MC samples.

A.2 Methodology

This section describes the general methodology to follow for the parameterization of any theoretical uncertainty using the CARL technique, which make use of the CARL Athena algorithm [315] and CARL-Torch package [316]. First, the key features that are sensitive to the hadronization model are identified. Then, the observables are implemented in the Athena framework to produce ROOT Ntuples with a format that is compatible with the CARL-Torch tool. After the preprocessing of the input, the CARL-Torch tool is used to train the NN and to evaluate the performance of the parameterization.

Identifying key features

The first part consists of identifying important features in order to build a phase space in which the theoretical uncertainties can be as much large as possible. This has been done using the RIVET Toolkit [317] aimed for validation of MC samples, which has allowed to perform quick comparisons between the two models for a wide variety of observables used in many ATLAS analyses. Most of such analyses were focused on the study of jet substructure observables, which were already implemented in *RIVET routines*. Different selection requirements and definitions of the jets are considered in these routines, but the chosen one for this study correspond to the anti-k_t algorithm [234] with $R = 0.4$.

Figures A.1 and A.2 illustrate some of the features showing discrepancies between the two set of MC samples. Figure A.1 shows the distributions of the two observables that define the Lund Plane [318] in the first row. These observables are computed per declustering step for each proto-jet pair and will be referred as *Lund z* (Figure A.1a) and *Lund* ΔR (Figure A.1b). The observables shown in the second row of Figure A.1 are track-based variables, such as the number of tracks per jet and the transverse momentum of each track with respect to the jet axis. From Figures A.2a and A.2b, it is noticed that the relative energy carried by the heavy hadrons in the jets is sensitive to the hadronization model implemented. In particular, the Cluster distribution peaks at higher values of the transverse momentum. Figure A.2c corresponds to the mass of the first jet, whose shapes are quite similar but the Lund String distributions is slightly shifted to higher masses. Figure A.2d shows variations on the jet charge content As it will be seen at Section A.3, the best performance of the training will be obtained for this observable.

Preprocessing dijet samples with Athena

Since the CARL-Torch tool reads ROOT ntuples as inputs, the Athena framework has been used to obtain ROOT Ntuples from TRUTH1 derivations. The TRUTH1 derivations are produced from the corresponding EVNT samples, and contain the necessary information to replicate the observables studied with RIVET at truth level. The RIVET routines used to study the key features apply different analysis-specific selections, but the NN need to be trained within a single and general phase space to obtain weights that are applicable for most ATLAS analyses:

- Events: at least 2 jets.
- Jets: anti-k_t R=0.4, $p_T^{\text{jet}} > 20$ GeV, $|\eta_{\text{jet}}| < 4.5$.
- Tracks: $p_T^{\text{track}} > 0.3$ GeV, $|\eta_{\text{track}}| < 4.9$.

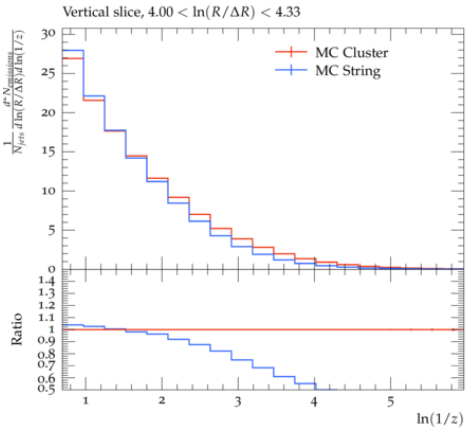

(a) Lund z observable.

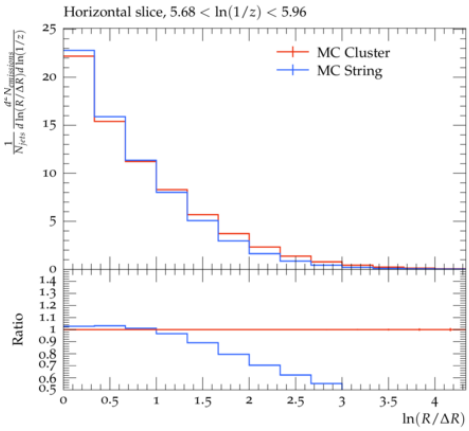

(b) Lund ΔR observable.

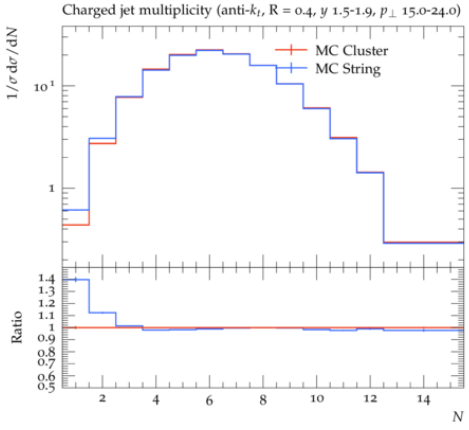

(c) Number of charged particles inside a jet.

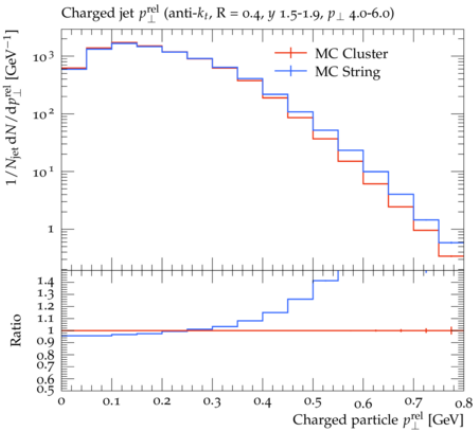

(d) Transverse momentum of charged particles relative to the axis of its jet.

Figure A.1: Key observables implemented in the RIVET routines (a),(b) *Lund jet plane with charged particles* and (c),(d) *Measurement of ATLAS track jet properties at 7 TeV* (second row).

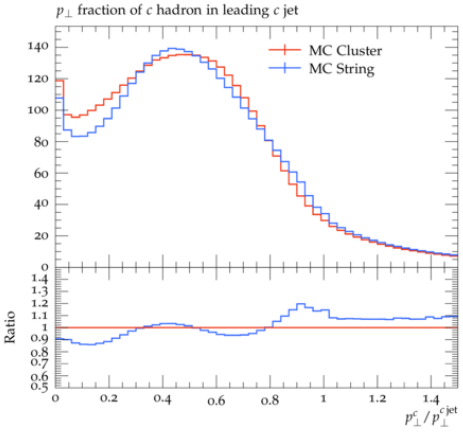

(a) Transverse momentum of the leading c-hadron (p_T-ordered) divided by the transverse momentum of its jet.

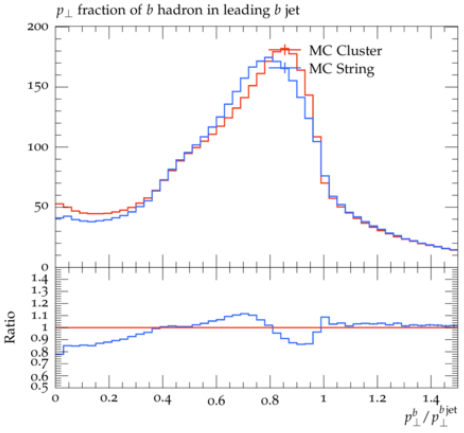

(b) Transverse momentum of the leading b-hadron (p_T-ordered) relative to the transverse momentum of its jet.

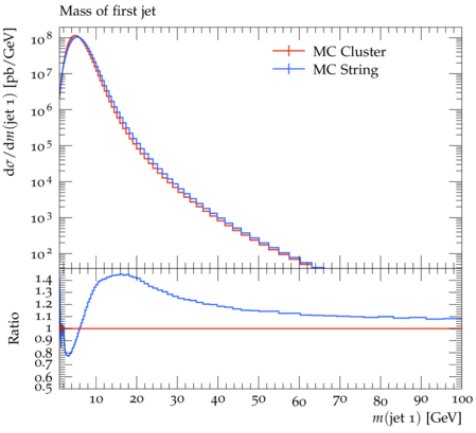

(c) Mass of the first jet (p_T-ordered).

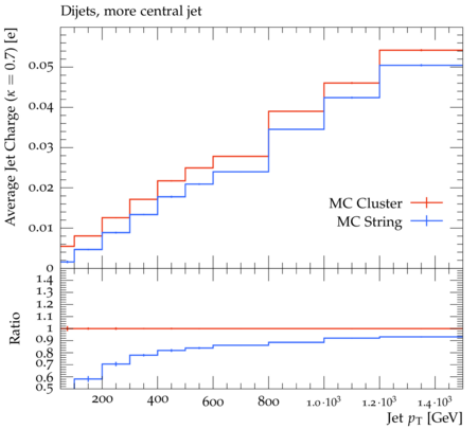

(d) Jet charge.

Figure A.2: Key observables implemented in the RIVET routines (a),(b) *Monte Carlo validation analysis to study heavy flavor production*, (c) *Monte Carlo validation observables for jet production* and (d) *Jet charge*.

All the variables for which any RIVET routine showed significant discrepancies between the two models are stored in the ROOT ntuples. Different types of variables are considered: per-event variables, such as the number of tracks in the event; per-jet variables, such as the transverse momentum of the leading jet; per-track variables, such as the momentum projection of the track in the jet axis; and declustering variables, such as the k_t-splitting or the Lund Plane variables.

CARL implementation

The workflow of the CARL-Torch toolkit can be understood in three different stages: input preparation, training and evaluation.

Input preparation

The NN is fed with numpy arrays, and only the input variables are stored. All the scalar and vector variables organized as branches in the ROOT ntuples are flattened into a one-dimensional input array per event. The padding of the vector variables, which depend on the variable number of jets per event or the number of tracks in each jet, introduces missing entries that are filled with dummy values equal to zero. To reduce the amount of dummy values to be given to the NN, a maximum of 3 entries for the per-track variables are considered. The range of the input features is scaled between 0 and 1 to avoid the importance of a feature to depend on the scale of the range values[1].

The list of variables used for the training is:

- Number of tracks in the event.
- Number of tracks in each jet.
- The jet charge of each jet, which is the sum of the charges of the tracks in a jet weighted by their transverse momentum.
- Mass, transverse momentum and pseudorapidity of each jet.
- Transverse momentum of the first three tracks (ordered by p_{T}) relative to the momentum of the jet.
- Lund z variable [318] at the first, second and third declustering steps.
- k_t-splitting of the first two declustering steps [319].

[1] The dummy values were not included in the scaling computation.

Despite the observables related to heavy flavor hadrons show significant discrepancies between the two models, they are not considered in the training because the fraction of jets with heavy hadrons is very low, introducing a huge proportion of dummy values. The Lund ΔR is not considered in the training since not important differences were found between the two models in the general phase space defined for the training.

Training setup

The whole dataset is randomly split into train (75%) and validation (25%) subsets. The training is performed using the train sample, while the validation sample is used to evaluate the performance of the NN. After each epoch, the performance of the NN is evaluated using a loss function, which was chosen to be the *categorical cross-entropy* [320].

$$\mathcal{L}(\phi) = - \mathop{\mathbb{E}}_{p(x)} [\mathcal{P}_\phi(y = 1|\vec{x})] - \mathop{\mathbb{E}}_{q(x)} [1 - \mathcal{P}_\phi(y = 1|\vec{x})] \ , \tag{A.3}$$

where the first term is the expectation value computed over the nominal events and the second one over the alternative events. The Loss function depends on the ϕ parameters of the NN, which are optimized during the training. The overfitting has been controlled with the L2 regularization [321] technique, which adds the term $L2 = \frac{\lambda}{2}\mathbb{E}[\phi]$ to avoid that the ϕ parameters take very large values.

The set of hyperparameters chosen for the results shown in Section A.3 are:

- 3 dense hidden layers with 100 neurons each. The activation function for these layers is the Rectified Linear Unit (ReLU).
- An output layer with one neuron for which the softmax activation function is used [322].
- Optimizer: AMSgrad variation of *Adam* (weight decay = 10^{-5}) [323].
- Learning rate decaying from 0.001 to 0.0001 .
- Batch size of 4096 raw events.

Evaluation and closure tests

Once the Neural Network is trained, the *CARL weights* can be obtained just by evaluating on the validation sample (25% of the events). Such weights are obtained from the NN output $P(y = 1|\vec{x})$ according to the following expression:

$$w = r^{-1}(x) = \frac{1 - P(y = 1|\vec{x})}{P(y = 1|\vec{x})} \ , \tag{A.4}$$

When applying the CARL weights to the nominal events, the distribution of the input features should map the alternative model distribution. Figure A.3 illustrates this closure test, where the nominal and alternative distributions are shown in blue and yellow, respectively. The black line corresponds to the nominal distribution with the CARL weights applied, which should map the yellow distribution in order to achieve a good closure. The ratio and residual plots are also shown, in which the alternative distribution corresponds to the horizontal line.

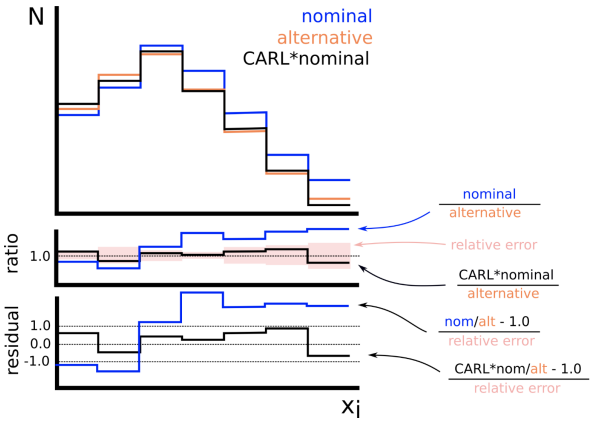

Figure A.3: Example of the closure test performed with the CARL weights. The nominal and alternative distributions are shown in blue and yellow, respectively. The black line corresponds to the nominal distribution with the CARL weights applied. The lower panels show the ratio and residual plots, in which the alternative distribution corresponds to the horizontal line.

An additional closure test presented in Section A.3 employs two ROC curves. The first compares the nominal and alternative classifications to evaluate the performance of the classifier[2], while the second contrasts the nominal distribution with CARL weights against the alternative distribution. In the latter case, an AUC equal to 0.5 indicates a perfect closure.

A.3 Results

The methodology has been described for the parameterization of hadronization uncertainties in dijet processes. This section presents the results obtained for the dijet processes, but it also explores the applicability of the technique to other processes, such as $t\bar{t}$ and Vqq.

[2]The ROC curves are built from binary classifications performed with a simplified NN.

Training on dijet samples

The different slices from Table A.1 need to be merged into a single dataset for each model, and the events are weighted according to the cross-section of the slice. Since there is a huge difference in terms of the effective cross section between the first and the last slices, the training will be driven by the low p_{T} regime. In addition, the highest p_{T} slices are characterized by a larger jet multiplicty coming from radiation. In order to simplify the event topologies, only events with 2 jets[3] will be considered in the training. Due to the low acceptance[4] of the high-p_{T} slices (up to 11%) to this selection, it was decided not to include the JZ slices from Table A.1 in the merged datasets. The total statistics used for training and validation are shown in Table A.2.

DSIDs	
Cluster & String	**Events**
364677 & 364686	3.25e+06
364678 & 364687	6.00e+05
364679 & 364688	1.00e+05
364680 & 364689	5.00e+04
Total	4.00e+06

Table A.2: Statistics used for the dijet training on the JZW slices.

Since the nominal and alternative samples mainly differ on subtle hadronization-related uncertainties coming from the implementation of the Cluster (nominal) and the Lund String (alternative) models, the classification task is not expected to be a simple discrimination. In fact, the blue ROC curve from Figure A.4 provides an AUC equal to 0.609. However, the CARL weights extracted from our NN training provide a succesful closure, as it is shown in the orange ROC curve, which provides an AUC of 0.499. This means that the NN has been able to learn the relevant differences between the two models and is able to properly parameterize the hadronization uncertainties.

This is also confirmed by the good closure obtained for both train and validation samples when looking at the distributions of the input variables. Some of these distributions corresponding to the validation set are presented in Figure A.5. Three different distributions are observed in those plots. The nominal and the alternative ones are, respectively, the blue and yellow distributions (the brown color corresponds to the intersection between these two models). The third distribution is given by the black line which is the nominal model with

[3] According to the list of observables used for the training presented before, fixing the number of jets to 2 also fix the number of input variables to 27.

[4] It has been checked that the acceptance for the 2 jets selection is the same for both models, so no bias is introduced when studying the uncertainties.

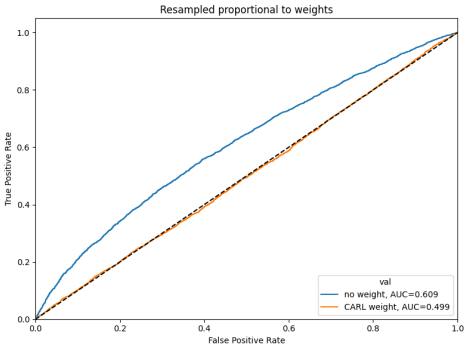

Figure A.4: The ROC curves for the validation set are shown. The blue curve corresponds to the performance on classifying the nominal and alternative samples. The orange curve is a closure test between the nominal sample with the CARL weights applied and the alternative sample. For the latter one, the optimal AUC would be 0.5.

CARL weights applied, and it should map the yellow distribution in order to achieve a good closure. The ratio and residual plots are also shown, in which the alternative distribution corresponds to the the horizontal line.

Applicability of the dijet training

This project aims to provide a parameterization of theoretical uncertainties useful for the whole collaboration. In fact, the goal is to integrate the evaluation of the NNs in the generation workflow of the ntuple production, so that the weights can be obtained for different processes. Therefore, the training needs to be general enough to be applicable to most analyses.

It seems clear that the performance of the NN will not be optimal when evaluating on a phase space different from the one learnt during the trainig. A priori, this problem could be solved by training the NN on a general enough phase space and almost all analyses could benefit from it. However, it is observed in Figure A.6 that the closure is also degraded in certain subregions of the trained phase space where the statistics entering the training was lower. According to Table A.2, the first slice covering a p_T range for the leading jet between 20 and 60 GeV is the most relevant for the training with around an 81% of the statistics. The second slice, with a leading jet between 60 and 160 GeV, shows a comparable closure despite being just a 15%. The reason for this is that the NN has learnt to map the whole set of input features and the subspace corresponding to the second slice is still similar to the subspace covered by the first slice when considering all the features. This is not the case for the last two slices, which sum up a 3.75% of the total statistics, such that

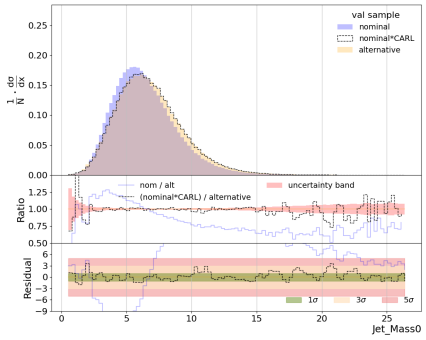

(a) Mass of jet 1.

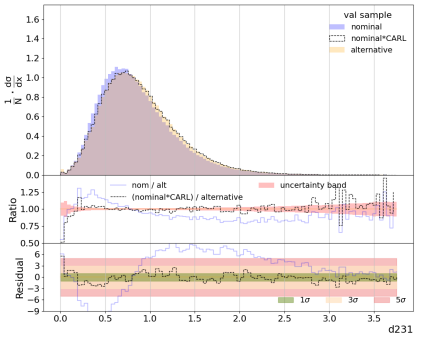

(b) k_t-splitting for second declustering step of jet 2.

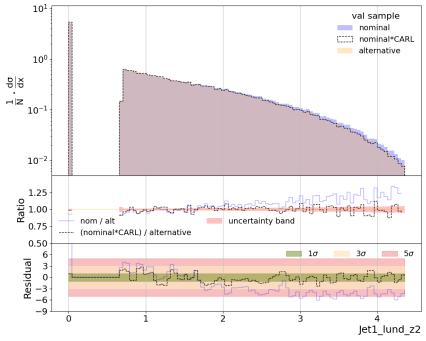

(c) Lund z variable for third declustering step corresponding to jet 1.

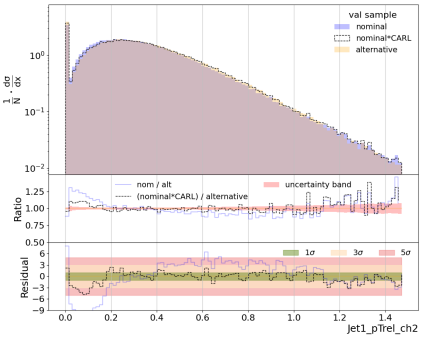

(d) Transverse momentum of third track relative to jet 1.

Figure A.5: Distributions of key features for dijet training using the validation samples. Three different distributions are shown in each plot: nominal (blue), alternative (yellow) and nominal with CARL weights applied (black line). Closure is achieved if the black line maps properly the yellow distribution. In the ratio and residual plots, since the alternative distribution is the horizontal line, the good closure is achieved if the black line fits in the uncertainty band.

analyses exploring phase spaces in the high p_T regime would not benefit from the trained NN. Thus, a satisfactory training should balance the phase space coverage to provide a reliable parameterization for most analyses. A different approach would be to split the phase space into different regions and train a NN for each of them, similarly to the approach followed in this study when focusing on the JZW slices or when selecting 2 jets in the final state to simplify the event topologies.

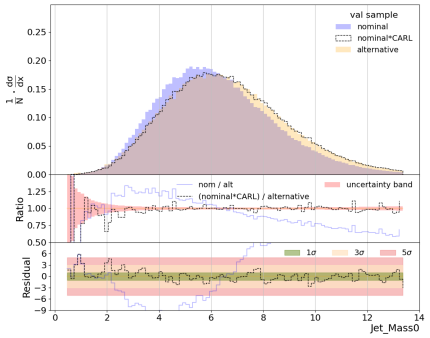

(a) Leading jet p_T in the range 20 and 60 GeV.

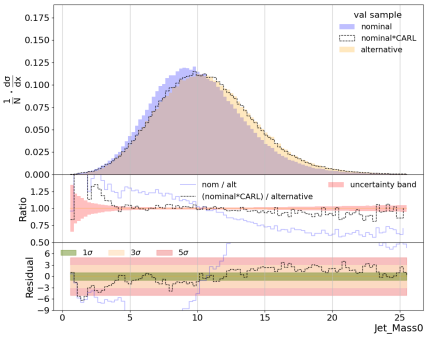

(b) Leading jet p_T in the range 60 and 160 GeV.

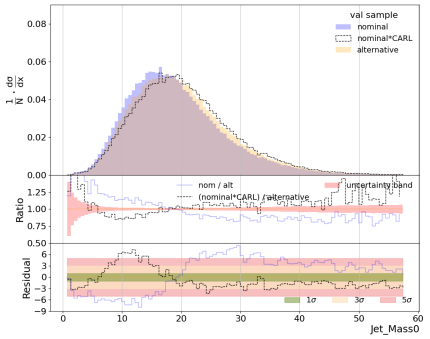

(c) Leading jet p_T in the range 160 and 400 GeV.

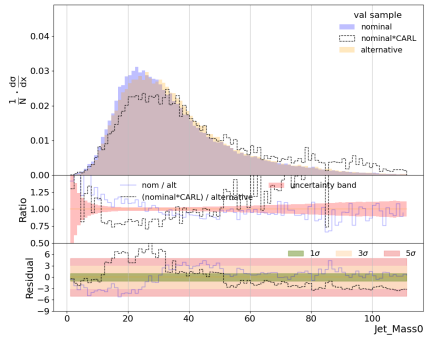

(d) Leading jet p_T in the range 400 and 800 GeV.

Figure A.6: Evaluation of dijet training on part of the trained phase space. Closure for Mass of the first jet.

In addition, the performance of the NN is not optimal when evaluating on a sample different from the one used for the training. The chosen processes to be evaluated are $t\bar{t}$ dilepton and Vqq events, both of which produce 2 jets

at tree level. Tables A.3 and A.4 show the available statistics, respectively, for the $t\bar{t}$ dilepton and Vqq samples. These events were also generated with SHERPA 2.2.8. The same selection criteria than for the dijet samples have been applied, except for the cuts $|\eta| < 2.1$ for jets and $|\eta| < 2.5$ for tracks. This is done because most of the analyses working with these processes will be interested in the central region. Figure A.7 shows a bad closure in both cases, indicating that the training is not process-independent. Instead of learning exclusively the information related to the hadronization uncertainties, the NN has also learnt the topological features of the particular process. One possible solution to this problem would be to perform a per-jet training, which would allow to take a more process-independent approach that focuses on the hadronization process that forms the jets.

DSID	**SumW**	**Entries**	**Events**	**2 jets** (%Accept.)
Cluster model				
950255	9.59e+12	2.00e+07	1.89e+07	3.66e+06 (18.7%)
Lund string model				
950264	9.26e+12	1.93e+07	1.83e+07	3.55e+06 (18.7%)

Table A.3: Statistics workflow for $t\bar{t}$ dilepton Sherpa 2.2.8 MC samples.

DSID	**SumW**	**Entries**	**Events**	**2 jets** (%Accept.)
Cluster model				
700040	1.78e+06	1.49e+06	1.44e+06	2.41e+05 (16.7%)
700041	9.74e+05	1.00e+06	9.72e+05	1.48e+05 (15.1%)
700042	4.51+05	1.64e+06	1.59e+06	2.45e+05 (15.3%)
Lund string model				
700043	9.31e+05	7.80e+05	7.56e+05	1.28e+05 (16.7%)
700044	3.70e+05	3.80e+05	3.69e+05	5.69e+04 (15.1%)
700045	3.13e+05	1.14e+06	1.11e+06	1.73e+05 (15.3%)

Table A.4: Statistics workflow for the Vqq Sherpa 2.2.8 MC samples. The pairs of DSIDs {700040,700043}, {700041,700044} and {700042,700045} corresponds, respectively, to Wqq, Zqq and Zbb processes.

Training on $t\bar{t}$ dilepton and Vqq samples

At this stage, applying this technique to other processes would require to perform a different training for each process. Thus, exactly 3 million events for each model of the $t\bar{t}$ dilepton process were selected for the training, from which

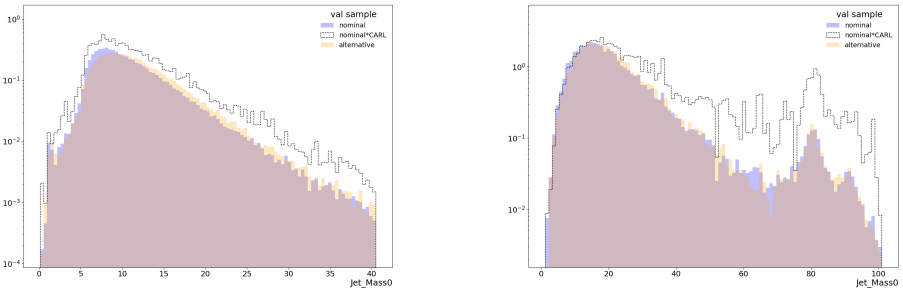

(a) (b)

Figure A.7: Evaluation of dijet training on $t\bar{t}$ (left) and Vqq samples.

around a 25% was saved as validation sample. The same set of hyperparameters mentioned previously was used for the training. Additionally, it was assumed that the same set of observables used for the dijet training will capture the hadronization uncertainties for the $t\bar{t}$ dilepton training. And in fact, the jet mass of the leading jet and the jet substructre observables are still the most discriminant variables. Figure A.8 shows the closure of the parameterization for the $t\bar{t}$ dilepton samples for some of these distributions.

Analogously, a training on Vqq was also performed, but the low statistics available for this process did not allow to achieve a good closure. The mass of the first jet is the only observable shown in Figure A.9, which shows a small separation between the two models in spite of the huge statistical fluctuations.

A.4 Conclusions

This study presents the methodology to follow for the parameterization of hadronization uncertainties using the CARL technique. The technique has been introduced from a general perspective in Section A.1, while the methodology of this study has been described in detail along Section A.2. The first results provided by this technique have been shown in Section A.3, where the performance of the NN has been evaluated focusing on dijet samples.

The first step was to identify the key features to be used as input to the NN. These features have been selected using the Rivet routine, which provides a set of observables that show significant differences between the Cluster and the Lund String models. The most important observables are related to the jet mass and the jet substructure, as well as observables related to heavy flavor hadrons, which have not been considered in the training due to the low fraction of jets with heavy hadrons. A general selection criteria on the dijet samples has

been applied, followed by a scaling of the input variables before feeding them to the NN. The good closure of the results obtained for these samples demonstrate that a NN is able to learn the hadronization uncertainties from the input observables provided. However, two issues have been highlighted concerning the applicability of this training in the context of the ATLAS collaboration. In first place, the training has shown to be phase space dependent, showing a degradation of the closures in certain subregions of the trained phase space where the statistics entering the training was much lower. In second place, it has been shown that the training is not process-independent, as the performance of the NN is not optimal when evaluating on a sample different from the one used for the training. This has been illustrated by a low-performing closure obtained when evaluating the dijet training on $t\bar{t}$ dilepton and Vqq samples.

Different approaches have been proposed to solve these issues in future developments of this technique. The lower performance on low statistic regions could be solved by balancing the phase space coverage to provide a reliable parameterization for most analyses. A different approach would be to split the phase space into different regions and train a NN for each of them. The process dependency could be solved by performing a per-jet training, which would allow to take a more process-independent approach that focuses on the hadronization process that forms the jets.

At the end of this study, a training has been performed for the $t\bar{t}$ dilepton. The results obtained for the $t\bar{t}$ dilepton samples show a good closure for the key features identified with Rivet, which confirms that the same observables used for the dijet training are useful for the $t\bar{t}$ dilepton training.

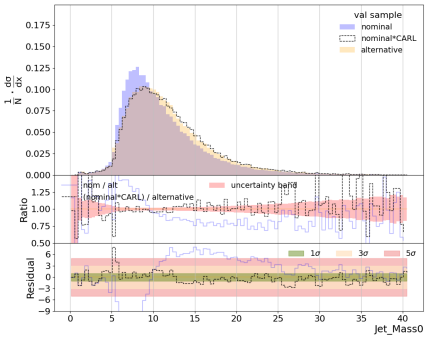

(a) Mass of jet 1

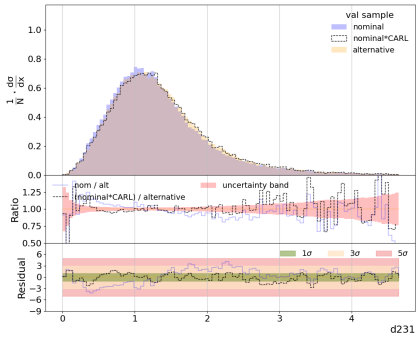

(b) k_t-splitting for second declustering step of jet 2

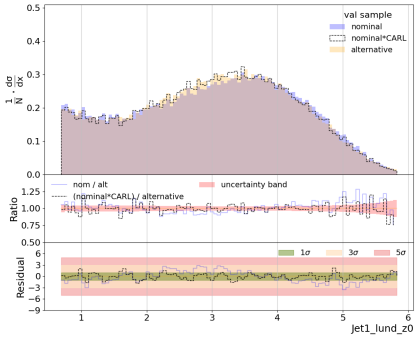

(c) Lund z variable for third declustering step corresponding to jet 1.

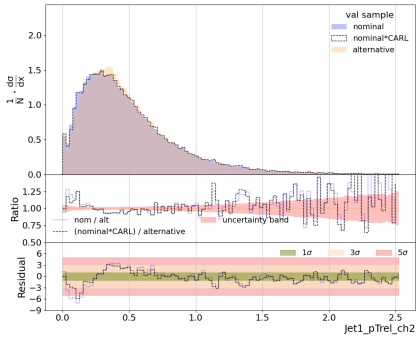

(d) Transverse momentum of third track relative to jet 1.

Figure A.8: Distributions of key features for ttbar training using the validation samples. Three different distributions are shown in each plot: nominal (blue), alternative (yellow) and nominal with CARL weights applied (black line). Closure is achieved if the black line maps properly the yellow distribution. In the ratio and residual plots, since the alternative distribution is the horizontal line, the good closure is achieved if the black line fits in the uncertainty band.

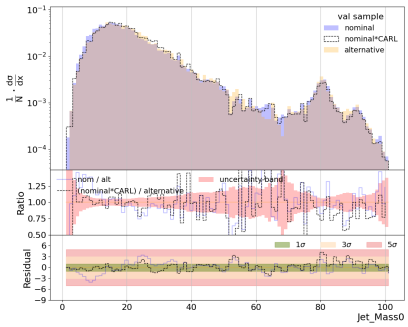

Figure A.9: CARL weights distribution and closure obtained for the $V \to qq$ samples.

Resumen

R.1 Marco teórico: el Modelo Estándar

Hasta el siglo XIX, la estructura interna de la materia era completamente desconocida, y su conocimiento era inaccesible para la ciencia. La física se sustentaba en la mecánica de Newton, el electromagnetismo de Maxwell y la termodinámica desarrollada por físicos como Carnot, Clausius y Thomson. De hecho, este último, conocido como Lord Kelvin, llegó a afirmar que no existía nada más por descubrir en la física. No fue hasta finales del siglo XIX y principios del siglo XX, cuando se dieron una serie de descubrimientos como el electrón (de Thomson en 1897) y el efecto fotoeléctrico (de Einstein en 1905), que la comunidad científica no empezó a replantearse la estructura de la materia. El desarrollo de la mecánica cuántica, la relatividad especial y la teoría cuántica de campos llevaron a la formulación del Modelo Estándar (SM, de sus siglas en inglés) de física de partículas, que describe las partículas fundamentales y sus interacciones. El descubrimiento del bosón de Higgs en 2012 fue el último gran hito que confirmó la validez del marco teórico del SM, el cual sigue describiendo con mucha precisión una amplia gama de fenómenos físicos.

Dado que el SM es una teoría cuántica de campos, la información de la dinámica de un sistema viene descrita por un lagrangiano. A partir del lagrangiano se derivan las ecuaciones del movimiento, cuyas partículas vienen descritas por objetos matemáticos llamados *campos*. Cuando se exige que un lagrangiano cumpla cierta *simetría gauge* local, campos adicionales con espín 1 emergen naturalmente en el lagrangiano como términos aditivos que representan interacciones entre partículas con una intensidad proporcional a una constante de interacción, la cual se determina experimentalmente. Estos campos adicionales son los *bosones gauge* mediadores de las interacciones fundamentales, y la aparición de éstas simetrías conllevan la conservación de nuevas magnitudes físicas, conocidas como *cargas*.

El SM predice la existencia de 17 partículas fundamentales: 12 fermiones (y sus antipartículas) que componen la materia, 4 bosones gauge que median las interacciones, y el bosón de Higgs, responsable de las masas de las partículas.

A pesar de la complejidad matemática de esta teoría cuántica de campos, el SM es una teoría fenomenológica que viene determinada por 19 parámetros medidos experimentalmente: las masas de los quarks (6), las masas de los leptones (3), los elementos de la matriz Cabibbo-Kobayashi-Maskawa ó CKM (4), las constantes de acoplamiento de las interacciones (3), el valor esperado del vacío, la masa del bosón de Higgs y el ángulo del vacío de QCD.

Las partículas fundamentales y sus interacciones

Los fermiones tienen espín 1/2 y están organizados en tres familias o generaciones con propiedades idénticas que solo difieren en su masa y número cuántico que identifica las familias. La primera generación es la más ligera y no se desintegra en otras partículas, estando presente en la materia estable. La segunda y tercera generaciones son más pesadas y menos estables, produciéndose solo en procesos muy energéticos y desintegrándose en partículas de la primera generación después de un tiempo muy corto. Estos fermiones consisten en 6 quarks y 6 leptones. Las generaciones de leptones están formadas por una partícula cargada (siendo el electrón, el muón o el tau) y su neutrino asociado, que no tiene carga eléctrica. Los quarks tienen cargas eléctricas no enteras en unidades de la carga del electrón. Según la terminología usual, los quarks con carga eléctrica $+2/3$ se llaman quarks de tipo *up* (arriba, encanto y cima) y los que tienen carga eléctrica $-1/3$ se llaman quarks de tipo *down* (abajo, extraño y fondo), denominados $u\,, c\,, t$ y $d\,, s\,, b$, respectivamente.

Acorde con el modelo estándar, las partículas fundamentales se comunican a través de 3 tipos de interacciones: la interacción electromagnética, la interacción débil y la interacción fuerte. Por un lado, la cromodinámica cuántica (QCD) describe la interacción fuerte responsable de mantener unidos a los quarks dentro de los protones y neutrones, y a estos últimos, a su vez, dentro del núcleo atómico. Esta interacción, con constante de acoplamiento α_s, es mediada por los gluones, bosones de espín 1 que surgen tras imponer al lagrangiano la simetría gauge no abeliana $\mathrm{SU}(3)_C$, conocida como simetría de color. Así, quarks y gluones son portadores de la carga de color, la cual se conserva y puede tomar tres valores diferentes: rojo, verde y azul.

Por otro lado, la teoría electrodébil (EW) describe de manera conjunta las interacciones electromagnética y débil. En principio, la electrodinámica cuántica permite describir la interacción electromagnética que surge de la simetría gauge abeliana U(1) y está mediada por el fotón con constante de acoplamiento g, responsable de la interacción entre partículas con carga eléctrica. Sin embargo, las interacciones débiles y electromagnéticas se pueden describir de manera conjunta a través de una simetría gauge no abeliana conjunta $\mathrm{U}(1)_Y \otimes \mathrm{SU}(2)_L$. La interacción débil es responsable de la desintegración de los núcleos atómicos, a través de la cual un fermión inestable da lugar a un

estado más estable de la materia. Los bosones gauge de espín 1 que median la interacción débil son W^+, W^- y Z, con constante de acoplamiento g'. En estas interacciones debe conservarse la *hipercarga* Y, la cual está relacionada con la carga eléctrica Q y la tercera componente del *isospín débil* T_3 a través de la relación $Y = Q - T_3$.

A diferencia de la interacción fuerte y electromagnética, se observa que la interacción débil solo actúa sobre partículas de quiralidad *levógira*, es decir, aquellas con espín en dirección opuesta a su momento lineal. Así, esta interacción actúa sobre dobletes de isospín débil compuestos por la componente levogira de quarks o leptones de la misma familia, donde los quarks tipo *up* y los neutrinos tienen isospín $T_3 = +1/2$, mientras que los quarks tipo *down* y los leptones cargados tienen isospín $T_3 = -1/2$:

$$\begin{pmatrix} \nu_l \\ l \end{pmatrix}_L , \quad l = e\,, \mu\,, \tau\,,$$
$$\begin{pmatrix} q_u \\ q_d \end{pmatrix}_L , \quad q_u = u\,, c\,, t\,, \quad q_d = d\,, s\,, b\,.$$

Las interacciones mediadas por los bosones $W^\pm$ son las únicas que pueden mezclar el sabor de los fermiones, cuyos autoestados de sabor no coinciden con los autoestados de masa. Para los quarks, ésta transformación unitaria viene dada por la matriz de CKM, con 4 parámetros libres que se determinan experimentalmente: 3 ángulos de mezcla y 1 fase que viola la simetría Conjugación-Paridad (CP). En el sector leptónico, dado que el SM originalmente asume que los neutrinos no tienen masa, un leptón cargado solo se acopla a su neutrino asociado y no se considera mezcla de sabores. Con la medición de las oscilaciones de neutrinos, se ha demostrado que los neutrinos tienen masa, lo que implica que también existe mezcla de sabores en el sector leptónico, la cual se describe a través de la matriz de Pontecorvo-Maki-Nakagawa-Sakata (PMNS), añadiendo parámetros adicionales a la teoría.

Mecanismo de Higgs

La formulación del SM explicada previamente no contempla que las partículas tengan masa, lo cuál es incompatible con la realidad. El mecanismo de Brout-Englert-Higgs [27, 28] permite la generación de masas de las partículas respetando la unitariedad y renormalizabilidad de la teoría. Para ello, se introduce un trozo de lagrangiano que describe el potencial de un campo escalar complejo ϕ, el campo de Higgs, que contiene un mínimo no trivial. Este campo escalar es un doblete de $\mathrm{SU}(2)_L$ con hipercarga $Y = 1/2$, y su componente neutra se acopla a los bosones gauge $W^\pm$ y Z a través de la interacción débil. Dicho mecanismo se basa en la ruptura espontánea de la simetría electrodébil

$U(1)_Y \otimes SU(2)_L$, que ocurre cuando el campo de Higgs adquiere un valor esperado en el vacío no nulo $\langle 0 \left| \phi \right| 0 \rangle = v/2$. Al expandir el campo de Higgs alrededor de su mínimo, se obtiene un bosón escalar masivo, el bosón de Higgs, que se acopla a los bosones gauge $W^{\pm}$ y Z a través de la interacción débil, otorgándoles masa:

$$m_Z = \frac{vg}{2\cos\theta_W} \ , m_W = \frac{m_Z}{\cos\theta_W} = \frac{vg}{2} \, . \tag{R.5}$$

Por su lado, los fermiones adquieren masa a través de la interacción con el campo de Higgs a través de un término de Yukawa. Este término es proporcional al valor esperado del vacío v y al acoplamiento de Yukawa y_f del fermión f, que se determina experimentalmente midiendo las masas de los fermiones $m_f = y_f v/\sqrt{2}$.

Limitaciones del modelo estándar

El SM describe con precisión las partículas fundamentales y sus interacciones, pero presenta problemas teóricos y observacionales aún abiertos, de los cuáles la existencia de materia oscura (DM) y la jerarquía de masas son los más relevantes para esta tesis.

La DM es un componente del Universo que no interactúa con la luz, pero se manifiesta a través de su influencia gravitacional. Se estima que representa aproximadamente el 27% de la energía del Universo, mientras que la materia ordinaria solo representa alrededor del 5% (el resto correspondería a la energía oscura, cuya naturaleza también es desconocida). Existen diversas evidencias indirectas de su existencia, como la curva de rotación de las galaxias, la radiación cósmica de fondo y la formación de estructuras a gran escala. Sin embargo, no se ha detectado directamente en experimentos, lo que plantea interrogantes sobre su naturaleza y composición. Entre sus candidatos más plausibles, se encuentran los *WIMPs* (Weakly Interacting Massive Particles), que son partículas masivas, neutras y no relativistas que interactúan débilmente con la materia ordinaria. Acorde con las medidas del fondo cósmico de microondas, se estima que la masa de los WIMPs debe estar en el rango de unos 10 GeV a varios TeV. Sin embargo, hasta la fecha no se ha medido ninguna partícula que cumpla con estas características.

Por otro lado, el problema de la jerarquía de masas se refiere a la diferencia entre la escala electrodébil, alrededor de la masa medida del bosón de Higgs 125.11 ± 0.11 GeV [106], y la escala de Planck (10^{19} GeV), en la cual los efectos cuánticos de la fuerza gravitatoria comienzan a ser relevantes. A escalas tan altas, las correcciones radiativas a la masa del Higgs son demasiado grandes y un ajuste muy forzado o "antinatural" sería necesario para obtener una predicción acorde con la masa medida. Por tanto, este es un problema de

naturalidad que no refleja una incosistencia del Modelo Estándar en sí mismo, sino que aparece al suponer la existencia de nueva física a escalas muy superiores a la electrodébil. En este contexto aparecen ciertas teorías que proponen nuevas partículas a escalas no tan alejadas. Ejemplos de este tipo de teorías más allá del Modelo Estándar (beyond SM ó BSM) son los modelos de *Composite Higgs* [109] y los modelos de *Little Higgs* [110, 111]. Entre los nuevos estados que surgen en estas teorías, los *Quarks Vectoriales* (VLQs) emergen como una característica común. Los VLQs tendrían componentes levógira y dextrógira con las mismas transformaciones bajo el grupo gauge electrodébil. Con espín 1/2 y carga de color, los VLQs son los BSM quarks más simples aún permitidos por los resultados experimentales, ya que los términos de masa de los VLQs pueden añadirse al lagrangiano del SM respetando la invariancia gauge, sin depender del mecanismo de Higgs.

R.2 Dispositivo experimental: LHC y ATLAS

Los datos analizados en esta Tesis corresponden a colisiones protón-protón que fueron registrados por el experimento ATLAS [93] durante el período de adquisición de datos del Run 2 del Gran Colisionador de Hadrones (LHC [137, 138], por sus siglas en inglés), el cual tuvo lugar de 2015 a 2018. Para poder interpretar correctamente los datos es necesario comprender las condiciones en que se producen las colisiones en el LHC, así como el funcionamiento del detector ATLAS, que es el encargado de registrar las colisiones.

Gran colisionador de hadrones (LHC)

El LHC [137, 138] es el acelerador de partículas más grande y potente del mundo, siendo parte de la Organización Europea para la Investigación Nuclear (CERN) [139]. Ubicado en la frontera entre Francia y Suiza, cerca de Ginebra, el acelerador se encuentra a $\sim$ 100 m bajo tierra y tiene una circunferencia de 27 km. El LHC está diseñado para acelerar protones o iones pesados a energías muy altas en dos haces con direcciones opuestas. Los haces se cruzan en cuatro puntos de intersección. Para colisiones protón-protón, el haz se divide en diferentes paquetes con 10^{11} protones cada uno, separados temporalmente por 25 ns.

Cuatro experimentos están ubicados en los puntos de intersección: ATLAS [93], CMS[94], LHCb [141] y ALICE [142]. Los detectores ATLAS y CMS son detectores de propósito general, cuyo primer objetivo era descubrir el bosón de Higgs. Sin embargo, estos detectores están diseñados para estudiar los diversos procesos físicos provenientes de colisiones protón-protón, incluyendo medidas de precisión del SM y la búsqueda de nuevas partículas.

A pesar de sus objetivos comunes, los dos experimentos tienen diseños y estrategias diferentes, lo que permite realizar comprobaciones de los resultados obtenidos entre ellos. El detector LHCb está enfocado en el estudio de la física del sabor relacionada con el quark b. Este detector tiene un diseño realizado para cubrir la región hacia delante, ya que se espera que los hadrones-b se produzcan principalmente cerca del haz en colisiones protón-protón. El detector ALICE está diseñado para estudiar las propiedades del plasma de quarks y gluones producido en colisiones de iones pesados. Este estado de la materia, en el cual dominan las interacciones fuertes, permite reproducir las condiciones de los primeros momentos del Universo después del Big Bang.

El objetivo final del acelerador LHC es proveer a estos cuatro experimentos de un gran número de colisiones energéticas para aumentar la probabilidad de que ocurran procesos raros. Por lo tanto, las dos magnitudes principales que determinan el rendimiento del LHC, y de cualquier otro colisionador enfocado en estudios de física de altas energías, son la *energía en el centro de masa* y la *luminosidad*.

La energía de una colisión de dos haces en direcciones opuestas se mide en el sistema del centro de masa, en el cual los dos haces tienen la misma energía ($E_{cm} = 2E_{beam}$) y el momento en el plano transversal es cero. Cuanto mayor sea la energía del haz, mayor será la energía de la colisión, y más probable será la producción de procesos interesantes que contengan partículas pesadas.

La luminosidad es la cantidad que mide la capacidad de un acelerador para producir colisiones por unidad de tiempo y área. Dado que los procesos interesantes suelen ser muy raros (baja sección eficaz de producción), alcanzar altas luminosidades es crucial para medir un número razonable de sucesos. Así, la tasa de colisiones puede definirse como $R = \sigma \times \mathcal{L}$, donde σ es la sección eficaz y $\mathcal{L}$ es la *luminosidad instantánea*. Integrando la luminosidad instantánea a lo largo del período de adquisición de datos, se obtiene la *luminosidad integrada*, con unidades de fb^{-1} (femtobarn inverso), a partir de la cual se puede estimar el número total de sucesos de cualquier proceso con sección eficaz σ'.

Otro concepto importante para los colisionadores es el *pile-up* (μ), que es el número de interacciones que ocurren en un único cruce de paquetes. Dado que la tasa de colisiones puede expresarse como $R = \mu \times f$, teniendo en cuenta la ecuación anterior de la tasa de colisiones, el pile-up puede calcularse como $\mu = \sigma \times \mathcal{L}/f$, donde f es la frecuencia de los cruces de paquetes. Aunque un pile-up alto permite aumentar la probabilidad de que ocurran procesos raros, también es un problema para la reconstrucción de las colisiones relevantes, ya que el detector tendrá que procesar un gran número de partículas provenientes de diferentes interacciones en el mismo cruce de paquetes.

Los datos analizados en esta Tesis corresponden a una luminosidad integrada de 139 fb^{-1} de colisiones protón-protón a una energía en el centro de masas de 13 TeV, que fueron registradas por el experimento ATLAS durante el

período de adquisición de datos del Run 2 del LHC, de 2015 a 2018. El pile-up fue en promedio $\mu \sim 25$ durante este período.

Detector ATLAS

El detector ATLAS [151] es un detector de propósito general ubicado en uno de los cuatro puntos de interacción del LHC, con una forma toroidal cuyas dimensiones son 25 m de diámetro y 44 m de longitud, con un peso de 7000 toneladas. Fue diseñado inicialmente para descubrir el bosón de Higgs, pero también se utiliza para estudiar una amplia gama de procesos físicos provenientes de colisiones protón-protón, incluyendo medidas de precisión del Modelo Estándar y la búsqueda de nuevas partículas.

Para reconstruir los diferentes tipos de partículas producidas en las colisiones, el detector ATLAS está compuesto por varios subdetectores con diferentes características, que están dispuestos en capas cilíndricas alrededor del haz, junto con detectores en las regiones de delantera y trasera para cubrir el ángulo sólido completo. También se utiliza un sistema de adquisición de datos para seleccionar los sucesos más interesantes para el análisis posterior, reduciendo la cantidad de datos a almacenar y procesar.

Detector Interno (ID): este es el subdetector más interno, que está ubicado dentro de un imán solenoidal que genera un campo magnético de 2 T. El ID se utiliza para medir el momento de las partículas cargadas e identificarlas, y está compuesto por tres subdetectores: el detector de píxeles, el detector de trazas con semiconductores y el detector de trazas por radiación de transición.

Calorímetros: estos están colocados después del imán solenoidal que rodea al ID, siendo la parte más pesada del detector ATLAS. Son instrumentos cuya respuesta al paso de partículas es la producción de una señal proporcional a la energía de la partícula, para lo cual es necesario una absorción total de la partícula dentro del material [156]. Para lograr esto, las capas con detectores (activas) se alternan con materiales muy densos (pasivos) cuyo único propósito es detener las partículas. El detector ATLAS tiene dos tipos de calorímetros: el calorímetro electromagnético (ECAL) y el calorímetro hadrónico (HCAL). El ECAL recoge señales provenientes de la ionización producida por las partículas cargadas en el material activo. El HCAL mide las partículas secundarias provenientes de la desexcitación que sufren los núcleos tras el impacto de los hadrones.

Espectrómetro de Muones (MS): esta es la parte más externa y más grande del detector ATLAS. Está diseñado para medir las trayectorias de los muones, que escapan de los calorímetros sin perder toda su energía. De forma

simular al ID, aunque independiente, las trayectorias de los muones se curvan en el MS debido al campo magnético generado por un sistema de imanes toroidales.

Sistema de selección de sucesos (*trigger*, en inglés): el *trigger* es una parte fundamental en el sistema de adquisición de datos (DAQ) de cualquier tipo de experimento, pero se vuelve crucial para los experimentos del LHC ya que es técnicamente imposible registrar todas las colisiones producidas. Las colisiones de ATLAS durante el Run-2 fueron filtradas en línea con un sistema de *trigger* de dos niveles [159–161]: el *trigger* de Nivel-1 (L1) y el *trigger* de Alto Nivel (HLT). El *trigger* L1 está integrado a nivel de hardware y maneja información de baja granularidad de los calorímetros y las cámaras de muones dedicadas para decidir rápidamente si un suceso es filtrado o no. El HLT es un software que refina la selección utilizando la salida del *trigger* L1, reconstruyendo el suceso completo y aplicando selecciones más sofisticadas.

R.3 Simulación y reconstrucción de sucesos

Fenomenología y modelización de las colisiones de protones

Para generar sucesos simulados con métodos Monte Carlo (MC), es necesario comprender los distintos tipos de fenómenos que ocurren durante las colisiones de protones. Los protones son un tipo de hadrones que contienen tres quarks de valencia (uud) y un mar de quarks provenientes de la división de gluones. Dado que la QCD no es perturbativa a las energías dentro del protón, es difícil modelar estos sistemas complejos, lo cual es el punto de partida de la cadena de generación. El *modelo de partones* es el mejor enfoque en este contexto. Este modelo fenomenológico asume que los hadrones están formados por constituyentes puntuales, conocidos como partones, donde cada tipo de partón tiene una probabilidad de llevar una fracción de momento x_i, a una cierta escala de energía Q, dada por su Función de Densidad de Probabilidad (PDF, por sus siglas en inglés).

En colisiones suficientemente energéticas, un partón de cada protón interactúa independientemente de los otros partones en el protón. Esto permite factorizar la sección eficaz de las colisiones de protones en dos términos: un término universal que incluye las PDFs de los partones en el estado inicial, y otro término que incluye la sección eficaz del *hard scattering*, que describe la interacción entre los partones. La sección eficaz del hard scattering se calcula utilizando QCD perturbativa, y es una función de las fracciones de momento de los partones que interaccionan, x_i y x_j, y de una escala de factorización μ_F que representa el límite entre bajas y altas energías. La serie de perturbación se expande en términos de la constante de acoplamiento de la interacción fuerte

α_s, donde órdenes más altos corresponden a bucles virtuales adicionales o más radiación de gluones o quarks, con respecto al diagrama de nivel árbol del proceso.

Los diagramas de Feynman permiten calcular la sección eficaz del hard scattering con generadores de elementos de matriz (ME) hasta cierto orden de perturbación en α_s, como MadGraph o Powheg. Dado que los cálculos de ME no pueden modelar la emisión de partones colineales de baja energía, estos generadores se conectan con algoritmos de *parton shower* (PS), como Pythia y Herwig, para simular la radiación de partones adicionales en el estado final en cada orden de perturbación. El PS evoluciona hasta que la energía alcanza la escala de hadronización $q^2 = Q_0^2 \sim 1$ GeV, lo que lleva a la formación de los hadrones en el estado final. La hadronización también es un proceso no perturbativo, para el cual se implementan dos modelos fenomenológicos diferentes en los generadores MC: el *modelo de clúster* y el *modelo Lund*, implementados en Herwig y Pythia, respectivamente.

Finalmente, la desintegración de los hadrones pesados, como los mesones B, se simula después del PS y la hadronización con el generador EvtGen [176]. Además de las partículas del estado final provenientes del hard scattering, también se añaden componentes menos energéticos como un suceso subyacente (UE), tales como interacciones múltiples de partones (MPI) y remanentes del haz.

Simulación del detector

La salida de los generadores MC es una lista de cuadrimomentos para todas las partículas estables en el estado final de la colisión protón-protón. Esta etapa de la generación de sucesos se conoce como el *nivel truth* o *nivel de partícula*. Para comparar los sucesos simulados con los datos experimentales, es necesario simular la respuesta del detector ATLAS a las partículas.

El software de simulación del detector se basa en Geant4 [183], que modela la interacción de las partículas y sus productos de desintegración con los materiales activos y pasivos del detector ATLAS. La *simulación completa* [182] es una tarea altamente intensiva donde la respuesta del calorímetro requiere la mayor cantidad de recursos computacionales. La llamada *simulación rápida* (AFII [184, 185]) se implementa frecuentemente para muestras alternativas, haciendo uso de técnicas de simulación más rápidas y menos refinadas, especialmente para el desarrollo de las cascadas de partículas en los calorímetros.

Reconstrucción de objetos

La reconstrucción de los objetos producidos en las colisiones es un paso crucial para el análisis de los datos. La información registrada por el detector es

una colección de señales electrónicas que necesitan ser traducidas en objetos reconstruidos y cantidades físicas, para lo cual se utilizan los mismos algoritmos tanto para los datos como para las muestras de MC. Los objetos reconstruidos de interés para esta Tesis se explican a continuación.

Trazas y vértices: las trazas son las trayectorias reconstruidas de las partículas cargadas determinadas a partir de los depósitos en el ID. Las trazas siguen trayectorias curvas debido al campo magnético, y su punto más cercano a la línea del haz se identifica como su vértice de origen. El vértice primario (PV) es aquel con la mayor suma cuadrática de momento transverso de todas las trazas asociadas a éste.

Electrones y muones: los electrones se identifican a partir de los depósitos de energía en los calorímetros y las trazas asociadas en el ID. La identificación de muones utiliza principalmente los impactos del ID y el MS, pero también puede combinarse con información de los calorímetros. En ambos casos, se establece un criterio de aislamiento para reducir la cantidad leptones *falsos*. Para considerar que sus trazas provienen del hard scattering, deben ser compatibles con el PV.

Jet ($R = 0.4$): cuando un quark o gluón es producido en las colisiones, el proceso de PS y hadronización produce una cascada o *jet* de partículas contenidas en un cono de radio R, centrado alrededor de la dirección del quark o gluón inicial. Los jets necesitan definirse a partir de información a nivel de detector, para lo cual el algoritmo más popular en ATLAS es el algoritmo anti-k_t [234] con $R = 0.4$. Se utilizan técnicas adicionales para discernir si un jet proviene de un gluón o un quark, y en este último caso, para identificar su sabor. Los más relevantes son aquellos algoritmos que determinan la probabilidad de que un jet provenga de un quark b (denominado b-jet), como los algoritmos MV2c10 [324] y DL1r [244], los cuales usan información de la subestructura del jet, así como de sus trazas y vértices asociados.

Jet de gran radio ($R = 1.0$): partículas pesadas y con alto momento, como los bosones de Higgs o los quarks top, se desintegran hadrónicamente produciendo hadrones generalmente muy colimados que pueden ser reconstruidos como jets de gran tamaño utilizando el algoritmo anti-k_t con $R = 1.0$. Cada partícula pesada produce una topología particular, de modo que las variables de subestructura de los jets de radio grande pueden usarse para definir un criterio basado en cortes o en redes neuronales para identificar la partícula pesada original.

Momento transverso faltante ($E_{\mathrm{T}}^{\mathrm{miss}}$): se define como la suma vectorial negativa de los momentos transversales de todos los objetos reconstruidos en el suceso, incluyendo las trazas asociadas al PV pero que no coinciden con ningún objeto reconstruido. El $E_{\mathrm{T}}^{\mathrm{miss}}$ se utiliza para identificar sucesos que producen partículas que has escapado del detector, como neutrinos o candidatos a DM.

Dado que los datos simulados y experimentales no son idénticos, los algoritmos de reconstrucción e identificación de objetos podrían llevar a un sesgo en las eficiencias de selección, lo cual necesita corregirse mediante diferentes técnicas de calibración, como el método de *tag-and-probe* [231] para electrones y muones.

Al realizar un análisis, es necesario concretar la definición de los objetos considerados en la selección de sucesos. Para ello, se encuentran los puntos de trabajo y las eficiencias de selección de los algoritmos de reconstrucción e identificación que permiten optimizar la sensitividad del análisis.

R.4 Búsqueda de sucesos mono-top

Este análisis, denominado Monotop [1], explora los datos registrados por el detector ATLAS durante el período Run 2 del LHC, con una luminosidad integrada total de 139 fb^{-1}, para buscar sucesos con un gran momento transverso faltante junto con un único quark top que se desintegra a hadrones. Esta topología de *mono-top* se espera en colisiones que producen partículas de DM, ya que no se espera que estas interactúen con el detector y se necesita un objeto adicional para poder registrar el suceso. También se explora una interpretación en términos de una búsqueda de quarks vectoriales (VLQ), ya que la producción individual de un quark top vectorial (o quark T) puede producir una topología de mono-top. Esto ocurre cuando el quark T se desintegra en un quark top y un bosón Z, que a su vez se desintegra de manera invisible en neutrinos.

Se utilizan muestras simuladas para modelar los procesos de señal y fondo, evaluar la aceptación del detector, proporcionar una comparación con los datos experimentales y realizar inferencias estadísticas. La colaboración realiza la generación de estos sucesos siguiendo la cadena de simulación descrita en la sección anterior. Un resumen de la configuración de los fondos simulados se presenta en la Tabla R.5.

Muestras de Materia Oscura

Se generaron muestras simuladas correspondientes a dos modelos simplificados que producen partículas de DM utilizando MadGraph [186], uno con un mediador escalar y otro con un mediador vectorial. El *modelo de mediador escalar* incorpora un bosón escalar con carga eléctrica $+2/3$ y carga de color, ϕ, que

Proceso	Generador ME	PDF ME	PS y hadronización	UE	Cálculo de sección eficaz
$t\bar{t}$	POWHEG BOX v2	NNPDF3.0NLO	PYTHIA 8.230	A14	NNLO+NNLL [193–198]
Single top	POWHEG BOX v2	NNPDF3.0NLO	PYTHIA 8.230	A14	NNLO+NNLL [202–204]
$t\bar{t}V$ ($V = W/Z$); tZq	MG5AMC@NLO2.3.3	NNPDF3.0NLO	PYTHIA 8.230	A14	NLO [187]
V+jets ($V = W/Z$)	SHERPA2.2.1	NNPDF3.0NLO	SHERPA	Default	NNLO [213]
Diboson	SHERPA2.2.1	NNPDF3.0NLO	SHERPA	Default	NLO
$t\bar{t}H$	POWHEG BOX v2	NNPDF3.0NLO	PYTHIA 8.230	A14	NLO [187]
tWZ	MG5AMC@NLO2.3.3	NNPDF3.0NLO	PYTHIA 8	A14	NLO [187]
$t\bar{t}WW$, $t\bar{t}t\bar{t}$	MADGRAPH 5	NNPDF2.3LO	PYTHIA 8	A14	LO [187]

Table R.5: Resumen de las muestras nominales de simulaciones de fondo. La producción de quarks top individuales incluye el canal-t, el canal-tW y el canal-s. La parte inferior corresponde a muestras de fondo adicionales que se consideran exclusivamente en los análisis HTZT o OSML, los cuáles son presentados secciones posteriores.

se produce como una resonancia en el canal-s y se desintegra en un quark top y una partícula de DM de espín-1/2. El *modelo de mediador vectorial* se caracteriza por una interacción de corriente neutra con cambio de sabor (FCNC, por sus siglas en inglés) en la que un hipotético mediador vectorial masivo V conecta los quarks tipo *up* de la primera y segunda familias con el quark top. El mediador V se produce ya sea en el canal-s o en el canal-t, y se desintegra en un par de partículas de DM. Los diagramas de Feynman de estos dos modelos simplificados se muestran en la Figura R.10.

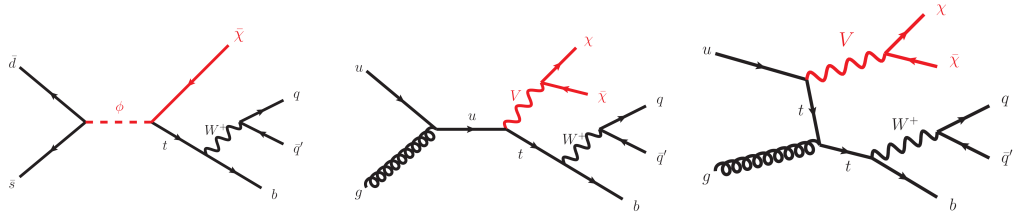

Figure R.10: Diagramas para los modelos simplificados considerados en la búsqueda de Materia Oscura: (a) mediador escalar, (b) mediador vectorial en el canal-s, y (c) mediador vectorial en el canal-t.

Estos modelos simplificados se caracterizan por parámetros libres que definen la interacción entre la DM y las partículas del SM. Para el modelo de mediador escalar, los parámetros incluyen las masas del mediador escalar (m_ϕ) y la partícula de DM (m_χ), la constante de acoplamiento λ_q (interacción con partículas del SM) y el parámetro de mezcla y_χ (interacción con el quark top). Para el modelo de mediador vectorial, los parámetros incluyen las masas del

mediador vectorial (m_V) y la partícula de DM (m_χ), el acoplamiento a (interacción con el quark top vía FCNC) y el acoplamiento g_χ (controla la desintegración en pares de DM). Se generaron un total de 256 puntos de señal para ambos modelos, cubriendo el espacio de parámetros con alta granularidad. Para reducir los costes computacionales, la mayoría de las muestras se simularon a *nivel truth*, y se utilizó una técnica de reponderación para estimar las distribuciones a *nivel reco* para estas muestras.

Muestras de Quarks Vectoriales

La búsqueda de VLQs en el LHC puede clasificarse ampliamente en dos modos de producción: producción en pares y producción individual. La producción en pares domina para masas bajas [112] y está mediada por la interacción fuerte, mientras que la sección eficaz del modo de producción individual comienza a dominar para valores superiores a 1 TeV, pero está mediada por la interacción electrodébil. La producción individual de un quark T se genera con MadGraph de acuerdo con el modelo fenomenológico descrito en Ref. [114], que permite realizar búsquedas independientes de VLQs mediante un lagrangiano simplificado.

Considerando el quark T en el límite de grandes masas, que es el caso para estas búsquedas, dicho lagrangiano puede ser re-parametrizado en términos de cinco parámetros que controlan la cinemática de los procesos: la masa del quark T m_T, el acoplamiento κ_T, y los acoplamientos relativos ξ_W, ξ_Z y ξ_H a los bosones W, Z y H, respectivamente, tales que $\sum_{V=W,Z,H} \xi_V = 1$. Mientras que κ_T representa la intensidad del acoplamiento electrodébil del quark T a los quarks del SM, los parámetros ξ_V corresponden a las fracciones de desintegración del quark T en $T \to Vq$.

Los valores específicos de los acoplamientos relativos ξ_V están asociados a una representación SU(2) concreta del quark T. Por ejemplo, los escenarios de singlete y doblete corresponden a $\{\xi_W, \xi_Z, \xi_H = 0.5, 0.25, 0.25\}$ y $\{\xi_W, \xi_Z, \xi_H = 0, 0.5, 0.5\}$, respectivamente. Esta búsqueda se centra en la representación de singlete, ya que esta es la dominante en la producción de sucesos mono-top, como se muestra en la Figura R.11.

Las muestras de señal se generaron para un valor predeterminado de κ_T igual a 1.0 y diferentes valores de la masa del quark T, m_T, entre 1.1 y 2.7 TeV, en pasos de 0.2 TeV. Con el fin de aumentar la granularidad del espacio de parámetros, se calculan pesos internos durante la generación que permiten interpolar los puntos de masa intermedios y cubrir un rango de κ_T hasta 0.1.

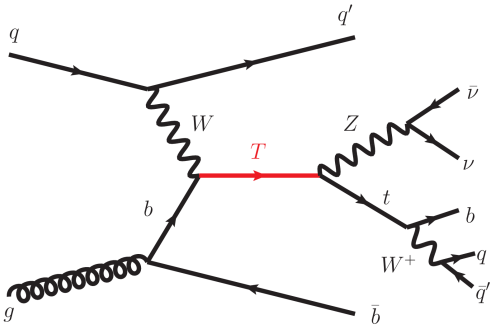

Figure R.11: Diagramas de Feynman para la producción individual de un quark top vectorial. El quark T se desintegra en un quark top y un bosón Z, que a su vez se desintegra de manera invisible en neutrinos.

Selección de sucesos y definición de regiones

Se aplican criterios de *pre-selección* a todos los sucesos del conjunto de datos, diseñados para garantizar que el estado final de los sucesos sea compatible con la topología esperada de la señal. Los criterios de esta búsqueda son:

- Se aplica un veto a los leptones.
- Se requiere que el $E_{\mathrm{T}}^{\mathrm{miss}}$ sea mayor a 250 GeV, reduciendo drásticamente el fondo de multi-jets.
- Se requiere al menos un jet de gran radio etiquetado como top, con $p_T >$ 350 GeV, $|\eta| < 2.0$ y $m_T \in [40, 600]$ GeV, donde m_T es la masa transversa reconstruida del jet de gran radio[5].
- Se requiere una distancia angular mínima en el plano transversal entre el $E_{\mathrm{T}}^{\mathrm{miss}}$ y cualquier jet, $\Delta\phi(\mathrm{j}, E_{\mathrm{T}}^{\mathrm{miss}})$, mayor a 0.2 para suprimir la contaminación del fondo inducido por el haz (BIB) [6].

Se realiza un análisis multivariable (MVA) basado en árboles de decisión (BDT), que consiste en un algoritmo de aprendizaje automatizado que permite optimizar la identificación de sucesos de señal frente a sucesos de fondo. Utilizando la librería XGBoost [261, 262], dicho algoritmo se entrena con variables sensibles a los procesos de señal. Así, todos los sucesos simulados que cumplen con los criterios de preselección se utilizan para entrenar[7] la BDT

[5] Los cortes en la cinemática del jet de gran radio se deben al rango de calibración del algoritmo de identificación.

[6] El fondo BIB proviene de las pérdidas del haz, principalmente producidas por interacciones con el gas cerca del haz.

[7] De hecho, todos los sucesos simulados que cumplen con la preselección se utilizan tanto para el entrenamiento como para la validación utilizando el método de k-folding con $K = 5$.

para una tarea de clasificación binaria, en la cual los sucesos de señal se discriminan de los sucesos de fondo.

Se entrenan tres BDTs correspondientes a cada modelo de señal, para los cuales se utilizan los puntos de señal de referencia. Cada BDT proporciona una puntuación, o *score*, entre 0 y 1 a cada suceso, que se utiliza como una variable discriminante para definir las regiones enriquecidas en señal. Las variables correspondientes al número de b-jets, $N_{b-\text{jets}}$, y el ángulo acimutal mínimo entre un jet y el $E_{\text{T}}^{\text{miss}}$, $\Delta\phi_{\text{min}}(j, E_{\text{T}}^{\text{miss}})$, no se incluyen en el entrenamiento, ya que se utilizan por separado para dividir el espacio de fase en las regiones de señal, control y validación, como se muestra en la Figura R.12.

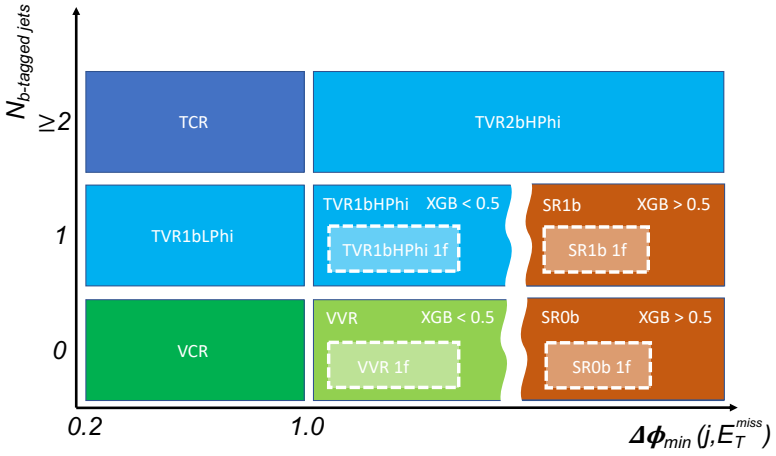

Figure R.12: Representación esquemática de las regiones de control, validación y señal. Las regiones se definen en términos de la multiplicidad de jets etiquetados como b, $N_{b\text{-tagged jets}}$, y el ángulo acimutal mínimo entre los jets de un suceso y su $E_{\text{T}}^{\text{miss}}$, $\Delta\phi_{\text{min}}(j, E_{\text{T}}^{\text{miss}})$. La notación "XGB> 0.5" indica el corte en el *score* de la BDT que define las regiones de señal, respectivamente. Estas regiones están separadas esquemáticamente por la línea vertical curva. La etiqueta "1f" indica que se requiere al menos un jet hacia adelante en el suceso. Las selecciones utilizadas para definir las regiones se describen en la Tabla **??**.

Se definen dos regiones de señal para cada modelo aplicando los siguientes cortes: un valor de XGBoost score superior a 0.5, $\Delta\phi_{\text{min}}(j, E_{\text{T}}^{\text{miss}}) > 1.0$ y 0 ó 1 b-jet, correspondientes a SR0b y SR1b, respectivamente. También se requiere al menos un jet hacia adelante para las regiones de señal del modelo VLQ.

Dado que los principales procesos de fondo que contaminan las regiones de

señal son sucesos de $t\bar{t}$ y $V+$jets, se definen dos regiones de control (CRs) para estimar sus contribuciones. Estas CRs son las mismas para los tres modelos, ya que no aplican ninguna selección en el XGBoost score. La CR dedicada a la estimación de $t\bar{t}$, denominada TCR, se define requiriendo al menos dos jets etiquetados como b y $\Delta\phi_{\min}(j, E_{\mathrm{T}}^{\mathrm{miss}}) < 1.0$. La CR para la producción de $V+$jets, denominada VCR, se define requiriendo exactamente un jet etiquetado como b y $\Delta\phi_{\min}(j, E_{\mathrm{T}}^{\mathrm{miss}}) < 1.0$.

Finalmente, se definen dos regiones de validación (VR) comunes a todos los modelos y otras dos específicas para cada modelo. Las primeras, denominadas TVR1bLPhi y TVR2bHPhi, se definen requiriendo exactamente un b-jet y $\Delta\phi_{\min}(j, E_{\mathrm{T}}^{\mathrm{miss}}) < 1.0$, y dos jets etiquetados como b y $\Delta\phi_{\min}(j, E_{\mathrm{T}}^{\mathrm{miss}}) > 1.0$, respectivamente. Las segundas, denominadas VVR y TVR1bHPhi, tienen la misma definición que las regiones de señal SR0b y SR1b, respectivamente, pero con valores de XGBoost score inferiores a 0.5. El propósito de estas VRs es validar la estimación de fondo en las proximidades de las regiones de señal, pero no se utilizan para el análisis estadístico.

Análisis estadístico

El análisis de inferencia estadística realizado hace uso de histogramas que comparan los datos experimentales con las predicciones teóricas de los procesos de señal y fondo. Estas predicciones de MC dependen de ciertos parámetros que deben estimarse a partir de los datos:

- La *normalización de la señal*, la cual viene dada por el parámetro de interés (POI), μ. Éste parámetro de normalización de la señal corresponde al cociente entre la sección eficaz medida del proceso de señal y su predicción teórica.

- Los factores de normalización de los principales fondos, $\mathrm{NF}_{t\bar{t}}$ y $\mathrm{NF}_{V+\mathrm{jets}}$, que se utilizan para normalizar los sucesos simulados de los procesos $t\bar{t}$ y $V+$jets a los sucesos de datos observados.

- Los parámetros de incertidumbre sistemática (NPs) se dividen en dos categorías: 29 de incertidumbres teóricas y 147 de incertidumbres experimentales.

De acuerdo con el Principio de Máxima Verosimilitud, la mejor estimación de estos parámetros se puede obtener maximizando la función de verosimilitud, que se define como:

$$\mathcal{L}(\mu, \boldsymbol{\theta}) = \prod_{j=1}^{N} \mathrm{Pois}(n_j|\nu_j) \prod_{k=1}^{M} \mathrm{Gauss}(a_k|\theta_k), \tag{R.6}$$

El primer término es el producto de distribuciones de Poisson para los datos observados en cada bin del histograma, donde n_j es el número de sucesos observados en el bin j y ν_j es el número esperado de sucesos en ese bin, el cual depende del POI, los NFs y los NPs. La función de verosimilitud construida para este análisis considera dos SRs con 4 bins cada una y dos CRs con 1 bin cada una, por lo que $N = 10$. El segundo término (o auxiliar) es el producto de distribuciones gaussianas, cuya media y varianza han sido estimadas previamente a partir de medidas de calibración. Se consideran $M = 176$ incertidumbres sistemáticas.

La compatibilidad del valor ajustado del POI con la hipótesis nula puede evaluarse a través del *p-value*. Pero en ausencia de excesos o incompatibilidades, es interesante cuantificar la sensitividad del análisis al proceso de señal que se busca. Esto se obtiene a partir del límite superior observado (esperado) en la normalización de la señal, μ_{up}, que representa el valor máximo del POI compatible con los datos (predicción del SM) a un nivel de confianza (ó CL) dado, establecido convencionalmente en 95% CL. Así, el límite superior observado (esperado) en la sección eficaz se define como $\sigma_{up}^{95\%CL} = \mu_{up} \times \sigma_{\text{theory}}$, donde σ_{theory} es la sección eficaz teórica del proceso de señal.

Resultados

El ajuste se repite para todos los puntos de señal disponibles, cada uno con diferentes valores de los parámetros de los modelos. Así, el espacio de parámetros se divide en dos regiones: la región excluida, con los puntos de señal para los cuales $\sigma_{\text{up}}^{95\%\text{CL}} < \sigma_{\text{theory}}$, y la región permitida, con los puntos de señal para los cuales $\sigma_{\text{up}}^{95\%\text{CL}} > \sigma_{\text{theory}}$ y que no pueden ser excluidos por el análisis. A partir de esta división, se obtienen límites de exclusión sobre los parámetros de los modelos.

Se obtienen límites de exclusión unidimensionales escaneando sobre las masas de los mediadores de los modelos de DM, m_ϕ y m_V, y sobre la masa del VLQ, m_T. Los resultados se muestran en la Figura R.13, para la cual los valores de referencia de los otros parámetros están fijados y se considera el escenario de singlete ($\mathcal{B}(T \to Zt) = 25\%$) del quark T. La línea negra sólida (discontinua) representa el límite superior observado (esperado) en la sección eficaz al 95% CL, y las bandas amarilla y verde representan la incertidumbre de $\pm 1\sigma$ y $\pm 2\sigma$ del límite superior esperado en la sección eficaz. La sección eficaz teórica del proceso de señal se muestra como una línea roja sólida, y su intersección con la línea del límite superior observado (esperado) indica el máximo valor de masa observado (esperado) que puede ser excluido al 95% CL.

La sección eficaz del modelo de mediador escalar de DM se excluye para valores superiores a ~ 2 fb, lo que permite excluir masas del mediador escalar

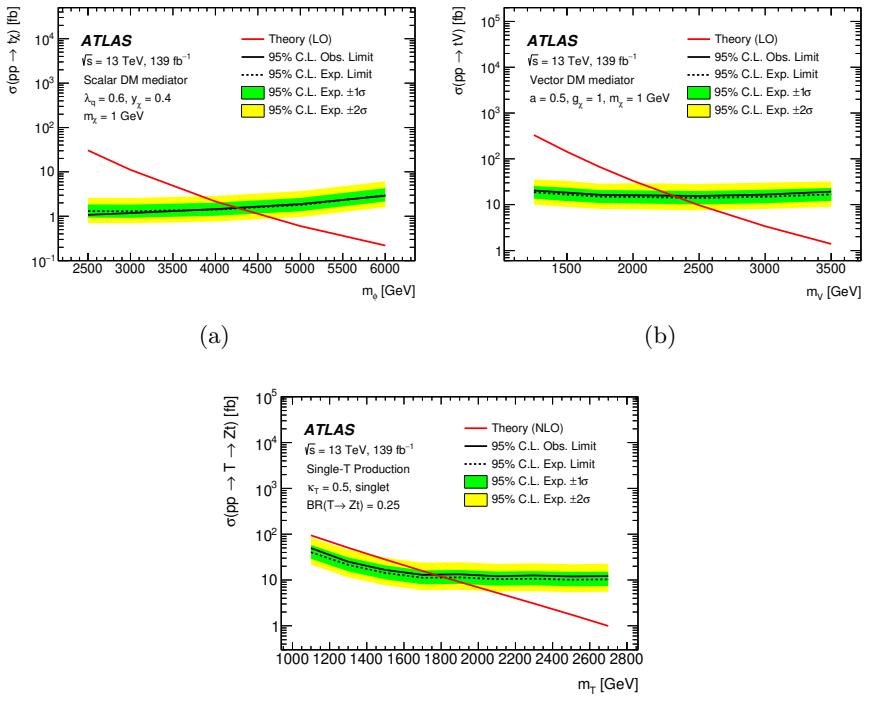

Figure R.13: Límites superiores al 95% CL en la sección eficaz de los modelos de señal considerados en función de: (a) la masa del mediador escalar m_ϕ del modelo de DM (para parámetros del modelo fijos de $\lambda_q = 0.6$, $y_\chi = 0.4$ y $m_\chi = 1$ GeV), (b) la masa del mediador vectorial m_V del modelo de DM (para $a = 0.5$, $g_\chi = 1$ y $m_\chi = 1$ GeV) y (c) la masa del quark T (para $\kappa_T = 0.5$).

por debajo de 4.3 TeV. Para el modelo de mediador vectorial de DM, la sección eficaz se excluye para valores superiores a $\sim$ 20 fb, lo que permite excluir masas del mediador vectorial por debajo de 2.3 TeV. Estos límites en la masa corresponden a una mejora de alrededor de 800 GeV y 300 GeV, respectivamente, con respecto a los resultados anteriores [260]. Finalmente, la sección eficaz de la producción individual del quark T, multiplicada por la fracción de desintegración a Zt, se excluye para valores superiores a $\sim$ 15 fb, lo que permite excluir masas por debajo de 1.8 TeV.

También se pueden escanear los límites en función de algún otro parámetro de los modelos, que junto a las masas de los mediadores y del VLQ, pueden interpretarse a través de mapas bidimensionales, donde el eje Z representa el límite superior observado en la normalización de la señal. Las Figuras R.14,R.15,R.16 muestran los límites de exclusión en diferentes planos del espacio de parámetros

de los modelos.

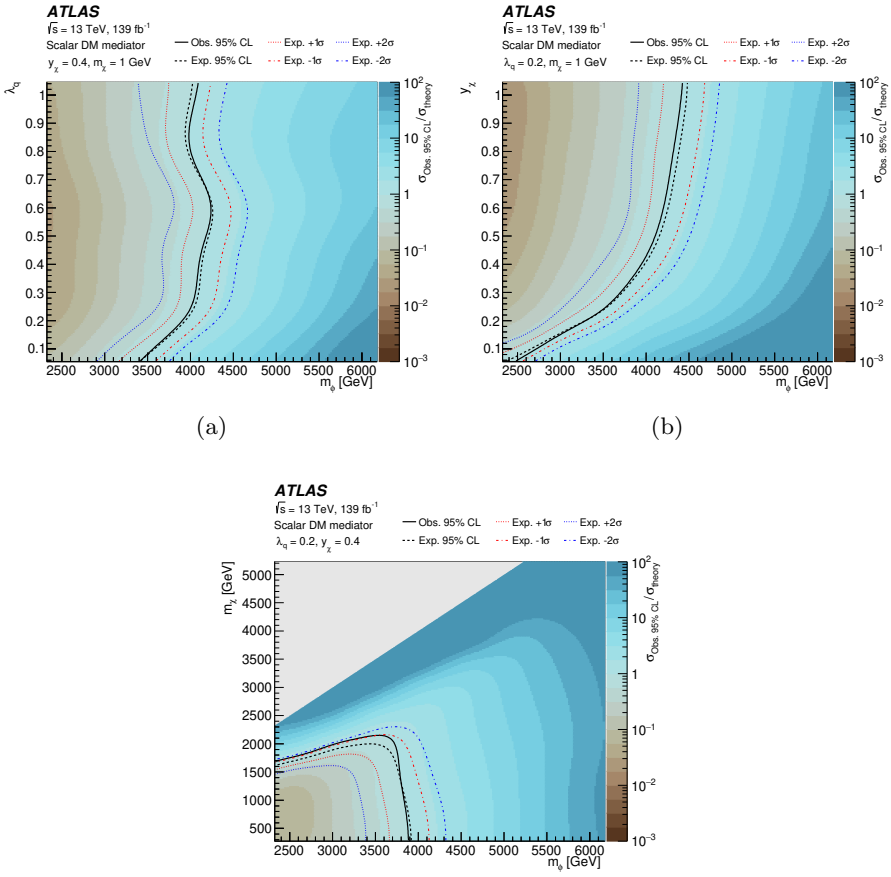

Figure R.14: Límites superiores al 95% CL observados en la normalización de la señal del modelo de DM mediado por un escalar en tres planos del espacio de parámetros del modelo: (a) (m_ϕ, λ_q), (b) (m_ϕ, y_χ) y (c) (m_ϕ, m_χ). Los límites de exclusión observados (esperados) al 95% CL sobre los parámetros se representan como líneas sólidas (discontinuas). También se muestran las desviaciones estándar de ± 1 y ± 2 alrededor del límite esperado.

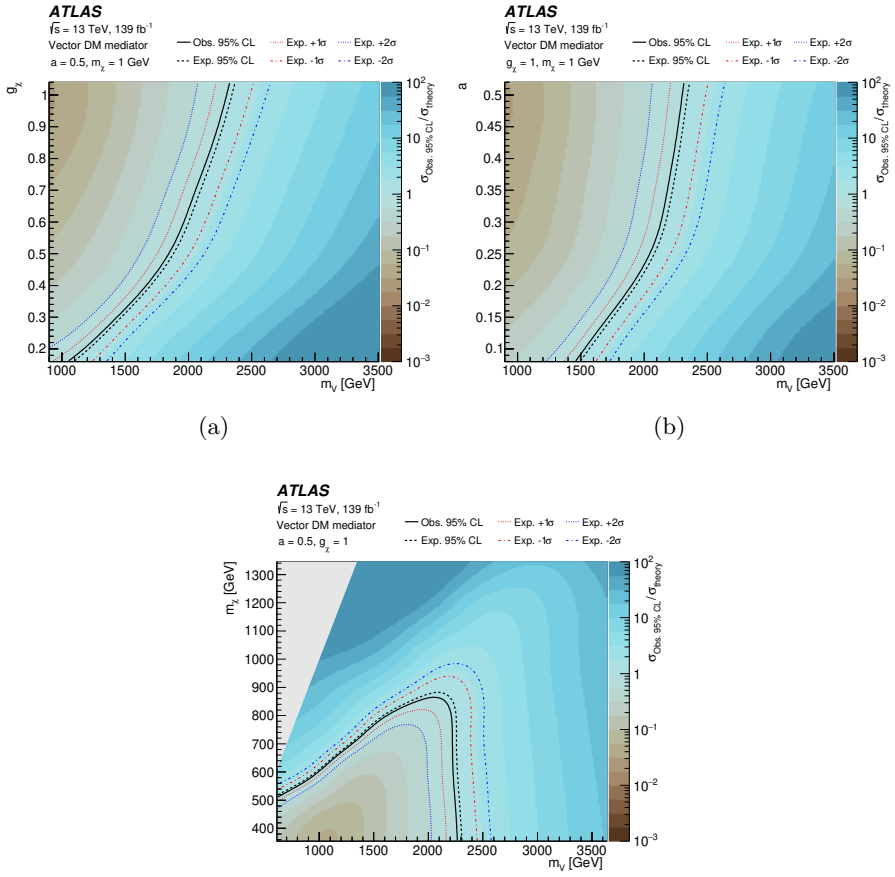

Figure R.15: Límites superiores observados al 95% CL en la normalización de la señal del modelo de DM mediado por un vector en tres planos del espacio de parámetros del modelo: (a) (m_V, g_χ), (b) (m_V, a) y (c) (m_V, m_χ). Los límites de exclusión observados (esperados) al 95% CL sobre los parámetros se representan como líneas sólidas (discontinuas). También se muestran las desviaciones estándar de ± 1 y ± 2 alrededor del límite esperado.

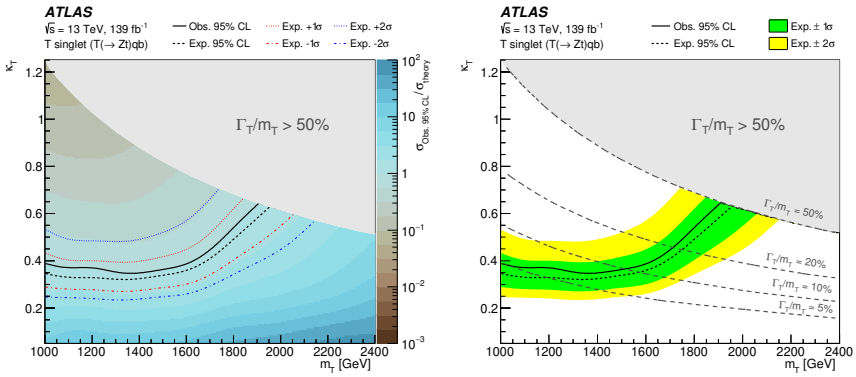

Figure R.16: Límites de exclusión en términos de la constante de acoplamiento universal κ_T y la masa del quark T en el escenario de singlete SU(2), en el régimen donde $\Gamma_T/m_T \leq 50\%$, para el cual los cálculos teóricos son válidos. (a) Límites superiores observados al 95% CL en la normalización de la señal como función de κ_T y la masa del quark T. Los límites de exclusión observados (esperados) al 95% CL sobre los parámetros se representan como líneas sólidas (discontinuas), con todos los valores de κ_T por encima de la línea de contorno negra siendo excluidos en cada punto de masa. También se muestran las desviaciones estándar de ± 1 y ± 2 alrededor del límite esperado. (b) Límites de exclusión esperados (línea discontinua) y observados (línea sólida) al 95% CL en κ_T y la masa del quark T. Diferentes hipótesis de Γ_T/m_T se muestran como líneas discontinuas. Las bandas sombreadas corresponden a desviaciones estándar de ± 1 y ± 2 alrededor del límite esperado.

R.5 Combinación de búsquedas de quarks vectoriales

Esta sección presenta la primera combinación de búsquedas de la producción individual de un quark top vectorial [2]. Ésta combinación añade a la búsqueda Monotop presentada anteriormente otras dos búsquedas, denominadas HtZt [129] y Osml [128]. Estos análisis también hacen uso del conjunto completo de datos del Run 2 recopilados por el experimento ATLAS en el LHC, a una energía de colisión de $\sqrt{s} = 13$ TeV y una luminosidad integrada de 139 fb^{-1}.

Basándose en el mismo modelo de VLQ, la combinación de los tres análisis explora cuatro modos de producción diferentes: $T(\rightarrow Zt)qb$, $T(\rightarrow Zt)qt$, $T(\rightarrow Ht)qb$ y $T(\rightarrow Ht)qt$. Una ilustración del diagrama de Feynman a nivel árbol se muestra en la Figura R.17. Los análisis son ortogonales por construcción acorde con el número de leptones en el estado final: el análisis Monotop

considera el modo de desintegración Zt en el canal de 0 leptones, el análisis HtZt explora los modos de desintegración Ht y Zt en el canal de 1 leptón, y el análisis Osml corresponde al modo de desintegración Zt en los canales de 2 y 3 leptones. Ambas búsquedas HtZt y Osml son sensibles a las representaciones de singlete y doblete SU(2) del quark T.

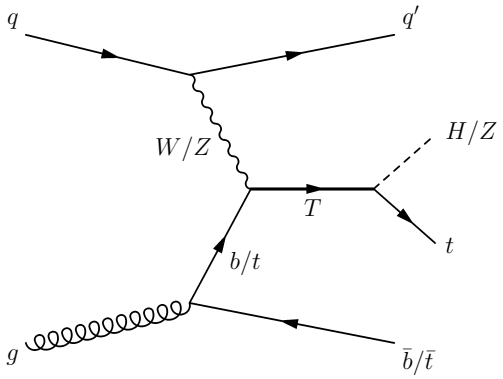

Figure R.17: Diagrama de Feynman a orden árbol de la producción singular de un quark vectorial T en asociación con un quark t o b y su posterior desintegración en Ht o Zt.

En el análisis HtZt, los sucesos se preseleccionan exigiendo la presencia de exactamente un leptón con $p_{\mathrm{T}} > 30\,\mathrm{GeV}$, al menos cinco jets de radio pequeño, y al menos un jet etiquetado como b. El principal fondo en las regiones de ajuste son los procesos $t\bar{t}$+jets. Las regiones de ajuste están diseñadas para ser puras en uno o más de los cuatro modos de producción de la señal, o en procesos de fondo específicos.

El análisis Osml se divide en dos canales ortogonales que se combinan estadísticamente para obtener el resultado final: un canal con exactamente dos leptones (dileptón) y un canal ortogonal con al menos tres leptones (trileptón). Ambos canales requieren una preselección que incluye un par de leptones de carga opuesta y mismo sabor con una masa invariante dentro de una ventana de 10 GeV alrededor de la masa del bosón Z. El fondo principal en el canal de dileptón proviene de la producción de bosones Z en asociación con jets, mientras que los procesos de dibosones y $t\bar{t}$ en asociación con un bosón vectorial dominan la composición del fondo en el canal de trileptón.

Resultados de la combinación

Se construye una función de verosimilitud combinada como un producto de términos de probabilidad de Poisson sobre todos los bins considerados en cada análisis. De manera similar a los ajustes individuales, el parámetro de interés

en el ajuste combinado es la normalización de la señal, μ. Sin embargo, en el ajuste combinado, μ escala la sección eficaz total de los cuatro modos de producción considerados: $T(\to Zt)qb$, $T(\to Zt)qt$, $T(\to Ht)qb$ y $T(\to Ht)qt$.

Todos los factores de normalización (NFs) y las incertidumbres teóricas se consideran no correlacionados para la combinación. Aquellas incertidumbres sistemáticas experimentales que son comunes a las tres búsquedas se tomaron como correlacionadas. Sin embargo, hay algunas fuentes de incertidumbres experimentales que son específicas de cada canal o corresponden a criterios de calibración alternativos que vienen representados por un conjunto distinto de NPs, en cuyo caso se considera un esquema no correlacionado entre los canales. Sin embargo, no se ha observado ningún efecto en los resultados finales correspondiente a esta elección.

De manera equivalente a los resultados mostrados previamente para el análisis MONOTOP, los límites superiores en la sección eficaz pueden traducirse en límites de exclusión sobre los parámetros del modelo de señal. La Figura R.18 muestra los límites superiores observados (línea negra sólida) y esperados (línea negra discontinua) al 95% CL en la sección eficaz total $\sigma(pp \to T \to Ht/Zt)$ como función de m_T en la representación de singlete SU(2), asumiendo (a) $\kappa_T = 0.3$ y (b) $\kappa_T = 0.5$. También se muestran los límites superiores esperados de los análisis individuales. El análisis HTZT (línea azul discontinua) solo se incluye en el cálculo del límite hasta $m_T < 2.1$ TeV, ya que no se disponía de muestras de señal para masas mayores en este canal. Por lo tanto, el límite combinado para $m_T > 2.1$ TeV está dominado por los análisis MONOTOP y OSML. La Figura R.19 muestra los límites superiores para la representación de doblete SU(2). La línea correspondiente al análisis MONOTOP no se muestra debido a su muy baja sensitividad en este escenario, pero el canal MONOTOP se incluye por completitud en los cálculos de límites superiores de la combinación.

Los resultados muestran que los límites más estrictos se obtienen para la representación de singlete SU(2), excluyendo masas del quark T de hasta 1.8 (2.1) TeV para $\kappa_T = 0.3(0.5)$ al 95% CL. Para la representación de doblete SU(2), se excluyen masas de hasta 1.2 TeV para $\kappa_T = 0.5$ al 95% CL, pero no se excluyen masas en el rango explorado para $\kappa_T = 0.3$. En ambos escenarios, la combinación de los tres análisis mejora la sensitividad al modelo de señal, proporcionando límites más estrictos que los análisis individuales. El límite superior en la sección eficaz mejora aproximadamente en un factor de 2 en el escenario de singlete, extendiendo el rango de masas excluidas en 200 GeV. El rango de masas excluidas también se extiende en 100 GeV en el escenario de doblete.

Se pueden establecer límites de exclusión de los parámetros m_T y κ_T simultáneamente calculando el límite superior en la sección eficaz para cada punto en el plano (m_T,κ_T). La Figura R.20 superpone los contornos de exclusión observados y esperados para la combinación de los tres análisis, tanto

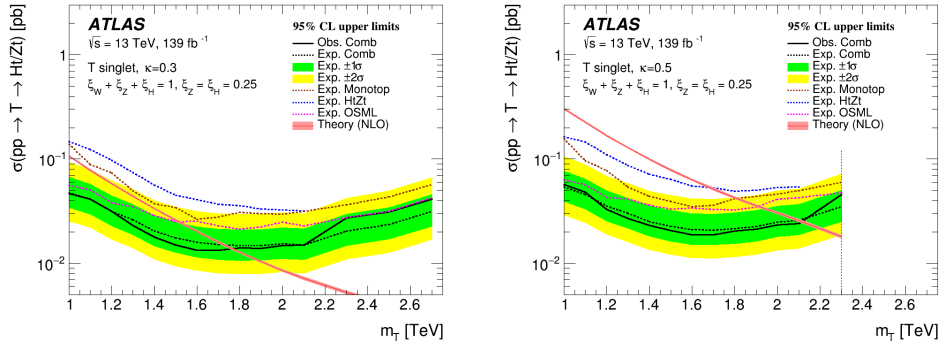

(a) (b)

Figure R.18: Límites superiores observados (línea sólida) y esperados (línea discontinua) al 95% CL en la sección eficaz total $\sigma(pp \to T \to Ht/Zt)$ como función de la masa del quark T en la representación de singlete SU(2), asumiendo (a) $\kappa_T = 0.3$ y (b) $\kappa_T = 0.5$. Las bandas verde y amarilla corresponden, respectivamente, a 1 y 2 desviaciones estándar alrededor del límite esperado. Una línea discontinua vertical indica el límite inferior de la región con $\Gamma_T/m_T > 50\%$, para la cual los cálculos teóricos ya no son válidos. Se muestran los límites esperados para los análisis individuales. El análisis HtZt solo se incluye en el cálculo del límite para $m_T < 2.1$ TeV. La línea roja muestra la predicción teórica de la sección eficaz a NLO, con la banda sombreada correspondiente a la incertidumbre asociada.

para las representaciones de singlete **??** como de doblete **??**. Los contornos de exclusión esperados para los canales individuales también se muestran como comparación. El valor excluido de κ_T se reduce en 1.5 unidades, excluyendo valores de hasta 0.4 para masas grandes alrededor de 2 TeV en el escenario de singlete y 0.5 alrededor de 1.5 TeV en el escenario de doblete. La mejora es menos significativa para masas más bajas, donde el análisis OSML es considerablemente más sensible.

Los límites de exclusión pueden generalizarse para valores arbitrarios del acoplamiento relativo ξ_W, que corresponde a la fracción de desintegración del quark T a través del bosón W en el límite de grandes masas (> 1 TeV). La Figura R.21 muestra en el eje Z los límites de exclusión observados (a) y esperados (b) al 95% CL sobre la masa del quark T como función del ancho relativo de resonancia Γ_T/m_T y del parámetro de acoplamiento relativo ξ_W. Los límites más estrictos se obtienen para $\xi_W = 0.5$ (singlete SU(2)) ya que este escenario permite los modos de producción mediados por Z y W al mismo tiempo que las desintegraciones del quark T en Zt y Ht corresponden al 50% de la fracción de desintegración total. Para $\xi_W = 0.0$ (doblete SU(2)), solo se

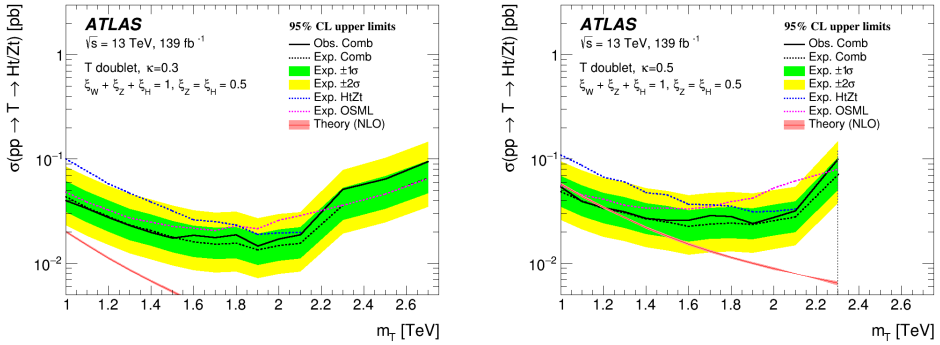

(a) (b)

Figure R.19: Límites superiores observados (línea sólida) y esperados (línea discontinua) al 95% CL en la sección eficaz total $\sigma(pp \to T \to Ht/Zt)$ como función de la masa del quark T en la representación de doblete SU(2), asumiendo (a) $\kappa_T = 0.3$ y (b) $\kappa_T = 0.5$. Las bandas verde y amarilla corresponden, respectivamente, a 1 y 2 desviaciones estándar alrededor del límite esperado. Una línea discontinua vertical indica el límite inferior de la región con $\Gamma_T/m_T > 50\%$ para la cual los cálculos teóricos ya no son válidos. Se muestran los límites esperados para los análisis HtZt y Osml. La línea roja muestra la predicción teórica de la sección eficaz a NLO, con la banda sombreada correspondiente a la incertidumbre asociada.

permite el modo de producción mediado por Z, y para valores de ξ_W cercanos a 1, las desintegraciones del quark T en Zt y Ht están suprimidas, resultando en una pérdida completa de aceptancia en estos canales.

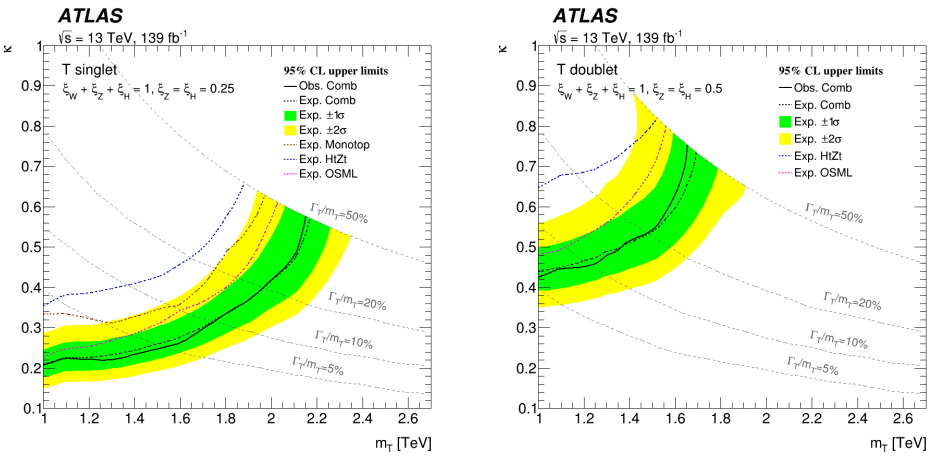

(a) (b)

Figure R.20: Límites de exclusión observados (línea sólida) y esperados (línea discontinua) al 95% CL en la constante de acoplamiento universal κ_T como función de la masa del quark T en las representaciones (a) singlete SU(2) y (b) doblete SU(2) para la combinación. Las líneas grises discontinuas representan configuraciones de (m_T, κ_T) con un mismo valor de Γ_T/m_T. Los límites solo se presentan en el régimen $\Gamma_T/m_T < 50\%$, donde los cálculos teóricos son válidos.

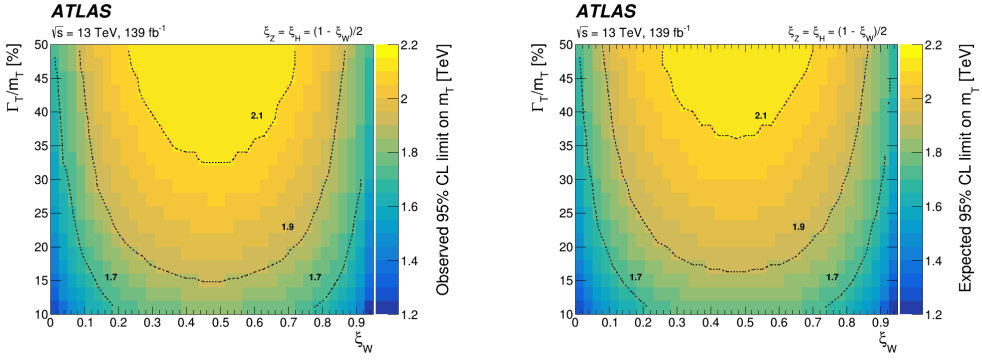

(a) (b)

Figure R.21: Límites superiores (a) observados y (b) esperados al 95% CL sobre la masa del quark T como función del ancho relativo de resonancia (Γ_T/m_T) y el parámetro de acoplamiento relativo ξ_W, bajo la suposición $\xi_Z = \xi_W$. Las líneas de contorno discontinuas denotan límites de exclusión de igual masa en unidades de TeV.

R.6 Detección de anomalías para buscar nueva física

Motivados por las limitaciones del SM para explicar ciertos fenómenos, se ha dedicado un enorme esfuerzo a la búsqueda de nueva física por parte de los experimentos de física de altas energías. A pesar del desarrollo de técnicas sofisticadas y la gran cantidad de datos analizados a lo largo de miles de búsquedas, no se ha observado hasta ahora evidencia significativa de nueva física. En este contexto, la detección de anomalías (AD, por sus siglas en inglés) surge como un enfoque independiente de modelos para buscar nueva física. Las técnicas de AD no se centran en un modelo de señal específico, sino que buscan anomalías o sucesos atípicos en los datos.

Gran parte de estas búsquedas han integrado técnicas de aprendizaje automático (ML, por sus siglas en inglés) en la cadena de análisis, aumentando su sensibilidad a procesos específicos de nueva física y definiendo regiones óptimas enriquecidas en señal. Así, un clasificador aprende a discriminar entre sucesos de señal y de fondo simulados siguiendo un entrenamiento "supervisado". En ausencia de un modelo de señal específico, las nuevas técnicas de entrenamiento para AD se basan principalmente en la simulación del fondo o directamente en los datos experimentales. Dado que este estudio no tuvo acceso a datos experimentales, el entrenamiento se realizó necesariamente con sucesos simulados de fondo. Cuando no intervengan sucesos simulados de señal, se denominará *entrenamiento no supervisado*. Se denominará entrenamiento *semi-supervisado* en aquellos casos en los que se utilicen sucesos simulados de señal para guiar el entrenamiento.

La comunidad del LHC, incluidos los experimentos ATLAS y CMS, ya ha estado explorando el uso de técnicas de AD para buscar nueva física. También se llevaron a cabo programas de búsqueda adicionales para impulsar el desarrollo de nuevas técnicas de AD, como las *LHC Olympics* [276] y el *Dark Machines Anomaly Score Challenge* [277].

Muestra de datos de Dark Machines

La iniciativa Dark Machines es una colaboración internacional que integra el desarrollo de nuevas técnicas de aprendizaje automático en diferentes campos de la física de altas energías, como astropartículas y la física de colisionadores. Centrándose en la búsqueda de materia oscura, este programa interdisciplinario tiene como objetivo proporcionar conjuntos de datos de referencia y técnicas para orientar los esfuerzos de la comunidad hacia objetivos bien definidos. Este estudio hace uso de las muestras de datos simulados proporcionadas para el *Dark Machines Anomaly Score Challenge* [277].

Las colisiones protón-protón fueron simuladas a una energía en el centro de masas de 13 TeV. El *hard scattering* fue generado utilizando MAD-

GRAPH5_AMC@NLO 2.7 [280], conectado a PYTHIA 8 [282] para el PS. Se realizó una simulación rápida del detector utilizando `Delphes` [284] con una configuración simplificada del detector ATLAS [285]. Además de los procesos del SM, el conjunto de datos también incluye varias señales simuladas de BSM, algunas predichas por Supersimetría (SUSY) y otras que predicen un mediador hipotético Z'. Esto permite evaluar la sensitividad de los modelos entrenados para discriminar fenómenos para los cuales ya existen búsquedas supervisadas dedicadas.

Las muestras de datos de Dark Machines contienen la información de las colisiones simuladas, guardando las etiquetas y los cuadrimomentos de los objetos reconstruidos en cada suceso. Se consideran siete tipos diferentes de objetos: jet, b-jet, electrón, positrón, muón, anti-muón y fotón. El conjunto de datos se divide en cuatro canales, cada uno con diferentes criterios de selección resumidos en la Tabla **??**.

Criterio de seleccion	**Canal 1**	**Canal 2a**	**Canal 2b**	**Canal 3**
H_T [GeV]	≥ 600	-	≥ 50	≥ 600
E_T^{miss} [GeV]	≥ 200	≥ 50	≥ 50	≥ 100
E_T^{miss}/H_T	≥ 0.2	-	-	-
b-jets with $p_T > 50$ GeV	≥ 4	-	-	-
b-jet with $p_T > 200$ GeV	1	-	-	-
N^{lep} (with $p_T^{lep} > 15$ GeV)	-	≥ 3	≥ 2	-

Table R.6: Criterios de selección para los cuatro canales de Dark Machines.

El Canal 1, que contiene 214k entradas del SM y 38k entradas de BSM, se centra en actividad hadrónica con gran cantidad de energía faltante, siendo particularmente sensible a firmas de materia oscura tipo mono-jet, así como a señales de SUSY. Tanto el Canal 2a como el Canal 2b reducen el fondo exigiendo la presencia de leptones, mejorando así su sensibilidad a señales mediadas por interacciones electrodébiles. Específicamente, el Canal 2a contiene 20k entradas del SM y 11k entradas de BSM, mientras que el Canal 2b incluye 340k entradas del SM y 90k entradas de BSM. Finalmente, el Canal 3 está diseñado para ser más inclusivo y captura la mayoría de las señales (excepto las electrodébiles menos energéticas), con un tamaño de muestra grande de 8.5M entradas del SM y 1M entradas de BSM.

Transformando clasificadores óptimos en detectores de anomalías

Este estudio [3] explora diferentes métodos para transformar clasificadores supervisados muy eficientes en detectores de anomalías introduciendo únicamente unas modificaciones mínimas, extendiendo potencialmente la aplicabilidad de

la AD en los análisis realizados en el LHC sin necesidad de un proceso de optimización adicional. Las arquitecturas consideradas en este trabajo son:

Perceptrón Multicapa (MLP): Este MLP consta de dos capas ocultas completamente conectadas, con 16 y 8 neuronas respectivamente. Se implementa una la función de activación "Unidad Lineal Rectificada", añadiendo no linealidad al modelo al introducir un umbral en cero. Además, cada capa está seguida por una capa de normalización por lotes, que normaliza la salida de la capa anterior. Esta arquitectura simple está destinada a proporcionar una base para la comparación de rendimiento.

Particle Transformer (ParT) [300]: es una arquitectura basada en *transformers* e inspirada en técnicas de procesamiento de lenguaje natural [302], pero diseñada para la clasificación de jets. Se introducen dos conjuntos de entrada en la red: el cuadrimomento de las partículas (u objetos) en el suceso y las variables de interacción por pares, tales como ΔR_{ij} y m^2_{ij}. Esta arquitectura se caracteriza por el *mecanismo de atención*, que conecta cada objeto con todos los demás, permitiendo al modelo capturar correlaciones complejas entre objetos. La arquitectura ParT puede extenderse para incluir variables adicionales por pares de objetos que codifiquen información física sobre las interacciones entre partículas. Se añade así pues una tercera variable de interacción que corresponde a las constantes de acoplamientos del SM. Esto se añade como una matriz de interacción en la que las entradas indican la intensidad de la interacción entre partículas, calculada utilizando los acoplamientos dependientes de la energía de las fuerzas fuerte, débil y electromagnética. Esta implementación del ParT se denomina ParT+SM [301]. Se espera que esta característica adicional mejore el rendimiento en la tarea de AD, ya que las señales de nueva física pueden manifestarse como desviaciones de las interacciones del SM.

Se estudian tres técnicas para adaptar estas arquitecturas para la tarea de AD: Deep Support Vector Data Description (DeepSVDD) [298], Deep Robust One-Class Classification (DROCC) [299] y Discriminatory Detection of Distortions (DDD). Estos métodos se basan en cambios en los conjuntos de datos o ajustes en la función de pérdida, excepto por cambios menores en la estructura de la red cuando resulta necesario. Tabla R.7 resume los tipos de cambios introducidos por cada uno de los tres métodos.

DeepSVDD: es reconocido como un método estándar de AD [298, 304–306], y consiguió uno de los mejores rendimientos en el reto de Dark Machines [277]. Sin embargo, el uso de arquitecturas complejas en combinación con esta técnica sigue sin explorarse en profundidad. Este método se basa en un entrenamiento

Método	Arquitectura	Función de Pérdida	Conjunto de Datos
DeepSVDD	✗	✗	
DROCC		✗	
DDD			✗

Table R.7: Resumen del tipo de cambios introducidos por cada método de AD.

no supervisado en el cual la función de pérdida es la distancia a un centro en el hiperespacio de salida. Dicho entrenamiento resulta en un clasificador de una sola clase que predice si un suceso de entrada pertenece al SM (y por tanto es *normal*) si éste se encuentra dentro de una hiperesfera. Se introducen modificaciones menores en la red, descritas en Ref. [298], para evitar un efecto conocido como "colapso de la esfera", donde el modelo predice el mismo resultado independientemente de la entrada.

DROCC: es un enfoque de clasificación de una sola clase que se basa en la hipótesis de que los datos normales residen en una región topológica localmente lineal y de baja dimensión. La función de pérdida se modifica para incluir una componente que busca activamente ejemplos adversarios cerca de los puntos de datos *normales*. Estos ejemplos adversarios son puntos de datos sintéticos que son versiones ligeramente perturbadas de los datos normales y, por tanto, se mapean cerca del límite de decisión entre las clases normales y anómalas. El objetivo es garantizar que el modelo pueda clasificar correctamente estos ejemplos desafiantes como anomalías, al mismo tiempo que se consigue robustez frente distintos tipos de anomalías. Este método sigue un entrenamiento semi-supervisado, ya que utiliza una mezcla de señales para guiar el proceso de entrenamiento.

DDD: Este enfoque propone que la transformación de un clasificador binario en un detector de anomalías se puede lograr simplemente sustituyendo las muestras de señal por una versión distorsionada del conjunto de datos de fondo. Dicha distorsión integra simultáneamente el desplazamiento aleatorio de las variables cinemáticas de los objetos y la adición/eliminación aleatoria de objetos. Si el fondo se distorsiona en exceso, la distinción se vuelve demasiado trivial; sin embargo, si la distorsión es mínima, la tarea resulta demasiado compleja. Por tanto, el nivel de distorsión se ajusta para que el clasificador tenga un buen rendimiento, aunque no demasiado óptimo.

Evaluación en los datos de Dark Machines

El rendimiento de un método no supervisado no puede determinarse evaluando el modelo en una señal particular, como ocurre con los métodos supervisados. Si un modelo no supervisado proporciona una buena identificación de una señal específica, esto no significa que sea, en general, un buen modelo para detectar anomalías. Por lo tanto, es importante evaluar el rendimiento de los modelos no supervisados en una amplia gama de señales y canales. El rendimiento de las arquitecturas MLP y ParT, en combinación con las técnicas DeepSVDD, DROCC y DDD, se evaluó en los cuatro canales del reto Dark Machines.

La Figura R.22 muestra el rendimiento en cada modelo de señal en términos del área bajo la curva ROC (AUC), donde ROC hace referencia a la "curva característica operativa del receptor", que es una representación gráfica de la tasa de verdaderos positivos frente a la tasa de falsos positivos en diferentes umbrales. El AUC es un valor escalar único que resume el rendimiento del modelo en todos los posibles umbrales. Un AUC igual a 0.5 indica predicciones aleatorias y un valor igual a 1 indica una clasificación perfecta. También se muestran las eficiencias de señal (ϵ_S) para una eficiencia de fondo (ϵ_B) del 1% para cada modelo de señal. Además, una *mejora de la significancia* (SI) igual a 1 se indica mediante una línea vertical en las gráficas. El SI es el cociente entre las significancias[8] después y antes de aplicar un corte en el *score* del algoritmo de AD.

Desde la perspectiva de las arquitecturas, el MLP muestra el rendimiento más bajo en los cuatro canales. Los pocos casos en los que supera a los modelos ParT corresponden a tareas simples en las que todos los modelos son muy precisos. Estos casos se caracterizan por una variable de entrada que ya discrimina muy bien la señal del fondo. En contraste, la arquitectura ParT+SM es la mejor en la mayoría de los casos, superando a la implementación más simple de ParT. Esto es aún más evidente cuando se combina con las técnicas DROCC y DDD. Esto es consistente con el hecho de que la tarea de aprendizaje propuesta en el método DeepSVDD es más simple que la propuesta por los métodos DROCC y DDD, lo que podría explicar por qué la información añadida por los acoplamientos del SM es menos relevante en este caso.

Desde la perspectiva de las técnicas de AD, el mejor método corresponde a DeepSVDD, siendo el más robusto y estable en todos los canales. Ya se había demostrado que este método proporciona buenos resultados en el reto de Dark Machines [277]. Sin embargo, los métodos DROCC y DDD han demostrado

[8]La significancia se define como el cociente entre el rendimiento de la señal S y la raíz cuadrada del rendimiento del fondo B, donde el número de rendimientos de fondo es lo suficientemente grande como para aproximar la distribución de Poisson con una Gaussiana. En tal caso, $\sqrt{B}$ es la desviación estándar y la significancia indica el número de desviaciones estándar por encima de la del fondo esperado.

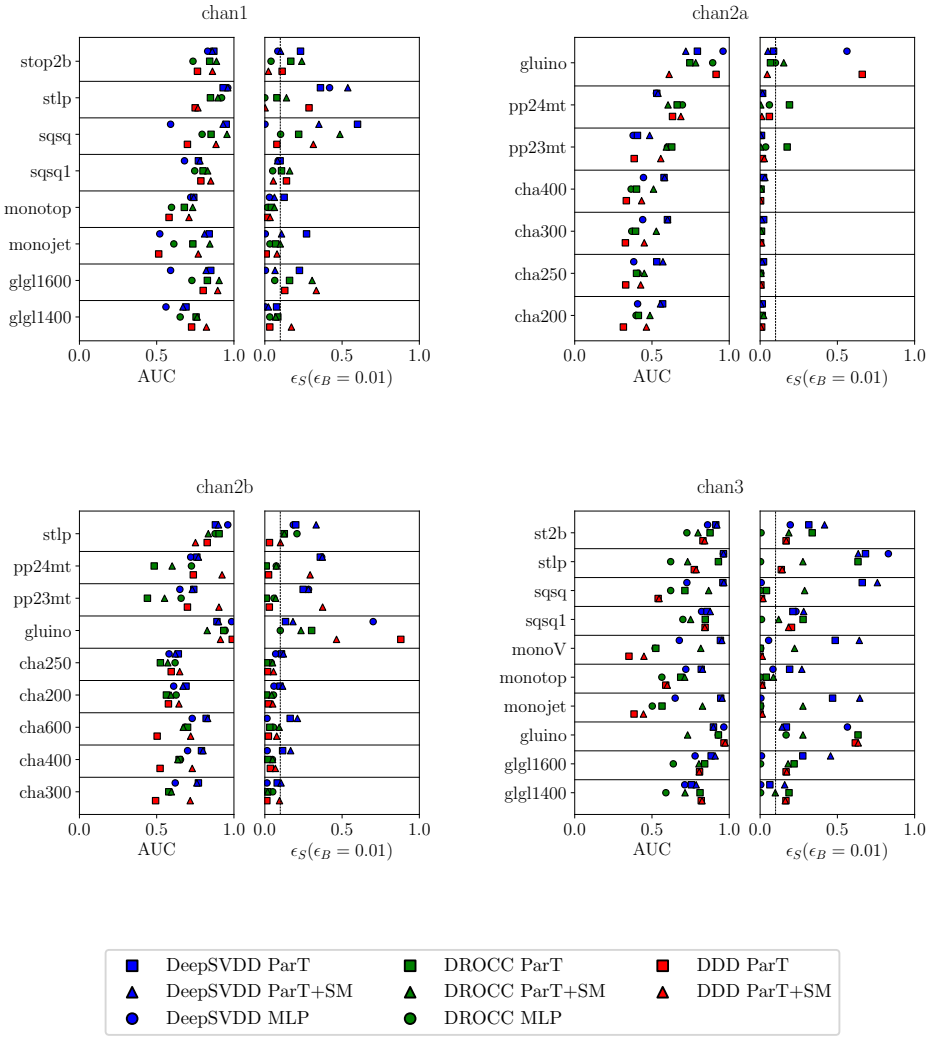

Figure R.22: Esta figura muestra el rendimiento de los ocho modelos en los cuatro canales del conjunto de datos de Dark Machines: Canal 1 (primera fila, izquierda), Canal 2a (primera fila, derecha), Canal 2b (segunda fila, izquierda) y Canal 3 (segunda fila, derecha). Para cada canal, se evalúan diferentes señales. Las métricas de rendimiento mostradas son el AUC y la eficiencia de señal (ϵ_S) asumiendo una eficiencia de fondo (ϵ_B) del 1%. Se añade una línea vertical para indicar una mejora de significancia igual a 1. Se utiliza un código de colores para distinguir entre las tres técnicas de entrenamiento: DeepSVDD (azul), DROCC (verde) y DDD (rojo). Se emplean diferentes formas para cada arquitectura: un círculo para el MLP, un cuadrado para el ParT sin interacciones, y un triángulo para el ParT con acoplamientos del SM.

ser muy competitivos e incluso mejores que DeepSVDD en algunos casos. La principal ventaja de estos métodos es que no requieren ninguna modificación del clasificador, por lo que no se necesita conocimiento previo de la arquitectura de la red. Además, el método DDD como un nuevo enfoque desarrollado en este trabajo, puede presentar margen de mejora explorando diferentes distorsiones de datos y ajustes de hiperparámetros.

Comparación con los algoritmos del reto de Dark Machines

Basado en la SI, la mejora total (TI) se utiliza para cuantificar la máxima SI a lo largo de las diversas señales físicas para cada una de las técnicas de AD y para combinar las señales en múltiples canales. Los valores mínimo, mediano y máximo de la TI a lo largo de las señales físicas se definen para obtener métricas de rendimiento generales que midan la robustez de los modelos entrenados.

La Figura R.23 proporciona un análisis comparativo de los valores de TI para diferentes modelos, incluidos los resultados de distintos modelos en el reto de Dark Machines y la mezcla de señales de Ref. [308]. La TI se calcula sobre diferentes cortes en la eficiencia de fondo ($\epsilon_B = 10^{-2}, 10^{-3}$, y 10^{-4}), y se toma el máximo, lo que típicamente conduce a $TI > 1$.

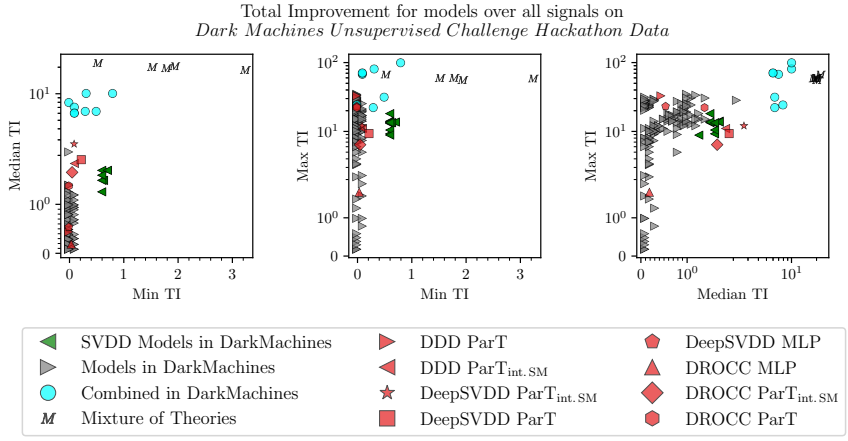

Figure R.23: El mínimo, la mediana y el máximo de la TI para cada técnica.

Esta comparación directa muestra que las métricas de TI mediana y TI máxima de los modelos con mejor desempeño de este estudio son competitivas con los mejores modelos del reto de Dark Machines. Sin embargo, el desempeño es significativamente menor en términos de la TI mínima. Cabe señalar que los mejores modelos de este reto fueron combinaciones de SVDDs con modelos basados en flujos de normalización (denominados “Combined in

DarkMachines" en la Figura R.23), lo que probablemente también mejoraría aún más el rendimiento de los modelos entrenados en este estudio.

Es importante recordar que el objetivo de este estudio era explorar la viabilidad de convertir un clasificador en un detector de anomalías sin añadir mayor esfuerzo, en lugar de presentar el mejor modelo posible para detectar anomalías. Y, por lo tanto, no se ha realizado una optimización de hiperparámetros para los modelos entrenados en este trabajo, a diferencia de los modelos del reto de Dark Machines. Esta contribución espera motivar a la comunidad del LHC a considerar la reinterpretación de sus búsquedas supervisadas como tareas de detección de anomalías, en combinación con los métodos tradicionales de inferencia estadística, siguiendo las pautas presentadas en este trabajo.

R.7 Conclusiones

Esta Tesis presenta diferentes contribuciones a la búsqueda de Nueva Física con el detector ATLAS. Para motivar el marco teórico, se ha presentado el SM como una descripción elegante de las partículas fundamentales y sus interacciones. Tras enumerar algunas de sus mayores limitaciones, se ha puesto especial énfasis en los problemas de la Materia Oscura y la jerarquía de masa.

Seguidamente, se ha descrito el montaje experimental, introduciendo magnitudes importantes de la física de colisionadores con un enfoque especial en las colisiones protón-protón del LHC. A su vez, se han presentado los diferentes subsistemas del detector ATLAS para comprender cómo se miden las características cinemáticas de las partículas. Posteriormente, se ha detallado la cadena de simulación de la colaboración ATLAS, así como el procedimiento de reconstrucción e identificación de objetos.

El primer análisis presentado representa una búsqueda de sucesos con un único quark top y momento transverso faltante. Este análisis es conocido como Monotop [1] y explora los datos registrados por el detector ATLAS durante el Run 2 del LHC (2015-2018), con una luminosidad integrada total de 139 fb^{-1}. Los resultados se interpretan en términos de dos modelos que predicen la producción de partículas de DM junto con un quark top, y un modelo de VLQ. No se ha observado ningún exceso significativo sobre las predicciones del SM, pero se han establecido límites superiores competitivos en la sección eficaz al 95% CL para cada modelo. Los límites de exclusión sobre la masa del mediador escalar m_ϕ son constantes para todos los valores de la masa de DM m_χ por debajo de 1.5 TeV, excluyendo valores de m_ϕ (m_χ) por debajo de 4.3 (2.2) TeV, tomando los valores de referencia de los acoplamientos $\lambda_q = 0.2$ y $y_\chi = 0.4$. Esto corresponde a una mejora de alrededor de 500 GeV para los límites de masa del mediador escalar con respecto a resultados anteriores de esta búsqueda [260]. De manera equivalente, se excluye un máximo de la

masa del mediador vectorial (partícula de DM) de 2.3 (1.5) TeV, tomando los valores de referencia de los acoplamientos $a = 0.5$ y $g_\chi = 1$. Esto corresponde a una mejora de alrededor de 300 GeV para los límites de masa del mediador vectorial con respecto a Ref. [260]. Para el modelo de VLQ, se excluyen los valores del acoplamiento κ_T por encima de 0.4 para valores de la masa del quark T, m_T, por debajo de 1.6 TeV. A su vez, se excluye un valor máximo de m_T =1.9 TeV correspondiente a valores de κ_T alrededor de 0.6 .

El segundo análisis descrito en esta Tesis consiste en una combinación [2] de tres búsquedas de quarks T producidos individualmente en la colaboración ATLAS, donde el análisis MONOTOP presentado previamente se combina con los análisis HTZT y OSML para mejorar la sensibilidad de las búsquedas individuales. Estas tres búsquedas son complementarias acorde con el número de leptones que requieren: MONOTOP veta la presencia de leptones, HTZT requiere un leptón y OSML requiere al menos dos leptones. Esta combinación establece límites en la sección eficaz inclusiva de cuatro modos de producción: $T(\to Zt)qb$, $T(\to Ht)qb$, $T(\to Zt)qt$ y $T(\to Ht)qt$. Los resultados muestran que los límites más competitivos se obtienen para la representación de singlete SU(2), para la cual la sección eficaz está restringida a valores inferiores a 15 fb en el rango de masas de 1.5 a 1.7 TeV y $\kappa_T = 0.3$. Todos los valores de κ_T por encima de 0.2 están excluidos para m_T acercándose a 1.0 TeV y un valor máximo de m_T de 2.1 TeV está excluido para κ_T alrededor de 0.7. Para la representación de doblete SU(2), la sección eficaz está restringida a valores inferiores a 30 fb para masas en el rango de 1.2 a 1.6 TeV y valores de κ_T entre 0.5 y 0.6 . Todos los valores de κ_T por encima de 0.45 están excluidos para $m_T = 1.0$ TeV y un valor máximo de m_T de 1.7 TeV está excluido para κ_T alrededor de 0.7. La combinación de las tres búsquedas mejora significativamente los límites de exclusión de los canales individuales en ambas representaciones, con un aumento de alrededor de 200 GeV en el límite de exclusión de m_T con respecto al canal más sensible. Para masas grandes, correspondientes a 2 TeV en el escenario de singlete y 1.5 TeV en el escenario de doblete, el límite de exclusión de κ_T se reduce en la combinación en 1.5 unidades. La mejora es menos significativa para masas más bajas, donde el análisis OSML ya es muy sensible.

El último análisis presentado es un esfuerzo que tiene como objetivo impulsar el desarrollo de técnicas de detección de anomalías (AD) en las búsquedas de ATLAS. Este estudio [3] hace uso de datos simulados del reto *Dark Machines Anomaly Score*, en el que se simulan colisiones protón-protón con una simplificación del detector ATLAS. Aparte de los procesos SM, este conjunto de datos contiene diferentes modelos BSM que se utilizan para evaluar el rendimiento de las técnicas AD a través de cuatro canales con diferentes topologías de sucesos. Se adaptaron dos clasificadores basados en *transformers* y un clasificador MLP (como referencia) para la tarea de AD utilizando tres técnicas diferentes:

DeepSVDD, DROCC y DDD. No se realizó ninguna optimización de hiperparámetros ni ajustes adicionales al aplicar estas técnicas, pero las principales modificaciones se aplicaron a la función de pérdida o a los datos de entrenamiento. Las evaluaciones en los procesos de señal se interpretan en términos del AUC y la eficiencia de señal ϵ_S para una eficiencia de fondo ϵ_B del 1%. Por un lado, la arquitectura ParT+SM superó a las otras dos arquitecturas, lo que indica que los mejores clasificadores tienen el potencial de convertirse en los mejores detectores de anomalías. Por otro lado, las tres técnicas muestran resultados similares, siendo DeepSVDD la que proporciona los mejores resultados en los cuatro canales. Por último, la evaluación de todos los modelos BSM en los distintos canales se combina en métricas más generales basadas en la significancia, como SI y TI. Esto permite demostrar que los modelos entrenados de este estudio son competitivos con respecto a los modelos del reto con mejores resultados, lo que indica que estas técnicas de AD no requieren un ajuste específico de las redes para la tarea AD.

Bibliography

[1] ATLAS Collaboration. "Search for new particles in final states with a boosted top quark and missing transverse momentum in proton-proton collisions at $\sqrt{s} = 13$ TeV with the ATLAS detector". *JHEP* 05 (2024), p. 263. DOI: 10.1007/JHEP05(2024)263. arXiv: 2402.16561 [hep-ex].

[2] ATLAS Collaboration. "Combination of searches for singly produced vector-like top quarks in pp collisions at $\sqrt{s} = 13$ TeV with the ATLAS detector". *Phys. Rev. D* 111.1 (2025), p. 012012. DOI: 10.1103/PhysRevD.111.012012. arXiv: 2408.08789 [hep-ex].

[3] S. Caron et al. "Universal anomaly detection at the LHC: transforming optimal classifiers and the DDD method". *Eur. Phys. J. C* 85.4 (2025), p. 415. DOI: 10.1140/epjc/s10052-025-14087-z. arXiv: 2406.18469 [hep-ph].

[4] E. Ward. "Key Particle Discoveries Timeline". General Photo. 2019. URL: https://cds.cern.ch/record/2665175.

[5] E. A. Davis and I. J. Falconer. *J.J. Thomson and the discovery of the electron*. 1997.

[6] A. Einstein. "On a Heuristic Viewpoint Concerning the Production and Transformation of Light". *Annalen der Physik* 17 (1905), pp. 132–148. DOI: 10.1002/andp.19053220607. URL: https://doi.org/10.1002/andp.19053220607.

[7] Z. Ajduk, M. Krawczyk, and A. K. Wroblewski, eds. *The Photon, its first hundred years and the future*. Vol. 37. 2006, pp.543–1006.

[8] N. Rowley. "Geiger-Marsden experiments: 100 years on". *J. Phys. Conf. Ser.* 381 (2012). Ed. by S. Freeman et al., p. 012086. DOI: 10.1088/1742-6596/381/1/012086.

[9] E. Rutherford. "Collision of α particles with light atoms. IV. An anomalous effect in nitrogen". *Philosophical Magazine* 90.sup1 (2010), pp. 31–37. DOI: 10.1080/14786431003659230. eprint: https://doi.org/10.1080/14786431003659230. URL: https://doi.org/10.1080/14786431003659230.

[10] J. Chadwick. "The Existence of a Neutron". *Proc. Roy. Soc. Lond. A* 136.830 (1932), pp. 692–708. DOI: 10.1098/rspa.1932.0112.

[11] P. A. M. Dirac. "A Theory of Electrons and Protons". *Proc. Roy. Soc. Lond. A* 126.801 (1930), pp. 360–365. DOI: 10.1098/rspa.1930.0013.

[12] P. Carlson. "Carl Anderson´s 1932 upward going positron". *PoS* ICRC2023 (2023), p. 337. DOI: 10.22323/1.444.0337.

[13] O. Piccioni. "The Discovery of the Muon". *NATO Sci. Ser. B* 352 (1996). Ed. by Harvey B. Newman and Thomas Ypsilantis, pp. 143–162. DOI: 10.1007/978-1-4613-1147-8_10.

[14] C. Jarlskog. "Birth of the neutrino, from Pauli to the Reines-Cowan experiment". *International Conference on History of the Neutrino: 1930-2018*. 2019.

[15] C. N. Yang. "Fermi's beta-decay Theory". *Asia Pac. Phys. Newslett.* 01 (2012), pp. 27–30. DOI: 10.1142/S2251158X12000045.

[16] S. L. Glashow. "The Renormalizability of Vector Meson Interactions". *Nuclear Physics* 10 (1959), p. 107.

[17] A. Salam and J. C. Ward. "Electromagnetic and weak interactions". *Phys. Lett.* 13 (1964), pp. 168–171. DOI: 10.1016/0031-9163(64)90711-5.

[18] S. Weinberg. "A Model of Leptons". *Physical Review Letters* 19 (1967), p. 1264.

[19] L. Di Lella and C. Rubbia. "The Discovery of the W and Z Particles". *Adv. Ser. Direct. High Energy Phys.* 23 (2015), pp. 137–163. DOI: 10.1142/9789814644150_0006.

[20] H. Fritzsch and M. Gell-Mann. "Light cone current algebra". *International conference on duality and symmetry in hadron physics*. 1971, pp. 317–374. arXiv: hep-ph/0301127.

[21] H. Fritzsch and M. Gell-Mann. "Current algebra: Quarks and what else?": *eConf* C720906V2 (1972). Ed. by J. D. Jackson and A. Roberts, pp. 135–165. arXiv: hep-ph/0208010.

[22] J. R. Ellis, M. K. Gaillard, and G. G. Ross. "Search for Gluons in e+ e- Annihilation". *Nucl. Phys. B* 111 (1976). [Erratum: Nucl.Phys.B 130, 516 (1977)], p. 253. DOI: 10.1016/0550-3213(77)90253-X.

[23] ATLAS Collaboration. "Observation of a new particle in the search for the Standard Model Higgs boson with the ATLAS detector at the LHC". *Physics Letters B* 716.1 (2012), pp. 1–29. ISSN: 0370-2693. DOI: https://doi.org/10.1016/j.physletb.2012.08.020. URL: https://www.sciencedirect.com/science/article/pii/S037026931200857X.

[24] CMS Collaboration. "Observation of a new boson at a mass of 125 GeV with the CMS experiment at the LHC". *Physics Letters B* 716.1 (2012), pp. 30–61. ISSN: 0370-2693. DOI: https://doi.org/10.1016/j.physletb.2012.08.021. URL: https://www.sciencedirect.com/science/article/pii/S0370269312008581.

[25] A. B. Arbuzov. "Quantum Field Theory and the Electroweak Standard Model". (2018). 35 pages, pp. 1–34. DOI: 10.23730/CYRSP-2017-004.1. arXiv: 1801.05670. URL: https://cds.cern.ch/record/2315477.

[26] G. Sudarshan. "The fundamental theorem on the relation between spin and statistics". *Proc. Natl. Inst. Sci. India A* 67 (1968), p. 284.

[27] F. Englert and R. Brout. "Broken Symmetry and the Mass of Gauge Vector Mesons". *Phys. Rev. Lett.* 13 (1964). Ed. by J. C. Taylor, pp. 321–323. DOI: 10.1103/PhysRevLett.13.321.

[28] P. W. Higgs. "Broken symmetries, massless particles and gauge fields". *Phys. Lett.* 12 (1964), pp. 132–133. DOI: 10.1016/0031-9163(64)91136-9.

[29] E. Noether. "Invariante Variationsprobleme". ger. *Nachrichten von der Gesellschaft der Wissenschaften zu Göttingen, Mathematisch-Physikalische Klasse* 1918 (1918), pp. 235–257. URL: http://eudml.org/doc/59024.

[30] W. Heisenberg. "The actual content of quantum theoretical kinematics and mechanics". *Zeitschrift für Physik* 43 (1927), pp. 172–198. DOI: 10.1007/BF01397280.

[31] R. Jackiw and C. Rebbi. "Vacuum Periodicity in a Yang-Mills Quantum Theory". *Phys. Rev. Lett.* 37 (1976). Ed. by J. C. Taylor, pp. 172–175. DOI: 10.1103/PhysRevLett.37.172.

[32] Curtis G. Callan Jr., R. F. Dashen, and David J. Gross. "The Structure of the Gauge Theory Vacuum". *Phys. Lett. B* 63 (1976). Ed. by J. C. Taylor, pp. 334–340. DOI: 10.1016/0370-2693(76)90277-X.

[33] M. C. Gonzalez-Garcia and M. Maltoni. "Phenomenology with massive neutrinos". *Physics Reports* 460.1 (2008), pp. 1–129. ISSN: 0370-1573. DOI: https://doi.org/10.1016/j.physrep.2007.12.004. URL: https://www.sciencedirect.com/science/article/pii/S0370157308000148.

[34] V. Brdar et al. "Type I seesaw mechanism as the common origin of neutrino mass, baryon asymmetry, and the electroweak scale". *Physical Review D* 100.7 (Oct. 2019). ISSN: 2470-0029. DOI: 10.1103/physrevd.100.075029. URL: http://dx.doi.org/10.1103/PhysRevD.100.075029.

[35] A. D. Sakharov. "Violation of CP Invariance, C asymmetry, and baryon asymmetry of the universe". *Pisma Zh. Eksp. Teor. Fiz.* 5 (1967), pp. 32–35. DOI: 10.1070/PU1991v034n05ABEH002497.

[36] Vera C. Rubin and W. Kent Ford Jr. "Rotation of the Andromeda Nebula from a Spectroscopic Survey of Emission Regions". *Astrophys. J.* 159 (1970), pp. 379–403. DOI: 10.1086/150317.

[37] A. Bosma. "21-cm line studies of spiral galaxies. 2. The distribution and kinematics of neutral hydrogen in spiral galaxies of various morphological types." *Astron. J.* 86 (1981), p. 1825. DOI: 10.1086/113063.

[38] E. Corbelli and P. Salucci. "The Extended Rotation Curve and the Dark Matter Halo of M33". *Mon. Not. Roy. Astron. Soc.* 311 (2000), pp. 441–447. DOI: 10.1046/j.1365-8711.2000.03075.x. arXiv: astro-ph/9909252.

[39] F. Zwicky. "Die Rotverschiebung von extragalaktischen Nebeln". *Helv. Phys. Acta* 6 (1933), pp. 110–127. DOI: 10.1007/s10714-008-0707-4.

[40] R. Clausius. "XVI. On a mechanical theorem applicable to heat". *The London, Edinburgh, and Dublin Philosophical Magazine and Journal of Science* 40.265 (1870), pp. 122–127. DOI: 10.1080/14786447008640370. eprint: https://doi.org/10.1080/14786447008640370. URL: https://doi.org/10.1080/14786447008640370.

[41] A. Refregier. "Weak gravitational lensing by large scale structure". *Ann. Rev. Astron. Astrophys.* 41 (2003), pp. 645–668. DOI: 10.1146/annurev.astro.41.111302.102207. arXiv: astro-ph/0307212.

[42] G. Bertone and D. Hooper. "History of dark matter". *Rev. Mod. Phys.* 90 (4 Oct. 2018), p. 045002. DOI: 10.1103/RevModPhys.90.045002. URL: https://link.aps.org/doi/10.1103/RevModPhys.90.045002.

[43] P. McDonald and A. Roy. "Clustering of dark matter tracers: generalizing bias for the coming era of precision LSS". *Journal of Cosmology and Astroparticle Physics* 2009.08 (Aug. 2009), p. 020. DOI: 10.1088/1475-7516/2009/08/020. URL: https://dx.doi.org/10.1088/1475-7516/2009/08/020.

[44] R. H. Dicke et al. "Cosmic Black-Body Radiation". *Astrophys. J.* 142 (1965), pp. 414–419. DOI: 10.1086/148306.

[45] Planck Collaboration et al. "Planck 2018 results - VI. Cosmological parameters". *A&A* 641 (2020), A6. DOI: 10.1051/0004-6361/201833910. URL: https://doi.org/10.1051/0004-6361/201833910.

[46] M. Milgrom. "MOND theory". *Canadian Journal of Physics* 93.2 (2015), pp. 107–118. DOI: 10.1139/cjp-2014-0211. eprint: https://doi.org/10.1139/cjp-2014-0211. URL: https://doi.org/10.1139/cjp-2014-0211.

[47] D. Clowe et al. "A direct empirical proof of the existence of dark matter". *Astrophys. J. Lett.* 648 (2006), pp. L109–L113. DOI: 10.1086/508162. arXiv: astro-ph/0608407.

[48] B. P. Abbott et al. "Observation of Gravitational Waves from a Binary Black Hole Merger". *Phys. Rev. Lett.* 116.6 (2016), p. 061102. DOI: 10.1103/PhysRevLett.116.061102. arXiv: 1602.03837 [gr-qc].

[49] B. P. Abbott et al. "GW170817: Observation of Gravitational Waves from a Binary Neutron Star Inspiral". *Phys. Rev. Lett.* 119.16 (2017), p. 161101. DOI: 10.1103/PhysRevLett.119.161101. arXiv: 1710.05832 [gr-qc].

[50] J. Billard et al. "Direct detection of dark matter—APPEC committee report*". *Rept. Prog. Phys.* 85.5 (2022), p. 056201. DOI: 10.1088/1361-6633/ac5754. arXiv: 2104.07634 [hep-ex].

[51] D. P. Bennett et al. "The MACHO project dark matter search". *ASP Conf. Ser.* 88 (1996), p. 95. arXiv: astro-ph/9510104.

[52] Ya. B. Zel'dovich and I. D. Novikov. "The Hypothesis of Cores Retarded during Expansion and the Hot Cosmological Model". *Sov. Astron.* 10 (1967), p. 602.

[53] G. Bertone, D. Hooper, and J. Silk. "Particle dark matter: Evidence, candidates and constraints". *Phys. Rept.* 405 (2005), pp. 279–390. DOI: 10.1016/j.physrep.2004.08.031. arXiv: hep-ph/0404175.

[54] J. M. Overduin and P. S. Wesson. "Dark matter and background light". *Phys. Rept.* 402 (2004), pp. 267–406. DOI: 10.1016/j.physrep.2004.07.006. arXiv: astro-ph/0407207.

[55] S. Palomares-Ruiz. "Model-independent bound on the dark matter lifetime". *Phys. Lett. B* 665 (2008), pp. 50–53. DOI: 10.1016/j.physletb.2008.05.040. arXiv: 0712.1937 [astro-ph].

[56] E. W. Kolb. *The Early Universe*. Vol. 69. Taylor and Francis, May 2019. ISBN: 978-0-429-49286-0, 978-0-201-62674-2. DOI: 10.1201/9780429492860.

[57] Graciela B. G. *TASI 2014 Lectures: The Hunt for Dark Matter*. 2015. arXiv: 1502.01320 [hep-ph]. URL: https://arxiv.org/abs/1502.01320.

[58] J. Kopp. "Sterile neutrinos as dark matter candidates". *SciPost Physics Lecture Notes* (Jan. 2022). DOI: 10.21468/SciPostPhysLectNotes.36.

[59] R. D. Peccei and H. R. Quinn. "CP Conservation in the Presence of Instantons". *Phys. Rev. Lett.* 38 (1977), pp. 1440–1443. DOI: 10.1103/PhysRevLett.38.1440.

[60] M. Fabbrichesi, E. Gabrielli, and G. Lanfranchi. "The Dark Photon". (May 2020). DOI: 10.1007/978-3-030-62519-1. arXiv: 2005.01515 [hep-ph].

[61] R. Coquereaux and G. Esposito-Farese. "The theory of Kaluza-Klein-Jordan-Thiry revisited". en. *Annales de l'I.H.P. Physique théorique* 52.2 (1990), pp. 113–150. URL: http://www.numdam.org/item/AIHPA_1990__52_2_113_0/.

[62] G. Arcadi et al. "The waning of the WIMP? A review of models, searches, and constraints". *Eur. Phys. J. C* 78.3 (2018), p. 203. DOI: 10.1140/epjc/s10052-018-5662-y. arXiv: 1703.07364 [hep-ph].

[63] J. L. Feng. "Dark Matter Candidates from Particle Physics and Methods of Detection". *Ann. Rev. Astron. Astrophys.* 48 (2010), pp. 495–545. DOI: 10.1146/annurev-astro-082708-101659. arXiv: 1003.0904 [astro-ph.CO].

[64] O. F. Piattella. *Lecture Notes in Cosmology*. UNITEXT for Physics. Cham: Springer, 2018. ISBN: 978-3-319-95569-8, 978-3-030-07060-1, 978-3-319-95570-4. DOI: 10.1007/978-3-319-95570-4. arXiv: 1803.00070 [astro-ph.CO].

[65] D. Hooper. "Particle Dark Matter". *Theoretical Advanced Study Institute in Elementary Particle Physics: The Dawn of the LHC Era*. 2010, pp. 709–764. DOI: 10.1142/9789812838360_0014. arXiv: 0901.4090 [hep-ph].

[66] X.-J. Bi, P.-F. Yin, and Q. Yuan. "Status of Dark Matter Detection". *Front. Phys. (Beijing)* 8 (2013), pp. 794–827. DOI: 10.1007/s11467-013-0330-z. arXiv: 1409.4590 [hep-ph].

[67] C. Pérez de los Heros. "Status of direct and indirect dark matter searches". *PoS* EPS-HEP2019 (2020), p. 694. DOI: 10.22323/1.364.0694. arXiv: 2001.06193 [astro-ph.HE].

[68] M. Pato et al. "Systematic uncertainties in the determination of the local dark matter density". *Phys. Rev. D* 82 (2 July 2010), p. 023531. DOI: 10.1103/PhysRevD.82.023531. URL: https://link.aps.org/doi/10.1103/PhysRevD.82.023531.

[69] H. Silverwood et al. "A non-parametric method for measuring the local dark matter density". *Mon. Not. Roy. Astron. Soc.* 459.4 (2016), pp. 4191–4208. DOI: 10.1093/mnras/stw917. arXiv: 1507.08581 [astro-ph.GA].

[70] C. Kelso et al. "The impact of baryons on the direct detection of dark matter". *Journal of Cosmology and Astroparticle Physics* 2016.08 (Aug. 2016), p. 071. DOI: 10.1088/1475-7516/2016/08/071. URL: https://dx.doi.org/10.1088/1475-7516/2016/08/071.

[71] E. Aprile et al. "The XENONnT dark matter experiment". *Eur. Phys. J. C* 84.8 (2024), p. 784. DOI: 10.1140/epjc/s10052-024-12982-5. arXiv: 2402.10446 [physics.ins-det].

[72] S. Li et al. "Search for Light Dark Matter with Ionization Signals in the PandaX-4T Experiment". *Phys. Rev. Lett.* 130.26 (2023), p. 261001. DOI: 10.1103/PhysRevLett.130.261001. arXiv: 2212.10067 [hep-ex].

[73] J. Aalbers et al. "First Dark Matter Search Results from the LUX-ZEPLIN (LZ) Experiment". *Phys. Rev. Lett.* 131 (4 July 2023), p. 041002. DOI: 10.1103/PhysRevLett.131.041002. URL: https://link.aps.org/doi/10.1103/PhysRevLett.131.041002.

[74] M. F. Albakry et al. "First Measurement of the Nuclear-Recoil Ionization Yield in Silicon at 100 eV". *Phys. Rev. Lett.* 131.9 (2023), p. 091801. DOI: 10.1103/PhysRevLett.131.091801. arXiv: 2303.02196.

[75] P. Agnes et al. "Search for low-mass dark matter WIMPs with 12 ton-day exposure of DarkSide-50". *Phys. Rev. D* 107.6 (2023), p. 063001. DOI: 10.1103/PhysRevD.107.063001. arXiv: 2207.11966 [hep-ex].

[76] P. Adhikari et al. "Precision measurement of the specific activity of ^{39}Ar in atmospheric argon with the DEAP-3600 detector". *Eur. Phys. J. C* 83.7 (2023), p. 642. DOI: 10.1140/epjc/s10052-023-11678-6. arXiv: 2302.14639 [physics.ins-det].

[77] G. Angloher et al. "Results on sub-GeV dark matter from a 10 eV threshold CRESST-III silicon detector". *Phys. Rev. D* 107.12 (2023), p. 122003. DOI: 10.1103/PhysRevD.107.122003. arXiv: 2212.12513 [astro-ph.CO].

[78] L. Balogh et al. "The NEWS-G detector at SNOLAB". *JINST* 18.02 (2023), T02005. DOI: 10.1088/1748-0221/18/02/T02005. arXiv: 2205.15433 [physics.ins-det].

[79] C. Amole et al. "Dark Matter Search Results from the PICO-2L C_3F_8 Bubble Chamber". *Phys. Rev. Lett.* 114.23 (2015), p. 231302. DOI: 10.1103/PhysRevLett.114.231302. arXiv: 1503.00008 [astro-ph.CO].

[80] R. Abbasi et al. "The IceCube Data Acquisition System: Signal Capture, Digitization, and Timestamping". *Nucl. Instrum. Meth. A* 601 (2009), pp. 294–316. DOI: 10.1016/j.nima.2009.01.001. arXiv: 0810.4930 [physics.ins-det].

[81] M. Ageron et al. "ANTARES: The first undersea neutrino telescope". *Nuclear Instruments and Methods in Physics Research Section A: Accelerators, Spectrometers, Detectors and Associated Equipment* 656.1 (2011), pp. 11–38. ISSN: 0168-9002. DOI: https://doi.org/10.1016/j.nima.2011.06.103. URL: https://www.sciencedirect.com/science/article/pii/S0168900211013994.

[82] G. Ferrara. "Neutrino astronomy in the Mediterranean and the KM3NeT/ARCA telescope". *Nuovo Cim. C* 47.3 (2024), p. 71. DOI: 10.1393/ncc/i2024-24071-6.

[83] O. Adriani et al. "An anomalous positron abundance in cosmic rays with energies 1.5-100 GeV". *Nature* 458 (2009), pp. 607–609. DOI: 10.1038/nature07942. arXiv: 0810.4995 [astro-ph].

[84] M. Aguilar et al. "Towards Understanding the Origin of Cosmic-Ray Positrons". *Phys. Rev. Lett.* 122.4 (2019), p. 041102. DOI: 10.1103/PhysRevLett.122.041102.

[85] M. Aguilar et al. "First Result from the Alpha Magnetic Spectrometer on the International Space Station: Precision Measurement of the Positron Fraction in Primary Cosmic Rays of 0.5–350 GeV". *Phys. Rev. Lett.* 110 (2013), p. 141102. DOI: 10.1103/PhysRevLett.110.141102.

[86] M. H. Israel. "An Alternative Approach to Understanding the Observed Positron Fraction". *Braz. J. Phys.* 44 (2014). Ed. by Ronald Cintra Shellard, pp. 530–533. DOI: 10.1007/s13538-014-0235-5.

[87] D. Hooper and L. Goodenough. "Dark Matter Annihilation in The Galactic Center As Seen by the Fermi Gamma Ray Space Telescope". *Phys. Lett. B* 697 (2011), pp. 412–428. DOI: 10.1016/j.physletb.2011.02.029. arXiv: 1010.2752 [hep-ph].

[88] M. Ackermann et al. "The Fermi Galactic Center GeV Excess and Implications for Dark Matter". *Astrophys. J.* 840.1 (2017), p. 43. DOI: 10.3847/1538-4357/aa6cab. arXiv: 1704.03910 [astro-ph.HE].

[89] E. Tempel, A. Hektor, and M. Raidal. "Fermi 130 GeV gamma-ray excess and dark matter annihilation in sub-haloes and in the Galactic centre". *JCAP* 09 (2012). [Addendum: JCAP 11, A01 (2012)], p. 032. DOI: 10.1088/1475-7516/2012/09/032. arXiv: 1205.1045 [hep-ph].

[90] K. N. Abazajian and M. Kaplinghat. "Detection of a Gamma-Ray Source in the Galactic Center Consistent with Extended Emission from Dark Matter Annihilation and Concentrated Astrophysical Emission". *Phys. Rev. D* 86 (2012). [Erratum: Phys.Rev.D 87, 129902 (2013)], p. 083511. DOI: 10.1103/PhysRevD.86.083511. arXiv: 1207.6047 [astro-ph.HE].

[91] R. Assmann, M. Lamont, and S. Myers. "A brief history of the LEP collider". *Nucl. Phys. B Proc. Suppl.* 109 (2002). Ed. by F. L. Navarria, M. Paganoni, and P. G. Pelfer, pp. 17–31. DOI: 10.1016/S0920-5632(02)90005-8.

[92] R. R. Wilson. "The Tevatron". *Phys. Today* 30N10 (1977), pp. 23–30. DOI: 10.1063/1.3037746.

[93] ATLAS Collaboration. "The ATLAS Experiment at the CERN Large Hadron Collider". *JINST* 3 (2008), S08003. DOI: 10.1088/1748-0221/3/08/S08003.

[94] CMS Collaboration. "The CMS Experiment at the CERN LHC". *JINST* 3 (2008), S08004. DOI: 10.1088/1748-0221/3/08/S08004.

[95] G. Busoni et al. "On the Validity of the Effective Field Theory for Dark Matter Searches at the LHC". *Phys. Lett. B* 728 (2014), pp. 412–421. DOI: 10.1016/j.physletb.2013.11.069. arXiv: 1307.2253 [hep-ph].

[96] A. Albert et al. "Recommendations of the LHC Dark Matter Working Group: Comparing LHC searches for dark matter mediators in visible and invisible decay channels and calculations of the thermal relic density". *Phys. Dark Univ.* 26 (2019), p. 100377. DOI: 10.1016/j.dark.2019.100377. arXiv: 1703.05703 [hep-ex].

[97] D. Abercrombie et al. "Dark Matter benchmark models for early LHC Run-2 Searches: Report of the ATLAS/CMS Dark Matter Forum". *Phys. Dark Univ.* 27 (2020). Ed. by Antonio Boveia et al., p. 100371. DOI: 10.1016/j.dark.2019.100371. arXiv: 1507.00966 [hep-ex].

[98] S. P. Martin. "A Supersymmetry primer". *Adv. Ser. Direct. High Energy Phys.* 18 (1998). Ed. by Gordon L. Kane, pp. 1–98. DOI: 10.1142/9789812839657_0001. arXiv: hep-ph/9709356.

[99] ATLAS Collaboration. "Search for dark matter candidates and large extra dimensions in events with a jet and missing transverse momentum with the ATLAS detector". *JHEP* 04 (2013), p. 075. DOI: 10.1007/JHEP04(2013)075. arXiv: 1210.4491 [hep-ex].

[100] G. D'Ambrosio et al. "Minimal flavor violation: An Effective field theory approach". *Nucl. Phys. B* 645 (2002), pp. 155–187. DOI: 10.1016/S0550-3213(02)00836-2. arXiv: hep-ph/0207036.

[101] J. Andrea, B. Fuks, and F. Maltoni. "Monotops at the LHC". *Phys. Rev. D* 84 (2011), p. 074025. DOI: 10.1103/PhysRevD.84.074025. arXiv: 1106.6199 [hep-ph].

[102] J.L. Agram et al. "Monotop phenomenology at the Large Hadron Collider". *Phys. Rev. D* 89.1 (2014), p. 014028. DOI: 10.1103/PhysRevD.89.014028. arXiv: 1311.6478 [hep-ph].

[103] I. Boucheneb et al. "Revisiting monotop production at the LHC". *JHEP* 01 (2015), p. 017. DOI: 10.1007/JHEP01(2015)017. arXiv: 1407.7529 [hep-ph].

[104] ATLAS Collaboration. "Dark matter summary plots for s-channel, 2HDM+a, Higgs portal and Dark Higgs models". (2024).

[105] CMS Collaboration. "Dark sector searches with the CMS experiment". (May 2024). arXiv: 2405.13778 [hep-ex].

[106] ATLAS Collaboration. "Combined Measurement of the Higgs Boson Mass from the H→$\gamma\gamma$ and H→ZZ*→4ℓ Decay Channels with the ATLAS Detector Using s=7, 8, and 13 TeV pp Collision Data". *Phys. Rev. Lett.* 131.25 (2023), p. 251802. DOI: 10.1103/PhysRevLett.131.251802. arXiv: 2308.04775 [hep-ex].

[107] G. F. Giudice. "Naturalness after LHC8". *PoS* EPS-HEP2013 (2013), p. 163. DOI: 10.22323/1.180.0163. arXiv: 1307.7879 [hep-ph].

[108] C. T. Hill and E. H. Simmons. "Strong Dynamics and Electroweak Symmetry Breaking". *Phys. Rept.* 381 (2003). [Erratum: Phys.Rept. 390, 553–554 (2004)], pp. 235–402. DOI: 10.1016/S0370-1573(03)00140-6. arXiv: hep-ph/0203079.

[109] K. Agashe, R. Contino, and A. Pomarol. "The Minimal composite Higgs model". *Nucl. Phys. B* 719 (2005), pp. 165–187. DOI: 10.1016/j.nuclphysb.2005.04.035. arXiv: hep-ph/0412089.

[110] M. Schmaltz and D. Tucker-Smith. "Little Higgs review". *Ann. Rev. Nucl. Part. Sci.* 55 (2005), pp. 229–270. DOI: 10.1146/annurev.nucl.55.090704.151502. arXiv: hep-ph/0502182.

[111] N. Arkani-Hamed et al. "The Littlest Higgs". *Journal of High Energy Physics* 2002.07 (Aug. 2002), p. 034. DOI: 10.1088/1126-6708/2002/07/034. URL: https://dx.doi.org/10.1088/1126-6708/2002/07/034.

[112] ATLAS Collaboration. "Search for pair and single production of new heavy quarks that decay to a Z boson and a third generation quark in pp collisions at $\sqrt{s} = 8$ TeV with the ATLAS detector". (2014).

[113] J. A. Aguilar-Saavedra et al. "Handbook of vectorlike quarks: Mixing and single production". *Phys. Rev. D* 88.9 (2013), p. 094010. DOI: 10.1103/PhysRevD.88.094010. arXiv: 1306.0572 [hep-ph].

[114] M. Buchkremer et al. "Model Independent Framework for Searches of Top Partners". *Nucl. Phys. B* 876 (2013), pp. 376–417. DOI: 10.1016/j.nuclphysb.2013.08.010. arXiv: 1305.4172 [hep-ph].

[115] Michael S. Chanowitz and M. K. Gaillard. "The TeV physics of strongly interacting W's and Z's". *Nuclear Physics B* 261 (1985), pp. 379–431. ISSN: 0550-3213. DOI: https://doi.org/10.1016/0550-3213(85)90580-2. URL: https://www.sciencedirect.com/science/article/pii/0550321385905802.

[116] O. Matsedonskyi, G. Panico, and A. Wulzer. "On the interpretation of Top Partners searches". *Journal of High Energy Physics* 2014.12 (Dec. 2014), p. 97. ISSN: 1029-8479. DOI: 10.1007/JHEP12(2014)097. URL: https://doi.org/10.1007/JHEP12(2014)097.

[117] ATLAS Collaboration. "Search for pair and single production of new heavy quarks that decay to a Z boson and a third-generation quark in pp collisions at $\sqrt{s} = 8$ TeV with the ATLAS detector". *JHEP* 11 (2014), p. 104. DOI: 10.1007/JHEP11(2014)104. arXiv: 1409.5500 [hep-ex].

[118] J. A. Aguilar-Saavedra. *Protos - PROgram for TOp Simulations*. Accessed: 2023-08-25. URL: http://jaguilar.web.cern.ch/jaguilar/protos/.

[119] ATLAS Collaboration. "Search for production of vector-like quark pairs and of four top quarks in the lepton-plus-jets final state in pp collisions at $\sqrt{s} = 8$ TeV with the ATLAS detector". *JHEP* 08 (2015), p. 105. DOI: 10.1007/JHEP08(2015)105. arXiv: 1505.04306 [hep-ex].

[120] ATLAS Collaboration. "Search for vector-like B quarks in events with one isolated lepton, missing transverse momentum and jets at $\sqrt{s} = 8$ TeV with the ATLAS detector". *Phys. Rev. D* 91.11 (2015), p. 112011. DOI: 10.1103/PhysRevD.91.112011. arXiv: 1503.05425 [hep-ex].

[121] CMS Collaboration. "Search for vector-like charge 2/3 T quarks in proton-proton collisions at sqrt(s) = 8 TeV". *Phys. Rev. D* 93.1 (2016), p. 012003. DOI: 10.1103/PhysRevD.93.012003. arXiv: 1509.04177 [hep-ex].

[122] CMS Collaboration. "Search for pair-produced vectorlike B quarks in proton-proton collisions at $\sqrt{s}$=8 TeV". *Phys. Rev. D* 93.11 (2016), p. 112009. DOI: 10.1103/PhysRevD.93.112009. arXiv: 1507.07129 [hep-ex].

[123] CMS Collaboration. "Search for Top-Quark Partners with Charge 5/3 in the Same-Sign Dilepton Final State". *Phys. Rev. Lett.* 112.17 (2014), p. 171801. DOI: 10.1103/PhysRevLett.112.171801. arXiv: 1312.2391 [hep-ex].

[124] ATLAS Collaboration. "Search for single production of vector-like quarks decaying into Wb in pp collisions at $\sqrt{s} = 8$ TeV with the ATLAS detector". *Eur. Phys. J. C* 76.8 (2016), p. 442. DOI: 10.1140/epjc/s10052-016-4281-8. arXiv: 1602.05606 [hep-ex].

[125] ATLAS Collaboration. "Search for pair-production of vector-like quarks in pp collision events at s=13 TeV with at least one leptonically decaying Z boson and a third-generation quark with the ATLAS detector". *Phys. Lett. B* 843 (2023), p. 138019. DOI: 10.1016/j.physletb.2023.138019. arXiv: 2210.15413 [hep-ex].

[126] ATLAS Collaboration. "Search for pair-production of vector-like quarks in lepton+jets final states containing at least one b-tagged jet using the Run 2 data from the ATLAS experiment". *Phys. Lett. B* 854 (2024), p. 138743. DOI: 10.1016/j.physletb.2024.138743. arXiv: 2401.17165 [hep-ex].

[127] ATLAS Collaboration. "Search for pair-production of vector-like quarks in lepton+jets final states containing at least one b-tagged jet using the Run 2 data from the ATLAS experiment". *Phys. Lett. B* 854 (2024), p. 138743. DOI: 10.1016/j.physletb.2024.138743. arXiv: 2401.17165 [hep-ex].

[128] ATLAS Collaboration. "Search for singly produced vectorlike top partners in multilepton final states with 139 fb-1 of pp collision data at s=13 TeV with the ATLAS detector". *Phys. Rev. D* 109.11 (2024), p. 112012. DOI: 10.1103/PhysRevD.109.112012. arXiv: 2307.07584 [hep-ex].

[129] ATLAS Collaboration. "Search for single production of vector-like T quarks decaying into Ht or Zt in pp collisions at $\sqrt{s} = 13$ TeV with the ATLAS detector". *JHEP* 08 (2023), p. 153. DOI: 10.1007/JHEP08(2023)153. arXiv: 2305.03401 [hep-ex].

[130] ATLAS Collaboration. "Search for single production of a vectorlike T quark decaying into a Higgs boson and top quark with fully hadronic final states using the ATLAS detector". *Phys. Rev. D* 105.9 (2022), p. 092012. DOI: 10.1103/PhysRevD.105.092012. arXiv: 2201.07045 [hep-ex].

[131] CMS Collaboration. "Search for pair production of vector-like quarks in leptonic final states in proton-proton collisions at $\sqrt{s} = 13$ TeV". *JHEP* 07 (2023), p. 020. DOI: 10.1007/JHEP07(2023)020. arXiv: 2209.07327 [hep-ex].

[132] CMS Collaboration. "Search for a vector-like quark T′→ tH via the diphoton decay mode of the Higgs boson in proton-proton collisions at $\sqrt{s} = 13$ TeV". *JHEP* 09 (2023), p. 057. DOI: 10.1007/JHEP09(2023)057. arXiv: 2302.12802 [hep-ex].

[133] CMS Collaboration. "Search for single production of a vector-like T quark decaying to a top quark and a Z boson in the final state with jets and missing transverse momentum at $\sqrt{s} = 13$ TeV". *JHEP* 05 (2022), p. 093. DOI: 10.1007/JHEP05(2022)093. arXiv: 2201.02227 [hep-ex].

[134] CMS Collaboration. "Review of searches for vector-like quarks, vector-like leptons, and heavy neutral leptons in proton-proton collisions at $\sqrt{s}$ = 13 TeV at the CMS experiment". (May 2024). arXiv: 2405.17605 [hep-ex].

[135] ATLAS Collaboration. "Search for single vector-like B quark production and decay via $B \to bH(b\bar{b})$ in pp collisions at $\sqrt{s} = 13$ TeV with the ATLAS detector". *JHEP* 11 (2023), p. 168. DOI: 10.1007/JHEP11(2023)168. arXiv: 2308.02595 [hep-ex].

[136] A. Banerjee et al. *Vector-like quarks: status and new directions at the LHC*. 2024. arXiv: 2406.09193 [hep-ph]. URL: https://arxiv.org/abs/2406.09193.

[137] "LHC Machine". *JINST* 3 (2008). Ed. by L. Evans and P. Bryant, S08001. DOI: 10.1088/1748-0221/3/08/S08001.

[138] "LHC Design Report. 3. The LHC injector chain". (Dec. 2004). Ed. by M. Benedikt et al. DOI: 10.5170/CERN-2004-003-V-3.

[139] *CERN: Accelerating science*. https://home.cern/.

[140] E. Mobs. "The CERN accelerator complex - August 2018. Complexe des accélérateurs du CERN - Août 2018". (2018). General Photo. URL: https://cds.cern.ch/record/2636343.

[141] A. Augusto Alves Jr. et al. "The LHCb Detector at the LHC". *JINST* 3 (2008), S08005. DOI: 10.1088/1748-0221/3/08/S08005.

[142] K. Aamodt et al. "The ALICE experiment at the CERN LHC". *JINST* 3 (2008), S08002. DOI: 10.1088/1748-0221/3/08/S08002.

[143] CMS and TOTEM collaborations. "CMS-TOTEM Precision Proton Spectrometer". (Sept. 2014).

[144] O. Adriani et al. "Technical design report of the LHCf experiment: Measurement of photons and neutral pions in the very forward region of LHC". (Feb. 2006).

[145] J. Pinfold et al. "Technical Design Report of the MoEDAL Experiment". (June 2009).

[146] H. Abreu et al. "Technical Proposal: FASERnu". (Jan. 2020). arXiv: 2001.03073 [physics.ins-det].

[147] M. Ferro-Luzzi. "Luminosity and luminous region shape for pure Gaussian bunches". (Sept. 2012).

[148] ATLAS Collaboration. "Luminosity determination in pp collisions at $\sqrt{s} = 13$ TeV using the ATLAS detector at the LHC". *Eur. Phys. J. C* 83.10 (2023), p. 982. DOI: 10.1140/epjc/s10052-023-11747-w. arXiv: 2212.09379 [hep-ex].

[149] ATLAS Collaboration. *Public ATLAS Luminosity Results for Run-2 of the LHC*. https://twiki.cern.ch/twiki/bin/view/AtlasPublic/LuminosityPublicResultsRun2.

[150] "High-Luminosity Large Hadron Collider (HL-LHC) : Preliminary Design Report". (Dec. 2015). Ed. by G. Apollinari et al. DOI: 10.5170/CERN-2015-005.

[151] ATLAS Collaboration. "ATLAS: Detector and physics performance technical design report. Volume 1". (May 1999).

[152] R. M. Bianchi. "ATLAS experiment schematic or layout illustration". General Photo. 2022. URL: https://cds.cern.ch/record/2837191.

[153] J. Pequenao. "Computer generated image of the ATLAS inner detector". 2008. URL: https://cds.cern.ch/record/1095926.

[154] M. Capeans et al. "ATLAS Insertable B-Layer Technical Design Report". (Sept. 2010).

[155] B. Mindur. "ATLAS Transition Radiation Tracker (TRT): Straw tubes for tracking and particle identification at the Large Hadron Collider". *Nucl. Instrum. Meth. A* 845 (2017). Ed. by G. Badurek et al., pp. 257–261. DOI: 10.1016/j.nima.2016.04.026.

[156] F. Cavallari. "Performance of calorimeters at the LHC". *J. Phys. Conf. Ser.* 293 (2011). Ed. by Yifang Wang, p. 012001. DOI: 10.1088/1742-6596/293/1/012001.

[157] J. Pequenao. "Computer Generated image of the ATLAS calorimeter". 2008. URL: https://cds.cern.ch/record/1095927.

[158] J. Pequenao. "Computer generated image of the ATLAS Muons subsystem". 2008. URL: https://cds.cern.ch/record/1095929.

[159] ATLAS Collaboration. "Performance of the ATLAS Trigger System in 2015". *Eur. Phys. J. C* 77.5 (2017), p. 317. DOI: 10.1140/epjc/s10052-017-4852-3. arXiv: 1611.09661 [hep-ex].

[160] ATLAS Collaboration. *2015 start-up trigger menu and initial performance assessment of the ATLAS trigger using Run-2 data*. Tech. rep. Geneva: CERN, 2016. URL: https://cds.cern.ch/record/2136007.

[161] ATLAS Collaboration. "Operation of the ATLAS trigger system in Run 2". *JINST* 15.10 (2020), P10004. DOI: 10.1088/1748-0221/15/10/P10004. arXiv: 2007.12539 [physics.ins-det].

[162] W. Panduro Vazquez. *The ATLAS Data Acquisition system in LHC Run 2*. Tech. rep. 3. Geneva: CERN, 2017. DOI: 10.1088/1742-6596/898/3/032017. URL: https://cds.cern.ch/record/2244345.

[163] R. P. Feynman. "The behavior of hadron collisions at extreme energies". *Conf. Proc. C* 690905 (1969), pp. 237–258.

[164] R. D. Ball et al. "Parton distributions for the LHC Run II". *JHEP* 04 (2015), p. 040. DOI: 10.1007/JHEP04(2015)040. arXiv: 1410.8849 [hep-ph].

[165] A. D. Martin et al. "Parton distributions for the LHC". *Eur. Phys. J. C* 63 (2009), pp. 189–285. DOI: 10.1140/epjc/s10052-009-1072-5. arXiv: 0901.0002 [hep-ph].

[166] H.-L. Lai et al. "New parton distributions for collider physics". *Phys. Rev. D* 82 (2010), p. 074024. DOI: 10.1103/PhysRevD.82.074024. arXiv: 1007.2241 [hep-ph].

[167] J. Pumplin et al. "New generation of parton distributions with uncertainties from global QCD analysis". *JHEP* 07 (2002), p. 012. DOI: 10.1088/1126-6708/2002/07/012. arXiv: hep-ph/0201195.

[168] J. M. Campbell, J. W. Huston, and W. J. Stirling. "Hard Interactions of Quarks and Gluons: A Primer for LHC Physics". *Rept. Prog. Phys.* 70 (2007), p. 89. DOI: 10.1088/0034-4885/70/1/R02. arXiv: hep-ph/0611148.

[169] T. Sjostrand, S. Mrenna, and P. Z. Skands. "A Brief Introduction to PYTHIA 8.1". *Comput. Phys. Commun.* 178 (2008), pp. 852–867. DOI: 10.1016/j.cpc.2008.01.036. arXiv: 0710.3820 [hep-ph].

[170] M. Bahr et al. "Herwig++ Physics and Manual". *Eur. Phys. J. C* 58 (2008), pp. 639–707. DOI: 10.1140/epjc/s10052-008-0798-9. arXiv: 0803.0883 [hep-ph].

[171] S. Catani et al. "QCD matrix elements + parton showers". *JHEP* 11 (2001), p. 063. DOI: 10.1088/1126-6708/2001/11/063. arXiv: hep-ph/0109231.

[172] M. L. Mangano et al. "Matching matrix elements and shower evolution for top-quark production in hadronic collisions". *JHEP* 01 (2007), p. 013. DOI: 10.1088/1126-6708/2007/01/013. arXiv: hep-ph/0611129.

[173] B. Andersson et al. "Parton Fragmentation and String Dynamics". *Phys. Rept.* 97 (1983), pp. 31–145. DOI: 10.1016/0370-1573(83)90080-7.

[174] B.R. Webber. "A QCD Model for Jet Fragmentation Including Soft Gluon Interference". *Nucl. Phys. B* 238 (1984), pp. 492–528. DOI: 10.1016/0550-3213(84)90333-X.

[175] T. Gleisberg et al. "Event generation with SHERPA 1.1". *JHEP* 02 (2009), p. 007. DOI: 10.1088/1126-6708/2009/02/007. arXiv: 0811.4622 [hep-ph].

[176] D. J. Lange. "The EvtGen particle decay simulation package". *Nucl. Instrum. Meth. A* 462 (2001). Ed. by S. Erhan, P. Schlein, and Y. Rozen, pp. 152–155. DOI: 10.1016/S0168-9002(01)00089-4.

[177] T. Sjostrand and M. van Zijl. "A Multiple Interaction Model for the Event Structure in Hadron Collisions". *Phys. Rev. D* 36 (1987), p. 2019. DOI: 10.1103/PhysRevD.36.2019.

[178] ATLAS Collaboration. "Measurement of the underlying event in jet events from 7 TeV proton-proton collisions with the ATLAS detector". *Eur. Phys. J. C* 74.8 (2014), p. 2965. DOI: 10.1140/epjc/s10052-014-2965-5. arXiv: 1406.0392 [hep-ex].

[179] R. D. Ball et al. "Parton distributions with LHC data". *Nucl. Phys. B* 867 (2013), pp. 244–289. DOI: 10.1016/j.nuclphysb.2012.10.003. arXiv: 1207.1303 [hep-ph].

[180] "The Pythia 8 A3 tune description of ATLAS minimum bias and inelastic measurements incorporating the Donnachie-Landshoff diffractive model". (Aug. 2016).

[181] ATLAS Collaboration. "Measurement of the Inelastic Proton-Proton Cross Section at $\sqrt{s} = 13$ TeV with the ATLAS Detector at the LHC". *Phys. Rev. Lett.* 117.18 (2016), p. 182002. DOI: 10.1103/PhysRevLett.117.182002. arXiv: 1606.02625 [hep-ex].

[182] ATLAS Collaboration. "The ATLAS Simulation Infrastructure". *Eur. Phys. J. C* 70 (2010), pp. 823–874. DOI: 10.1140/epjc/s10052-010-1429-9. arXiv: 1005.4568 [physics.ins-det].

[183] S. Agostinelli et al. "GEANT4–a simulation toolkit". *Nucl. Instrum. Meth. A* 506 (2003), pp. 250–303. DOI: 10.1016/S0168-9002(03)01368-8.

[184] W. Lukas. "Fast Simulation for ATLAS: Atlfast-II and ISF". *J. Phys. Conf. Ser.* 396 (2012). Ed. by M. Ernst et al., p. 022031. DOI: 10.1088/1742-6596/396/2/022031.

[185] J. Schaarschmidt. "The new ATLAS Fast Calorimeter Simulation". *J. Phys. Conf. Ser.* 898.4 (2017). Ed. by R. Mount and C. Tull, p. 042006. DOI: 10.1088/1742-6596/898/4/042006.

[186] J. Alwall et al. "MadGraph 5 : Going Beyond". *JHEP* 06 (2011), p. 128. DOI: 10.1007/JHEP06(2011)128. arXiv: 1106.0522 [hep-ph].

[187] J. Alwall et al. "The automated computation of tree-level and next-to-leading order differential cross sections, and their matching to parton shower simulations". *JHEP* 07 (2014), p. 079. DOI: 10.1007/JHEP07(2014)079. arXiv: 1405.0301 [hep-ph].

[188] P. Nason. "A New method for combining NLO QCD with shower Monte Carlo algorithms". *JHEP* 11 (2004), p. 040. DOI: 10.1088/1126-6708/2004/11/040. arXiv: hep-ph/0409146.

[189] S. Frixione, P. Nason, and C. Oleari. "Matching NLO QCD computations with Parton Shower simulations: the POWHEG method". *JHEP* 11 (2007), p. 070. DOI: 10.1088/1126-6708/2007/11/070. arXiv: 0709.2092 [hep-ph].

[190] S. Alioli et al. "A general framework for implementing NLO calculations in shower Monte Carlo programs: the POWHEG BOX". *JHEP* 06 (2010), p. 043. DOI: 10.1007/JHEP06(2010)043. arXiv: 1002.2581 [hep-ph].

[191] S. Frixione et al. "Angular correlations of lepton pairs from vector boson and top quark decays in Monte Carlo simulations". *JHEP* 04 (2007), p. 081. DOI: 10.1088/1126-6708/2007/04/081. arXiv: hep-ph/0702198.

[192] P. Artoisenet et al. "Automatic spin-entangled decays of heavy resonances in Monte Carlo simulations". *JHEP* 03 (2013), p. 015. DOI: 10.1007/JHEP03(2013)015. arXiv: 1212.3460 [hep-ph].

[193] P. Bärnreuther, M. Czakon, and A. Mitov. "Percent Level Precision Physics at the Tevatron: First Genuine NNLO QCD Corrections to $q\bar{q} \to t\bar{t} + X$". *Phys. Rev. Lett.* 109 (2012), p. 132001. DOI: 10.1103/PhysRevLett.109.132001. arXiv: 1204.5201 [hep-ph].

[194] M. Czakon and A. Mitov. "Top++: A Program for the Calculation of the Top-Pair Cross-Section at Hadron Colliders". *Comput. Phys. Commun.* 185 (2014), p. 2930. DOI: 10.1016/j.cpc.2014.06.021. arXiv: 1112.5675 [hep-ph].

[195] M. Czakon and A. Mitov. "NNLO corrections to top-pair production at hadron colliders: the all-fermionic scattering channels". *JHEP* 12 (2012), p. 054. DOI: 10.1007/JHEP12(2012)054. arXiv: 1207.0236 [hep-ph].

[196] M. Czakon and A. Mitov. "NNLO corrections to top pair production at hadron colliders: the quark-gluon reaction". *JHEP* 01 (2013), p. 080. DOI: 10.1007/JHEP01(2013)080. arXiv: 1210.6832 [hep-ph].

[197] M. Czakon, P. Fiedler, and A. Mitov. "Total Top-Quark Pair-Production Cross Section at Hadron Colliders Through $O(\alpha_S^4)$". *Phys. Rev. Lett.* 110 (2013), p. 252004. DOI: 10.1103/PhysRevLett.110.252004. arXiv: 1303.6254 [hep-ph].

[198] M. Cacciari et al. "Top-pair production at hadron colliders with next-to-next-to-leading logarithmic soft-gluon resummation". *Phys. Lett. B* 710 (2012), pp. 612–622. DOI: 10.1016/j.physletb.2012.03.013. arXiv: 1111.5869 [hep-ph].

[199] S. Frixione et al. "Single-top hadroproduction in association with a W boson". *JHEP* 07 (2008), p. 029. DOI: 10.1088/1126-6708/2008/07/029. arXiv: 0805.3067 [hep-ph].

[200] R. D. Ball et al. "Parton distributions for the LHC Run II". *JHEP* 04 (2015), p. 040. DOI: 10.1007/JHEP04(2015)040. arXiv: 1410.8849 [hep-ph].

[201] T. Sjöstrand et al. "An introduction to PYTHIA 8.2". *Comput. Phys. Commun.* 191 (2015), pp. 159–177. DOI: 10.1016/j.cpc.2015.01.024. arXiv: 1410.3012 [hep-ph].

[202] N. Kidonakis. "Two-loop soft anomalous dimensions for single top quark associated production with a W- or H-". *Phys. Rev. D* 82 (2010), p. 054018. DOI: 10.1103/PhysRevD.82.054018. arXiv: 1005.4451 [hep-ph].

[203] N. Kidonakis. "NNLL resummation for s-channel single top quark production". *Phys. Rev. D* 81 (2010), p. 054028. DOI: 10.1103/PhysRevD.81.054028. arXiv: 1001.5034 [hep-ph].

[204] N. Kidonakis. "Next-to-next-to-leading-order collinear and soft gluon corrections for t-channel single top quark production". *Phys. Rev. D* 83 (2011), p. 091503. DOI: 10.1103/PhysRevD.83.091503. arXiv: 1103.2792 [hep-ph].

[205] T. Gleisberg and S. Hoeche. "Comix, a new matrix element generator". *JHEP* 12 (2008), p. 039. DOI: 10.1088/1126-6708/2008/12/039. arXiv: 0808.3674 [hep-ph].

[206] F. Cascioli, P. Maierhofer, and S. Pozzorini. "Scattering Amplitudes with Open Loops". *Phys. Rev. Lett.* 108 (2012), p. 111601. DOI: 10.1103/PhysRevLett.108.111601. arXiv: 1111.5206 [hep-ph].

[207] S. Hoeche et al. "A critical appraisal of NLO+PS matching methods". *JHEP* 09 (2012), p. 049. DOI: 10.1007/JHEP09(2012)049. arXiv: 1111.1220 [hep-ph].

[208] S. Hoeche et al. "QCD matrix elements and truncated showers". *JHEP* 05 (2009), p. 053. DOI: 10.1088/1126-6708/2009/05/053. arXiv: 0903.1219 [hep-ph].

[209] S. Hoeche et al. "QCD matrix elements + parton showers: The NLO case". *JHEP* 04 (2013), p. 027. DOI: 10.1007/JHEP04(2013)027. arXiv: 1207.5030 [hep-ph].

[210] C. Anastasiou et al. "High precision QCD at hadron colliders: Electroweak gauge boson rapidity distributions at NNLO". *Phys. Rev. D* 69 (2004), p. 094008. DOI: 10.1103/PhysRevD.69.094008. arXiv: hep-ph/0312266.

[211] J. Bellm et al. "Herwig 7.0/Herwig++ 3.0 release note". *Eur. Phys. J. C* 76.4 (2016), p. 196. DOI: 10.1140/epjc/s10052-016-4018-8. arXiv: 1512.01178 [hep-ph].

[212] L. A. Harland-Lang et al. "Parton distributions in the LHC era: MMHT 2014 PDFs". *Eur. Phys. J. C* 75.5 (2015), p. 204. DOI: 10.1140/epjc/s10052-015-3397-6. arXiv: 1412.3989 [hep-ph].

[213] ATLAS Collaboration. *The ATLAS simulation of boson plus jets processes in Run 2*. Tech. rep. Geneva: CERN, May 2017. URL: https://cds.cern.ch/record/2261937.

[214] ATLAS Collaboration. "ATLAS Pythia 8 tunes to 7 TeV data". (Nov. 2014).

[215] A. Roy et al. "Novel interpretation strategy for searches of singly produced vectorlike quarks at the LHC". *Physical Review D* 101.11 (June 2020). DOI: 10.1103/physrevd.101.115027. URL: https://doi.org/10.1103%2Fphysrevd.101.115027.

[216] A. Roy and T. Andeen. "Non-resonant diagrams for single production of top and bottom partners". *Physics Letters B* 833 (Oct. 2022), p. 137330. DOI: 10.1016/j.physletb.2022.137330. URL: https://doi.org/10.1016%2Fj.physletb.2022.137330.

[217] G. Cacciapaglia et al. "Next-to-leading-order predictions for single vector-like quark production at the LHC". *Physics Letters B* 793 (2019), pp. 206–211. DOI: https://doi.org/10.1016/j.physletb.2019.04.056.

[218] J. Butterworth et al. "PDF4LHC recommendations for LHC Run II". *J. Phys. G* 43 (2016), p. 023001. DOI: 10.1088/0954-3899/43/2/023001. arXiv: 1510.03865 [hep-ph].

[219] ATLAS Collaboration. *The ATLAS Pythia 8 tunes to 7 TeV data*. Tech. rep. ATL-PHYS-PUB-2014-021. Geneva: CERN, Nov. 2014. URL: https://cds.cern.ch/record/1966419.

[220] J. K. Anders and M. D'Onofrio. *V+Jets theoretical uncertainties estimation via a parameterisation method*. Tech. rep. Geneva: CERN, Jan. 2016. URL: https://cds.cern.ch/record/2125718.

[221] ATLAS Collaboration. "Evidence for the $H \to b\bar{b}$ decay with the ATLAS detector". *JHEP* 12 (2017), p. 024. DOI: 10.1007/JHEP12(2017)024. arXiv: 1708.03299 [hep-ex].

[222] J. Butterworth et al. *Single Boson and Diboson Production Cross Sections in pp Collisions at* $\sqrt{s} = 7$ *TeV*. Tech. rep. Geneva: CERN, Aug. 2010. URL: https://cds.cern.ch/record/1287902.

[223] ATLAS Collaboration. *Cross-section NLO ttV*. URL: https://twiki.cern.ch/twiki/bin/view/AtlasProtected/CrossSectionNLOttV.

[224] J. Pequenao. "How ATLAS detects particles: diagram of particle paths in the detector". 2013. URL: https://cds.cern.ch/record/1505342.

[225] ATLAS COLLABORATION. "Performance of the ATLAS Track Reconstruction Algorithms in Dense Environments in LHC Run 2". *Eur. Phys. J. C* 77.10 (2017), p. 673. DOI: 10.1140/epjc/s10052-017-5225-7. arXiv: 1704.07983 [hep-ex].

[226] T. Cornelissen et al. "The new ATLAS track reconstruction (NEWT)". *J. Phys. Conf. Ser.* 119 (2008). Ed. by Randall Sobie, Reda Tafirout, and Jana Thomson, p. 032014. DOI: 10.1088/1742-6596/119/3/032014.

[227] R. Fruhwirth. "Application of Kalman filtering to track and vertex fitting". *Nucl. Instrum. Meth. A* 262 (1987), pp. 444–450. DOI: 10.1016/0168-9002(87)90887-4.

[228] ATLAS Collaboration. "Electron reconstruction and identification in the ATLAS experiment using the 2015 and 2016 LHC proton-proton collision data at $\sqrt{s} = 13$ TeV". *Eur. Phys. J. C* 79.8 (2019), p. 639. DOI: 10.1140/epjc/s10052-019-7140-6. arXiv: 1902.04655 [physics.ins-det].

[229] ATLAS Collaboration. "Electron and photon performance measurements with the ATLAS detector using the 2015–2017 LHC proton-proton collision data". *JINST* 14.12 (2019), P12006. DOI: 10.1088/1748-0221/14/12/P12006. arXiv: 1908.00005 [hep-ex].

[230] ATLAS Collaboration. "Topological cell clustering in the ATLAS calorimeters and its performance in LHC Run 1". *Eur. Phys. J. C* 77 (2017), p. 490. DOI: 10.1140/epjc/s10052-017-5004-5. arXiv: 1603.02934 [hep-ex].

[231] ATLAS Collaboration. "Electron efficiency measurements with the ATLAS detector using 2012 LHC proton–proton collision data". *Eur. Phys. J. C* 77.3 (2017), p. 195. DOI: 10.1140/epjc/s10052-017-4756-2. arXiv: 1612.01456 [hep-ex].

[232] ATLAS Collaboration. "Muon reconstruction performance of the ATLAS detector in proton–proton collision data at $\sqrt{s}$ =13 TeV". *Eur. Phys. J. C* 76.5 (2016), p. 292. DOI: 10.1140/epjc/s10052-016-4120-y. arXiv: 1603.05598 [hep-ex].

[233] ATLAS Collaboration. "Muon reconstruction and identification efficiency in ATLAS using the full Run 2 *pp* collision data set at $\sqrt{s} = 13$ TeV". *Eur. Phys. J. C* 81.7 (2021), p. 578. DOI: 10.1140/epjc/s10052-021-09233-2. arXiv: 2012.00578 [hep-ex].

[234] M. Cacciari, G. P. Salam, and G. Soyez. "The anti-k_t jet clustering algorithm". *JHEP* 04 (2008), p. 063. DOI: 10.1088/1126-6708/2008/04/063. arXiv: 0802.1189 [hep-ph].

[235] H. L. Li. *Search for $W' \to tb$ in the hadronic final state with the ATLAS Detector*. http://hep.uchicago.edu/seminars/semwin2015/holingli.pdf. Image from presentation by Ho Ling Li, accessed on January 5, 2015. 2015.

[236] ATLAS Collaboration. "Jet reconstruction and performance using particle flow with the ATLAS Detector". *Eur. Phys. J. C* 77.7 (2017), p. 466. DOI: 10.1140/epjc/s10052-017-5031-2. arXiv: 1703.10485 [hep-ex].

[237] ATLAS Collaboration. "Jet energy scale and resolution measured in proton–proton collisions at $\sqrt{s} = 13$ TeV with the ATLAS detector". *Eur. Phys. J. C* 81.8 (2021), p. 689. DOI: 10.1140/epjc/s10052-021-09402-3. arXiv: 2007.02645 [hep-ex].

[238] ATLAS Collaboration. "Performance of pile-up mitigation techniques for jets in *pp* collisions at $\sqrt{s} = 8$ TeV using the ATLAS detector". *Eur. Phys. J. C* 76.11 (2016), p. 581. DOI: 10.1140/epjc/s10052-016-4395-z. arXiv: 1510.03823 [hep-ex].

[239] ATLAS Collaboration. "Identification and rejection of pile-up jets at high pseudorapidity with the ATLAS detector". *The European Physical Journal C* 77.9 (2017), p. 580. DOI: 10.1140/epjc/s10052-017-5081-5. URL: https://doi.org/10.1140/epjc/s10052-017-5081-5.

[240] ATLAS Collaboration. "Optimisation of large-radius jet reconstruction for the ATLAS detector in 13 TeV proton–proton collisions". *Eur. Phys. J. C* 81.4 (2021), p. 334. DOI: 10.1140/epjc/s10052-021-09054-3. arXiv: 2009.04986 [hep-ex].

[241] D. Krohn, J. Thaler, and L.-T. Wang. "Jet Trimming". *JHEP* 02 (2010), p. 084. DOI: 10.1007/JHEP02(2010)084. arXiv: 0912.1342 [hep-ph].

[242] ATLAS Collaboration. "In situ calibration of large-radius jet energy and mass in 13 TeV proton–proton collisions with the ATLAS detector". *Eur. Phys. J. C* 79.2 (2019), p. 135. DOI: 10.1140/epjc/s10052-019-6632-8. arXiv: 1807.09477 [hep-ex].

[243] ATLAS Collaboration. "ATLAS b-jet identification performance and efficiency measurement with $t\bar{t}$ events in pp collisions at $\sqrt{s} = 13$ TeV". *Eur. Phys. J. C* 79.11 (2019), p. 970. DOI: 10.1140/epjc/s10052-019-7450-8. arXiv: 1907.05120 [hep-ex].

[244] ATLAS Collaboration. "ATLAS flavour-tagging algorithms for the LHC Run 2 pp collision dataset". *Eur. Phys. J. C* 83.7 (2023), p. 681. DOI: 10.1140/epjc/s10052-023-11699-1. arXiv: 2211.16345 [physics.data-an].

[245] ATLAS Collaboration. "Measurement of b-tagging Efficiency of c-jets in $t\bar{t}$ Events Using a Likelihood Approach with the ATLAS Detector". (Mar. 2018).

[246] ATLAS Collaboration. "Calibration of light-flavour jet b-tagging rates on ATLAS proton-proton collision data at $\sqrt{s} = 13$˜TeV". (Apr. 2018).

[247] ATLAS Collaboration. "Boosted hadronic vector boson and top quark tagging with ATLAS using Run 2 data". (2020).

[248] ATLAS Collaboration. "Performance of top-quark and W-boson tagging with ATLAS in Run 2 of the LHC". *Eur. Phys. J. C* 79.5 (2019), p. 375. DOI: 10.1140/epjc/s10052-019-6847-8. arXiv: 1808.07858 [hep-ex].

[249] D. E. Soper and M. Spannowsky. "Finding top quarks with shower deconstruction". *Phys. Rev. D* 87 (2013), p. 054012. DOI: 10.1103/PhysRevD.87.054012. arXiv: 1211.3140 [hep-ph].

[250] M. Cacciari, G. P. Salam, and G. Soyez. "The catchment area of jets". *Journal of High Energy Physics* 2008.04 (Apr. 2008), p. 005. DOI: 10.1088/1126-6708/2008/04/005. URL: https://dx.doi.org/10.1088/1126-6708/2008/04/005.

[251] ATLAS Collaboration. "Performance of missing transverse momentum reconstruction with the ATLAS detector using proton-proton collisions at $\sqrt{s} = 13$ TeV". *Eur. Phys. J. C* 78.11 (2018), p. 903. DOI: 10.1140/epjc/s10052-018-6288-9. arXiv: 1802.08168 [hep-ex].

[252] D. Krohn, J. Thaler, and L.-T. Wang. "Jets with Variable R". *JHEP* 06 (2009), p. 059. DOI: 10.1088/1126-6708/2009/06/059. arXiv: 0903.0392 [hep-ph].

[253] ATLAS Collaboration. *Luminosity determination in pp collisions at $\sqrt{s} = 13$ TeV using the ATLAS detector at the LHC*. Tech. rep. The ATLAS-CONF-2019-021. Geneva: CERN, June 2019. URL: https://cds.cern.ch/record/2677054.

[254] G. Avoni et al. "The new LUCID-2 detector for luminosity measurement and monitoring in ATLAS". *JINST* 13.07 (2018), P07017. DOI: 10.1088/1748-0221/13/07/P07017.

[255] ATLAS Collaboration. *Jet Calibration and Systematic Uncertainties for Jets Reconstructed in the ATLAS Detector at $\sqrt{s} = 13$ TeV*. Tech. rep. Geneva: CERN, July 2015. URL: https://cds.cern.ch/record/2037613.

[256] ATLAS Collaboration. "Jet energy measurement with the ATLAS detector in proton-proton collisions at $\sqrt{s} = 7$ TeV". *Eur. Phys. J. C* 73.3 (2013), p. 2304. DOI: 10.1140/epjc/s10052-013-2304-2. arXiv: 1112.6426 [hep-ex].

[257] ATLAS Collaboration. *Tagging and suppression of pileup jets with the ATLAS detector*. Tech. rep. Geneva: CERN, May 2014. URL: https://cds.cern.ch/record/1700870.

[258] ATLAS Collaboration. *Measurement of the ATLAS Detector Jet Mass Response using Forward Folding with 80 fb^{-1} of $\sqrt{s} = 13$ TeV pp data*. Tech. rep. Geneva: CERN, July 2020. URL: https://atlas.web.cern.ch/Atlas/GROUPS/PHYSICS/CONFNOTES/ATLAS-CONF-2020-022.

[259] ATLAS Collaboration. "Search for large missing transverse momentum in association with one top-quark in proton-proton collisions at $\sqrt{s} = 13$ TeV with the ATLAS detector". *JHEP* 05 (2019), p. 041. DOI: 10.1007/JHEP05(2019)041. arXiv: 1812.09743 [hep-ex].

[260] ATLAS Collaboration. "Search for large missing transverse momentum in association with one top-quark in proton-proton collisions at $\sqrt{s}$ = 13 TeV with the ATLAS detector". *Journal of High Energy Physics* 2019.5 (May 2019). ISSN: 1029-8479. DOI: 10.1007/jhep05(2019)041. URL: http://dx.doi.org/10.1007/JHEP05(2019)041.

[261] T. Chen and C. Guestrin. "XGBoost: A Scalable Tree Boosting System". *Proceedings of the 22nd ACM SIGKDD International Conference on Knowledge Discovery and Data Mining*. KDD '16. San Francisco, California, USA: Association for Computing Machinery, 2016, pp. 785–794. ISBN: 9781450342322. DOI: 10.1145/2939672.2939785. URL: https://doi.org/10.1145/2939672.2939785.

[262] XGBoost documentation. URL: https://xgboost.readthedocs.io/en/latest/tutorials/model.html.

[263] P. Beja-Battais. *Overview of AdaBoost : Reconciling its views to better understand its dynamics*. 2023. arXiv: 2310.18323 [cs.LG]. URL: https://arxiv.org/abs/2310.18323.

[264] W. Verkerke and D. Kirkby. *The RooFit toolkit for data modeling*. 2003. arXiv: physics/0306116 [physics.data-an].

[265] L. Moneta et al. *The RooStats Project*. 2011. arXiv: 1009.1003 [physics.data-an].

[266] *TRExFitter framework*. URL: https://trexfitter-docs.web.cern.ch/trexfitter-docs/.

[267] *WorkspaceCombiner*. URL: https://twiki.cern.ch/twiki/bin/view/AtlasProtected/WorkspaceMaker.

[268] P. Virtanen et al. "SciPy 1.0: Fundamental Algorithms for Scientific Computing in Python". *Nat. Methods* 17 (2020), pp. 261–272. DOI: 10.1038/s41592-019-0686-2. arXiv: 1907.10121.

[269] L. M. Dery et al. "Weakly Supervised Classification in High Energy Physics". *JHEP* 05 (2017), p. 145. DOI: 10.1007/JHEP05(2017)145. arXiv: 1702.00414 [hep-ph].

[270] E. M. Metodiev, B. Nachman, and J. Thaler. "Classification without labels: Learning from mixed samples in high energy physics". *JHEP* 10 (2017), p. 174. DOI: 10.1007/JHEP10(2017)174. arXiv: 1708.02949 [hep-ph].

[271] ATLAS Collaboration. "Weakly supervised anomaly detection for resonant new physics in the dijet final state using proton-proton collisions at $\sqrt{s}$ = 13 TeV with the ATLAS detector". (Feb. 2025). arXiv: 2502.09770 [hep-ex].

[272] ATLAS Collaboration. "Dijet resonance search with weak supervision using $\sqrt{s} = 13$ TeV pp collisions in the ATLAS detector". *Phys. Rev. Lett.* 125.13 (2020), p. 131801. DOI: 10.1103/PhysRevLett.125.131801. arXiv: 2005.02983 [hep-ex].

[273] ATLAS Collaboration. "Anomaly detection search for new resonances decaying into a Higgs boson and a generic new particle X in hadronic final states using $\sqrt{s} = 13$ TeV pp collisions with the ATLAS detector". *Phys. Rev. D* 108 (2023), p. 052009. DOI: 10.1103/PhysRevD.108.052009. arXiv: 2306.03637 [hep-ex].

[274] ATLAS Collaboration. "Search for New Phenomena in Two-Body Invariant Mass Distributions Using Unsupervised Machine Learning for Anomaly Detection at $\sqrt{s} = 13$ TeV with the ATLAS Detector". *Physical Review Letters* 132.8 (2024). DOI: 10.1103/physrevlett.132.081801. arXiv: 2307.01612 [hep-ex].

[275] *Model-agnostic search for dijet resonances with anomalous jet substructure in proton-proton collisions at $\sqrt{s} = 13$ TeV*. Tech. rep. CMS-PAS-EXO-22-026. Geneva: CERN, 2024. URL: https://cds.cern.ch/record/2892677.

[276] G. Kasieczka et al. "The LHC Olympics 2020: A Community Challenge for Anomaly Detection in High Energy Physics". (Jan. 2021). arXiv: 2101.08320 [hep-ph].

[277] T. Aarrestad et al. "The Dark Machines Anomaly Score Challenge: Benchmark Data and Model Independent Event Classification for the Large Hadron Collider". *SciPost Physics* 12.1 (Jan. 2022). ISSN: 2542-4653. DOI: 10.21468/scipostphys.12.1.043. URL: http://dx.doi.org/10.21468/SciPostPhys.12.1.043.

[278] DarkMachines Community. *DarkMachines*. http://www.darkmachines.org.

[279] M. van Beekveld. *Unsupervised-Hackathon*. Zenodo, July 2020. DOI: 10.5281/zenodo.3961917. URL: https://doi.org/10.5281/zenodo.3961917.

[280] J. Alwall et al. "The automated computation of tree-level and next-to-leading order differential cross sections, and their matching to parton shower simulations". *JHEP* 07 (2014), p. 079. DOI: 10.1007/JHEP07(2014)079. arXiv: 1405.0301 [hep-ph].

[281] R. D. Ball et al. "Parton distributions from high-precision collider data". *Eur. Phys. J. C* 77.10 (2017), p. 663. DOI: 10.1140/epjc/s10052-017-5199-5. arXiv: 1706.00428 [hep-ph].

[282] T. Sjöstrand et al. "An introduction to PYTHIA 8.2". *Comput. Phys. Commun.* 191 (2015), pp. 159–177. DOI: 10.1016/j.cpc.2015.01.024. arXiv: 1410.3012 [hep-ph].

[283] M. L. Mangano et al. "ALPGEN, a generator for hard multiparton processes in hadronic collisions". *JHEP* 07 (2003), p. 001. DOI: 10.1088/1126-6708/2003/07/001. arXiv: hep-ph/0206293.

[284] J. de Favereau et al. "DELPHES 3, A modular framework for fast simulation of a generic collider experiment". *JHEP* 02 (2014), p. 057. DOI: 10.1007/JHEP02(2014)057. arXiv: 1307.6346 [hep-ex].

[285] M. van Beekveld. *Delphes card of the ATLAS detector for Unsupervised DarkMachines*. https://github.com/melli1992/unsupervised_darkmachines/blob/master/delphes_card_ATLAS.dat.

[286] M. Cacciari, G. P. Salam, and G. Soyez. "FastJet user manual: (for version 3.0.2)". *The European Physical Journal C* 72.3 (Mar. 2012). ISSN: 1434-6052. DOI: 10.1140/epjc/s10052-012-1896-2. URL: https://doi.org/10.1140/epjc/s10052-012-1896-2.

[287] "Expected performance of the ATLAS b-tagging algorithms in Run-2". (July 2015).

[288] L. Basso et al. "Phenomenology of the minimal $B-L$ extension of the standard model: Z' and neutrinos". *Phys. Rev. D* 80 (5 Sept. 2009), p. 055030. DOI: 10.1103/PhysRevD.80.055030. URL: https://link.aps.org/doi/10.1103/PhysRevD.80.055030.

[289] F. F. Deppisch, W. Liu, and M. Mitra. "Long-lived heavy neutrinos from Higgs decays". *JHEP* 08 (2018), p. 181. DOI: 10.1007/JHEP08(2018)181. arXiv: 1805.00001 [hep-ph].

[290] S. Amrith et al. "LHC constraints on a B-L gauge model using Contur". *JHEP* 05 (2019), p. 154. DOI: 10.1007/JHEP05(2019)154. arXiv: 1902.10171 [hep-ph].

[291] X.-G. He et al. "New-Z' phenomenology". *Phys. Rev. D* 43 (1 Jan. 1991), R22–R24. DOI: 10.1103/PhysRevD.43.R22. URL: https://link.aps.org/doi/10.1103/PhysRevD.43.R22.

[292] X.-G. He et al. "Simplest Z' model". *Phys. Rev. D* 44 (7 Oct. 1991), pp. 2118–2132. DOI: 10.1103/PhysRevD.44.2118. URL: https://link.aps.org/doi/10.1103/PhysRevD.44.2118.

[293] R. Barbier et al. "R-parity-violating supersymmetry". *Phys. Rept.* 420.1-6 (2005), pp. 1–195. DOI: 10.1016/j.physrep.2005.08.006.

[294] B. Fuks. "Beyond the Minimal Supersymmetric Standard Model: from theory to phenomenology". *International Journal of Modern Physics A* 27.07 (2012), p. 1230007. DOI: 10.1142/S0217751X12300074. URL: https://doi.org/10.1142/S0217751X12300074.

[295] J. Rosiek. "Complete set of Feynman rules for the minimal supersymmetric extension of the standard model". *Phys. Rev. D* 41 (11 June 1990), pp. 3464–3501. DOI: 10.1103/PhysRevD.41.3464. URL: https://link.aps.org/doi/10.1103/PhysRevD.41.3464.

[296] H. Haber. "The search for supersymmetry: Probing physics beyond the Standard Model". *Phys. Rept.* 117 (1985), pp. 75–263. DOI: 10.1016/0370-1573(85)90051-1.

[297] H. P. Nilles. "Supersymmetry, supergravity and particle physics". *Phys. Rept.* 110 (1984), pp. 1–162. DOI: 10.1016/0370-1573(84)90008-5.

[298] L. Ruff et al. "Deep One-Class Classification". *Proceedings of the 35th International Conference on Machine Learning*. Ed. by Jennifer Dy and Andreas Krause. Vol. 80. Proceedings of Machine Learning Research. PMLR, July 2018, pp. 4393–4402. URL: https://proceedings.mlr.press/v80/ruff18a.html.

[299] Sachin Goyal et al. "DROCC: Deep Robust One-Class Classification". (2020). arXiv: 2002.12718 [cs.LG]. URL: https://arxiv.org/abs/2002.12718.

[300] H. Qu, C. Li, and S. Qian. "Particle Transformer for Jet Tagging". (Feb. 2022). DOI: 10.48550/arXiv.2202.03772. arXiv: 2202.03772 [hep-ph].

[301] L. Builtjes et al. "Attention to the strengths of physical interactions: Transformer and graph-based event classification for particle physics experiments". (Nov. 2022). arXiv: 2211.05143 [hep-ph].

[302] A. Vaswani et al. "Attention Is All You Need". *CoRR* abs/1706.03762 (2023). DOI: 10.48550/arXiv.1706.03762. arXiv: 1706.03762 [cs.CL]. URL: https://arxiv.org/abs/1706.03762.

[303] D. Hendrycks and K. Gimpel. "Gaussian Error Linear Units (GELUs)". (June 2016). arXiv: 1606.08415 [cs.LG].

[304] S. Caron, L. Hendriks, and R. Verheyen. "Rare and Different: Anomaly Scores from a combination of likelihood and out-of-distribution models to detect new physics at the LHC". *SciPost Phys.* 12.2 (2022), p. 077. DOI: 10.21468/SciPostPhys.12.2.077. arXiv: 2106.10164 [hep-ph].

[305] D. J. Kösters et al. "Benchmarking energy consumption and latency for neuromorphic computing in condensed matter and particle physics". *APL Mach. Learn.* 1.1 (2023), p. 016101. DOI: 10.1063/5.0116699. arXiv: 2209.10481 [cs.ET].

[306] M. Crispim Romão, N. F. Castro, and R. Pedro. "Finding New Physics without learning about it: Anomaly Detection as a tool for Searches at Colliders". *Eur. Phys. J. C* 81.1 (2021). [Erratum: Eur.Phys.J.C 81, 1020 (2021)], p. 27. DOI: 10.1140/epjc/s10052-021-09813-2. arXiv: 2006.05432 [hep-ph].

[307] X. Deng and Z. Zhang. "Nonlinear Chemical Process Fault Diagnosis Using Ensemble Deep Support Vector Data Description". *Sensors* 20 (Aug. 2020), p. 4599. DOI: 10.3390/s20164599.

[308] S. Caron, R. Ruiz de Austri, and Z. Zhang. "Mixture-of-Theories training: can we find new physics and anomalies better by mixing physical theories?": *Journal of High Energy Physics* 2023.3 (Mar. 2023). ISSN: 1029-8479. DOI: 10.1007/jhep03(2023)004. URL: http://dx.doi.org/10.1007/JHEP03(2023)004.

[309] B. M. Dillon et al. "Anomalies, Representations, and Self-Supervision". (Jan. 2023). arXiv: 2301.04660 [hep-ph].

[310] L. Favaro et al. "Semi-visible jets, energy-based models, and self-supervision". (Dec. 2023). arXiv: 2312.03067 [hep-ph].

[311] G. Kasieczka et al. "Anomaly detection under coordinate transformations". *Phys. Rev. D* 107.1 (2023), p. 015009. DOI: 10.1103/PhysRevD.107.015009. arXiv: 2209.06225 [hep-ph].

[312] D. Jimenez Rezende and S. Mohamed. "Variational Inference with Normalizing Flows". May 2015. arXiv: 1505.05770 [stat.ML].

[313] K. Cranmer, J. Pavez, and G. Louppe. *Approximating Likelihood Ratios with Calibrated Discriminative Classifiers*. 2016. arXiv: 1506.02169 [stat.AP].

[314] A. Buckley et al. "General-purpose event generators for LHC physics". *Physics Reports* 504.5 (July 2011), pp. 145–233. ISSN: 0370-1573. DOI: 10.1016/j.physrep.2011.03.005. URL: http://dx.doi.org/10.1016/j.physrep.2011.03.005.

[315] "CARL Athena algorithm". URL: https://gitlab.cern.ch/sjiggins/carlathenaonnx/-/tree/master/carlAthenaOnnx.

[316] "CARL-Torch package". URL: https://github.com/sjiggins/carl-torch.

[317] A. Buckley et al. “Rivet user manual”. *Computer Physics Communications* 184.12 (Dec. 2013), pp. 2803–2819. ISSN: 0010-4655. DOI: 10.1016/j.cpc.2013.05.021. URL: http://dx.doi.org/10.1016/j.cpc.2013.05.021.

[318] ATLAS Collaboration. “Measurement of the Lund Jet Plane Using Charged Particles in 13 TeV Proton-Proton Collisions with the ATLAS Detector”. *Phys. Rev. Lett.* 124.22 (2020), p. 222002. DOI: 10.1103/PhysRevLett.124.222002. arXiv: 2004.03540 [hep-ex].

[319] ATLAS Collaboration. “Jet substructure in ATLAS”. *Meeting of the APS Division of Particles and Fields*. Oct. 2011. arXiv: 1110.1094 [hep-ex].

[320] Z. Zhang and M. R. Sabuncu. *Generalized Cross Entropy Loss for Training Deep Neural Networks with Noisy Labels*. 2018. arXiv: 1805.07836 [cs.LG].

[321] A. Valerio Miceli Barone et al. *Regularization techniques for fine-tuning in neural machine translation*. 2017. arXiv: 1707.09920 [cs.CL].

[322] C. Nwankpa et al. *Activation Functions: Comparison of trends in Practice and Research for Deep Learning*. 2018. arXiv: 1811.03378 [cs.LG].

[323] S. J. Reddi, S. Kale, and S. Kumar. “On the Convergence of Adam and Beyond”. *International Conference on Learning Representations*. 2018. URL: https://openreview.net/forum?id=ryQu7f-RZ.

[324] “Optimisation and performance studies of the ATLAS *b*-tagging algorithms for the 2017-18 LHC run”. (July 2017).

Esta Tesis ha sido financiada por la Agencia Estatal de Investigación y por el Ministerio de Ciencia, Innovación y Universidades, con cargo al proyecto PID2021-124912NB-I00.